Spring 2017

Magma genesis beneath active continental rifts

Kimberly Aviado
University of New Hampshire, Durham

MAGMA GENESIS BENEATH ACTIVE CONTINENTAL RIFTS

BY

KIMBERLY AVIADO
B.A., New York University, 2011

DISSERTATION

Submitted to the University of New Hampshire
in Partial Fulfillment of
the Requirements for the Degree of

Doctor of Philosophy in
Earth and Environmental Sciences

May, 2017

This dissertation has been examined and approved in partial fulfillment of the requirements for the degree of Doctor of Philosophy in Earth and Environmental Sciences by:

Dissertation Co-Director, Julia G. Bryce, Professor of Earth Sciences

Dissertation Co-Director, Samuel B. Mukasa, Affiliate Professor of Earth Sciences

William C. Clyde, Professor of Earth Sciences

Gianluca Bianchini, Associate Professor of Georesources and Mineralogical-Petrographic Applications, University of Ferrara

David W. Graham, Professor of Geology and Geophysics, Oregon State University

On April 10, 2017

Original approval signatures are on file with the University of New Hampshire Graduate School.

DEDICATION

This dissertation is dedicated to my parents, my husband, and in loving memory of Christopher R. Arayata.

ACKNOWLEDGMENTS

This work presented in this dissertation would not have been possible without the guidance and support of my co-advisors, Julie Bryce and Sam Mukasa. Thank you, Julie and Sam, for committing your time and resources to helping me grow as a scientist and student during my time at UNH, and for providing me with many opportunities to conduct great science. I would also like to thank my dissertation committee members Gianluca Bianchini, Will Clyde, and David Graham for their contributions to this project. Gianluca, thank you as well for providing samples and serving as an excellent host during my stays in Ferrara. I would also like to thank Jo Laird and Joe Licciardi for their support and advice during my time at UNH. A heartfelt thanks goes to Florencia Fahnestock for consistently going above and beyond to provide analytical (and moral) support. This work has also benefitted from the efforts of several post-docs, including Martin Guitreau and Joan Cabato. It is also built from the work of several authors, including work by Sarah Rilling-Hall and Claudio Natali, whom I thank for their contributions. I would also like to thank Wesley Le Masurier for providing samples and contributing his considerable expertise on West Antarctic volcanism to the development of Chapter III. Analytical work for this project involved many labs around the world, and I thank Dustin Trail and the Bruce Watson lab at RPI for providing laboratory space, materials, and experimental expertise while developing the homogenization protocol, and for Dustin's input in developing Chapter III of this dissertation. I am also grateful to Brian Monteleone and Nobu Shimizu for support while conducting SIMS analyses at WHOI, Nilanjan Chatterjee for assisting with electron microprobe analyses at MIT, and Janne Blichert-Toft and Phillipe Telouk for support for the MC-ICP-MS analyses at ENS-Lyon.

I am grateful to have been part of a supportive student body in the Earth Sciences department, and would like to thank Lizz Huss, Ashley Norton, Grace Delgado, Kiley Remiszewski, Abby D'Ambrosia, Kim Delong, Brian Madore, and Lorne Loudin for being great colleagues and friends. At the University of Ferrara, Paolo Sgualdo, Chiara Marchina, and Pier Paolo Giacomoni have also been wonderfully supportive colleagues.

I am grateful for NSF grants ANT-0739617, ANT-1321588, and EAR-125588 for providing support to carry out the work presented in Chapter II of this dissertation. The work in Chapter III was funded by NSF Grant 77-27546, ANT-0739617, ANT-1321588, and EAR-1255888. Analytical expenses for Chapter IV were paid for in part by a grant from an UNH ESCI-EOS graduate student award and NSF EAR-125588. Travel to several conferences to present this dissertation work was funded by UNH Graduate School Travel Grants. I was supported by teaching and research assistantships from the Department of Earth Sciences, a UNH Graduate School fellowship providing two years of summer research support, and a UNH Summer TA Fellowship providing one summer of support.

TABLE OF CONTENTS

LIST OF TABLES

LIST OF FIGURES

ABSTRACT

MAGMA GENESIS BENEATH ACTIVE CONTINENTAL RIFTS

by

Kimberly B. Aviado

University of New Hampshire, May, 2017

The East African Rift System (EARS) and the West Antarctic Rift System (WARS) are two of the largest continental rift systems on Earth, but the processes governing rift dynamics remain controversial. The large volume and distinct chemistry of Cenozoic rift-related lavas, combined with geophysical evidence for low-density mantle underlying both rifts, have traditionally been interpreted as evidence for anomalously hot mantle plumes actively rising from the deep mantle beneath both regions. However, in light of increasing evidence that these mantle structures may also be chemical in nature, alternative explanations highlight the role of heterogeneous, easily-fusible mantle components in driving magma genesis in the absence of significant thermal anomalies. These heterogeneous mantle domains may be linked to the complex tectonic histories of continents, which often involve multiple stages of accretion and associated recycling of materials between the crust and the mantle. In this dissertation, detailed chemical investigations of rift-related volcanic rocks provide critical new insight into the nature of the mantle underlying the two active rifts. In particular, the role of volatiles such as H_2O and CO_2 is highlighted due to the ability of these components to enhance mantle melting during rift-related decompression.

In Chapter II, the first geochemical information from submarine lavas in the Ross Embayment of West Antarctica are reported alongside subaerial lavas from islands and mainland

localities, which together provide evidence that volatilized, recycled mantle domains generated during ancient long-lived subduction along the paleo-Pacific margin of Gondwana are key components in the temporally evolving source of Cenozoic magmas (Aviado et al., 2015). In Chapter III, the first rift-wide study of magmatic volatiles recorded in olivine-hosted melt inclusions confirms that the West Antarctic mantle is enriched in H_2O and CO_2 on a wide scale, and links the production of hydrated and carbonated components to subduction-related metasomatic processes. These results provide a compelling link between continental assembly, the production of easily fusible, heterogeneous chemical domains in the sub-continental lithospheric mantle (SCLM) and upper mantle, and rifting plus associated magmatism. These links are further explored in Chapter IV, in which the trace element and radiogenic isotope (Sr-Nd-Hf-Pb) systematics of mantle xenoliths from the East African Rift System (EARS) illustrate that the SCLM bears witness to a complex history involving Proterozoic melt depletion events, Pan African continental assembly, late-stage metasomatism, and plume impingement. These results demonstrate that SCLM serves as an important long-lived host of heterogeneous recycled mantle domains that are sampled throughout multiple episodes of convergence and breakup.

Collectively, these chapters suggest that ongoing rifting and magmatism in the EARS and the WARS are in part tied to shallow mantle processes involving the heterogeneous SCLM, rather than having exclusively deep plume origins. These shallow processes emerge as a consequence of the complex, multistage evolution of continents.

CHAPTER I

INTRODUCTION

Voluminous alkaline magmatism that occurs away from active plate boundaries is often attributed to 'hotspot' or plume magmatism. In the classical model described by Morgan (1971), convective upwellings from the lower mantle supply heat and primordial material to the asthenosphere, where rapid decompression actively induces melting. Geophysical evidence for anomalous low-density mantle, combined with geochemical indications of alkali-rich, silica-undersaturated lavas and high-μ (μ = $^{238}U/^{204}Pb$) isotopic signatures, have suggested the existence of "plumes" of hot, chemically distinct materials that have traditionally been interpreted as originating from the deep mantle. Although plumes may contribute substantively to volcanism in certain areas such as Hawaii, in regions where intraplate magmatism is coupled with lithospheric extension, ambiguity may arise as to whether decompression melting arises due to active plume upwelling or as a passive response to thinning and extension of the lithosphere (e.g., McKenzie and Bickle, 1988). Melting dynamics may be further complicated by increasing evidence that many plumes are thermochemical structures, and that anomalous low-density mantle observed in many plume settings may in part be tied to compositional heterogeneity in the mantle (e.g., Hauri, 1996; Rooney et al., 2014). In particular, Schilling et al. (1980) were among the first to propose that "hot spots" were also "wet spots," highlighting the importance of water in inducing melting by lowering the mantle solidus, resulting in the potential for enhanced passive decompression melting relative to anhydrous mantle conditions (e.g., Green, 1973; Asimow and Langmuir, 2003). In addition to water, the presence of carbon dioxide, pyroxenite, and other easily fusible components in the mantle are

significant sources of mantle compositional heterogeneity that may contribute to melting anomalies observed in intraplate settings.

It has been proposed that volatiles and other similarly fusible chemistries such as eclogite are introduced into the mantle via recycling of subducted lithosphere, a process that has been linked to chemical heterogeneity in the mantle and the origins of deep mantle plumes (e.g., White and Hofmann, 1982). Present-day continents are the culmination of complex tectonic histories involving multiple phases of accretion, during which more shallow recycling of similarly volatile-rich, metasomatized and/or eclogitized materials can create heterogeneities in the lithospheric and sublithospheric mantle. In particular, the dense, metasomatized and eclogitized roots of continents may develop gravitational instabilities that cause the higher-density materials to founder into the convective mantle through mechanisms such as delamination or lithospheric drip (Elkins-Tanton, 2007; Lee et al., 2010), effectively thinning the lithosphere and introducing easily fusible, heterogeneous domains into the upper mantle that may contribute to the generation of continental intraplate magmas. In continental rifts, these dynamic processes raise questions regarding the extent to which recycling and subsequent fertilization with volatiles are the result of shallow lithospheric processes or have deep plume origins.

In the West Antarctic Rift System (WARS; Figure 1-1) and the East African Rift System (EARS; Figure 1-2), the processes governing rift dynamics remain controversial. Unusual Cenozoic volcanism, notable in terms of the anomalously large volumes and alkaline chemical compositions of erupted magmas, coupled with seismic imaging of low-density mantle structures, have been explained by the presence of mantle plumes actively welling up from the deep mantle as the major driver for tectonic and magmatic activity in the EARS and the WARS (Behrendt et al., 1994; Ebinger and Sleep, 1998; Wörner, 1999; Pik, 1999). However, where

geophysical (e.g., Hansen et al., 2012; 2014), structural, or geochemical evidence remains ambiguous, the mantle plume hypothesis may fail as an encompassing model for rift-wide magma genesis, and alternative models highlight the role of melting from volatilized, easily fusible components in the mantle underlying both rifts (Bell and Tilton, 2001; Beccaluva et al., 2011; Rooney et al., 2012; Aviado et al., 2015; Hudgins et al., 2015).

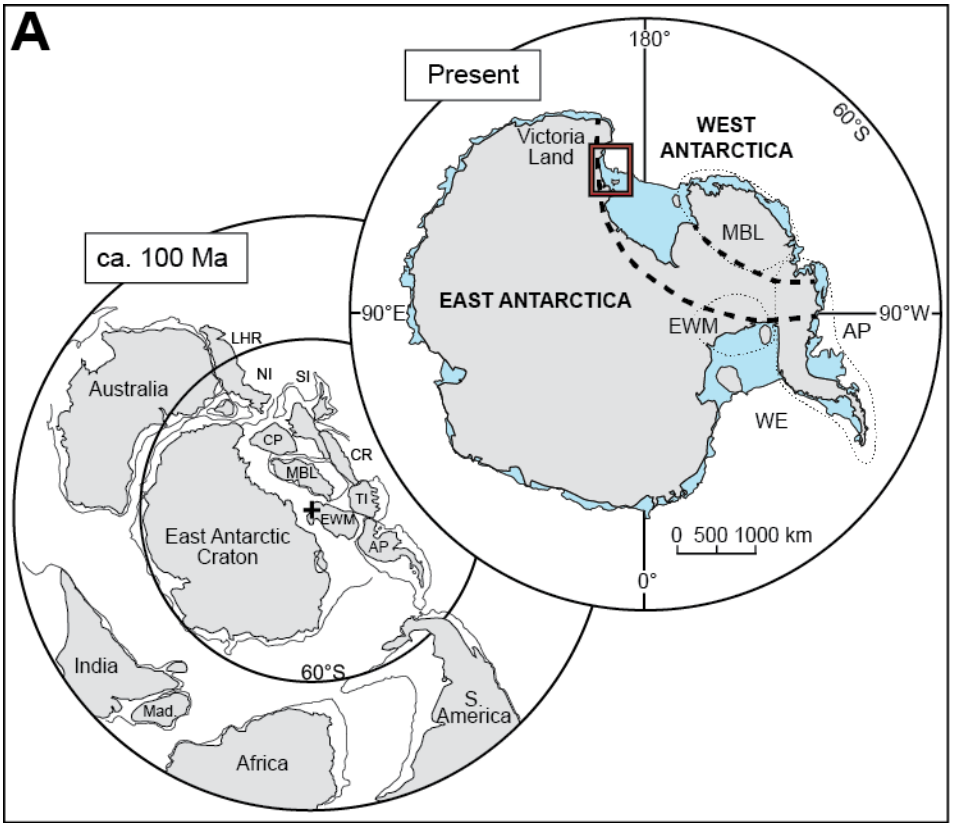

Figure 1-1. Sketch map (from Aviado et al., 2015) of Antarctica showing present-day East Antarctica, West Antarctica, the Weddell Embayment and the crustal blocks that comprise West Antarctica: MBL – Marie Byrd Land; EWM – Ellsworth Mountains; AP – Antarctic Peninsula. Thick dashed lines indicate the approximate boundary of the West Antarctic Rift System (after Rocchi et al., 2002). The map on the lower left is a tectonic reconstruction of the paleo-Pacific margin of Gondwana at ca. 100 Ma (after Mukasa and Dalziel, 2000). AP – Antarctic Peninsula; CP – Campbell Plateau; CR – Chatham Rise; EWM – Ellsworth-Whitmore block; LHF – Lord Howe Rise; NI – North Island, New Zealand; SI – South Island, New Zealand; TI – Thurston Island block. Bold crosshair indicates South Pole position (DiVenere et al., 1994).

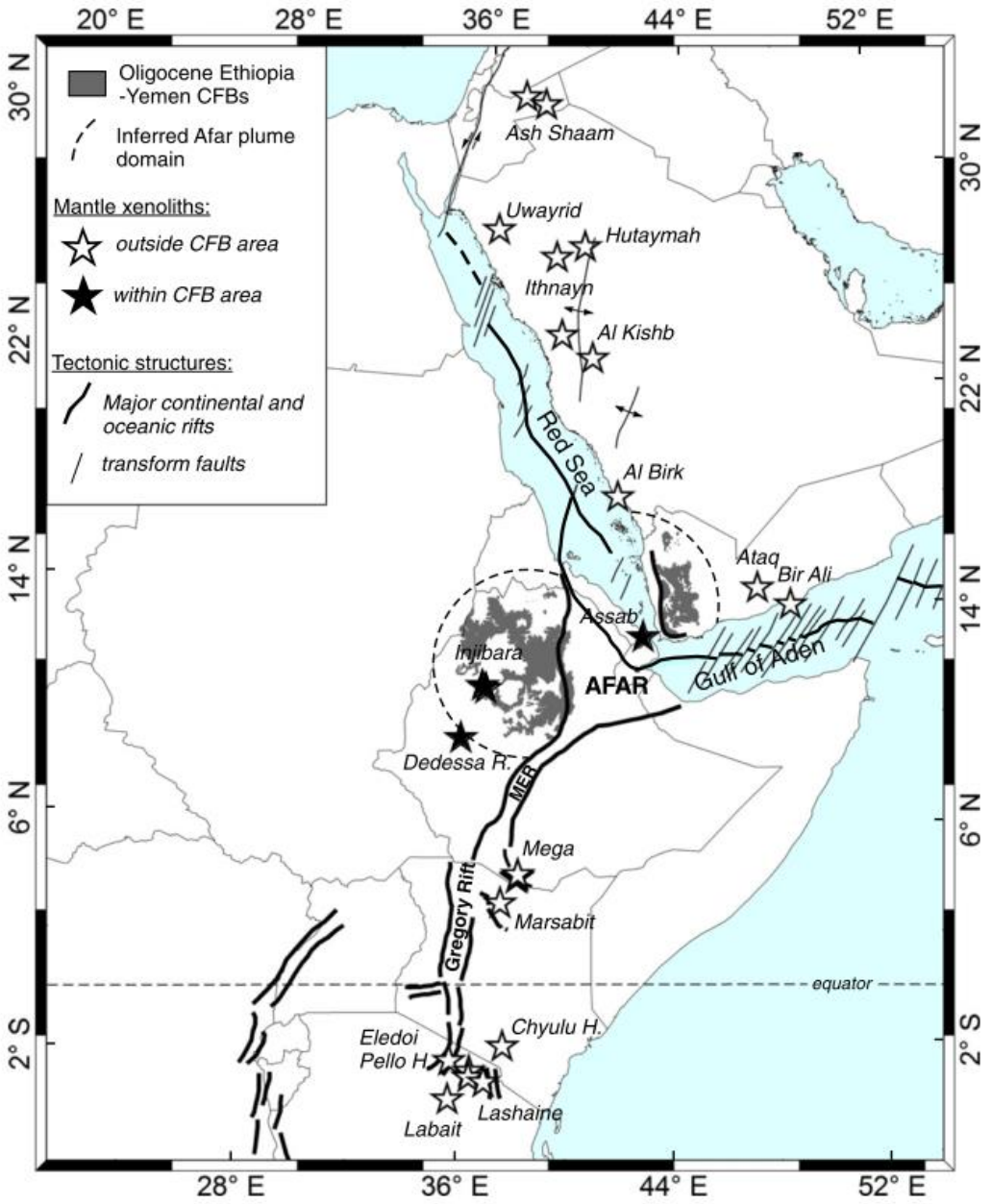

Figure 1-2. Sketch map (after Sgualdo et al., 2015) of the East African–Arabian domain showing Oligocene continental flood basalts (CFBs; Beccaluva et al., 2009) and mantle xenolith occurrences related to Neogene–Quaternary alkaline volcanism (Aulbach et al., 2011; Baker et al., 1998; Beccaluva et al., 2011; Henjes-Kunst et al., 1990; Kaeser et al., 2006; Shaw et al., 2007; Teklay et al., 2010). The main tectonic lineaments are after Bosworth et al. (2005) and Rogers (2006).

Tectonic history

The West Antarctic Rift System (WARS)

In the West Antarctic Rift System, active versus passive rifting mechanisms are also debated. Lithospheric extension, high heat flow, and voluminous volcanism occur in a setting surrounded by mid-ocean ridges, making an identification of a source of extensional plate boundary force difficult (Ruppel, 1995). Furthermore, the extensive ice cover and relative aseismicity, and therefore limited number of geological and geophysical studies available compared to, for example, the East African Rift System, contribute to significant uncertainty regarding the exact timing, architecture, and evolution of the WARS (Fitzgerald et al., 1986; LeMasurier, 1990; Tessensohn and Worner, 1991). Passive interpretations of the forces driving rift-related tectonomagmatic activity include rift induction via transfer of dextral shear from the mid ocean ridge in the Southern Ocean into the Antarctic Plate interior (Storti et al., 2008), or as a result of Eocene reorganization of mantle flow patterns at the boundary between the thick East Antarctic craton and the Antarctic lithosphere that generated buoyancy forces, reactivated Paleozoic crustal weaknesses, and triggered decompression melting (Nardini et al., 2009). Alternative models that support an active rift-driving force are bolstered by evidence for tectonic doming, interpreted to be related to impingement of a mantle plume, beneath Marie Byrd Land (MBL; LeMasurier and Rex, 1989). The existence of a 600 km-diameter plume head has been argued to explain voluminous alkaline volcanism in MBL and throughout the WARS (e.g., Hole and LeMasurier, 1994). However, geophysical (e.g., Hansen et al., 2014; Emry et al., 2015), structural (e.g., Rilling et al., 2009), and geochemical (e.g., Nardini et al., 2009; Aviado et al., 2015) lines of evidence increasingly support a passive rifting mechanism for Cenozoic extension and magmatism.

Although rift-related magmatism and lithospheric extension in the WARS proper has been active since the Oligocene, this rifting regime must be considered in the larger context of Gondwana supercontinent breakup. West Antarctica and its constituent tectonic blocks were once amalgamated with the Chatham Rise, Campbell Plateau, New Zealand and several other crustal blocks collectively referred to as Zealandia along the paleo-Pacific margin of Gondwana. In the Middle Jurassic, the emplacement of voluminous Karoo flood basalt magmatism and the initiation of continental breakup has been linked to a plume centered on the South Africa-East Antarctica junction (White and McKenzie, 1989; Elliot and Fleming, 2000). The Zealandia block was completely rifted away from the present-day Pacific margin of Antarctica in Marie Byrd Land (MBL) by ~80 Ma (Bradshaw, 1989; Eagles et al., 2004; Brown et al., 2006). Following this initial Gondwana breakup, the timing of rifting has generally been interpreted to have occurred in two major pulses (Schmidt and Rowley, 1986; Stump and Fitzgerald, 1992; Elliot, 1992; Storey, 1996). During the first pulse in the Cretaceous, major crustal thinning occurred and was largely amagmatic (Salvini et al., 1997). Estimates of the amount of crustal extension that occurred during this phase are variable; some authors argue on the basis of crustal thickness balancing for a maximum late Cretaceous-present crustal extension of 250 – 350 km in the WARS (e.g., Fitzgerald et al., 1986; Behrendt and Cooper, 1991), but others call for as much as 1000 km of post-Cretaceous extension between East Antarctica and Pacific West Antarctica based on paleomagnetic measurements (DiVenere et al., 1994; Luyendyk et al., 1996). This main amagmatic rifting phase was followed by lesser Cenozoic rifting localized primarily in the western Ross Embayment (Behrendt et al., 1991; Tessensohn and Worner, 1991; Behrendt, 1999). The timing and distribution of the extension between these two pulses is still debated. There is some evidence that much of the extension in fact occurred prior to Zealandia-West

Antarctica breakup at ~80 Ma (e.g., Lawver and Gahagan, 1994; Davey and Brancolini, 1995; Mukasa and Dalziel, 2000; Luyendyk et al., 2001; Siddoway et al., 2004). Other authors argue for as little as 50 km of Cenozoic extension (Lawver and Gahagan, 1994), or ~180 km of extension in the Eocene-Oligocene (Cande et al., 2000; Cande and Stock, 2004).

The major phase of Cretaceous extension was followed by dramatic uplift of the Transantarctic Mountains (TAM) at ~60 Ma. The TAM represent a continuous transcontinental range varying in elevation from 4500 m where they form the rift shoulder in Northern Victoria Land (NVL) to 1-2 km by the Weddell Sea (Fitzgerald et al., 1996; Behrendt and LeMasurier, 1991). The TAM are characterized a lack of folding in the exposed Precambrian/Cambrian metasedimentary and metavolcanic rocks, and exhibit evidence that they have been built in a tensional field (Fitzgerald, 1986; Behrendt and LeMasurier, 1991). Additionally, despite their high elevation, gravity modeling indicates that the crustal thickness underlying them is only 40 – 45 km, comparable to thicknesses of topographically depressed areas of the adjacent East Antarctic craton (Woollard, 1962; Smithson, 1972; Bentley, 1983). TAM uplift can be accounted for by elastic flexure of two cantilevered plates separated by a stress-free edge (Stern and ten Brink, 1989), and therefore can be attributed to flexural uplift driven by the thermal gradient between thick, cold lithosphere of the East Antarctic craton and thinned (20-30 km thick; Fitzgerald et al., 1986), warm lithosphere under extension in West Antarctica. The lack of a distinct rift shoulder on opposing Amundsen-Bellingshausen flank of the Ross Embayment highlights the asymmetry of WARS rifting. In the Ross embayment, horst and graben topography has been inferred from seismic profiling and likely extends throughout the WARS (Behrendt et al., 1991; LeMasurier and Thompson, 1990). These features may be attributed to the presence of very rigid lithosphere underlying East Antarctica adjacent to the TAM-NVL rift

shoulder, in contrast with less rigid oceanic lithosphere offshore of the Amundsen-Bellinghausen. The characteristics of horst and graben topography (i.e. accommodation of relatively small displacements along widely distributed normal faults), contrasted with large-scale block faulting at the Transantarctic Mountains, and overall large magnitude of total extension support the classification of the WARS as a wide or diffuse rift, although more recent Oligocene-Miocene rifting and volcanic activity has been localized into discrete rift basins within the Ross Embayment. Wide rift formation is favored in regions with weak, heterogeneous lithosphere that has undergone crustal shortening during a previous episode of convergence; this is certainly appropriate for WARS, as West Antarctica and Zealandia comprised part of a long-lived subduction zone along the paleo-Pacific margin of Gondwana (Figure 1-1). Almost 500 Myr of convergence (Rocchi, 1998; Mukasa and Dalziel, 2000) could lead to the introduction of crustal thickness variations, structural defects, and weak, hydrated rheologies in the crust and upper mantle beneath West Antarctica. In light of this tectonic inheritance, passive rifting of significantly weakened lithosphere may explain WARS extension and associated volcanism where geophysical and geochemical (e.g., Aviado et al., 2015) evidence for mantle plume activity are lacking.

The East African Rift System (EARS)

The East African Rift System is considered the archetypal narrow rift endmember, yet the roles of active versus passive rifting processes remains controversial. Roughly 30-40 km of estimated extension between the Nubian and Somalian proto-plates over the past 11 Ma (e.g., Wolfenden et al., 2004). This extension has largely been accommodated in discrete rift segments that exhibit variable ages and stages of rifting (Ebinger, 2005). The presence of the Afar plume in northern Ethiopia establishes an active rifting driver in the region, and generally, the amount

of lithospheric extension increases to the north along the rift axis, in the direction of the Afar Depression (Ebinger et al., 1993). However, although emplacement of voluminous continental flood basalts in Afar at ~ 30 Ma is roughly coeval with the onset of continental rifting in the Red Sea-Gulf of Aden system (Wolfenden et al., 2004), and is typically considered to mark the inception of plume-related activity in the region, this magmatic episode is predated by more southern Ethiopian and Kenyan basalt volcanism that began at around 45 Ma (Davidson and Rex, 1980; Furman et al., 2006; Ebinger et al., 1993; Ebinger et al., 2000; McDougall et al., 2009). Tectonic doming and geochemical evidence for a distinct source of Kenya rift volcanism have been attributed to a second plume acting beneath the region (Rogers et al., 2000; Pik et al., 2006), and this Eocene volcanism pre-dates the major episode of Oligocene extension and tectonic doming in Kenya and Ethiopia. Alternatively, although geophysical imaging of the shallow mantle beneath Afar and Turkana, Kenya supports the existence of separate upwelling structures, it is possible that these seemingly distinct plumes may be connected to the African superplume at depth (Debayle et al., 2001; Benoit et al., 2006; Nyblade et al., 2000; Weeraratne et al., 2003; Furman et al., 2005). The African superplume is a well-documental, large-scale low-density feature of the deep mantle (Ritsema et al., 1999; Gurnis et al., 2000; Zhao, 2001). However, active processes may not explain all rift activity in the EARS, especially where geochemical evidence for passive melt generation occurs (e.g., Mega; Beccaluva et al., 2011)

Rift morphology also diverges from a 50 km-wide rift in the north to a 200 km-wide rift zone consisting of multiple narrow segments further to the south (Figure 1-2). In Kenya and Tanzania, the rift segments bifurcate and undergo a change in orientation in faulting as they encounter the old, 250 km-thick, 3 Ga Tanzanian craton (Foster et al., 1997; Ritsema et al., 1998). Deformation is localized to the boundaries between the Tanzania craton and thinner (~35

km-thick), weaker lithosphere (Ebinger, 2005). The Eastern branch of the rift system, at an age of less than 5 million years old, represents the formation of a young rift system. Here, lithospheric extension is mainly in response to plate-driving forces, reactivating zones of weakness such as the suture between the Tanzania craton and the young, thin lithosphere bordering it to the east (Foster et al., 1997). The rift structure in this young segment is characterized by asymmetric flanks and a deep (3.6 km) rift basin overlying a narrow zone of thinned mantle lithosphere (Green et al., 1991; Birt et al., 1997). Seismic tomography reveals evidence for small-volume melts in the mantle and magmatic intrusions in the crust (Green et al., 1991; Ibs-von Seht et al., 2001). Collectively, these observations imply that the upper mantle beneath the Eastern branch of the EARS is strong, and that the rifting is driven by decompression melting of anomalously hot asthenosphere, aided by pre-existing lithospheric weaknesses (Ebinger, 2005; and references therein) – in this case, the suture zone created during the Neoproterozoic East African Orogen (Corti, 2009, and references therein).

In the more northern Kenya rift, rift basins are ~15 million years old, and can be considered to represent a more mature rifting stage. Between 30 and 35 Ma, faulting, extension, and crustal thinning began in the northern portion of the Kenya Rift (Hendrie et al., 1994), and up to ~35 – 40 km of crustal stretching has since been accommodated in the ~175 km-wide rift segment (Hendrie et al., 1994). In the north, estimates of crustal thickness are ~20 km. By contrast, in more southern portions of the Kenya rift, 5 - 10 km of extension has occurred in crust ~35 km thick through the formation of asymmetrical rift basins similar to those observed in the Eastern branch of the EARS (Mechie et al., 1997). Beneath the uplifted Kenya dome, the crust has been additionally thinned to ~30 km, and low seismic velocities and an abrupt shallowing of the Moho depth are consistent with focused upwelling of anomalously hot mantle material in this

region. These observations are consistent with an increase in lithospheric stretching and shallowing of the lithosphere-asthenosphere boundary in a northward direction, leading to an increase in the amount of decompression-driven partial melting. The presence of weak thermally and magmatically eroded lithosphere toward the north is also supported by a progressive decrease in the depth of earthquake hypocenters and faulting from 35 km in Tanzania to 27 km in northern Kenya (Ibs-von Seht et al., 2001).

Although the Main Ethiopian Rift (MER)-Red Sea Rift-Gulf of Aden appears to be an archetypal triple junction radiating out from the Afar Depression, Wolfenden et al. (2004) found that there is little evidence that the inception of extension in the MER was synchronous with Africa-Arabia separation. Instead, Oligocene-Miocene rifting in Kenya propagated northward into southern Ethiopia at ~20 Ma (Bonini et al., 2005), resulting in the formation of high-angle faults bordering chains of volcanic centers. Over time, progressive narrowing of the zones of deformation have localized the most recent (<1.8 Ma) tectonomagmaic activity in 20 km-wide, 60 km-long "magmatic segments" characterized by aligned eruptive centers, fissures, and short faults in the central portion of the rift (Ebinger and Casey, 2001). There is evidence that these shorter, narrower magmatic segments are superimposed on the older border faults of the previously existing broad extension basin, and this implies that the elastic thickness of the lithosphere has decreased since long border faults had formed (Ebinger et al., 1999). Tomographic imaging supports the existence of melt volumes beneath the surface expression of the rifts along a 150 km-wide zone focused under the MER (Bastow et al., 2008). At its northern terminus in the Afar Depression, the Ethiopian plateau, built up by continental flood basalt volcanism and tectonic uplift, gives way to a subsided basin. In this region, decreasing lithospheric thickness and increasing extension and asthenospheric upwelling results in

magmatic intrusion accommodating the majority of the extension, and the rift is essentially a slow-spreading mid-ocean ridge (Wolfenden et al., 2004).

This work

The complex, multistage tectonic histories of East Africa and West Antarctica lend themselves to the creation of heterogeneous mantle domains in the sub-continental lithospheric mantle (SCLM) and the asthenosphere that may contribute to ongoing extension and magmatic activity. The objectives of this dissertation therefore seek to explore the nature and provenance of heterogeneous mantle domains underlying the active rift systems through detailed geochemical analyses of mafic rift-related rocks from the WARS and the EARS, particularly with respect to volatiles and volatilized lithologies, and to use this information to develop or refine regional models for melting and metasomatic histories that reconcile geophysical and geochemical observations with the histories of the Antarctic and African continents.

To accomplish these objectives, this dissertation is divided into chapters that address different facets of continental rift petrogenesis. In Chapter II, the first geochemical information from submarine lavas in the Ross Embayment of West Antarctica are reported alongside subaerial lavas from islands and mainland Northern Victoria Land (NVL), which together provide evidence that volatilized, recycled mantle domains generated during ancient long-lived subduction along the paleo-Pacific margin of Gondwana have been contributed to Cenozoic tectonomagmatic activity. This work was published in *Geochemistry, Geophysics, Geosystems* in December 2015, and is reproduced in this dissertation. In Chapter III, olivine-hosted melt inclusions from mafic lavas in West Antarctica confirm that high H_2O and CO_2 are prevalent in the mantle source of rift-related magmas on a wide scale throughout the WARS, and show that volatilized mantle domains can persist and continue to facilitate to magma genesis long after

subduction cessation. Chapter IV investigates the petrography and geochemistry of peridotite and pyroxenite mantle xenoliths from the southern Main Ethiopian Rift in the East African Rift System as well as peridotites from the Ethiopian plateau to evaluate the history of thermochemical events that have affected the EARS SCLM, and the role of SCLM in rift petrogenesis and long-term continental evolution. In this chapter, the geochemical systematics of the mantle xenolith suite testify to a history that includes ancient melt extraction during Pan African continental assembly, followed by more recent metasomatic processes triggered by both low-volume carbonated fluids and alkaline melts as well as subalkaline asthenospheric melts. These findings illustrate that relatively small scale chemical heterogeneities in the SCLM may be created and/or preserved during large scale geologic processes such as continent formation and breakup, and that the SCLM serves as an important long-lived chemical reservoir of components produced during continental assembly, recycling, and evolution.

CHAPTER II

SUBMARINE AND SUBAERIAL LAVAS IN THE WEST ANTARCTIC RIFT SYSTEM: TEMPORAL RECORD OF SHIFTING MAGMA SOURCE COMPONENTS FROM THE LITHOSPHERE AND ASTHENOSPHERE[1]

Abstract

The petrogenesis of Cenozoic alkaline magmas in the West Antarctic Rift System (WARS) remains controversial, with competing models highlighting the roles of decompression melting due to passive rifting, active plume upwelling in the asthenosphere, and flux melting of a lithospheric mantle metasomatized by subduction. In this study, seamounts sampled in the Terror Rift region of the Ross Sea provide the first geochemical information from submarine lavas in the Ross Embayment in order to evaluate melting models. Together with subaerial samples from Franklin Island, Beaufort Island, and Mt. Melbourne in North- ern Victoria Land (NVL), these Ross Sea lavas exhibit ocean island basalt (OIB)-like trace element signatures and isotopic affinities for the C or FOZO mantle endmember. Major-oxide compositions are consistent with the presence of multiple recycled lithologies in the mantle source region(s), including pyroxenite and volatile-rich lithologies such as amphibole-bearing, metasomatized peridotite. We interpret these observations as evidence that ongoing tectonomagmatic activity in the WARS is facilitated

[1] A version of this chapter was previously published as Aviado, K. B., S. Rilling-Hall, J. G. Bryce, and S. B. Mukasa (2015), Submarine and subaerial lavas in the West Antarctic Rift System: Temporal record of shifting magma source components from the lithosphere and asthenosphere, *Geochemistry, Geophysics, Geosystems*, *18*, 1541–1576, doi:10.1002/2015GC006076. This work has been reprinted here in accordance with the policies of AGU. Copyright 2015 American Geophysical Union.

by melting of subduction-modified mantle generated during 550–100 Ma subduction along the paleo-Pacific margin of Gondwana. Following ingrowth of radiogenic daughter isotopes in high-μ (U/Pb) domains, Cenozoic extension triggered decompression melting of easily fusible, hydrated metasomes. This multistage magma generation model attempts to reconcile geochemical observations with increasing geophysical evidence that the broad seismic low-velocity anomaly imaged beneath West Antarctica and most of the Southern Ocean may be in part a compositional structure inherited from previous active margin tectonics

1. Introduction

Voluminous volcanism away from active plate boundaries is often attributed to ‘‘hotspot’’ or plume magmatism. Within rifts, intraplate magmatism coupled with lithospheric extension may be explained by active upwelling of buoyant plume material, or arise from passive decompression accompanying the thinning and pulling apart of the lithosphere (e.g., McKenzie and Bickle, 1988). Geophysical (e.g., seismic tomographic imaging) and geochemical (e.g., observations of alkali-rich, silica-undersaturated lavas, and high-m isotopic signatures; $\mu = {}^{238}U/{}^{204}Pb$) lines of evidence suggest the existence of ‘‘plumes’’ of low-density, chemically distinct mantle beneath many intraplate settings that have classically been interpreted as originating from the deep mantle. The West Antarctic Rift System (WARS) is one of the largest continental rift systems on Earth, with estimates of lithospheric extension in the Ross Sea between 250 and 500 km, and as much as 1000 km from the Cretaceous to Recent (Fitzgerald et al., 1986; DiVenere et al., 1994; Trey et al., 1999). Lesser Cenozoic extension, on the order of 50–180 km (Kamp and Fitzgerald, 1987; Lawver and Gahagan, 1994), was accompanied by voluminous alkaline volcanism throughout the WARS. Tomographic evidence for low- velocity seismic anomalies beneath West Antarctica has been attributed to temperature anomalies

associated with deep mantle upwelling (Sieminski et al., 2003; Watson et al., 2006), but compelling geophysical evidence for a classical plume (e.g., Morgan, 1971) remains elusive.

Previous explanations for WARS volcanism have included a single plume beneath Marie Byrd Land (Behrendt et al., 1994; Hole and LeMasurier, 1994; Behrendt et al., 1996), an injected subduction signature mixed with multiple enriched mantle sources (Hart et al., 1995), and decompressional melting of a fossilized plume head or stratified mantle source beneath the entire region (Rocholl et al., 1995; Hart et al., 1997; Panter et al., 2000). LeMasurier and Rex (1989) argued that crustal doming in Marie Byrd Land (MBL), inferred from radial melt migration around a topographically elevated center (exhibiting an estimated ~3 km of structural relief) and associated with the inception of alkaline volcanism in the region around 30 Ma can be explained by a mantle plume $600 km in diameter beneath MBL. Coeval volcanism in the Erebus Volcanic Province in Northern Victoria Land (NVL) has been explained by a separate 40 km diameter plume beneath NVL (Kyle et al., 1992; Esser et al., 2004), or by enlargement of the MBL plume to encompass roughly 1500 km by 2500 km of geochemically similar volcanism in the Ross Sea and NVL (Hole and LeMasurier, 1994). While this may explain coeval young volcanism on both flanks for the WARS, no geophysical or structural evidence for plume-related crustal doming has been established in NVL.

Several alternative explanations for WARS volcanism have focused on the concept of a fossilized plume head or stratified mantle source beneath the region. The Jurassic Ferrar dolerites of the Antarctic Peninsula are believed to be derived from the mantle plume that gave rise to the Karoo large igneous province during initial breakup of Gondwana (Elliot and Fleming, 2000; Storey et al., 2001; Riley et al., 2001). Underplating of the Antarctic lithosphere with the remnants of this plume to produce a compositionally stratified mantle, with deep depleted

MORB-type asthenosphere overlain by HIMU- or FOZO-like plume material (with HIMU and FOZO defined by Hart et al. (1986, 1992)), could explain isotopically diverse magmas associated with thinning of the WARS lithosphere (Hart et al., 1997; Worner, 1999). Rocholl et al. (1995) called for at least three mantle end-members (MORB-type or DMM, EM, and HIMU-like) in the source components, and suggested that some of the geochemical differences result from varying degrees and depths of melting, attributed to the distance of volcanism from the WARS rift shoulder. Alternatively, Panter et al. (2000) suggested lavas with HIMU-like isotopic compositions were instead results of smaller degree partial melts, with melts demonstrating a mixture of isotopic signatures resulting from higher degrees of melting. These arguments collectively fit that of the stratified mantle source, with fossil mantle plume material defining a layer below the lithospheric mantle, although many of these hypotheses suggest that the mantle solidus has been lowered by involvement of hydrous and/or pyroxenitic components (e.g., Hart et al., 1997; Panter et al., 2000).

Recent work highlighting the potential involvement of hydrated mantle in producing the observed seismic anomalies beneath the WARS (Hansen et al., 2014; Emry et al., 2015) is consistent with the idea that many plumes are thermochemical structures, and that such anomalies are in part compositional (e.g., White and Hofmann, 1982; Hofmann and White, 1982; Hauri, 1996; Rooney et al., 2012a). Recycled subducted slab materials capable of inciting deep melting, including pyroxenite and volatiles (particularly CO_2 and H_2O) have been implicated as a significant source of compositional heterogeneity in the mantle (e.g., among many others, Asimow and Langmuir (2003); Kogiso et al. (2003); Dasgupta et al. (2007)). Given the >100 million year history of active subduction along the paleo-Pacific margin of Gondwana during the early Mesozoic (Rocchi et al., 1998; Mukasa and Dalziel, 2000), this process may be integral to

reconciling geophysical observations with the geochemistry of voluminous alkaline magmatism and associated Cenozoic rifting in West Antarctica.

Sparse sampling over poorly exposed units within the WARS have complicated determinations of magma source region characteristics and even impacted the ability to understand overall evolution of the rift. This study provides new chemical information on sampled Cenozoic submarine and subaerial lavas from the Ross Sea, as well as additional chemical analyses on lava samples in the Mt. Melbourne region of northern Victoria Land, and addresses questions about the composition of the mantle source(s) below the WARS.

2. The West Antarctic Rift System (WARS)

West Antarctica (Figure 2-1) is comprised of several tectonic blocks that were once amalgamated with the Chatham Rise, Campbell Plateau, and New Zealand to form the long-lived subduction zone along the paleo-Pacific margin of the supercontinent Gondwanaland (Dalziel and Elliot, 1982; Dalziel et al., 1994). The Granite Harbor Intrusive suite provides evidence for the inception of subduction-related magmatism by ~530 Ma along the Trans-Antarctic Mountains (TAM) region (Rocchi et al., 1998). This subduction continued, perhaps episodically, through the Mesozoic and began a progressive west to east cessation between 110 Ma in western present day Marie Byrd Land (MBL) and 94 Ma in eastern MBL (Mukasa and Dalziel, 2000).

This period of convergence along the paleo-Pacific margin of Gondwana was followed by break-up and dispersal of several crustal blocks collectively referred to as Zealandia. Recent studies estimate the complete separation of the Zealandia crustal blocks (North Island, South Island, Campbell Plateau, Chatham Rise, and Lord Howe Rise) from West Antarctica by ~83 Ma (Eagles et al., 2004; Brown et al., 2006). Initiation of West Antarctic Rift System (WARS) extension and opening of the Ross Sea embayment began in the Cretaceous, initially with

primarily amagmatic processes (Salvini et al., 1997). Rift-related magmatism in Northern Victoria Land (NVL) began at ~48 Ma (Rocchi et al., 2002) and in MBL at ~30 Ma (Hart et al., 1997). The volume of Cenozoic eruptive products in the WARS is thought to exceed 10^6 km^3, with a sizeable fraction of this material thought to underlie the West Antarctic Ice Sheet (Behrendt, 1999). Volcanism of similar age and composition is found in all tectonic blocks that were once amalgamated along the paleo-Pacific Gondwanan margin, although they are now separated by ocean basins and distances upwards of 2000 km, leading Finn et al. (2005) to term this area the Diffuse Alkaline Magmatic Province (or DAMP)

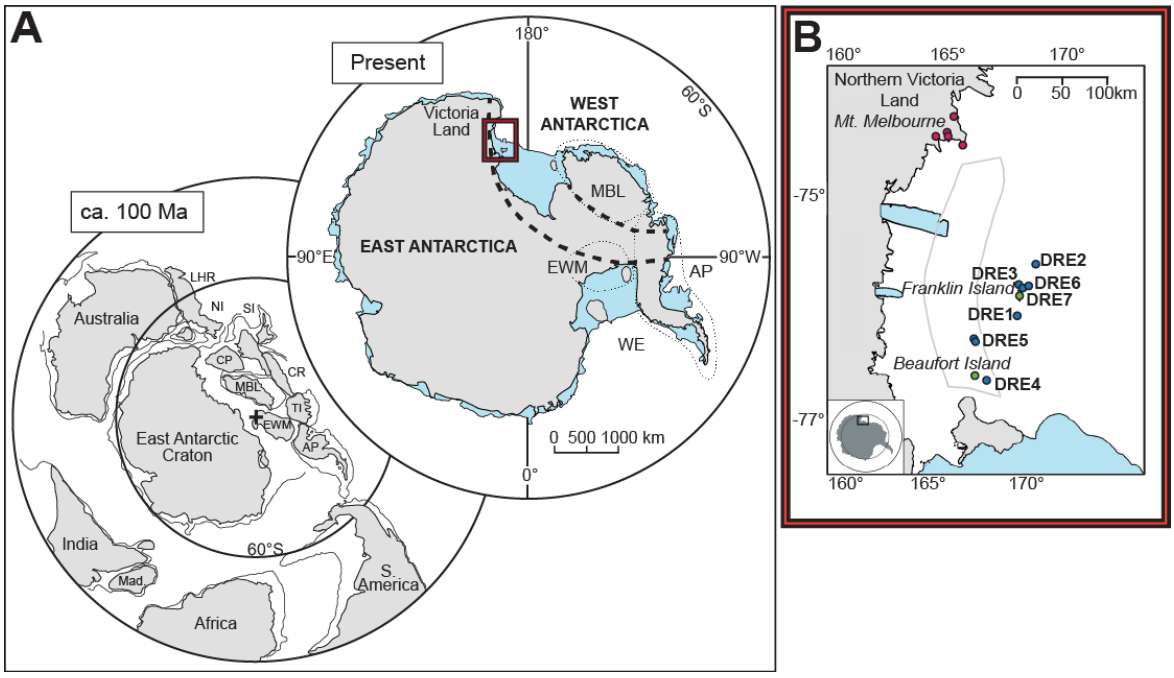

Figure 2-1. A) Sketch map of Antarctica showing present-day East Antarctica, West Antarctica, the Weddell Embayment and the crustal blocks that comprise West Antarctica: MBL – Marie Byrd Land; EWM – Ellsworth Mountains; AP – Antarctic Peninsula. Thick dashed lines indicate the approximate boundary of the West Antarctic Rift System (after Rocchi et al., 2002). The map on the lower left is a tectonic reconstruction of the paleo-Pacific margin of Gondwana at ca. 100 Ma (after Mukasa and Dalziel, 2000). AP – Antarctic Peninsula; CP – Campbell Plateau; CR – Chatham Rise; EWM – Ellsworth-Whitmore block; LHF – Lord Howe Rise; NI – North Island, New Zealand; SI – South Island, New Zealand; TI – Thurston Island block. Bold crosshair indicates South Pole position (DiVenere et al., 1994). B) Map inset of Northern Victoria Land subaerial sample locations (red symbols), islands (green symbols), and submarine dredges (blue symbols) collected during the NBP-0401 research cruise. Grey polygon outlines the Terror Rift.

3. Sampling and Methods

Lava samples were collected in the field as described in Rilling (2009). Seven seamounts, Franklin Island, Beaufort Island, and several mainland locations surrounding Mt. Melbourne were sampled (Figure 2-1B). Submarine samples were dredged from seven volcanic edifices identified with multibeam bathymetry during the 2004 NBP-0401 research cruise on the research icebreaker *Nathaniel B. Palmer*. Additional details of the dredged features and collected materials can be found in Wilson et al. (2004). Subaerial samples from Franklin Island were collected by members of the cruise with a zodiac from *Nathaniel B. Palmer*. Samples from Beaufort Island were collected by helicopter during GPS installations for another study by members of our party. Wesley LeMasurier collected samples from northern Victoria Land during several field seasons.

Mineral compositions were determined with a Cameca SX 100 electron microprobe at the University of Michigan Electron Microbeam Analysis Laboratory (EMAL). Major oxides, Rb, Sr, and Zr were analyzed by x-ray fluorescence (XRF), and trace elements were obtained on the same glass disks by laser ablation inductively coupled plasma mass spectrometer (LA-ICP-MS) at Michigan State University using the techniques described by Deering et al. (2008) and Rooney et al. (2012). Reproducibility using these techniques is typically better than 5% for trace elements based on standard analyses (Vogel et al., 2006). Samples were sorted by major-oxide data, removing those with low totals (less than 96 wt. %, inferred to indicate high LOI) from further consideration in the isotopic analyses that followed. For more detailed descriptions of mineralogical, major oxide, and trace elemental analyses, see Appendix 1.1.

Sample chips for Sr, Nd, and Hf isotopic analysis were washed ultrasonically in deionized water and soaked in 2.5N HCl prior to pulverization. Sample dissolution and column

chemistry techniques for Nd and Sr are described by Reisberg and Zindler (1986). Analysis of Sr and Nd isotopic compositions were carried out using the VG Sector thermal ionization mass spectrometer (TIMS) at the University of Michigan according to the procedures of Mukasa et al. (1991). Total procedural blanks averaged 0.2 ng for Sr and 0.04 ng for Nd. The Sr and Nd isotopic ratios were exponentially normalized to correct for instrumental mass fractionation using $^{86}Sr/^{88}Sr = 0.1194$ and $^{146}Nd/^{144}Nd = 0.7219$, respectively. Replicate analyses of NBS-987 and La Jolla standards gave $^{87}Sr/^{86}Sr = 0.710255 \pm 0.000011$ (N = 30, 2σ) and $^{143}Nd/^{144}Nd = 0.511848 \pm 0.000019$ (N = 30, 2σ). Hf isotopic compositions were measured on the Nu Plasma multi-collector inductively coupled plasma mass spectrometer (MC-ICP-MS), also at the University of Michigan, following the columns chemistry and analytical methods of Choi et al. (2006). A mean $^{176}Hf/^{177}Hf$ of 0.282166 ± 0.000042 (N = 14, 2σ was determined from measured values of standard JMC-475, and total average procedural planks for Hf were 0.02 ng. Sample $^{87}Sr/^{86}Sr$, $^{146}Nd/^{144}Nd$, and $^{176}Hf/^{177}Hf$ values were corrected for instrumental drift using standard-sample bracketing.

Sample chips for Pb isotopic analysis were leached in hot (120°C) 6N HCl following the procedures of Blichert-Toft and Albarède (2009), then purified using column separation procedures described in Bryce and DePaolo (2004). High-resolution Pb isotopic measurements were obtained with the Nu Plasma II ES at the University of New Hampshire. Instrumental mass fractionation was corrected using the Tl normalization method of White et al. (2000), and instrumental drift corrected by standard-sample-standard bracketing as described in Albarède et al. (2004) using NIST SRM-981 normalizing values from Eisele et al. (2003). Average isotopic ratios for SRM-981 were $^{208}Pb/^{204}Pb = 36.726 \pm 0.0076$ (N = 20, 2σ), $^{207}Pb/^{204}Pb = 15.496 \pm$

0.0031 (N = 20, 2σ), $^{206}Pb/^{204}Pb$ = 16.941 ± 0.0025 (N = 20, 2σ). Procedural Pb blanks for this work were <150 pg, negligible for the size of the samples analyzed.

4. Results

4.1. Petrography

Of the seven dredged seamounts, samples from only five were selected for further study. Multiple samples processed from dredge locations are typically chemically and mineralogically similar, with the exception of Dredge 4, which has two very different samples. The dredged samples, with few exceptions, are highly vesicular and porphyritic with few phenocrysts, typically consisting of coarse olivine (Mg# 68 – 88) and zoned clinopyroxene (Figure 2-2B) in a groundmass consisting of clinopyroxene, olivine, and oxides ± plagioclase. They exhibit a range in extents of chemical alteration (indicated by vesicles lined with secondary carbonate) and contain varying amounts of ultramafic xenoliths and resorbed xenocrysts (xenocrystic olivine Mg# 85 – 89.7; Figure 2-2B), with a few samples containing rare granitic xenoliths. Full sample petrography and mineral compositions are described in Rilling (2009).

4.2 Major oxides and trace elements

Major-oxide and trace-element concentrations of all samples analyzed are reported in Appendix 1.2. Lava compositions range mostly to basanite and primitive foidite on the total alkalis versus silica diagram (Figure 2-2A), with two Beaufort Island samples evolved toward phonolite. Sample NV-12A from Edmonton Point (Northern Victoria Land), a trachyandesite, is the most evolved of the sample suite. MgO concentrations range from 13.70 wt. % down to 1.28 wt. % for the most evolved sample. SiO_2 versus MgO and Ni versus MgO trends are consistent with olivine and clinopyroxene fractionation in the full sample suite (Table 1). TiO_2 and Al_2O_3

relationships with MgO also generally exhibit respective decreasing and increasing trends expected for crystal fractionation (see Appendix 1.2).

All samples are enriched in incompatible elements relative to primitive mantle (Figure 2-3A-C). To focus solely on the differences in magma sources rather than the effect of crystal fractionation, only the seventeen samples with SiO_2 < 45 wt. % and MgO > 7 wt. % are included in the following discussion. Primitive mantle-normalized trace element abundances exhibit enriched patterns with large variability in concentrations and a marked negative Pb anomaly (Figure 2-3A-C) and negative anomalies for fluid-mobile elements (Rb, Th, and U). Sample elemental distribution patterns can be sorted into three distinctive trends: samples 12-19-01-5 and DRE4-75 show the most pronounced negative anomalies for Rb and Pb and an overall concave-down shape for LILE (Figure 2-3A); in contrast, the remaining samples show either less pronounced negative Rb anomaly (Figure 2-3C), or a flat distribution pattern for LILE (Figure 2-3B). Each of these three groups represent similar ranges of SiO_2, MgO, and Al_2O_3, suggesting that differences in the elemental distribution pattern are not uniquely the result of crystal fractionation or other magma chamber processing. Although subaerial weathering is capable of removing highly fluid-mobile Rb, the moderate (12 – 86 ppm) Rb concentrations among primitive (MgO > 7 wt. %) Ross Sea lavas suggests that these samples preserve magmatic Rb signatures. Chondrite-normalized rare earth element distributions display a steep pattern of enrichment in LREE (Figure 2-3D), with La_N ranging between 124 and 872 and La_N/Lu_N between 12.6 and 24.4. The strong enrichment in light REE relative to MORB compositions is typical for melting of a mantle source containing residual garnet (Harrison and Wood, 1980). This observation is in contrast to geodynamical studies in the WARS which suggest melting just

below anomalously thin crust (Trey et al., 1999), but agrees with thermobarometry estimates of melting at pressures up to 4 - 5 GPa (Perinelli et al., 2006).

4.3. Pb, Sr, Nd, and Hf isotopes

Isotopic ratios for all samples analyzed are reported in Table 1, and occupy narrow ranges comparable to values observed in other NVL and MBL lavas (Hart et al., 1997; Panter et al., 2000; Nardini et al., 2009). $^{87}Sr/^{86}Sr$ values range from 0.70212 ± 0.00001 to 0.70394 ± 0.00001, and $^{143}Nd/^{144}Nd$ values range from 0.51282 ± 0.00001 to 0.51301 ± 0.00001. $^{176}Hf/^{177}Hf$ values are remarkably homogenous, ranging between 0.282983 ± 0.000003 and 0.283065± 0.000005. $^{206}Pb/^{204}Pb$, $^{207}Pb/^{204}Pb$, and $^{208}Pb/^{204}Pb$ isotopic compositions for the Ross Sea samples range from 19.432 ± 0.0011 to 20.228 ± 0.0006, 15.521 ± 0.0011 to 15.659 ± 0.0006, and 38.920 ± 0.0014 to 39.916 ± 0.0012, respectively, and generally fall on or below the Northern Hemisphere Reference Line (NHRL) defined by Hart (1984). Collectively, the isotopic signatures of the lavas suggest involvement of a high-μ mantle source with respect to Sr, Nd, and Hf isotopic systems, but range to less radiogenic $^{206}Pb/^{204}Pb$ isotopic values similar to the C component (Hanan and Graham, 1996) or FOZO (Hart et al., 1992) mantle end member (Figures 2-4 and 2-5).

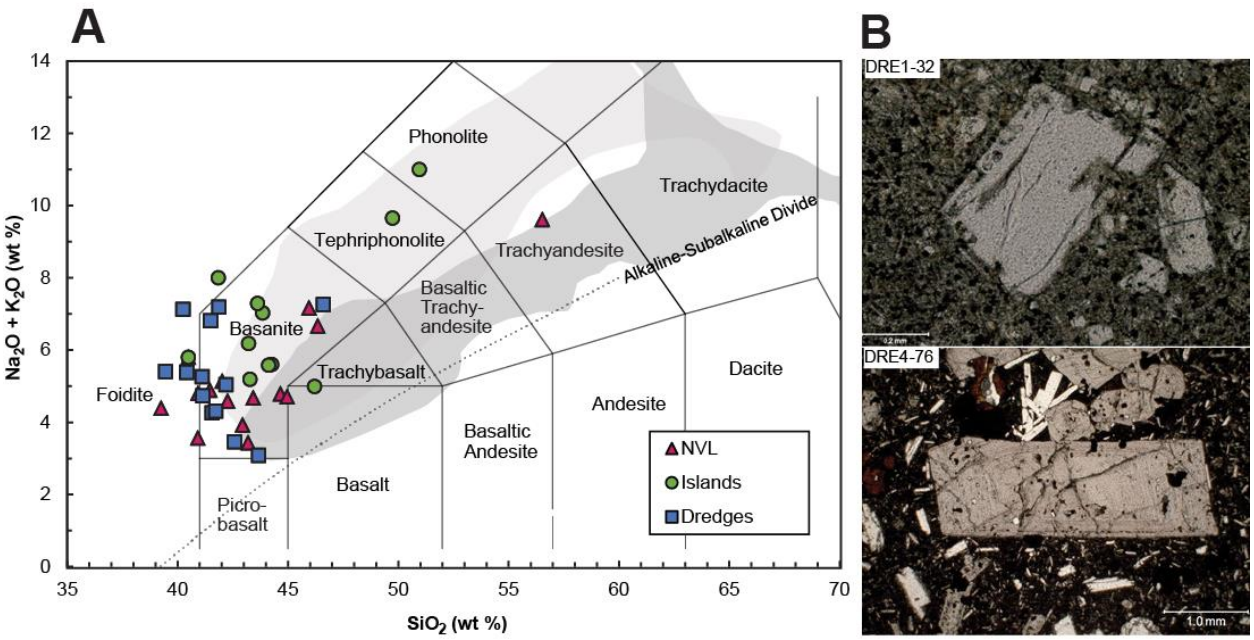

Figure 2-2. A) Volcanic Rock classification diagram (Le Bas et al., 1986). For comparison, light grey field shows lavas from the Erebus volcanic province (Le Masurier and Thompson, 1990; Kyle et al., 1992), and darker grey field shows lavas from the Melbourne and Hallett volcanic provinces (Le Masurier and Thompson, 1990; Armienti et al., 1991). B) Example of phenocryst resorption texture (upper panel) and common zonation in Ti-augite (lower panel).

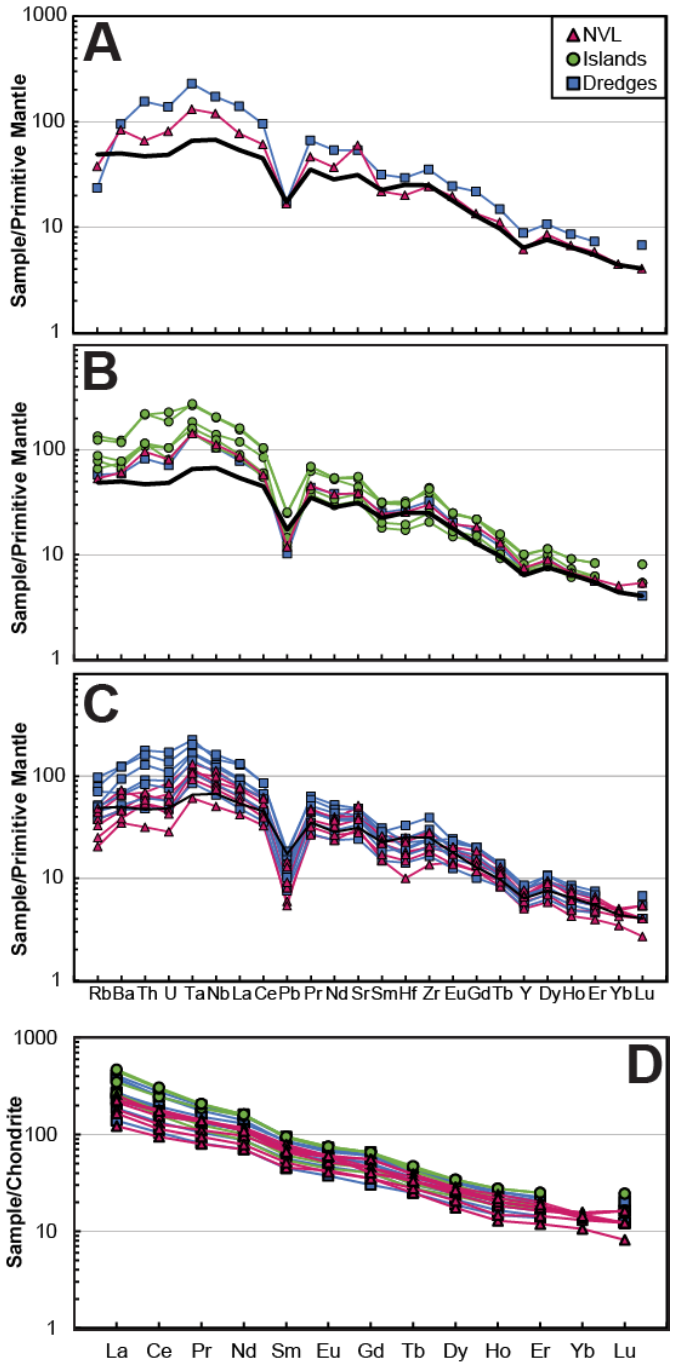

Figure 2-2. Primitive mantle-normalized elemental distribution diagram for samples with SiO_2 < 45 wt. % and MgO > 7 wt. %. Normalizing values are from Sun and McDonough (1989). Three distinct distribution patterns are observed: A) Two samples with pronounced negative Rb and Pb anomalies and concave-down patterns for LILE; B) Samples with flatter distribution patterns for Rb and LILE; and C) Samples with less pronounced Rb anomalies. Typical OIB values for comparison are indicated by thick black line. D) Rare-earth element (REE) diagram for all samples with SiO_2 < 45 wt. % and MgO > 7 wt. %. Normalizing values are from McDonough and Sun (1995).

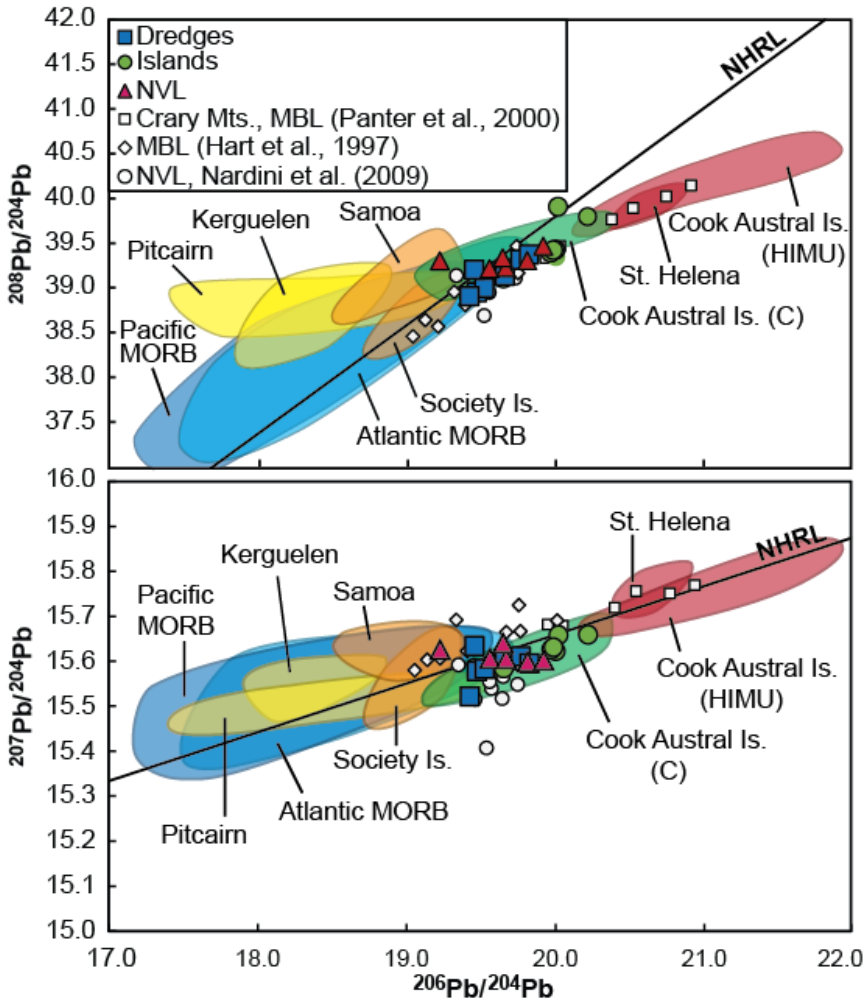

Figure 2-4. Pb isotopic compositions of Ross Sea lavas. Colored fields indicate mantle endmembers defined by Hart et al. (1986): blue fields represent the depleted MORB mantle source (DMM); yellow and orange fields represent enriched mantle endmembers EMI and EMII, respectively; red fields indicate the extreme high-μ endmember sampled at St. Helena and Mangaia ("HIMU"). Data for these fields are from the compilation by Stracke et al. (2002), and references therein. Green field indicates the C component (Hanan and Graham, 1996) or the FOZO endmember (Hart et al., 1992). Cook-Austral C data are for the islands of Ruturu (young volcanics; Chauvel et al., 1997) and Raivavae (Lassiter et al., 2003). Black line indicates the Northern Hemisphere reference line (NHRL; Hart, 1984).

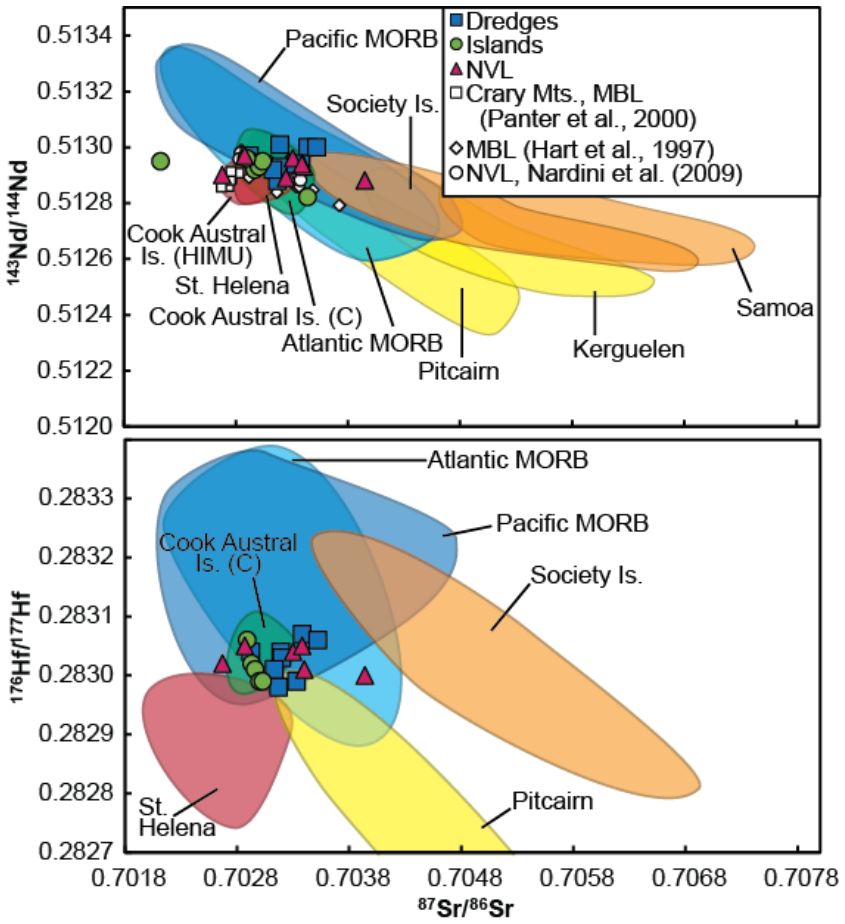

Figure 2-5. Nd, Hf, and Sr isotopic compositions from a sample subset. MORB-DMM (blue fields), EMI (yellow fields), EMII (orange fields), and HIMU (red fields) data for comparison are from the compilation of Stracke et al., (2002), and references therein. Cook-Austral C data are for the islands of Ruturu (young volcanics; Chauvel et al., 1997) and Raivavae (Lassiter et al., 2003).

5. Discussion

5.1. Source Characteristics

The overall incompatible element enrichments in the Ross Sea lavas, shown on the multi-element distribution and REE diagrams (Figure 2-3), are similar to those observed elsewhere in the WARS (Kyle and Rankin, 1976; LeMasurier et al., 1994; Hart et al., 1995, 1997; Panter et al., 2000; Rocchi et al., 2002), suggesting either a shared source beneath the entire region with varying degrees of partial melting or only a slightly heterogeneous source. Several of the geochemical characteristics of the Ross Sea lavas, including incompatible element enrichments

relative to primitive mantle, positive Nb-Ta anomalies, and a Pb negative anomaly, are also common to many OIB and often attributed to the presence of recycled oceanic lithosphere in the melt source (Weaver, 1991; Hofmann, 1997; Stracke et al., 2005). Subduction zone processing of oceanic lithosphere generates both volatilized peridotite through hydration and metasomatism of the overriding mantle wedge by slab fluids, and eclogite/pyroxenite through dehydration and metamorphism of the down going slab; both of these lithologies may therefore be relevant to magma genesis in the WARS, where over 500 Myr of punctuated subduction occurred along the paleo-Pacific margin of Gondwana during the Paleozoic and Mesozoic (Mukasa and Dalziel, 2000).

Many recent geochemical filters have been proposed to evaluate the potential melt source composition of mantle-derived melts on the basis of mafic volcanic rock major-oxide compositions (e.g., Herzberg and Asimow, 2008; Gurenko et al., 2008; Herzberg, 2011). Herzberg and Asimow (2008) argue for the discrimination between peridotite and pyroxenite sources on the basis of the MgO and CaO compositions of primitive volcanic rocks that have fractionated only olivine. Experimental studies by Walter (1998) and Herzberg (2006) have shown that accumulated fractional melts of peridotite plot above a line defined by CaO = 13.81 - 0.274*MgO, whereas many experimental partial melts of pyroxenite plot below this line (e.g., Hirschmann et al., 2003). Deviation from the peridotite-pyroxenite divide can be expressed as a 'pyroxenite index' = (13.81 - 0.274*MgO) - CaO. Using this definition, partial melts of peridotite that plot above the divide have negative values, whereas partial melts of pyroxenite that plot below have positive values. Analogously, a 'volatilized peridotite index' (= CaO - (2.318* SiO_2 - 93.626)) can be established to quantify deviation from the approximate peridotite-volatilized peridotite dividing line on the CaO versus SiO_2 diagram (Herzberg and Asimow,

2008). Again, partial melts of volatilized peridotite that plot above the volatilized peridotite divide exhibit positive values for the volatilized peridotite index.

Ross Sea lavas were filtered for MgO > 8 wt. % for application of these indexes (shown alongside the alkalinity index in Figure 2-6). Primitive lavas generally exhibit calcium enrichments for a given SiO_2, and accordingly exhibit positive values for the volatilized peridotite index; for comparison, experimental melting of peridotite containing 1.0 - 2.5 wt. % carbonate (Hirose, 1997; Dasgupta et al., 2007) produce silicate partial melts with values between 6 and 100 for the volatilized peridotite index. Analyzed lavas throughout all samples demonstrate a range in values for the pyroxenite index between -2.5 and 2.3, and generally show little correlation across the entire sample suite between the two indexes and major oxide, trace element, and most isotopic trends. These poor elemental correlations may reflect that mixing between multiple lithologies, as opposed to simple binary mixtures between peridotite and pyroxenite and/or peridotite ± volatiles, is responsible for generating the geochemical signature of Ross Sea magmas. On a smaller spatial scale, such as in the dredged seamounts from the Ross Sea, we find good correlations between the pyroxenite index and $^{206}Pb/^{204}Pb$ ($r^2 = 0.80$), Ce/Pb ($r^2 = 0.93$), and TiO_2 ($r^2 = 0.89$).

The modeled source lithologies (pyroxenite and peridotite ± volatiles) are consistent with multiple source contributions to the Ross Sea lavas, and may also be evaluated in a temporal framework where age constraints are available. The dredged seamounts dated by Rilling et al. (2009) exhibit age relationships with respect to both the pyroxenite and volatilized peridotite indexes that are consistent with a transition from a dominantly pyroxenite source to a dominantly volatilized peridotite source over the past 5 Ma (Figure 2-6). Given high-pressure experimental work has found that the pyroxenite solidus is up to ~50°C cooler than the peridotite solidus

(Kogiso et al., 2003), our findings suggest that in the Terror Rift, readily fusible pyroxenite lithologies characterized by high $^{206}Pb/^{204}Pb$ and elevated Ce/Pb were removed during earlier episodes of magmatism, leaving the residual mantle increasingly peridotitic in character over time.

Though we find these source filters useful, it is important to note that the role of volatilized pyroxenite does not achieve an unambiguous classification from this treatment. Low-MgO experimental melts of carbonated eclogite (e.g., Dasgupta et al., 2006; Gerbode and Dasgupta, 2010) often generate negative values for the pyroxenite index, but positive values for the volatilized peridotite index due to the calcium enrichments associated with carbonation. Furthermore, depletion of Ca as an effect of clinopyroxene fractionation, either in shallow magma chambers or at mantle conditions, can yield geochemical signatures similar to melts of a pyroxenite source (Herzberg and Asimow, 2008). Modeling of fractional crystallization using MELTS (Ghiorso and Sack, 1995; Asimow and Ghiorso, 1998; Gualda and Ghiorso, 2015) for the most primitive (MgO = 13.70 wt. %) sample composition indicates that clinopyroxene may crystallize even in primitive Ross Sea lavas with < 9.5 wt. % MgO, which agrees with petrographic observations of phenocrystic clinopyroxene in the dredge samples. Modeled high pressure fractionation of approximately 10% clinopyroxene, as melts evolve from 9.5 to 8.5 wt. % MgO, can cause values for the pyroxenite index to increase by ~1.3 units. Samples filtered for MgO > 9.5 wt. % maintain the good correlations between $^{206}Pb/^{204}Pb$, Ce/Pb, and TiO_2 and the pyroxenite index, as well as age relationships between both the pyroxenite and volatilized peridotite indexes observed among the dredged seamounts, suggesting that these trends are not dominated by clinopyroxene fractionation.

Comparisons with high pressure melting experiments of various source lithologies provide further insight into the major element systematics of the Ross Sea lavas (Figure 2-7). In these studies, partial melt experiments were conducted at comparable pressures to the melting of the mantle below the Ross Sea, 1.5 - 5 GPa, but at higher temperatures (1150 - 1700°C) than the Ross Sea geothermal gradient, which has a temperature range of 1100 - 1150°C at the estimated pressures (Berg et al., 1989; Perinelli et al., 2006). Estimated Ross Sea primary magma compositions, represented by the most primitive of the analyzed lavas (samples 04DRE4-74 and 05DRE5-85; MgO = 11.27 and 12.43 wt. %, respectively), range to SiO_2, Al_2O_3, and Na_2O contents that are too low to be derived from anhydrous peridotite, fertile peridotite, and fertile peridotite with basaltic veins (Hirose and Kushiro, 1993; Kogiso et al., 1998; Walter, 1998). Primitive Ross Sea magmas generally fall between fields for melts of carbonated peridotite (Hirose, 1997; Dasgupta et al., 2007), silica-deficient garnet pyroxenite (Hirschmann et al., 2003; Kogiso et al., 2003), and carbonated eclogite (Dasgupta et al., 2006; Gerbode and Dasgupta, 2010; Kiseeva et al., 2012), consistent with a source region composed of mixed lithologies. Primary magma compositions overlap with those of garnet pyroxenite melts at pressures between 2.5 and 5 GPa, corresponding to ~90 - 110 km depth. Considering that lithospheric thickness beneath the WARS has been modeled at ~80 km (Huerta and Harry, 2007), this suggests that the source region is, at least in part, sublithospheric. A garnet-bearing source is further supported by elevated light to heavy REE ratios and steep patterns of LREE enrichment on the multi-element diagram. Carbonated peridotite yields another potential match between experimental melts and Ross Sea primary magmas, although the primitive Ross Sea compositions plot at lower MgO wt. % than the experimental melts of carbonated peridotite at 3 GPa (Hirose 1997; Dasgupta et al. 2007). This difference can be explained by crystal fractionation, which would simultaneously

decrease MgO and Al_2O_3 and increase SiO_2. Both olivine and clinopyroxene phenocrysts are present in these lavas, supporting the occurrence of this process.

Pilet et al. (2008) postulate that involvement of amphibole in the melt region can explain trace element distribution patterns observed in OIB that share many characteristics with primitive Ross Sea lavas, including positive Ta-Nb and negative Pb and Rb anomalies (Figure 2-3A-C). Additionally, the Ba/Rb (9.5 - 44) and Rb/Sr (0.076 - 0.013) of Ross Sea lavas range to values suggestive of melting in the presence of metasomatic hydrous phases such as phlogopite and amphibole in the lithosphere (Furman and Graham, 1999). Although preferential removal of Rb during subaerial weathering can alter Ba/Rb, moderate Rb concentrations (12 – 86 ppm) do not indicate that these ratios are primarily a weathering feature. Correlation between Ba/Rb and high Na_2O/K_2O (1.68 – 4.42 for samples with MgO > 7 wt. %) in the Ross Sea lavas lends further support for melting in the presence of Na-amphibole. Experimental melts of hornblendite and hornblendite veins in peridotite at 1.5 GPa match the SiO_2, CaO, and Na_2O contents of Ross Sea primary magmas, but are too rich in Al_2O_3 to fully explain the observed lava compositions (Pilet et al., 2008). Amphibole has been observed in metasomatic veins crosscutting mantle xenoliths from the region (e.g., Perinelli et al., 2006) and would typically suggest a lithospheric, rather than sublithospheric source, although thermodynamic modeling indicates that amphibole may be stable to pressures of 2.5 GPa in the presence of >700 ppm H_2O (Asimow et al., 2004). Generally, the Ross Sea lavas exhibit trace element signatures (e.g., LILE/HFSE, including Hf/Rb and Sr/Nb) that suggest both asthenosphere and fluid-modified lithosphere have been sampled, although inconclusive correlations between these trace element pairs and isotopic signatures indicate that multiple episodes and different types of melting may have modified the magma source beneath the region through removal of fluid-mobile LILE.

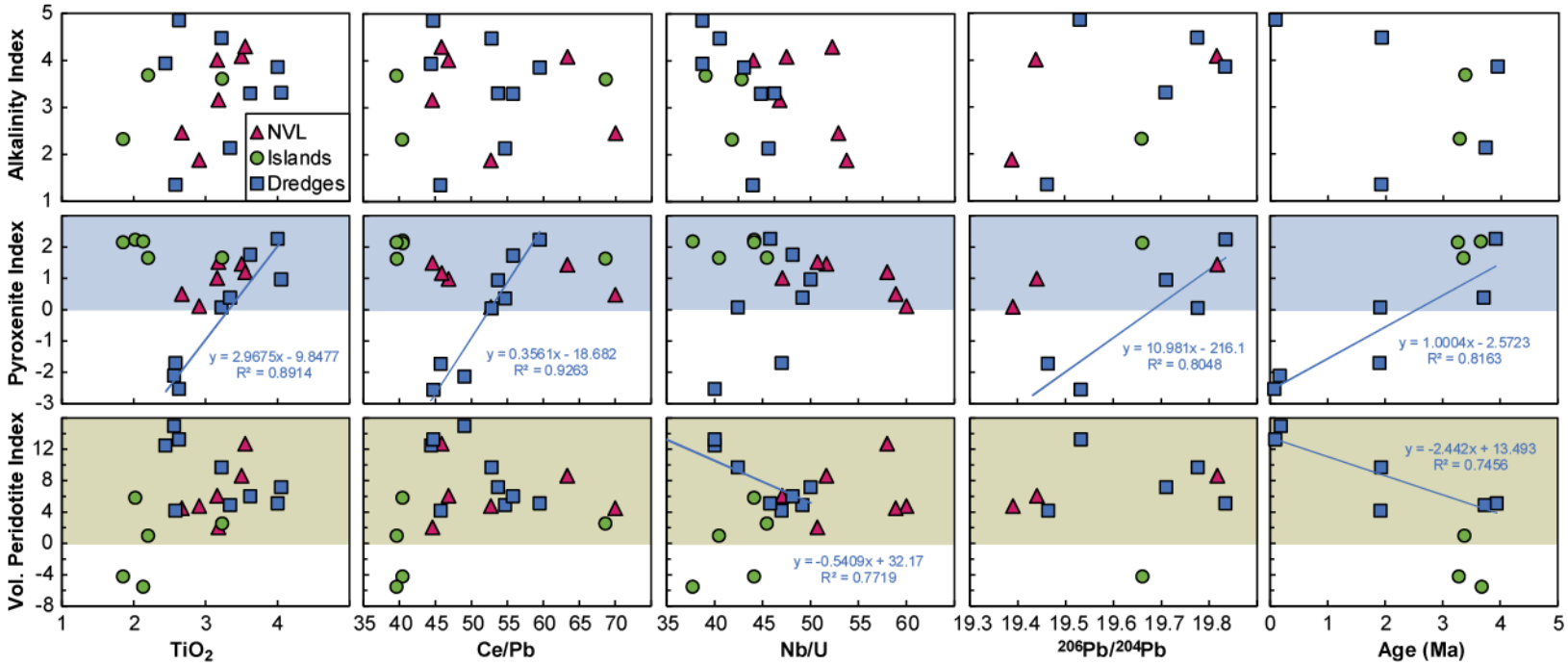

Figure 2-6. Alkalinity index (= total alkali – (SiO_2*0.37 – 14.43), pyroxenite index (= [13.81 – 0.274*MgO] – CaO), and volatilized peridotite index (= CaO – [2.318* SiO_2 – 93.626]) versus various isotopic, trace element, and major oxide data for primitive (MgO > 8 wt. %) Ross Sea lavas. Blue line indicates linear regressions for dredged seamounts in the Ross Sea, only. Light blue shaded area indicates melts derived from a pyroxenite source with values for the pyroxenite index > 0, whereas light green shaded field indicates melts derived from a volatilized peridotite source with values for the volatilized peridotite index > 0 (Herzberg and Asimow, 2008). Age data for Ross Sea dredged seamounts are from Rilling et al. (2009).

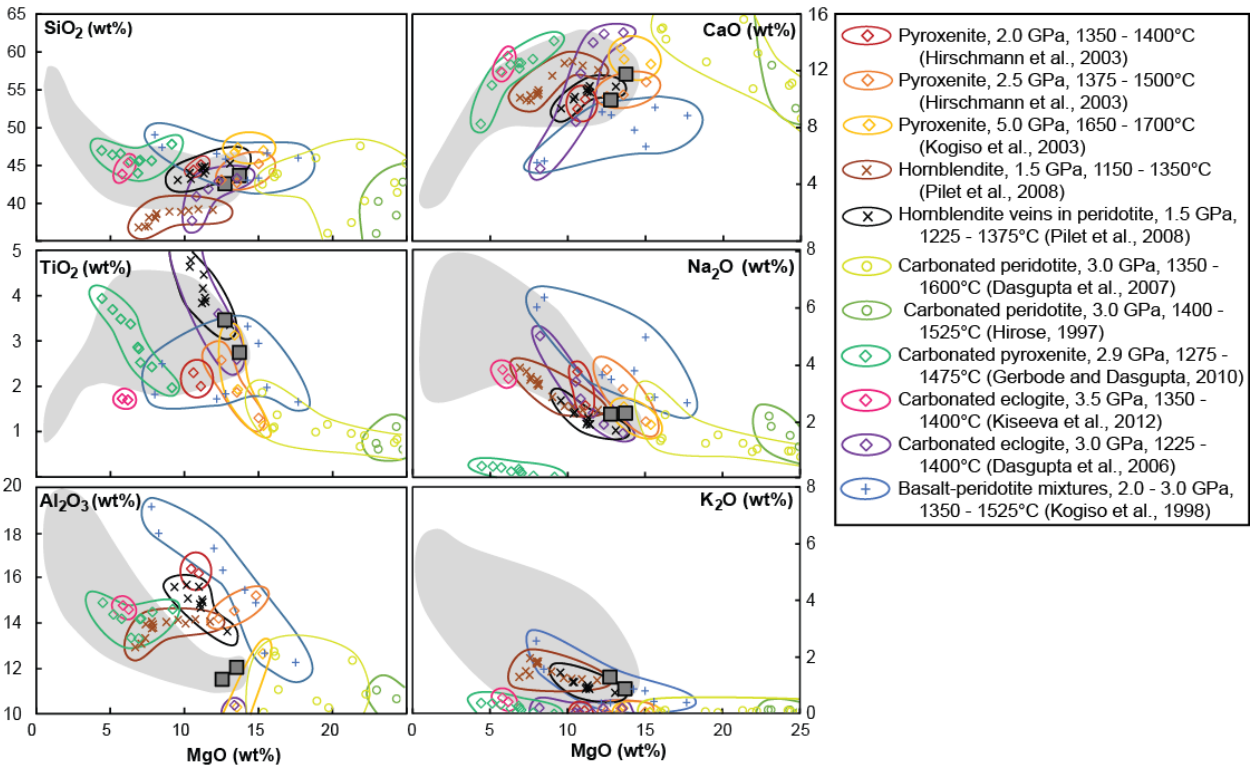

Figure 2-7. Comparisons of estimated Ross Sea primary melt compositions (dark grey squares) with high-pressure experimental melt compositions. Light grey shaded region indicates all magma compositions from this study.

The overall enrichment of incompatible elements relative to primitive mantle, positive Nb-Ta anomalies and Pb negative anomaly, and Sr-Nd-Hf-Pb isotopic ratios of Ross Sea lavas suggest the involvement of a high-μ component in the source. The lavas plot near extreme high-μ lavas from St. Helena and Mangaia (which, going forward, we will simply refer to as "HIMU," using the endmember definition of Hart et al., 1986) and C/FOZO-type lavas from the Cook-Austral Islands with respect to Sr, Nd, and Hf isotopic ratios (Stracke et al., 2005, and references therein), and at very radiogenic values for $^{206}Pb/^{204}Pb$ that fall between the MORB array and HIMU. This decoupling of the Pb isotopic system from Nd and Sr was noted previously by Hart et al. (1995), and is consistent with lavas throughout the WARS (Hart and Kyle, 1993; Hart et al., 1997; Panter et al., 2000, 2006; Nardini et al., 2009). Although many previous studies have interpreted these isotopic signatures in a traditional HIMU context – that is, the extreme

radiogenic Pb-isotope endmember sampled by lavas at St. Helena and Mangaia and thought to represent deeply recycled ancient subducted ocean lithosphere – the less radiogenic $^{206}Pb/^{204}Pb$ values observed in this study show distinct affinities for the C or FOZO mantle end member. Particularly with consideration of $^{87}Sr/^{86}Sr$ and $^{208}Pb/^{206}Pb$ relationships (Figure 2-8), moderately radiogenic Pb and Sr isotopic signatures in C or FOZO-type lavas can be readily discerned from very radiogenic Pb and relatively low $^{87}Sr/^{86}Sr$ exhibited by endmember HIMU lavas (Stracke et al., 2005). Unlike traditional HIMU, for which there is increasing evidence to support an origin as a relatively rare mantle component sampled in only a few type localities (Stracke et al., 2005), the range of C-like isotopic compositions can be attributed to the global process of continuous recycling of ocean lithosphere (crust + mantle), with varying isotopic compositions as the result of variable age, marine sediment composition, and U/Pb of the precursor material (Hart et al., 1992; Hanan and Graham, 1996; Stracke et al., 2005; Castillo, 2014).

The most radiogenic C signatures, HIMU, and high-μ domains in general are traditionally thought to be derived from recycled ocean lithosphere with high $^{238}U/^{204}Pb$ that has been sequestered in the mantle, potentially at the core-mantle boundary, for times scales on the order of 10^9 years until remobilized by ascending mantle plumes (Hofmann and White, 1982; Hart et al., 1986). This material may continue to be cycling through the sublithospheric mantle beneath the WARS, or may be frozen as melt veins in the lithospheric mantle. Alternative explanations suggest that high-μ domains may be generated in the lithosphere (Stein et al., 1997; Halliday et al., 1995; Panter et al., 2006; Rooney et al., 2014) by subduction processes that produce enrichment of U relative to Pb at shallow depths over time scales on the order of 10^8 years. In models for subduction-generated chromatographic metasomatism, deeply dehydrated slab-derived fluids (including aqueous fluids, silicate melts, and supercritical silicate-aqueous fluids)

interact with the overlying mantle wedge to form metasomes containing amphibole, phlogopite, and Nb-oxide that are highly retentive of (and therefore concentrate) Nb in the lowermost portion of the mantle wedge (Navon and Stolper, 1987; Ivanov and Hofmann, 1995; Stein et al., 1997; Pilet et al., 2005). Subsequent partial dehydration of this metasomatized region depletes it in fluid mobile Rb and Pb relative to Th, U, and Nb. After cessation of subduction, metasomatized domains with elevated Nb, U/Pb, and Th/Pb and low Rb/Sr may be preserved as veins in the lithosphere over time scales sufficient to generate the most radiogenic C and high-μ isotopic signatures. In addition to this lithospheric source, slab remnants may pollute the upper mantle and can be preserved if inefficiently homogenized by convection (as opposed to being transported to the core-mantle boundary to stagnate prior to ascent as a mantle plume). A high-μ source for the Ross Sea lavas located at least partially in the lithosphere and/or foundered in the upper mantle and related to the region's history of subduction during the Paleozoic and Mesozoic (Mukasa and Dalziel, 2000) would be consistent with major-oxide and trace-element trends suggesting that Ross Sea lavas sample multiple lithologies, including amphibole-bearing metasomatic veins, eclogite or pyroxenite (as remnants or crystallized transient melts of altered subducted ocean crust), and carbonated pyroxenite or peridotite in the SCLM and upper mantle.

High-μ type magmas are characterized by elevated Nb/Th and Ce/Pb and low Ba/Nb and La/Nb, consistent with the involvement of ancient, subduction-modified ocean lithosphere in their source. The Ross Sea lavas exhibit Nb/Th (6.84 - 15.2), Ba/Nb (5.08 - 14), Ce/Pb (34.8 - 70), and La/Nb (0.624 - 0.856) that overlap with values characteristic of both high-μ and EM sources (Figure 2-9). The Ross Sea lavas also plot between the C, EMI, and EMII end members on the $^{177}Hf/^{176}Hf$ versus $^{87}Sr/^{86}Sr$ diagram, which suggests some contribution of continental material in the melt source. Although radiogenic Sr isotopic compositions may reflect crustal

assimilation, Ross Sea lavas exhibit relatively low Ba/Nb and La/Nb in sharp contrast with higher Ba/Nb (~124) and La/Nb (~2.2) expected for continental crust (Weaver. 1991), as well as elevated Nb/U (average of ~48) poorly correlated with $^{87}Sr/^{86}Sr$ that collectively do not indicate extensive crustal assimilation. Radiogenic Sr isotopic signatures characteristic of EM sources are believed to be produced through variable enrichment of the upper mantle by lower and upper continental crust ± marine sediment (Hofmann and White, 1982; Weaver, 1991; Chauvel et al., 1992; Willbold et al., 2006; Jackson et al., 2007; Chauvel et al., 2008; Jackson and Dasgupta, 2008; Willbold et al., 2010). Both addition of continental sediments into the subduction trench and mechanical erosion of the continental lithosphere during subduction (e.g., von Huene et al., 2004) would provide reasonable mechanisms for the delivery of continental material to the upper mantle, and again would be consistent with West Antarctica's history as an active margin. In the model described by Willbold et al. (2010), recycling of continental and ocean lithosphere to form EM and C components, respectively, occurs simultaneously during subduction processes, such that the two reservoirs are genetically linked (Hanan and Graham, 1996; Stracke et al., 2005).

In summary, we identify a dominantly C-like component, with minor contributions from EM components, as the major sources of Ross Sea magmatism. Isotopic and major-oxide systematics of the Ross Sea lavas are consistent with a history in which 550 - 110 Ma subduction along the paleo-Pacific margin of Gondwana generated hydrated amphibole and/or phlogopite-bearing metasomes in the lithosphere, dispersed pyroxenite bodies in the form of crystallized transient melts or slab remnants, as well as minor amounts of eroded continental lithosphere throughout the upper mantle, and broadly infused the upper mantle beneath the region with volatiles. A 60 Myr hiatus elapsed before the inception of amagmatic rifting in the Cretaceous (Salvini et al., 1997). Within the Terror Rift, positive correlations between the pyroxenite index

and both $^{206}Pb/^{204}Pb$ and Ce/Pb suggest that pyroxenite is the high-μ source lithology. Given the similarities between the most primitive dredged samples from the Terror Rift and 2.5 - 5.0 GPa experimental melts of silica-deficient garnet pyroxenite (Hirschmann et al., 2003; Kogiso et al., 2003) and carbonated eclogite (Dasgupta and Hirschmann, 2006; Gerbode and Dasgupta, 2010; Kiseeva et al., 2012), the pyroxenite domains may exist as fragments of subduction-modified ocean lithosphere dispersed in the upper mantle beneath the rift, or as crystallized melts pervading through the lithosphere. Experimental partial melts indicate that the pyroxenite solidus is ~50°C cooler than the anhydrous peridotite solidus (Kogiso et al., 2003), and in the presence of carbonate may be up to 100°C cooler than the solidus for a volatile-free lithology (Dasgupta and Hirschmann, 2006; Gerbode and Dasgupta, 2010). It is therefore a reasonable hypothesis that readily fusible pyroxenite would be preferentially melted out during lithospheric stretching and associated decompression over the past 50 Myr. As these sources have become exhausted, the latest magmas to be produced beneath the WARS increasingly reflect the volatilized peridotite character of the background mantle throughout the region.

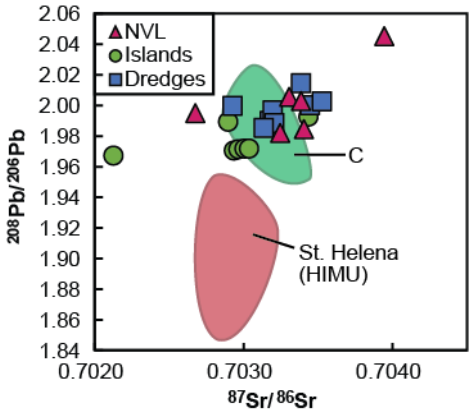

Figure 2-8. $^{208}Pb/^{206}Pb$ versus $^{87}Sr/^{86}Sr$ for analyzed Ross Sea lavas. Red field indicates data for St. Helena (Chaffey et al., 1989; Newsom et al., 1986; Chauvel, 1992; Salters and White, 1998) and Mangaia (Woodhead, 1996) HIMU basalts. Green field indicates data for Austral-Cook C/FOZO (Lassiter et al., 2003) basalts.

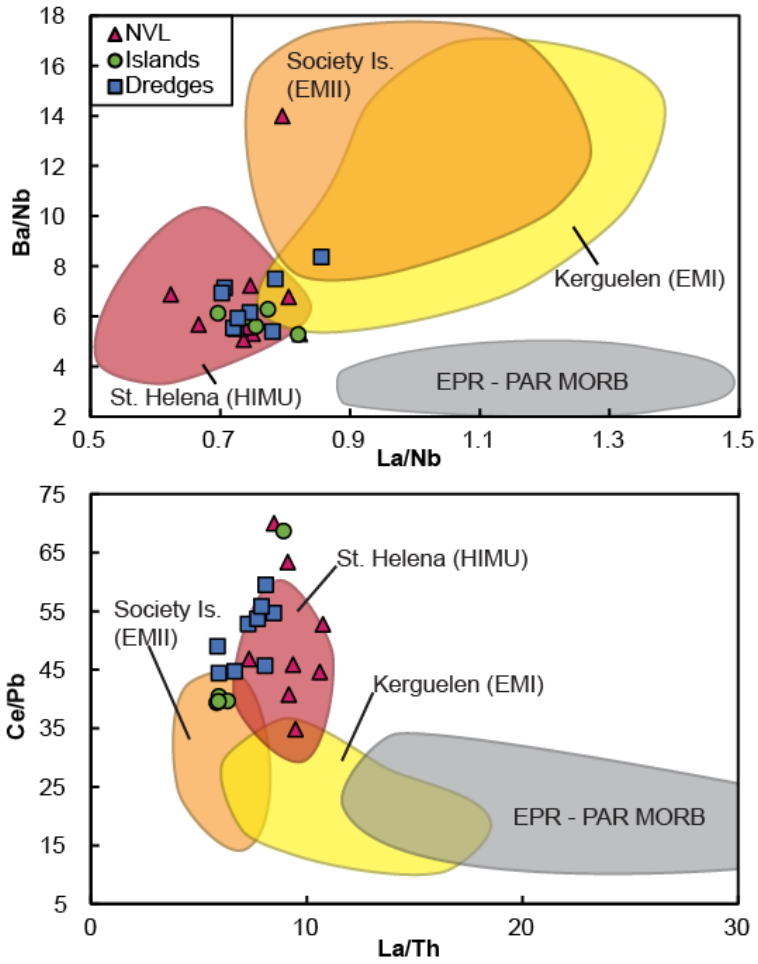

Figure 2-9. Ba/Nb versus La/Nb and Ce/Pb versus La/Th for Ross Sea lavas. Shaded fields for St. Helena, Society Islands, Kerguelen, and East Pacific Rise (EPR)-Pacific Antarctic Ridge (PAR) basalts are for data compiled from the GeoROC database (http://georoc.mpch-mainz.gwdg.de/georoc/). References for this compilation are available in the supporting information.

5.2. Existing magma source models

The mantle plume concept has been proposed in the MBL portion of the WARS due to geophysical evidence of crustal doming (LeMasurier and Rex, 1989; Behrendt, 1999; LeMasurier et al., 2003). LeMasurier and Landis (1996) calculated a maximum of ~3 km of tectonic Neogene uplift associated with the MBL plume, but more recent studies have challenged key assumptions regarding pre-plume versus syn-plume topography and plume-related uplift (Wilch and McIntosh, 2000; Luyendyk et al., 2001). Recent geophysical studies identify upper

mantle thermal anomalies associated with evidence for a partially hydrated transition zone (Emry et al., 2015) and a deep-seated (>800 km depth) seismic low-velocity anomaly (Hansen et al., 2014) as further evidence for a mantle plume beneath Marie Byrd Land, but geophysical evidence is not supportive of the plume model for the Cenozoic volcanism in NVL (Berg et al., 1989; Perinelli et al., 2006), where crustal doming similar to MBL has not been observed. Although a low-velocity anomaly has been identified beneath Ross Island (Hansen et al., 2014), its relatively shallow depth (~200 - 300 km) and broad lateral extent is inconsistent with the 40 km diameter plume head proposed by Kyle (1992) and Esser (2004), and it does not appear to be connected to the MBL low-velocity anomaly at depth.

The broad, diffuse geometry of both the Ross Sea seismic anomaly and the DAMP seismic anomaly imaged beneath most of the Southern Ocean (Finn et al., 2005), coupled with active magmatism that spans thousands of kilometers over the past 30 Myrs, lends doubt over these features being generated by a deep-seated mantle plume. Alternative models (e.g., Rocholl et al., 1995; Hart et al., 1997; Wörner , 1999; LeMasurier et al., 2003) suggest that WARS magmatism was produced by two-stage melting punctuated by a considerable amount of time, but still require an enriched mantle plume source or upwelling during initial Gondwana breakup in the Jurassic, followed by second-stage melting due to rift-induced decompression. Because of these complications and the fact that the geochemical data presented in this study are best explained by other processes, we infer that a mantle plume is not the dominant mechanism responsible for Ross Sea magmatism.

Anomalous seismic structures observed below the WARS, previously interpreted within a mantle plume framework, may also be explained by the history of subduction along the paleo-Pacific margin of Gondwana. Numerous tomographic studies (Sieminski et al., 2003; Finn et al.,

2005; Watson et al., 2006) have attributed slow seismic anomalies below the WARS to hotter mantle temperatures in this region. More recent seismic studies using P-wave tomography (Hansen et al., 2014) and P-wave receiver functions (Emry et al., 2015) have identified the presence of potential deeper low velocity zones (~ 800 km) beneath Marie Byrd Land (Hansen et al., 2014), and two regions where the mantle transition zone may be hotter due to upwelling from below (Emry et al., 2015). An alternative explanation is that these anomalous mantle structures are due to chemical variations (e.g., Emry et al., 2015) introduced during ancient subduction. As the lithosphere thinned during rifting, the mantle underwent decompression; small amounts of either water, carbon, or pyroxenite could account for larger amounts of melting than expected in an anhydrous peridotite mantle (Asimow and Langmuir, 2003; Kogiso et al., 2003). Several authors (Zipfel and Worner, 1992; Coltorti et al., 2004; Perinelli et al., 2006; Cooper et al., 2007) have noted the presence of hydrous phases, including amphiboles and phlogopite, in mantle xenoliths from Victoria Land, which in concert with the broad low-velocities anomalies identified by extended seismic coverage (e.g., Emry et al., 2015) supports the hydrated mantle hypothesis.

5.3. New magma source model

Our proposed model calls for multistage melt generation sampling a multi-lithologic source, and is summarized in Figure 2-10. Between 550 and ~110 Ma, subduction took place along the paleo-Pacific Gondwanan margin (Mukasa and Dalziel, 2000). Flux melting preferentially removed LILE and fluid mobile elements, including Pb, from the overlying mantle wedge, continuously creating domains of high (U, Th)/Pb and low Rb/Sr, while interactions between slab dehydration fluids and mantle peridotite generated amphibole- and phlogopite-rich veins. Pyroxenite was simultaneously generated as crystallized transient melt pervading through

the lithospheric mantle, or as fragments of subducted ocean lithosphere shallowly cycling through the upper mantle beneath the region. Mechanical erosion of the continental lithosphere likely contributed additional heterogeneity to the upper mantle to produce more radiogenic $^{87}Sr/^{86}Sr$ in the Ross Sea lavas that trend toward EM. Radiogenic ingrowth of these diverse compositional domains continued after the cessation of subduction and during the largely amagmatic rifting that followed. WARS rifting began in the late Mesozoic, thinning the lithosphere and changing patterns of mantle convection after the end of subduction (Finn et al., 2005). Magmas were generated from both decompression of hot, volatilized asthenosphere and thermal erosion of the metasomatized lithosphere. During the latest stages of Cenozoic rifting, melting became more localized as a result of broad extension transitioning to the opening of separate basins (Rossetti et al., 2006). Decompression and thermal erosion in the Ross Sea basins are not significant enough to melt pure anhydrous peridotite sources, but could initiate melting of carbonated peridotite and gt-pyroxenite inferred to exist in the upper mantle. This is especially definitive considering that significant amounts of water are also present in olivine-hosted melt inclusions (Aviado et al., 2013; Chapter III of this dissertation), as is also supported by observations of amphibole and phlogopite in mantle xenoliths from the region.

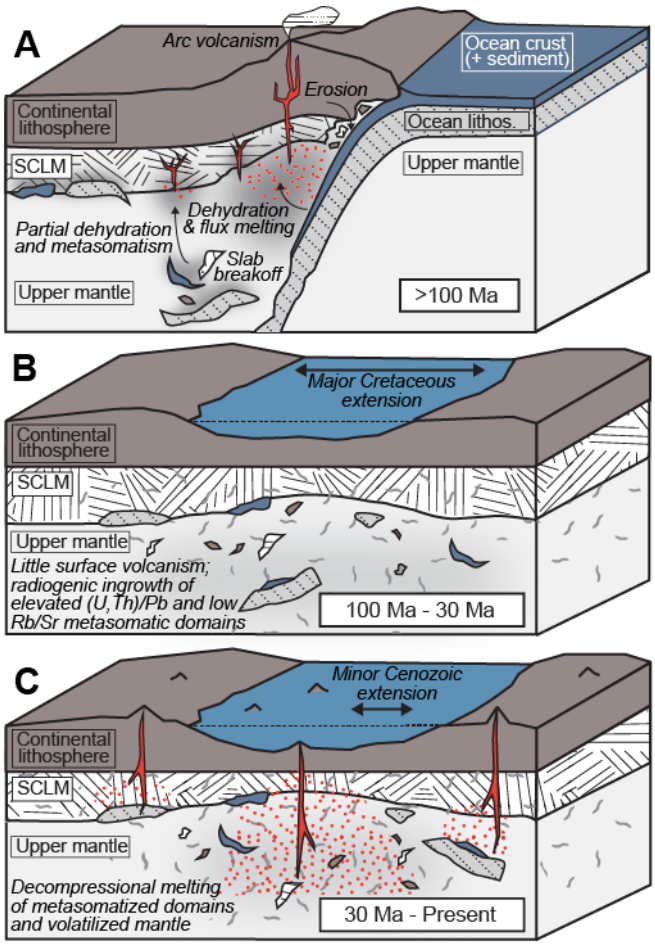

Figure 2-10. Schematic of a new magma source model for Ross Sea magmatism. A) The 550 – 100 Ma subduction zone along the paleo-Pacific margin of Gondwana (Mukasa and Dalziel, 2000); percolation of slab dehydration fluids and associated flux melting remove LILE and fluid-mobile Pb and Rb in the mantle wedge, precipitate amphibole in lithospheric veins, and broadly volatilize the upper mantle beneath West Antarctica. Subduction-processed slab remnants, including eclogite ± marine sediment, are isolated at the base of the lithosphere or poorly convected in the upper mantle after cessation of subduction. These processes generate reservoirs with elevated (U, Th)/Pb and Nb and low Rb/Sr that are precursors to high-μ domains, while eroded continental material generates the EM component. B) Radiogenic ingrowth of high-μ domains produced in the lithosphere and upper mantle since 550 Ma continues until largely amagmatic Cretaceous rifting associated with breakup of Gondwana. This extension may have been accompanied by production of small-degree melts that crystallized in lithospheric veins (e.g., Nardini et al., 2009). C) Lesser Cenozoic extension generates magmas through decompression of hot, volatilized asthenosphere and metasomatized lithosphere, sampling high-μ and EM domains.

6. Conclusion

Alkaline basaltic samples dredged from seamounts in the Ross Sea, Franklin and Beaufort Islands, and the Mt. Melbourne region of northern Victoria Land are chemically similar to other volcanic rocks throughout the WARS. A mantle plume model has been invoked previously to explain Cenozoic WARS magmatism, but comparisons to experimental melts of fertile peridotite do not match the major-oxide concentrations of the Ross Sea lavas. The analyzed lavas exhibit major-oxide trends indicative of a multi-lithologic source that potentially includes carbonated peridotite, carbonated eclogite/pyroxenite, and amphibole-bearing metasomes. The pressures associated with experimental melts of these diverse source lithologies range from lithospheric (1.5 GPa) to sublithospheric (2.5 - 5.0 GPa), suggesting that Ross Sea lavas sample both metasomatized thinning lithosphere and upwelling volatilized asthenosphere. These source lithologies are consistent with the region's long-lived subduction history. The Ross Sea lavas possess an overall enrichment in incompatible elements; however, the large negative Pb anomaly and the LILE distribution patterns support a model in which fluid-mobile elements are removed from the residual mantle lithosphere source during the subduction-related volcanism along the paleo-Pacific Gondwanan margin. Heterogeneity in the extent of LILE removal suggests that melts are polybaric with varying degrees of asthenospheric and lithospheric contributions.

In the Terror Rift, considered the locus of the most recent rifting and magmatism, age relationships between the pyroxenite index and the volatilized peridotite index are consistent with a transition from a pyroxenite source to a volatilized peridotite source over the past 5 Ma. This would suggest that easily fusible pyroxenite lithologies characterized by elevated $^{206}Pb/^{204}Pb$ and Ce/Pb consistent with a high-μ source were removed preferentially during earlier

episodes of magmatism, leaving the residual mantle increasingly peridotitic in character over time. The Sr-Nd-Hf-Pb systematics of the Ross Sea lavas are similar to those of the C component (Hanan and Graham, 1996) or FOZO end member (Hart, 1986). Highly radiogenic (though not as extreme as the HIMU end member) $^{206}Pb/^{204}Pb$ in this source may be ascribed to continuous recycling of ocean lithosphere at subduction zones (Hart, 1986; Hanan and Graham, 1996; Stracke et al., 2005). Although C and other high-μ mantle domains are thought to be isolated in the deep mantle for long timescales, it is possible for similar isotopic, trace element, and major-oxide signatures to be generated over shorter timescales in the upper (and lithospheric) mantle, given the appropriate chemical processing of the precursor material through subduction zones. In the WARS, the history of subduction during the Paleozoic and Mesozoic would have provided a likely mechanism for such processing.

Table 2-1. Major oxide, trace element, and isotopic compositions of Ross Sea lavas

	Victoria Land										
Sample	NV-15B	NV-15	NV-14C	NV-14A	NV-13A	NV-12A	NV-11B	NV-6E	VC-21	NV-4B	VC-44
Location	Cape Washington		Oscar Point (1 km W)		Shield Nunatak	Edmonton Point	Baker Rocks	Downshire Cliffs		Foyn Island	Malta Plateau
Latitude	-74.6564	-74.6496	-74.5917	-74.5749	-74.5836		-74.3115	-71.6193	-71.6935	-71.9550	-73.1490
Longitude	165.4094	165.4015	164.8160	164.8094	164.1811		165.0148	170.5561	170.5574	171.0915	167.1647
Age (Ma)[a]											
SiO_2 (wt%)	42.02	40.92	44.66	43.42	43.19	56.53	44.96	39.25	41.46	42.94	40.91
TiO_2	3.16	3.50	2.73	3.27	2.91	0.94	2.65	3.55	2.99	2.67	4.36
Al_2O_3	12.15	12.06	15.96	15.61	13.48	15.96	16.51	12.56	13.43	12.79	13.68
Fe_2O_3	13.01	14.01	12.07	13.28	12.76	9.23	12.17	13.33	13.18	12.42	15.62
MnO	0.18	0.19	0.18	0.18	0.17	0.22	0.19	0.16	0.17	0.18	0.20
MgO	10.82	9.08	5.97	6.33	8.95	1.01	4.98	9.21	6.52	10.70	5.53
CaO	9.84	9.86	9.57	9.61	11.25	3.54	9.71	10.09	10.28	10.38	11.09
Na_2O	3.61	3.43	3.55	3.55	2.66	5.80	3.58	3.53	3.47	2.98	3.14
K_2O	1.52	1.37	1.23	1.12	0.77	3.81	1.12	0.86	1.42	0.94	0.42
P_2O_5	0.76	1.29	0.66	0.79	0.69	0.29	1.06	0.68	0.65	0.54	1.17
Rb (ppm)	34	24	17	18	13	78	13	21	75	16	12
Ba	425	328	616	307	244	1207	647	323	419	269	425
Th	8.2	5.6	3.8	4.1	2.7	14.3	4.0	4.6	6.4	4.6	4.2
U	1.7	1.2	0.8	0.8	0.6	2.7	0.7	1.0	2.3	0.9	1.8
Ta	5.9	4.8	3.4	3.8	2.5	8.7	3.3	4.4	5.1	3.8	3.9
Nb	80	62	44	52	36	121	43	58	68	53	47
La	60	51	35	40	29	83	40	43	49	39	45
Ce	103	95	65	74	58	148	74	78	84	70	82
Pb	2.2	1.5	1.8	1.1	1.1	8.4	1.7	1.7	1.9	1.0	1.1
Pr	12.6	12.6	8.5	9.6	7.4	17.8	9.8	10.3	10.6	8.8	11.4
Nd	51	54	37	41	32	70	44	44	44	36	51
Sr	817	844	846	839	642	433	900	800	695	592	843
Sm	10.9	11.6	7.8	8.9	6.7	14.6	9.6	9.7	9.1	7.6	11.1
Hf	7.9	7.7	4.1	4.7	3.1	12.4	4.0	5.6	5.3	4.6	5.0
Zr	336	319	172	201	153	538	196	225	311	203	193
Eu	3.3	3.4	3.3	2.9	2.4	4.5	3.9	2.9	2.8	2.3	3.7
Gd	11	11	8	9	7	14	9	9	9	7	10
Tb	1.4	1.4	1.0	1.2	0.9	2.0	1.1	1.2	1.2	1.0	1.4
Y	34	35	25	30	23	53	28	30	30	27	34
Dy	6.6	7.0	5.0	5.7	4.3	10.2	5.6	5.9	5.7	5.1	6.8
Ho	1.1	1.1	0.8	1.0	0.7	1.7	0.9	1.0	1.0	0.8	1.1
Er	2.8	2.8	2.2	2.6	1.9	4.6	2.4	2.6	2.5	2.3	2.9
Yb	2.5	2.5	2.0	2.3	1.7	4.6	2.1	2.4	2.4	2.1	2.5
Lu	0.4	0.4	0.3	0.3	0.2	0.7	0.3	0.3	0.4	0.3	0.4
Ni	388	461	281	213	193	162	282	435	373	411	382
Cu	132	111	182	65	57	119	198	226	206	101	176
Zn	93	102	84	85	79	124	89	75	80	78	99
V	184	187	166	180	226	0	132	235	240	209	291
Cr	227	198	75	85	343	4	62	225	218	395	10
$^{208}Pb/^{204}Pb$		39.330	39.242	39.251	39.361		39.329				39.493
$^{207}Pb/^{204}Pb$		15.596	15.604	15.603	15.638		15.623				15.600
$^{206}Pb/^{204}Pb$		19.817	19.563	19.673	19.651		19.229				19.924
$^{87}Sr/^{86}Sr$	0.70287	0.70340	0.70330	0.70267	0.70338		0.70394				0.70324
$^{143}Nd/^{144}Nd$	0.51297	0.51293	0.51296	0.51290	0.51294		0.51288				0.51289
$^{176}Hf/^{177}Hf$	0.28305	0.28301	0.28304	0.28302	0.28305		0.28300				

[a]Ages from Rilling et al., 2009

Table 2-1. Major oxide, trace element, and isotopic compositions of Ross Sea lavas (continued)

	Victoria Land										
Sample	VC-3	NV-3B	NV-3I	12.19-01-7	12-19-01-5	12-10-01-5	12-19-01-3	12-10-01-1	12-10-01-2	NV-5B	AW82-284
Location	Cotter Cliffs	Possession Island		Pleiades						Cape Adare	Beaufort Island
Latitude				-78.4331						-71.3178	
Longitude				163.5441						170.2651	
Age (Ma)[a]											
SiO_2 (wt%)	46.35	42.26	45.95	43.92	42.45	64.23	43.80	54.97	51.56	40.48	43.85
TiO_2	2.59	3.40	2.44	3.45	3.98	0.16	3.18	1.39	2.22	4.05	3.12
Al_2O_3	15.96	14.93	16.99	14.73	14.40	16.74	14.69	17.42	17.08	15.43	16.40
Fe_2O_3	11.49	13.56	11.14	11.65	12.69	3.70	11.86	8.58	9.64	13.81	11.62
MnO	0.23	0.21	0.22	0.22	0.22	0.15	0.21	0.23	0.19	0.21	0.20
MgO	3.78	6.09	3.51	7.86	7.44	0.04	8.53	1.78	3.39	5.24	4.21
CaO	7.23	9.79	7.81	10.61	10.32	0.92	9.95	4.32	6.02	10.01	9.13
Na_2O	5.05	3.44	5.31	3.66	3.14	7.04	3.43	5.96	4.68	4.05	4.58
K_2O	1.61	1.14	1.85	1.27	1.39	5.19	1.51	3.45	2.79	1.75	2.45
P_2O_5	1.23	0.91	1.21	0.74	0.78	0.02	0.93	0.56	0.76	1.12	1.03
Rb (ppm)	21	20	42	28	24	301	31	80	76	31	66
Ba	576	371	498	460	584	14	513	1130	806	541	774
Th	9.3	5.5	11.2	5.9	5.6	58.8	5.0	12.0	11.3	6.7	8.5
U	2.0	1.0	2.3	1.8	1.7	14.2	1.4	3.0	2.8	1.3	1.2
Ta	7.5	4.7	8.3	5.4	5.4	23.2	4.4	7.8	6.8	6.7	7.8
Nb	102	61	109	81	85	318	71	130	103	90	106
La	76	47	84	54	53	207	53	83	80	60	88
Ce	136	83	144	110	108	337	107	155	149	106	147
Pb	3.3	1.6	3.3	2.7	3.1	25.3	2.4	7.7	8.1	1.7	2.1
Pr	17.0	10.7	17.4	13.2	12.8	31.1	12.9	17.3	16.7	13.6	18.1
Nd	69	46	68	52	50	91	50	62	60	58	74
Sr	848	925	987	1052	1255	6	1094	654	774	996	1351
Sm	13.7	9.6	12.9	10.3	9.7	13.6	9.8	10.9	10.9	12.5	14.9
Hf	7.8	5.2	8.6	7.0	6.2	24.3	5.3	9.8	8.4	6.3	9.8
Zr	359	217	420	313	272	985	231	457	381	278	440
Eu	3.9	3.1	3.7	3.4	3.3	0.4	3.4	3.6	3.3	3.7	4.4
Gd	13	9	13	9	8	10	8	9	9	12	14
Tb	1.7	1.2	1.7	1.3	1.2	1.7	1.2	1.3	1.3	1.6	1.8
Y	43	28	39	31	28	56	30	4	34	39	42
Dy	8.1	5.6	7.4	6.9	6.3	10.3	6.6	7.5	7.2	7.6	8.4
Ho	1.4	0.9	1.2	1.3	1.1	2.1	1.2	1.4	1.3	1.2	1.4
Er	3.7	2.4	3.4	3.2	2.8	6.1	3.0	3.7	3.5	3.3	3.6
Yb	3.5	2.2	3.3	2.4	2.2	6.4	2.3	3.2	2.9	3.1	3.4
Lu	0.5	0.3	0.5	0.4	0.3	1.0	0.3	0.5	0.5	0.4	0.5
Ni	303	296	411	85	56	0	134	0	10	547	287
Cu	95	101	264	30	21	2	40	8	23	272	177
Zn	98	87	95	92	94	167	91	124	103	97	103
V	99	215	108	248	252	1	231	20	116	205	148
Cr	4	35	18	237	174	2	364	2	22	11	53
$^{208}Pb/^{204}Pb$		39.916	39.798								39.435
$^{207}Pb/^{204}Pb$		15.658	15.659								15.622
$^{206}Pb/^{204}Pb$		20.028	20.228								20.010
$^{87}Sr/^{86}Sr$		0.70343	0.70212								0.70293
$^{143}Nd/^{144}Nd$		0.51282	0.51295								0.51295
$^{176}Hf/^{177}Hf$											0.28302

Table 2-1. Major oxide, trace element, and isotopic compositions of Ross Sea lavas (continued)

	Islands									Dredges	
Sample	NV17A	BFT-1	BFT-2	BFT-5	NV-16B	04ANT1-6	04ANT1-8	04ANT1-9	04ANT5A-19	04DRE1-31	04DRE1-32
Location	Beaufort Island				Franklin Island					Dredge 1	
Latitude					-76.1706					-76.3449	
Longitude					168.3791					168.3856	
Age (Ma)[a]		6.76 ± 0.05	6.73 ± 0.03			3.28 ± 0.04		3.38 ± 0.04	3.68 ± 0.16	0.133 ±0.024	0.122 ± 0.026
SiO_2 (wt%)	43.21	50.95	49.74	43.27	41.84	46.20	44.26	44.12	43.62	41.49	41.86
TiO_2	2.97	1.53	1.90	3.23	2.02	1.85	2.17	2.20	2.13	2.68	2.69
Al_2O_3	15.16	19.57	18.91	12.52	12.62	13.74	13.66	13.43	13.31	12.85	12.92
Fe_2O_3	11.65	7.78	8.71	13.53	12.29	12.14	11.87	12.58	11.64	14.49	14.54
MnO	0.21	0.20	0.22	0.20	0.27	0.21	0.26	0.22	0.26	0.27	0.27
MgO	5.31	1.28	1.95	10.77	8.76	8.87	7.53	9.28	7.57	6.72	6.94
CaO	9.93	5.15	6.01	9.20	9.18	9.23	9.57	9.62	9.56	10.72	10.64
Na_2O	4.28	7.25	6.18	3.47	5.89	3.69	5.36	4.01	5.34	4.92	5.23
K_2O	1.90	3.75	3.47	1.72	2.11	1.30	0.24	1.57	1.95	1.89	1.96
P_2O_5	0.76	0.63	0.73	1.28	0.85	0.45	0.88	0.62	0.88	1.30	1.32
Rb (ppm)	42	129	112	42	50	50	86	56	79	47	52
Ba	627	1066	1034	528	471	471	864	546	824	1031	898
Th	6.5	15.3	14.6	9.2	9.8	9.8	18.4	9.8	18.8	14.0	14.3
U	1.2	4.0	3.8	2.2	1.7	1.7	4.8	2.2	3.9	3.3	2.8
Ta	6.0	13.2	13.2	7.6	5.9	5.9	10.9	6.6	11.3	9.2	9.7
Nb	83	174	164	100	75	75	145	89	147	125	133
La	64	117	116	82	58	58	107	62	111	101	107
Ce	111	196	199	151	97	97	181	107	186	168	177
Pb	1.6	4.4	3.9	2.2	2.4	2.4	4.6	2.7	4.7	3.0	3.6
Pr	14.1	20.0	21.1	17.3	10.3	10.3	19.0	11.6	19.2	18.0	19.0
Nd	58	73	80	71	40	40	73	46	73	71	75
Sr	1236	1316	1378	939	692	692	1126	802	1177	1087	1228
Sm	12.0	13.0	14.7	14.1	8.0	8.0	13.7	9.0	14.0	13.9	14.4
Hf	8.1	11.9	12.3	10.0	5.3	5.3	9.3	6.0	9.5	7.4	7.7
Zr	376	637	633	440	230	230	488	281	477	352	346
Eu	3.7	4.1	4.5	4.2	2.5	2.5	4.1	2.8	4.2	4.1	4.2
Gd	11	12	14	13	8	8	13	9	13	13	13
Tb	1.5	1.5	1.7	1.5	1.0	1.0	1.6	1.1	1.7	1.6	1.6
Y	35	40	44	37	32	32	45	33	46	42	43
Dy	6.9	7.4	8.3	7.4	5.7	5.7	8.4	6.2	8.4	8.0	8.2
Ho	1.1	1.3	1.4	1.2	1.0	1.0	1.5	1.1	1.5	1.4	1.4
Er	3.0	3.5	3.9	3.0	2.8	2.8	4.0	3.0	4.0	3.7	3.7
Yb	2.8										
Lu	0.4	0.5	0.5	0.4	0.4	0.4	0.6	0.4	0.6	0.5	0.5
Ni	330										
Cu	219										
Zn	94										
V	162	32	46	143	152	152	131	157	137	136	145
Cr	127	7	7	429	288	288	276	293	293	113	134
$^{208}Pb/^{204}Pb$	39.425	39.403	39.434			39.117				38.981	38.961
$^{207}Pb/^{204}Pb$	15.628	15.626	15.631			15.584				15.582	15.577
$^{206}Pb/^{204}Pb$	19.995	19.981	19.996			19.660				19.486	19.481
$^{87}Sr/^{86}Sr$	0.70296	0.70300	0.70303			0.70289				0.70344	0.70292
$^{143}Nd/^{144}Nd$	0.51292	0.51293	0.51295			0.51296				0.51300	0.51297
$^{176}Hf/^{177}Hf$	0.28301	0.28299	0.28299			0.28306					0.28304

Table 2-1. Major oxide, trace element, and isotopic compositions of Ross Sea lavas (continued)

	Dredges										
Sample	04DRE2-42	04DRE3-56	04DRE3-59	04DRE3-73	04DRE4-75	04DRE4-76	04DRE5-80	04DRE5-81	05DRE5-85	04DRE5-89	04DRE6-107
Location	Dredge 2	Dredge 3				Dredge 4	Dredge 5				Dreadge 6
Latitude	-76.7322	-75.9754				-76.9825	-76.5785				-75.9682
Longitude	168.7641	168.2267				167.4890	166.7026				168.6177
Age (Ma)[a]	1.00 ± 0.05	0.187 ± 0.176		0.089 ± 0.066	1.93 ± 0.04	1.92 ± 0.04	3.94 ± 0.08		3.73 ± 0.14		0.506 ± 0.024
SiO_2 (wt%)	46.60	39.45	41.14	40.41	41.11	43.66	42.19	41.56	42.57	41.73	40.24
TiO_2	2.81	2.56	2.44	2.63	3.22	2.58	4.00	4.05	3.34	3.62	3.39
Al_2O_3	16.89	11.84	12.33	12.01	12.47	12.07	13.17	11.95	11.54	12.19	13.09
Fe_2O_3	10.22	12.25	10.68	12.43	14.08	12.39	14.61	14.23	13.88	14.19	14.59
MnO	0.21	0.23	0.19	0.23	0.24	0.18	0.21	0.18	0.17	0.19	0.26
MgO	3.77	11.27	10.54	11.06	8.65	13.70	8.33	10.82	12.73	10.72	4.90
CaO	8.31	12.83	14.24	13.31	11.37	11.76	9.27	9.88	9.94	9.12	11.54
Na_2O	4.65	3.63	3.51	3.69	4.29	2.20	3.31	2.78	2.17	2.92	4.42
K_2O	2.61	1.77	1.22	1.69	0.97	0.88	1.73	1.48	1.29	1.39	2.71
P_2O_5	0.84	1.10	0.76	1.19	1.17	0.45	0.87	0.88	0.67	0.77	1.42
Rb (ppm)	62	62	33	50	15	24	45	37	29	32	78
Ba	812	870	657	869	664	326	479	415	363	457	1173
Th	11.0	15.2	11.0	13.7	13.2	4.1	7.8	7.0	5.2	7.1	15.2
U	2.8	3.6	2.3	2.9	2.9	1.0	1.9	1.5	1.2	1.6	3.6
Ta	9.2	9.3	7.0	8.4	9.4	3.5	6.8	5.9	4.4	5.8	10.9
Nb	125	104	92	116	123	47	87	75	59	77	152
La	94	89	65	91	96	33	63	54	44	56	118
Ce	168	152	111	152	169	64	119	102	82	106	198
Pb	3.6	3.1	2.5	3.4	3.2	1.4	2.0	1.9	1.5	1.9	4.5
Pr	18.4	17.5	12.4	16.3	18.4	7.5	14.1	12.1	9.7	12.2	21.6
Nd	72	71	50	64	73	32	59	52	40	51	86
Sr	1407	1018	776	1005	1132	514	874	798	705	823	1264
Sm	13.0	13.8	9.8	12.4	14.0	6.6	12.7	11.2	8.3	10.5	16.9
Hf	10.1	6.9	5.2	6.1	9.1	4.4	10.2	8.4	5.9	7.6	8.5
Zr	470	264	225	273	396	185	442	364	267	336	380
Eu	4.0	4.1	3.0	3.7	4.1	2.1	3.9	3.4	2.6	3.2	5.0
Gd	12	12	9	12	13	6	12	10	8	10	15
Tb	1.4	1.5	1.1	1.4	1.6	0.9	1.5	1.3	1.0	1.2	1.8
Y	37	35	30	36	40	24	39	32	26	31	48
Dy	6.9	7.9	6.0	7.0	7.9	4.6	7.8	6.7	5.2	6.0	9.2
Ho	1.2	1.4	1.0	1.2	1.4	0.8	1.3	1.1	0.9	1.0	1.6
Er	3.2	3.6	2.7	3.2	3.5	2.2	3.3	2.7	2.3	2.6	4.0
Yb											
Lu	0.5	0.5	0.3	0.4	0.5	0.3	0.4	0.3	0.3	0.3	0.6
Ni											
Cu											
Zn											
V	139	204	251	210	208	232	196	205	194	196	183
Cr	45	342	413	348	276	614	96	284	405	292	18
$^{208}Pb/^{204}Pb$	39.144			39.007	39.328	39.214	39.382				38.920
$^{207}Pb/^{204}Pb$	15.606			15.583	15.610	15.634	15.595				15.521
$^{206}Pb/^{204}Pb$	19.670			19.532	19.776	19.463	19.834				19.432
$^{87}Sr/^{86}Sr$	0.70317			0.70319	0.70338	0.70320	0.70313	0.70333			0.70352
$^{143}Nd/^{144}Nd$	0.51288			0.51301	0.51294	0.51293	0.51292	0.51294			0.51300
$^{176}Hf/^{177}Hf$	0.28298			0.28304	0.28307	0.28303	0.28301	0.28299			0.28306

CHAPTER III

WEST ANTARCTIC RIFT VOLCANISM ENHANCED BY A VOLATILE LEGAGY OF ANCIENT SUBDUCTION

Abstract

Volatile presence, particularly H_2O and CO_2, in the mantle source regions of basaltic magmas profoundly influences melt generation and productivity. In the West Antarctic Rift System (WARS), understanding the role of volatiles is critical to resolving questions regarding the production of unusually voluminous Cenozoic alkaline magmas and the geodynamics supporting ongoing rifting. Here, we present new major-oxide, trace-element, and volatile data from olivine-hosted melt inclusions to evaluate the chemical systematics of undegassed magmas. Melt inclusion compositions show that the West Antarctic mantle is broadly enriched in volatiles, likely due to modification by hydrous and CO_2-bearing fluids. We link these findings to recent geophysical studies of the region and ultimately the West Antarctic tectonic history, in which Paleozoic - Mesozoic subduction along the paleo-Pacific margin of Gondwana generated volatilized components in the mantle. We suggest that consequent fusible lithologies importantly contribute to rifting-driven decompression melting in the WARS.

1. Introduction

Mantle volatiles – particularly H_2O – play an important role in the petrogenesis of intraplate magmas by lowering the mantle solidus (Green, 1973) and influencing partial melt compositions (Grove et al., 2006). Geochemical similarities between intraplate alkaline magmas and high-pressure experimental melts of carbonated mantle lithologies have indicated that CO_2

is also critical to the generation of silica-undersaturated, highly alkalic magmas common to many ocean island basalts (OIB; Hirose, 1997; Dasgupta et al., 2007a; Dasgupta et al., 2006; Mallik and Dasgupta, 2014). Subduction-zone recycling of oceanic lithosphere and sediments serves as a key process for introducing H_2O, CO_2, and chemically heterogeneous domains into the mantle. However, many aspects of the nature, transport, and fate of these volatile-bearing components in the mantle remain enigmatic.

The West Antarctic Rift System (WARS), one of the largest continental extensional provinces in the world, is characterized by widespread Cenozoic volcanism dominated by alkaline products (LeMasurier and Thompson, 1990). In addition to its large size and unusually voluminous volcanism, the WARS mantle is associated with a low-velocity seismic anomaly that has been attributed to a plume acting beneath the region (e.g., Sieminski et al., 2003). Numerous mantle sources for rift lavas have been proposed, including a plume beneath Marie Byrd Land (MBL; LeMasurier and Landis, 1996; Hart et al., 1997; Wörner, 1999) and a source stratified with the remnants of a plume head related to the Karoo large igneous province (Riley, 2001). However, the shallow, diffuse geometry of the pervasive low-velocity anomaly underlying West Antarctica and extending between rifted margins that were once conjugate along the paleo-Pacific margin of Gondwana is inconsistent with classical models for a thermally buoyant plume (Ritzwoller et al., 2001; Finn et al., 2005). Observations of only modest heat flow beneath the rift (Ramirez et al., 2016) are similarly incongruous with magma genesis from a large thermal structure beneath the WARS. Alternative melting models highlight the possibility for decompression melting of volatilized and/or pyroxenitic components associated with lowered solidus temperatures even well after subduction cessation (Hart et al., 1\997; Panter et al., 2000; Perinelli et al., 2006; Aviado et al., 2015).

Recent geophysical studies have suggested that a volatile-rich mantle could produce the seismic anomalies beneath the WARS (Hansen et al., 2014; Emry et al., 2015; Graw et al., 2016), lending support to the idea that the low-density mantle structures are at least in part compositional (Hofmann and White, 1982). The paleo-Pacific margin of Gondwana underwent nearly 500 million years of episodic subduction prior to Cretaceous continental breakup (Rocchi et al., 1998; Mukasa and Dalziel, 2000), providing a reasonable mechanism for emplacement of volatilized, easily fusible lithologies capable of facilitating mantle melting. Subduction-zone processing of oceanic lithosphere is also consistent with the observed geochemistry of WARS lavas, particularly with respect to trace element systematics and observations of high- μ (μ = $^{238}U/^{204}Pb$) isotopic signatures (Hart et al., 1997; Wörner, 1999; Panter et al., 2000; Perinelli et al., 2006; Aviado et al., 2015) that suggest the involvement of slab-derived fluids in the production of amphibole-bearing metasomatic domains. While these observations collectively imply that volatile-rich subduction components in the upper mantle and lithosphere are contributing to WARS magmatism, a more comprehensive understanding of the volatile budget of the underlying mantle is critical if we are to reconcile geochemical, geophysical, and geodynamic observations within the rift. In this study, we present new major oxide, trace element, and volatile species (CO_2, H_2O, F, S, Cl) concentrations in olivine-hosted melt inclusions (MIs) to evaluate the nature and provenance of volatilization in the WARS mantle.

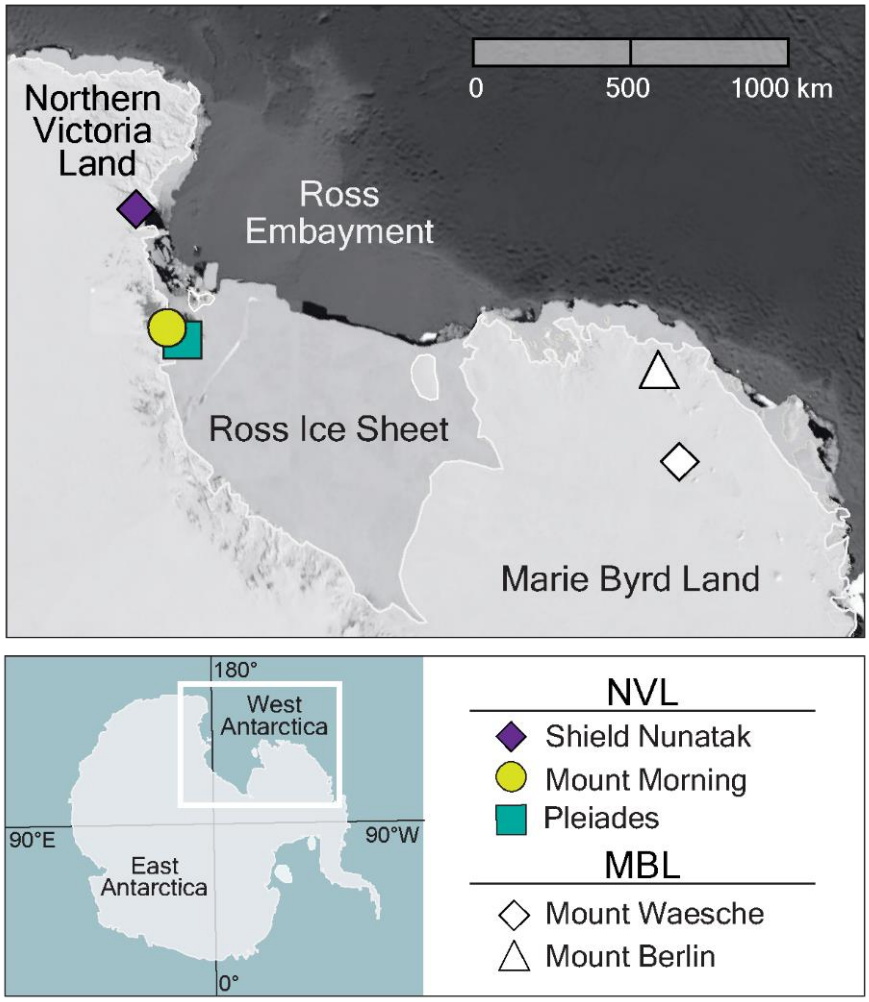

Figure 3-1. Map of Antarctica (inset, bottom left) showing sample locations in Northern Victoria Land (NVL) and Marie Byrd Land (MBL) on both flanks of the West Antarctic Rift System (WARS).

2. Samples and Methods

Olivine phenocrysts were selected from host lava flows in Northern Victoria Land (NVL) and Marie Byrd Land (MBL) to encompass both flanks of the WARS (Figure 3-1). The host lavas are comprised of relatively fresh, phyric basanites; more detailed sample descriptions and their geochemistry can be found in LeMasurier and Thompson (1990) and Aviado et al. (2015). It is significant to note that in MBL, inferences of crustal doming (LeMasurier and Landis, 1996), together with observations of Pb-isotopic signatures approaching the HIMU mantle endmember in Cenozoic lavas, have been interpreted as evidence for a ~600 km-diameter plume beneath the region (LeMasurier and Landis, 1996; Hart et al., 1997; Wörner, 1999; Panter et al., 2000). In NVL, however, a lack of similar compelling structural and geophysical (e.g., Graw et al., 2016) evidence do not support the occurrence of similar plume activity.

Because naturally homogeneous, glassy melt inclusions are rare in this suite of subaerial samples, we employed a rehomogenization procedure as described in Cabato et al. (2015). Because volatile solubility in silicate melts increases with increasing pressure (e.g., Moore et al., 1998), the rehomogenization was performed at elevated pressure (6 kbar) to minimize exsolution and bubble formation. The rehomogenization experiments were performed at the Piston Cylinder Laboratory at Rensselaer Polytechnic Institute using experimental cell and capsule designs modified from Trail et al. (2012). Olivine grains were packed in graphite powder inside graphite capsules and equilibrated in a NaCl pressure medium to a temperature of 1300°C and a pressure of 6 kbar for 10 minutes, then rapidly quenched. Inclusions were first analyzed for CO_2, H_2O, F, S, and Cl with the Cameca 1280 IMS secondary ion mass spectrometer (SIMS) at Woods Hole Oceanographic Institution using a $^{133}Cs^+$ primary beam and a 500 nA current rastered to a 20

μm-diameter spot. Secondary ions of ^{12}C, $^{16}O^{1}H$, ^{19}F, ^{30}Si, ^{32}S, and ^{35}Cl were monitored for a uniform ion image with the highest intensity signal centered on the field aperture. Individual measurements were collected after 240 seconds of pre-sputter, and then counted for a minimum of 10 cycles. Calibration curves were produced by repeat measurements of nine standard glasses of known volatile species abundances. Replicate measurements of standard glass Alvin 519-4-1 were conducted to monitor instrument performance and yielded relative error of 8.2% or better for C, F, S, and Cl, and 12.6% for H_2O.

Olivine major-oxide compositions were measured on the JEOL-JXA-8200 Superprobe at the Massachusetts Institute of Technology (MIT) Electron Microprobe Facility using a 15 kV accelerating voltage, 4 nA beam current, and a ~1μm focused beam. Melt-inclusion major-oxide compositions were measured at MIT using the same analytical conditions as host olivine grains, but with a 10 μm unfocused beam. Counting times were 5s for Na and 40s for all other elements. Replicate analyses of the glass standard Alvin 1690-20 yielded relative error of 1.72% for CaO, 0.19% for SiO_2, 0.11% for Al_2O_3, 1.50% for FeO, 0.89% for MgO, and 7.47% for K_2O (Grove et al., 1992). Li-U trace element abundances for MIs were determined using a Photon Machines 193 nm Excimer laser ablation platform and a NuAttoM HR single-collector ICP-MS at the University of New Hampshire. Analyses were conducted with a 25μm spot size, 5.40 J/cm^2 fluence, and a 4 Hz rep rate. Raw data were processed in Iolite (Paton et al., 2011) using as an internal standard ^{43}Ca (as determined from electron microprobe CaO measurements). Instrumental drift was corrected by bracketing unknowns with the KL2-G glass standard using reference values from Jochum et al. (2005). Replicate measurements (n = 15) of glass standard ML3-BG performed throughout analytical runs indicate that trace elements are accurate to ±11% for U, to ±8% or better for Li, V, Ni, Rb, and Sm, and to ±5% or better for all other elements

(Jochum et al., 2005). Full analytical details and standard reproducibility information are shown in Appendix 2.2.

3. Geochemistry of olivine hosted melt inclusions

3.1 Volatiles (CO_2, H_2O, F, S, and Cl)

Melt inclusion (MI) volatile compositions exhibit markedly variable enrichments relative to typical MORB values. Sources of MI compositional heterogeneity, particularly with respect to H_2O and CO_2, can arise from multiple processes, including post-entrapment modification, diffusive re-equilibration, inclusion of supersaturated heterogeneous melts, and polybaric conditions of entrapment. In particular, it has been well-documented that melt inclusion chemistry can be altered by post-entrapment modification during natural cooling or during laboratory rehomogenization (e.g., Danyushevsky et al., 2002; Jennings et al., 2017, among others). To evaluate the effects of post-entrapment crystallization (PEC) of olivine onto inclusions rims, which may concentrate incompatible species, including volatiles, in the remaining glassy melt, we performed incremental addition of olivine until inclusions were in equilibrium with the host using the Petrolog3 software package (Danyushevsky and Plechov, 2011). This was achieved by performing a reverse crystallization, which models the addition of crystallized minerals back into the melt, thus moving it along a cotectic towards a more primitive composition. We excluded melt inclusions with measured MgO contents less 7 wt. % (n = 24) for our PEC corrections and the discussion that follows, as the melts have likely fractionated additional phases, and can bear accordingly elevated CO_2 contents (Maclennan, 2017). The calculations were carried out at 1 kBar and $K_D^{ol\text{-}liq}$ (Fe^{2+}/Mg) = 0.28, a value appropriate for these highly alkaline, silica-undersaturated melts considering that $K_D^{ol\text{-}liq}$ decreases with increasing melt alkalinity and decreasing silica content (Gee and Sack, 1988). The resultant

amount of post-entrapment olivine required to achieve equilibrium with the host olivine forsterite content is then used to correct trace element and volatile species concentrations. The amount of olivine required to correct our MI compositions ranged from 0 to +23.8, although approximately one third of the MIs required no olivine addition. It is important to note that none of our MI compositions yielded negative values for olivine addition that would suggest Fe-gain by assimilation of host olivine into the melt during laboratory overheating (Danyushevsky et al., 2000). Melt inclusions exhibiting greater than 20% PEC (n = 11) were removed from the figures and discussion that follow, and excluding these highly-corrected samples, our sample suite required an average of 4.6% addition of olivine. Both the measured and corrected values are reported in Table 1, and comparisons of measured versus PEC-corrected H_2O and CO_2 are shown in Appendix 2.3.

Volatile species abundances (corrected for PEC) range up to 5755 ± 355 ppm for CO_2, 2.55 ± 0.18 wt. % for H_2O, 964 ± 25 ppm for F, 2353 ± 70 ppm for S, and 1222 ± 37 ppm for Cl in NVL MIs. High CO_2 and H_2O in these melts are consistent with reported maxima of 7300 ppm CO_2 and 1.75 wt. % H_2O measured in olivine-hosted MIs from basanitic lavas at currently active Mt. Erebus (Oppenheimer et al., 2011), but our results highlight the ubiquitous nature of volatiles in the region. MBL MIs exhibit systematically lower volatile abundances ranging up to 2620 ± 277 ppm CO_2, 1.11 ± 0.03 wt. % H_2O, 937 ± 33 ppm F, 1779 ± 56 ppm S, and 903 ± 28 ppm Cl. Melt inclusion water content generally increase and exhibit a greater range of values with increased melt MgO content and host-olivine Mg#. Ratios of volatile species to incompatible elements with similar partitioning behavior – such as H_2O/Ce, CO_2/(Ba, Nb), and S/Dy – are, with the exception of S, lower than suggested ratios for undegassed mantle melts (Michael, 1995; Saal et al., 2002; Cartigny et al., 2008, Le Voyer et al., 2017), suggesting MI

compositions have lost H_2O and CO_2 relative to their primary compositions (Figure 3-2). Ratios of CO_2 to Nb and Ba show consistent patterns (Figure 3-2b and d), and are scattered to relatively low values indicating that they have lost CO_2 relative these refractory trace elements. This suggests that even the most CO_2-rich inclusions do not capture the initial composition of the original undegassed melts (e.g., Rosenthal et al., 2015, and references therein). Using CO_2/Nb = 239 of undegassed Siquieros olivine-hosted melt inclusions (Saal et al., 2002), reconstructed CO_2 concentrations in the initial WARS undegassed melts may be as high as ~1 wt. %, which is consistent with high-pressure experimental melts of peridotite + 1 wt. % CO_2 (Dasgupta et al., 2007a). However, these predictions are based on the lower end of the observed range in CO_2/Nb among the global dataset of undegassed mantle melts, and if the undegassed CO_2/Nb is closer to the value of 557 suggested by Le Voyer et al. (2017), the WARS initial melts may be considerably more enriched. Recent work by Rosenthal et al. (2015) and Michael and Graham (2015) suggest that CO_2/Ba is instead a more reliable tool for reconstructing initial melt CO_2, as its incompatibility is more similar to CO_2 than is that of Nb. CO_2/Ba ratios predict even higher CO_2 in the initial melts that may have ranged up to ~3 wt. %.

Melt inclusion water contents generally increase and exhibit a greater range of values with increased melt MgO content and host-olivine Mg#. This attenuation of variability with decreasing host Mg# is mirrored in the La/Yb of the melt inclusions, which is consistent with the idea that the melts trapped closest to the mantle source record an enriched and heterogeneous source, whereas more evolved melts entrapped subsequently record increasing magma homogenization and degassing (e.g., Jennings et al., 2017). This suggests that the melt source beneath the WARS is likely poorly mixed, which may be attributed to fast magma ascent

rates through thinned rifted lithosphere, or may suggest that the source of these melts is not as hot as would be expected for a buoyant thermal plume.

Although it is possible that such enriched volatile contents may be attributed to or enhanced by a very small degree of partial melting, it is unlikely that the observed MI compositions are solely a manifestation of the extreme low-degree melts required to explain the observed volatile enrichment. The main lines of evidence arguing against degree of melting as the primarily control on volatile content are demonstrated by positively correlated H_2O and (high) MgO MI contents, as well as poorly correlated La/Yb and H_2O (Figure 3-3, both measured and predicted based on $H_2O/Ce = 180$, Michael, 1995; Hartley et al., 2015). Furthermore, relationships between elevated volatile content and enriched trace element signatures support the interpretation that the high volatile abundances are a feature related to the melt source rather than uniquely tied to the dynamics of the melting process itself (Figure 3-4).

Several recent studies have demonstrated that after trapping, olivine-hosted melt inclusion water contents may undergo rapid re-equilibration during natural cooling or laboratory rehomogenization that can contribute additional complexity to interpretations that link melt inclusion H_2O contents to melt source volatile enrichment. Significant flux of H^+ through the host olivine can occur on timescales of hours to days (Danyushevsky et al., 2002; Portnyagin et al., 2008; Gaetani et al., 2012), and can cause loss or gain of several wt. % H_2O without affecting incompatible trace elements. This may explain suites of melt inclusions that exhibit decoupling of H_2O and similarly incompatible melt components such as Ce and K_2O, as well as samples that exhibit low H_2O contents and enriched trace element signatures, or vice versa. In order to account for the effects of proton diffusion our melt inclusion suite, we therefore evaluate our observed H_2O contents within the context of their major oxide and trace elemental systematics

(e.g., Hartley et al., 2015). Generally, the most H_2O-rich melt inclusions are associated with enriched trace element compositions (Figure 3-4), with the exception of extensively dehydrated MIs with $H_2O/Ce < 8$, which often comprise the most enriched trace-element compositions. These inclusions, enriched in non-volatile incompatible elements yet depleted in volatiles, predict high H_2O contents (1.5 - 2 wt. %, based on $H_2O/Ce = 180$; Michael, 1995; Hartley et al., 2015) that possibly underwent dehydration through diffusive equilibration with less hydrous carrier melts (Hartley et al., 2015).

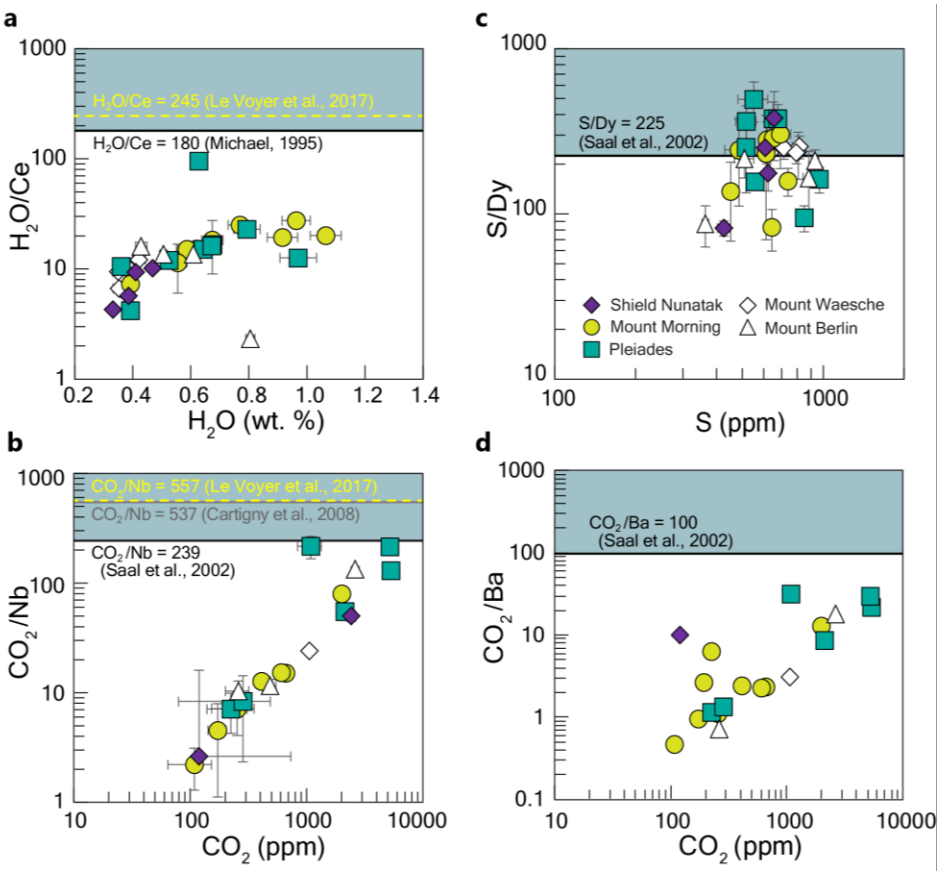

Figure 3-2. Volatile abundances of olivine-hosted melt inclusions plotted versus measured (**a**) H_2O/Ce, (**b**) CO_2/Nb, (**c**) S/Dy, and (**d**) CO_2/Ba. Black and grey solid and yellow dashed lines represent constant volatile/trace element values determined by Saal et al. (2002), Cartigny et al. (2008), and Le Voyer et al. (2017), respectively, for undegassed mantle melts (indicated by blue fields). The majority of samples plot below the values for undegassed mantle melts, which suggests that they have lost volatiles relative to the initial melts. Error bars are 2σ, and many are within symbols.

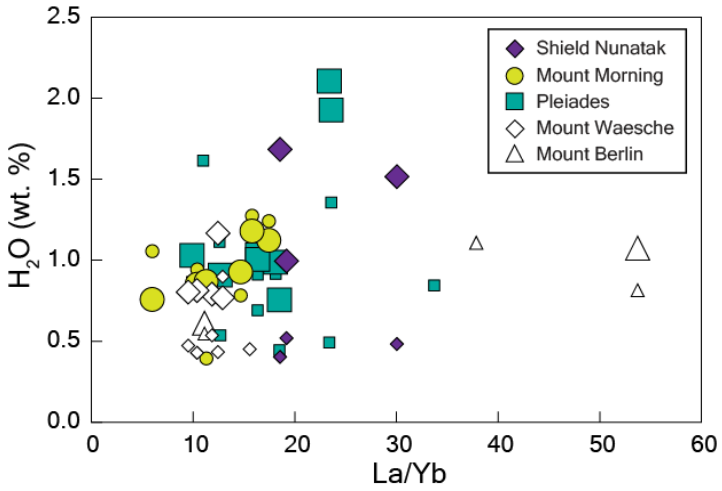

Figure 3-3. Ratios of La to Yb versus measured (small symbols) and predicted (large symbols, based on $H_2O/Ce = 180$, Michael, 1995; Hartley et al., 2015) H_2O for melt inclusions, illustrating the poor correlations that argue against degree of melting as the primary control on H_2O abundance.

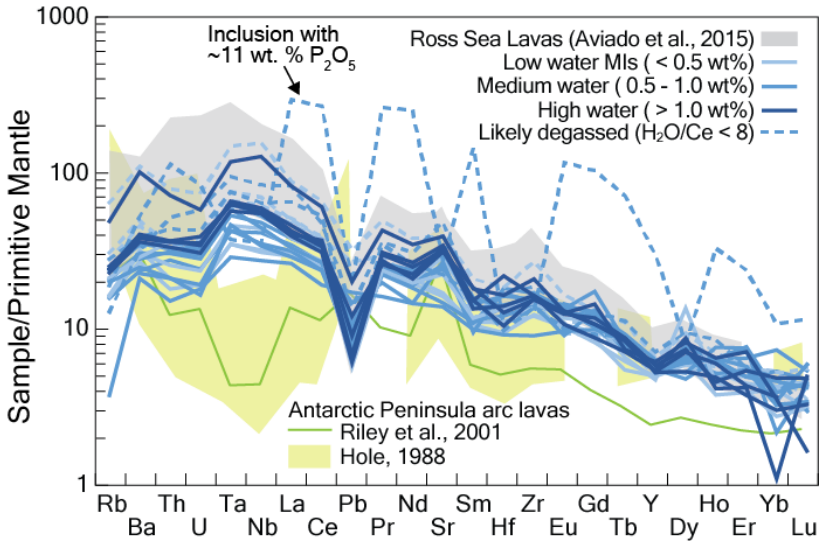

Figure 3-4. Primitive mantle-normalized (Sun and McDonough, 1989) elemental distribution diagram for high, medium, and low measured H_2O samples with $SiO_2 < 45$ wt. % and MgO > 7 wt. %. Likely degassed MIs (determined by very low H_2O/Ce) are shown by dashed lines, and often have the most enriched trace element compositions that suggest they have undergone the greatest degassing. Abundances for Ross Sea lavas (Aviado et al., 2015) and Antarctic Peninsula arc lavas (Hole, 1988; Riley, 2001) are shown for comparison. One exotic melt inclusion from MBL exhibiting erratic enrichments has extremely high measured P_2O_5, which is interpreted to represent an apatitic composition.

It is also possible that the melt inclusions exhibiting evidence for dehydration were altered during laboratory rehomogenization. Dehydration experiments performed by Gaetani et al. (2012) and Bucholz et al. (2013) found that diffusive H_2O-loss through the host olivine reduced the volatile content of melt inclusions by several wt. % H_2O and hundreds of ppm CO_2. Because it is the most H_2O-rich melt inclusions that are especially prone to diffusive dehydration, these authors suggest that high-H_2O inclusions preserved in a sample suite likely represent minimum estimates of the H_2O and CO_2 budget of the melt at the time of entrapment. Conversely, very few MIs exhibit evidence for diffusive hydration based on their incompatible trace element systematics. For example, only one sample exhibits, above analytical uncertainty for H_2O and Ce, a measured H_2O abundance that exceeds our estimates for the original H_2O content of the inclusion, reconstructed using $H_2O/Ce = 180$ (Michael, 1995) of undegassed mantle melts (e.g. Hartley et al., 2015). Additionally, given that more recent estimates for undegassed mantle H_2O/Ce may be as high as 245 (Le Voyer et al., 2017), our predicted H_2O may be only a conservative estimate, and all MIs in our sample suite are likely dehydrated. The vast majority of the MIs for which trace element data are available indicate that H_2O has been lost relative to Ce after original entrapment. This is not surprising considering that the hydration experiments carried out by Portnyagin et al. (2008) and Gaetani et al. (2012), in which melt inclusions gained as much as 2.5-3.5 wt. % H_2O, were performed by pressurizing olivines in pure liquid water. In the natural system, the activity gradient between the melt inclusion and carrier melt required to promote proton diffusion amounting to a gain of several wt. % H_2O is much less likely. We accordingly interpret our high (>1.5 wt. %) H_2O melt inclusions to be representative of an enriched source, rather than an artifact of diffusive re-equilibration.

3.2. Source Characteristics

Our findings of a volatile-rich mantle beneath the WARS support existing lines of evidence that include observations of hydrous metasomatic phases such as amphibole and phlogopite in mantle xenoliths, mantle xenolith thermobarometric estimates that place the NVL geothermal gradient close to or intersecting the hydrous mantle solidus (e.g., Coltorti et al., 2004; Perinelli et al., 2006), and inferences of a deep source for high CO_2 and H_2O in basanitic melt inclusions from Mt. Erebus (Oppenheimer et al., 2011). The new MI data presented in this study, however, are the first to confirm that volatile enrichment is prevalent in both MBL and NVL on a wide scale, and, combined with new major-oxide and trace-element data, provide further insight into the source of WARS mantle volatiles.

The MBL and NVL PEC-corrected melts are distinctly silica-undersaturated (Figure 3-5) and exhibit enriched incompatible trace-element compositions, prominent Rb, K and Pb negative anomalies, and positive Nb, Ta, and Sr anomalies, similar to alkalic OIB that are inconsistent with melting of anhydrous mantle peridotite. Melt-inclusion compositions overlap with, and also extend to more primitive, undersaturated compositions than previously analyzed subaerial and submarine rift-related lavas from the Ross Sea and NVL (Aviado et al., 2015) and from MBL (Hart et al., 1997; Wörner, 1999; Panter et al., 2000; LeMasurier et al., 2016). MBL and NVL melts are generally compositionally similar with respect to major oxides, although MBL melts are systematically lower in TiO_2 than those from NVL (Figure 3-6). These MBL compositions may reflect partial melting of a dominantly carbonated peridotite lithology (Hirose, 1997; Dasgupta et al., 2007a), whereas higher TiO_2 (> 3 wt. %) observed in NVL melts implies a mafic, pyroxene-rich source such as eclogite. Although melt inclusion compositions are similar to 2 -5 GPa anhydrous partial melts of silica-deficient pyroxenite (Figure 3-6;

Hirschmann et al., 2003; Kogiso et al., 2003), derivation of these melts from a volatile-free source is not likely considering the high observed CO_2. Deep, low-degree melting of carbonated eclogite (Gerbode and Dasgupta, 2010; Kiseeva et al., 2012) has been shown to produce partial melts with high SiO_2 and low MgO that do not overlap with the more primitive and undersaturated MIs. However, if these eclogite partial melts infiltrate the surrounding mantle peridotite, reaction in the presence of CO_2 and subsequent melting produce basanitic and nephelinitic melts, with silica undersaturation increasing with CO_2 content (Mallik and Dasgupta, 2014). This process may explain elevated TiO_2 in NVL melts, but it is likely that a hybridized source of carbonated peridotite and pyroxenite, as well as peridotite metasomatized by CO_2-rich eclogite partial melts, contribute to the volatilized, multi-lithologic source with solidus temperatures as much as 100°C cooler than those of volatile-free lithologies (Dasgupta et al., 2006; Gerbode and Dasgupta, 2010; Aviado et al., 2015).

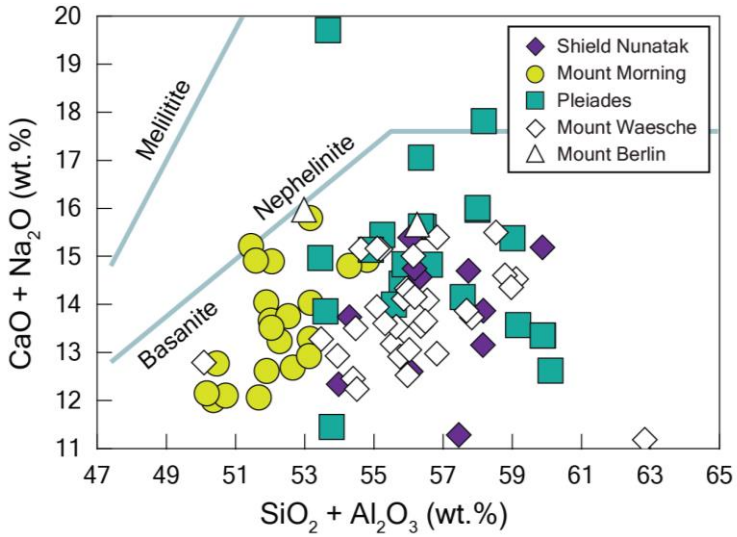

Figure 3-5. PEC-corrected melt inclusion compositions plotted according to the melt alkalinity classification by Le Bas (1989). Melt inclusion compositions range to highly alkaline, silica-undersaturated basanites and nephelinites.

Melt inclusions record increased compositional variability with increasing host olivine Mg#. The observed attenuation of variability in H_2O content with decreasing host Mg# is also mirrored in the trace element systematics of the MIs (quantified by La/Yb normalized to the sample mean), a phenomenon identified in MIs from Iceland and many continental flood basalt (CFB) provinces (Maclennan et al., 2008; Jennings et al., 2017). These trends are consistent with the idea that the primitive melts trapped closest to the mantle source by the earliest-formed olivine record an enriched and heterogeneous source, whereas more evolved melts entrapped subsequently record increasing magma homogenization and degassing. In settings where the earliest-formed heterogeneous melts encounter conditions amenable to mixing (i.e. hotter mantle temperatures and/or thicker lithosphere), even the most primitive melt inclusions will undergo almost complete homogenization prior to entrapment, and will not preserve this trend (Jennings et al., 2017). The NVL and MBL MIs hosted in high-Mg# olivines capture a range of $(La/Yb)_N$ between 3.3 and 0.3, which suggests that the melt source beneath the WARS is highly heterogeneous and capable of producing distinctive melt compositions that are not well mixed prior to trapping. These results may be an artifact of thinned, rifted lithosphere or may attest to a lack of a thermal anomaly beneath the WARS, as has been suggested by recent heat flow models (Ramirez et al., 2016).

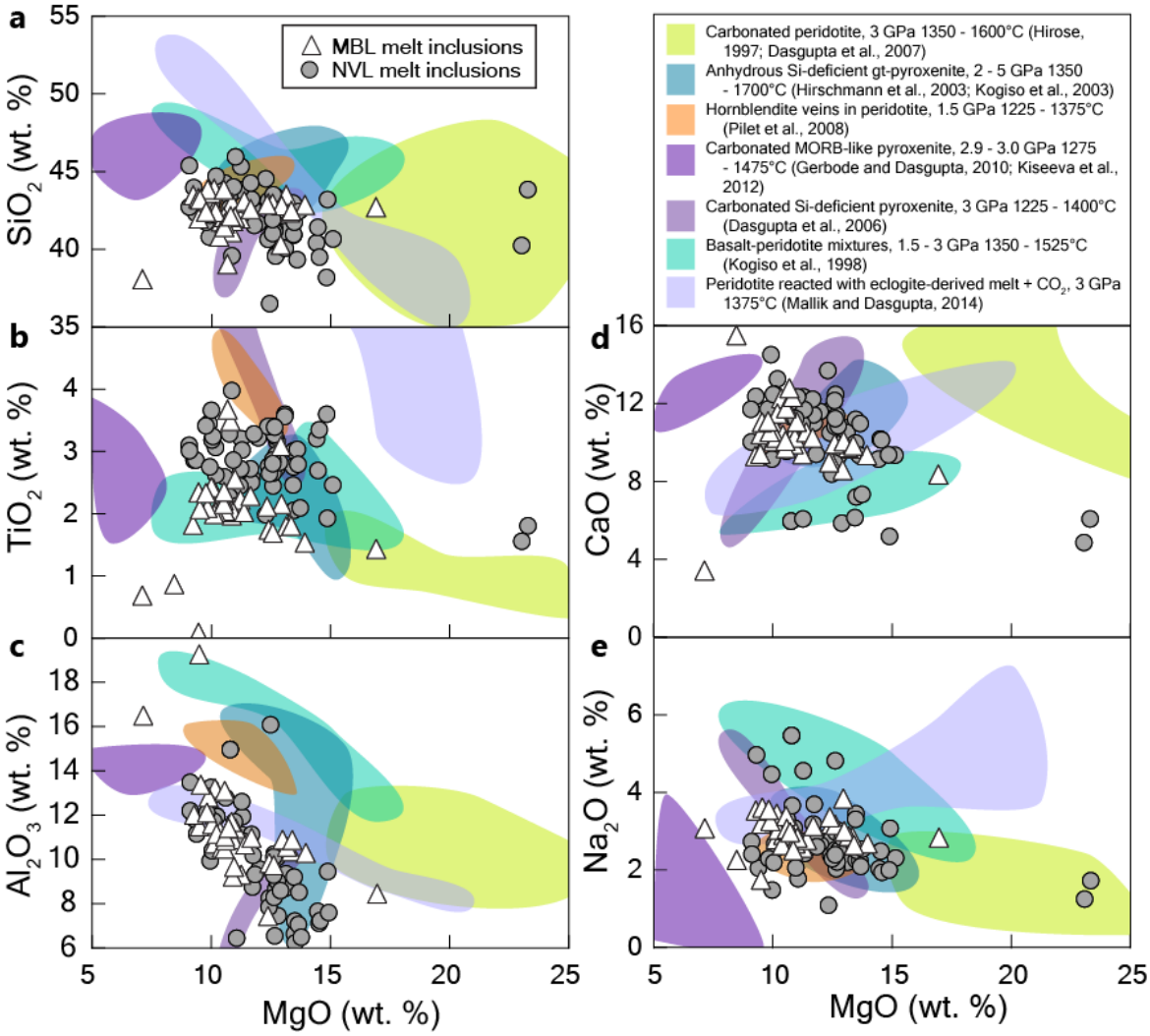

Figure 3-6. Comparisons of PEC-corrected melt inclusion compositions to high-pressure experimental partial melts of carbonated and/or pyroxenitic source lithologies.

4. Discussion

4.1 Evidence for a subduction-modified source

Melt generation from recycled subduction-zone-processed ocean lithosphere is consistent with several aspects of the geochemistry of WARS volcanism (e.g., Aviado et al., 2015), and has been invoked to explain similar Cenozoic Si-poor magmatism in New Zealand also once part of the paleo-Pacific active margin (e.g., Hoernle et al., 2006). For example, highly radiogenic Pb isotopic signatures observed in WARS lavas (Hart et al., 1997; Wörner, 1999; Panter et al., 2000; Perinelli et al., 2006; Aviado et al., 2015) may be explained by depletion of fluid-mobile large ion lithophile elements (LILE) by slab-derived fluids to produce high-μ domains. Fluid modification related to subduction may also explain Ba enrichment in MBL (LeMasurier et al., 2016). In the new NVL and MBL melt inclusion data, broadly correlated Ba/Rb and Cl, and the observation that the highest Ba/Rb sample shows evidence for the most extreme Cl enrichment (Cl = 971 ppm and Cl/Nb = 50) additionally support the role of slab fluids in metasomatic modification of the source (e.g., Rowe and Lassiter, 2009).

Elevated Na_2O/K_2O (> 7) and Ba/Rb (> 61) in NVL and MBL melt inclusions are consistent with ratios observed in Ross Sea lavas that were argued to be derived in part by melting of amphibole-bearing, metasomatized peridotite (Figure 3-7A; Furman and Graham, 1999; Aviado et al., 2015). Experimental partial melts of peridotite containing amphibole-bearing veins resemble the observed MI major-oxide compositions and have been argued as a possible origin for high-μ, alkalic ocean island and intracontinental basalts (Pilet et al., 2008; Rooney et al., 2014). Further, partial melting experiments relate to continental active margins by having fluids released in dehydration reactions in the subducting slab ascend to metasomatize deeper sectors of the overlying mantle wedge to produce amphibole-bearing veins enriched in Ta and Nb (Stein et al., 1997). Subsequent destabilization of amphibole and partial

dehydration of these deep metasomatic domains by buoyancy-driven or small-scale (e.g., the Rio Grande Rift; Van Wijk et al., 2008) convective flow deplete them in fluid-mobile Rb and Pb to produce elevated Nb, U/Pb, and Th/Pb materials that, if isolated in the lithosphere or at the base of the sub-continental lithospheric mantle or stagnated in the upper mantle, can generate the time-integrated, high-μ isotopic signatures observed in NVL and MBL lavas (Hart et al., 1997; Panter et al., 2000; Aviado et al., 2015; LeMasurier et al., 2016).

Although amphibole and phlogopite may be important hydrous metasomatic phases in the WARS mantle, evidence in favor of their presence remains inconclusive in certain areas of the rift (e.g., eastern MBL; LeMasurier et al., 2016), and more compelling relationships exist between H_2O and tracers for modification by carbonated fluid during subduction (Figure 3-7B). For example, correlated P_2O_5/TiO_2 and Nb/Hf in MIs and lavas suggest that apatite, rutile, or Ti-augite are present in a melt source modified by carbonatitic metasomatism (Trua et al., 1998), and high H_2O is associated with more extreme values for these diagnostic ratios. One exotic MI from MBL with measured P_2O_5 of ~11 wt. % has been interpreted as an apatite-rich inclusion, lending further support to the presence of these metasomatic phases in the melt source (Figure 3-4).

4.2 Implications of volatile-rich fusible lithologies for interpreting melting perturbations

The presence of CO_2 and H_2O in the mantle source region serves to lower the mantle solidus temperature and effectively expands the polybaric melting interval, facilitating both deeper melting and increased melt productivity (Dasgupta et al., 2007b). Deep melting initiated primarily by CO_2 will segregate H_2O into the carbonated silicate melts, and the combined effect of depolymerization and increased entropy is to further enhance melting (Dasgupta et al., 2007b). These carbonated silicate melts may be triggered by as little as 100 ppm CO_2 at

sublithospheric depths. The occurrence of a zone of hydrated partial melt in the mantle beneath the WARS is supported by several major lines of geophysical evidence. Regional-scale tomographic models (e.g., Ritzwoller et al., 2001; Sieminski et al., 2003; Watson et al., 2006; Hansen et al., 2014; Graw et al., 2016) have identified broad, seismically slow regions in the mantle beneath much of West Antarctica, with prominent low-velocity zones focused in the shallow mantle beneath Marie Byrd Land, the Ross Sea, and Victoria Land. Additionally, recent findings from P-wave receiver function studies indicate apparent depression of the 410-km transition zone beneath much of West Antarctica (Emry et al., 2015), which has been linked to hydrated remnants of Cretaceous paleo-Pacific subduction. Although some aspects of these features may alternatively be explained by thermal upwelling from the lower mantle now ponded below the transition zone, recent low-to-moderate values of heat flow across the WARS do not support rift-wide mantle plume activity (Ramirez et al., 2016).

The deeper-seated Marie Byrd Land slow anomaly may extend into the transition zone, but the Ross Island and Victoria Land anomalies appear to be restricted to the upper 200 - 300 km of the mantle (Hansen et al., 2014; Graw et al., 2016). These apparent differences in the MBL and Ross Sea physical mantle structures may help reconcile certain aspects of their differing geochemistry and tectonic features. In MBL, where the distinctive history of regional crustal doming (LeMasurier and Landis, 1996) and observations of low-density mantle anomalies extending to ~1000 km depth (Hansen et al., 2014) have been interpreted as a mantle plume, it is possible that increased thermal perturbation in this region has preferentially melted out easily fusible pyroxenitic lithologies emplaced during 550 – 110 Ma subduction and generated larger contributions of ambient mantle with a volatilized peridotite lithology. In NVL, where crustal doming has not been observed and slow mantle anomalies are restricted to the

upper mantle, melt compositions are more characteristic of decompression melting of easily fusible, volatilized pyroxenite, potentially hybridized with peridotite (Aviado et al., 2015).

The occurrence of volatilized, easily fusible mantle components in the WARS mantle may also factor into regional response to deglaciation considering the evidence for temporal and chemical links between increased volcanic activity and deglaciation in other regions of the world (Jull and McKenzie, 1996; Sims et al., 2013). For example, coupled geodynamic and thermodynamic modeling of rapid (1 ka) deglaciation of a 2-km ice sheet in Iceland predicts as much as a 30-fold increase in melt production rates during unloading due to enhanced isentropic decompression of anhydrous peridotite (Jull and McKenzie, 1996). A homogeneous, anhydrous depleted source beneath Iceland is not likely, however, and the occurrence of fusible lithologies in the Icelandic source region (Sims et al., 2013), as in West Antarctica, may further contribute to enhanced melt productivity at the onset of deglaciation. In the case of extreme volatile enrichment observed in West Antarctica, if we are to invoke the partial melting experiments with 1 wt. % CO_2 in mantle peridotite, we may predict an additional ~4-fold increase in melt fraction during partial melting relative to volatile-free peridotite at 3 GPa and 1500°C that is further magnified in combination with H_2O (Dasgupta et al., 2007b). In addition to depressing the mantle solidus and facilitating deeper melting, volatiles contribute to reactive melt channeling that enhances melt production and flux (Keller and Katz, 2016). Accordingly, the role of H_2O and CO_2 in increasing the fertility of the sublithospheric mantle beneath West Antarctica must therefore be considered in quantitative dynamic models to evaluate the potential for enhanced volcanism as a regional response to rapid deglaciation.

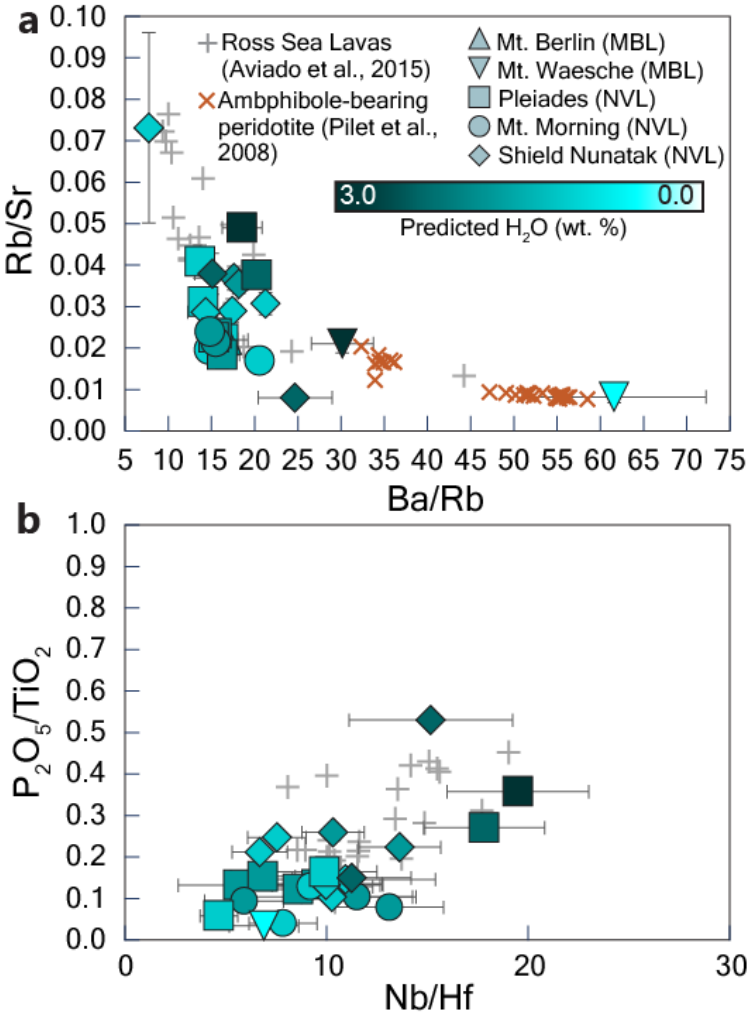

Figure 3-7. (**a**) Rb/Sr versus Ba/Rb for WARS melt inclusions, indicated by blue symbols colored by predicted H_2O content (e.g., Hartley et al., 2015) based on $H_2O/Ce = 180$ of undegassed mantle (Saal et al., 2002). Ross Sea lavas (Aviado et al., 2015) are shown in grey symbols for comparison. Experimental melts of hornblendite veins in peridotite (Pilet et al., 2008) are shown in red symbols that overlap with melt inclusion compositions in (**a**), which plots tracers for the presence of amphibole in the melt source (Furman and Graham, 1999). Panel (**b**) illustrates relationships between H_2O content and tracers for carbonatitic metasomatism, P_2O_5/TiO_2 versus Nb/Hf. Error bars are 2σ.

5. Conclusion

New olivine-hosted, melt-inclusion data support widespread volatilization of the mantle beneath the WARS. Systematically lower volatile abundances and TiO_2 in MBL melts relative to those from NVL suggest some variation in mantle source lithologies on a regional scale. In MBL, regional crustal doming (LeMasurier and Landis, 1996) coupled with a deep-seated low-density mantle anomaly (Hansen et al., 2014) have been interpreted as a mantle plume, which could be responsible for increased thermal perturbation in this region that has generated larger contributions of ambient mantle with a volatilized peridotite lithology. In NVL, where crustal doming or deep mantle anomalies have not been observed, melt compositions are more characteristic of extension-related decompression melting of a volatilized, hybridized pyroxenite-peridotite source generated during Cretaceous subduction (Aviado et al., 2015). Hydrous and carbonatitic metasomatism – both intricately linked with subduction zone processes – are thought to have modified the mantle beneath the WARS, which would explain the observed mantle density anomalies, the radiogenic isotopic compositions of the lavas, and the new MI volatile species and chemical systematics presented in this study. These findings suggest that the enriched volatile budget of the mantle underlying the WARS may significantly impact melt productivity in response to decompression associated with lithospheric extension, adiabatic plume rise, and rapid regional deglaciation. This potential for enhanced volcanism should accordingly be evaluated in models seeking to predict the consequences of the Western Antarctic Ice Sheet destabilization.

Table 3-1: Major oxide and volatile species compositions of MIs and host olivines

	Northern Victoria Land											
Locality	Mount Morning											
Host Lava	C88-89	C88-89	C88-89	C88-89	C88-89	C88-89	C88-89	C88-89	C88-89	C88-89	C88-89	C88-89
Sample ID	c88-89_1_68	c88-89_2_69	c88-89_3_70	c88-89_4_71	c88-89_5_72	c88-89_6_73	c88-89_7_75	c88-89_8_76	c88-89_9_77	c88-89_10_78	c88-89_11_79	c88-89_12_80
Host Olivines												
SiO_2 (wt.%)	39.45	39.49	39.61	39.61	39.73	39.67	40.01	39.44	39.32	39.54	39.67	39.67
TiO_2	0.04	0.01	0.01	0.01	0.01	0.01	0.01	0.02	0.02	0.02	0.02	0.02
Al_2O_3	0.04	0.08	0.01	0.01	0.03	0.07	0.06	0.06	0.07	0.04	0.06	0.06
FeO	14.45	15.55	14.73	14.73	12.70	14.09	12.45	15.12	14.77	14.42	13.47	13.47
MnO	0.18	0.22	0.22	0.22	0.17	0.19	0.16	0.21	0.20	0.18	0.19	0.19
MgO	46.16	45.22	45.89	45.89	47.55	46.50	47.55	45.59	45.96	46.20	46.58	46.58
CaO	0.24	0.26	0.26	0.26	0.22	0.26	0.28	0.24	0.26	0.27	0.28	0.28
NiO	0.13	0.11	0.16	0.16	0.22	0.16	0.15	0.11	0.16	0.16	0.18	0.18
Total	100.68	100.93	100.89	100.89	100.61	100.93	100.67	100.79	100.75	100.81	100.44	100.44
Mg#	85.06	83.83	84.74	84.74	86.97	85.48	87.19	84.31	84.73	85.1	86.04	86.04
Rehomogenized MI compositions												
SiO_2 (wt.%)	41.12			40.90	43.28	40.98	42.16	40.23	40.00	40.36	40.02	38.03
TiO_2	3.45			3.24	2.90	3.04	3.23	3.18	3.53	3.63	3.76	4.29
Al_2O_3	11.99			11.28	12.16	11.83	12.89	13.90	13.43	12.45	12.17	14.79
Cr_2O_3	0.00			0.39	0.06	0.30	0.08	0.47	0.65	0.16	0.24	0.24
FeO	14.30			15.13	11.81	16.44	13.66	15.06	14.57	13.57	15.15	15.11
MnO	0.19			0.22	0.15	0.20	0.20	0.25	0.17	0.14	0.20	0.15
MgO	10.13			14.57	10.70	8.53	8.88	10.81	10.44	13.18	11.41	9.35
CaO	11.36			9.15	12.13	11.40	12.07	9.92	11.13	10.73	11.26	11.04
Na_2O	3.00			2.10	2.97	2.91	3.03	3.27	3.33	2.40	2.23	2.43
K_2O	0.93			0.94	0.55	0.49	0.74	0.50	0.37	0.70	0.83	0.91
P_2O_5	0.55			0.34	0.24	0.18	0.25	0.40	0.26	0.27	0.30	0.38
NiO	0.02			0.02	0.05	0.00	0.03	0.01	0.00	0.00	0.01	0.00
F	0.04			0.02	0.16	0.00	0.01	0.07	0.00	0.04	0.06	0.00
Cl	0.06			0.07	0.04	0.02	0.04	0.04	0.02	0.02	0.03	0.03
S	0.11			0.07	0.28	0.26	0.25	0.17	0.14	0.31	0.32	0.30
Total	97.25			98.44	97.49	96.57	97.52	98.28	98.05	97.97	97.99	97.05
CO_2 (ppm)	181 (82)	456 (158)	225 (187)	109 (44)	2102 (72)	496 (14)	371 (37)	153 (156)	152 (121)	584 (188)	1164 (25)	341 (94)
H2O (wt. %)	1.23 (0.07)	1.01 (0.06)	0.87 (0.05)	0.49 (0.03)	1.11 (0.06)	1.05 (0.06)	1.64 (0.09)	0.97 (0.05)	0.9 (0.05)	0.94 (0.05)	1.37 (0.07)	1.15 (0.06)
F (ppm)	599 (16)	643 (17)	649 (17)	642 (17)	646 (17)	657 (17)	748 (20)	650 (17)	790 (21)	628 (17)	580 (15)	500 (13)
S (ppm)	458 (14)	1987 (61)	478 (15)	470 (14)	1037 (32)	1493 (46)	1449 (44)	950 (29)	727 (22)	1544 (47)	1478 (45)	1043 (32)
Cl (ppm)	500 (15)	457 (13)	422 (12)	383 (11)	267 (8)	255 (8)	369 (11)	380 (11)	310 (9)	354 (10)	416 (12)	335 (10)
PEC-Corrected MI Compositions												
PEC (% ol)	7.75			0.00	4.73	18.85	15.63	6.11	6.92	0.00	9.64	15.72
SiO_2 (wt.%)	40.86			40.50	43.20	40.75	41.49	39.75	39.63	40.14	39.58	38.26
TiO_2	3.17			3.21	2.77	2.47	2.70	2.95	3.25	3.61	3.36	3.61
Al_2O_3	11.02			11.17	11.60	9.61	10.78	12.90	12.38	12.38	10.87	12.45
Fe_2O_3	2.05			1.94	1.76	2.25	1.92	1.94	1.96	1.78	1.94	1.77
FeO	14.28			15.25	11.83	16.35	13.56	15.09	14.58	13.72	15.03	15.34
MnO	0.17			0.22	0.14	0.16	0.17	0.23	0.16	0.14	0.18	0.13
MgO	12.77			14.43	12.41	15.12	14.49	12.73	12.70	13.11	14.55	14.85
CaO	10.44			9.06	11.58	9.26	10.09	9.20	10.26	10.67	10.05	9.29
Na_2O	2.76			2.08	2.83	2.36	2.53	3.03	3.07	2.39	1.99	2.05
K_2O	0.85			0.93	0.52	0.40	0.62	0.46	0.34	0.70	0.74	0.77
P_2O_5	0.51			0.34	0.23	0.15	0.21	0.37	0.24	0.27	0.27	0.32
Cr_2O_3	0.00			0.39	0.06	0.24	0.07	0.44	0.60	0.16	0.21	0.20
H_2O	1.13			0.49	1.06	0.85	1.37	0.90	0.83	0.93	1.22	0.97
Total	100.01			100.01	99.99	99.97	100.00	99.99	100.00	100.00	99.99	100.01
CO_2 (ppm)	167 (82)			109 (44)	2003 (72)	403 (14)	313 (37)	144 (156)	142 (121)	584 (188)	1051 (25)	287 (94)
H_2O (wt. %)	1.13 (0.07)			0.49 (0.03)	1.06 (0.06)	0.86 (0.06)	1.39 (0.09)	0.91 (0.05)	0.83 (0.05)	0.94 (0.05)	1.24 (0.07)	0.97 (0.06)
F (ppm)	553 (16)			642 (17)	615 (17)	533 (17)	631 (20)	610 (17)	736 (21)	628 (17)	524 (15)	421 (13)
S (ppm)	423 (14)			470 (14)	988 (32)	1212 (46)	1222 (44)	892 (29)	677 (22)	1544 (47)	1336 (45)	879 (32)
Cl (ppm)	461 (15)			383 (11)	255 (8)	207 (8)	311 (11)	357 (11)	289 (9)	354 (10)	376 (12)	282 (10)

Table 3-1: Major oxide and volatile species compositions of MIs and host olivines (continued)

	Northern Victoria Land											
Locality	Mount Morning											
Host Lava	C88-89	C88-89	C88-89	C88-89	C88-89	C88-89	C88-89	C88-89	C88-89	C88-89	C88-89	C88-89
Sample ID	c88-89_13_81	c88-89_14_83	c88-89_15_84	c88-89_16_85	c88-89_17_86	c88-89_18_87	c88-89_19_88	c88-89_20_89	c88-89_21_90	c88-89_22_91	c88-89_23_92	c88-89_24_146
Host Olivines												
SiO_2 (wt.%)	39.65	39.84	39.26	39.58	39.05	39.58	39.80	39.80	39.68	39.68	39.68	39.36
TiO_2	0.01	0.00	0.04	0.00	0.02	0.03	0.01	0.01	0.01	0.01	0.01	0.02
Al_2O_3	0.06	0.04	0.08	0.06	0.07	0.07	0.00	0.00	0.03	0.03	0.03	0.05
FeO	13.43	13.49	17.46	15.51	16.05	15.37	13.70	13.70	14.52	14.52	14.52	13.96
MnO	0.16	0.18	0.27	0.24	0.20	0.22	0.18	0.18	0.19	0.19	0.19	0.19
MgO	47.23	46.70	43.55	45.35	44.65	45.27	46.74	46.74	46.18	46.18	46.18	46.63
CaO	0.23	0.29	0.30	0.25	0.29	0.22	0.22	0.22	0.25	0.25	0.25	0.26
NiO	0.15	0.17	0.08	0.07	0.14	0.12	0.15	0.15	0.12	0.12	0.12	0.17
Total	100.93	100.71	101.04	101.07	100.46	100.88	100.80	100.80	100.98	100.98	100.98	100.64
Mg#	86.24	86.05	81.64	83.9	83.22	84	85.88	85.88	85.01	85.01	85.01	85.62
Rehomogenized MI compositions												
SiO_2 (wt.%)	41.30	41.60	41.68	45.84	39.90	41.46	40.86	41.96	40.38	42.72	41.55	42.02
TiO_2	3.02	4.07	3.07	2.24	3.79	2.82	3.71	3.69	4.10	4.35	3.94	3.45
Al_2O_3	11.44	13.60	11.03	8.33	13.39	12.03	13.27	14.33	12.58	13.35	11.99	11.38
Cr_2O_3	0.06	0.22	0.00	0.00	0.00	0.02	0.30	0.09	0.02	0.00	0.01	0.00
FeO	13.91	13.35	15.88	15.41	17.36	19.12	12.72	12.20	17.05	12.85	14.09	16.83
MnO	0.20	0.21	0.26	0.29	0.27	0.30	0.18	0.20	0.24	0.26	0.28	0.30
MgO	10.63	8.84	13.68	9.12	7.17	7.43	7.67	7.30	7.79	6.87	7.91	7.87
CaO	12.17	11.90	10.05	15.29	11.56	10.60	12.77	13.15	12.03	13.93	14.31	10.53
Na_2O	3.84	2.57	2.35	1.28	2.85	2.71	2.48	3.07	2.62	2.77	2.40	3.16
K_2O	0.67	0.70	0.43	0.16	0.75	0.56	0.62	0.70	0.78	0.61	0.53	0.60
P_2O_5	0.12	0.40	0.40	0.19	0.37	0.21	0.29	0.21	0.32	0.32	0.25	0.46
NiO	0.00	0.01	0.01	0.02	0.05	0.02	0.00	0.01	0.08	0.04	0.08	0.02
F	0.00	0.00	0.02	0.00	0.03	0.16	0.00	0.00	0.05	0.00	0.14	0.00
Cl	0.02	0.03	0.05	0.01	0.08	0.05	0.02	0.04	0.07	0.06	0.05	0.05
S	0.31	0.32	0.32	0.04	0.40	0.33	0.25	0.29	0.46	0.14	0.17	0.13
Total	97.70	97.83	99.22	98.23	97.97	97.82	95.15	97.23	98.57	98.28	97.70	96.80
CO_2 (ppm)	836 (198)	205 (51)	80 (104)	43 (344)	313 (100)	412 (26)	581 (178)	2089 (1833)	665 (24)	121 (187)	199 (30)	212 (40)
H2O (wt. %)	1.03 (0.06)	1 (0.06)	0.39 (0.03)	0.98 (0.06)	0.97 (0.05)	1.34 (0.07)	1.25 (0.07)	1.09 (0.06)	1.5 (0.08)	0.65 (0.04)	0.85 (0.05)	1.21 (0.07)
F (ppm)	548 (14)	616 (16)	675 (18)	242 (6)	596 (16)	649 (17)	694 (18)	644 (17)	839 (22)	385 (11)	519 (14)	642 (17)
S (ppm)	1463 (45)	1644 (50)	1571 (48)	243 (7)	1822 (56)	1592 (49)	1541 (47)	1461 (45)	2286 (70)	616 (20)	722 (22)	676 (21)
Cl (ppm)	271 (8)	385 (11)	285 (8)	96 (3)	328 (10)	321 (9)	352 (10)	363 (11)	430 (13)	365 (12)	405 (12)	508 (15)
PEC-Corrected MI Compositions												
PEC (% ol)	8.27	11.97	0.00	9.63	18.98	23.79	13.26	12.61	20.89	13.18	13.25	21.87
SiO_2 (wt.%)	41.00	41.22	41.03	44.62	39.42	40.42	41.42	41.74	39.54	42.06	41.20	41.33
TiO_2	2.76	3.57	3.02	1.99	3.04	2.12	3.28	3.23	3.18	3.75	3.41	2.69
Al_2O_3	10.44	11.92	10.86	7.42	10.74	9.03	11.74	12.54	9.76	11.52	10.38	8.86
Fe_2O_3	2.15	1.77	2.11	2.44	2.24	2.44	1.82	1.77	2.17	1.91	2.08	2.28
FeO	13.67	13.53	15.84	15.03	17.49	18.73	13.26	12.54	16.81	13.09	14.18	16.63
MnO	0.18	0.18	0.26	0.26	0.22	0.23	0.16	0.18	0.19	0.22	0.24	0.23
MgO	13.46	13.10	13.47	12.30	13.62	15.45	12.66	11.98	14.97	11.66	12.63	15.56
CaO	11.11	10.43	9.89	13.62	9.27	7.96	11.30	11.51	9.33	12.02	12.38	8.20
Na_2O	3.50	2.25	2.31	1.14	2.29	2.03	2.19	2.69	2.03	2.39	2.08	2.46
K_2O	0.61	0.61	0.42	0.14	0.60	0.42	0.55	0.61	0.60	0.53	0.46	0.47
P_2O_5	0.11	0.35	0.39	0.17	0.30	0.16	0.26	0.18	0.25	0.28	0.22	0.36
Cr_2O_3	0.05	0.19	0.00	0.00	0.00	0.02	0.27	0.08	0.02	0.00	0.01	0.00
H_2O	0.94	0.88	0.38	0.87	0.78	1.01	1.11	0.95	1.16	0.56	0.74	0.94
Total	99.98	100.00	99.98	100.00	100.01	100.02	100.02	100.00	100.01	99.99	100.01	100.01
CO_2 (ppm)	767 (198)	180 (51)	80 (104)	39 (344)	254 (100)	314 (26)	504 (178)	1825 (1833)	526 (24)	105 (187)	173 (30)	166 (40)
H_2O (wt. %)	0.94 (0.06)	0.88 (0.06)	0.39 (0.03)	0.89 (0.06)	0.78 (0.05)	1.02 (0.07)	1.08 (0.07)	0.95 (0.06)	1.18 (0.08)	0.56 (0.04)	0.73 (0.05)	0.95 (0.07)
F (ppm)	503 (14)	543 (16)	675 (18)	219 (6)	483 (16)	495 (17)	602 (18)	563 (17)	664 (22)	334 (11)	450 (14)	501 (17)
S (ppm)	1342 (45)	1448 (50)	1571 (48)	220 (7)	1476 (56)	1214 (49)	1337 (47)	1277 (45)	1809 (70)	535 (20)	626 (22)	528 (21)
Cl (ppm)	249 (8)	339 (11)	285 (8)	87 (3)	266 (10)	244 (9)	306 (10)	317 (11)	340 (13)	317 (12)	351 (12)	397 (15)

Table 3-1: Major oxide and volatile species compositions of MIs and host olivines (continued)

	Northern Victoria Land											
Locality	Mount Morning									The Pleiades		
Host Lava	C88-89	C88-89	C88-89	C88-89	C88-89	C88-89	C88-89	C88-89	C88-89	12-19-01-3	12-19-01-3	12-19-01-3
Sample ID	c88-89_25_147	c88-89_26_148	c88-89_27_149	c88-89_28_150	c88-89_29_151	c88-89_30_152	13_C89_1_52	C89_1_53	17_C89_2_54	12-19-01-3_1	12-19-01-3_2	12-19-01-3_3
Host Olivines												
SiO_2 (wt.%)	39.36	39.16	39.89	39.89	39.38	39.61	39.00	39.00	39.23	39.47	39.31	39.03
TiO_2	0.02	0.01	0.01	0.01	0.03	0.01	0.03	0.03	0.02	0.00	0.02	0.01
Al_2O_3	0.05	0.05	0.03	0.03	0.07	0.01	0.04	0.04	0.04	0.07	0.03	0.08
FeO	13.96	15.19	13.14	13.14	15.90	14.73	15.50	15.50	15.48	12.34	15.07	14.58
MnO	0.19	0.20	0.18	0.18	0.22	0.22	0.22	0.22	0.22	0.17	0.21	0.21
MgO	46.63	45.39	47.17	47.17	45.01	45.89	45.03	45.03	45.54	47.60	46.10	46.43
CaO	0.26	0.28	0.25	0.25	0.23	0.26	0.29	0.29	0.26	0.26	0.24	0.24
NiO	0.17	0.14	0.18	0.18	0.08	0.16	0.10	0.10	0.08	0.18	0.15	0.17
Total	100.64	100.41	100.84	100.84	100.92	100.89	100.20	100.20	100.87	100.08	101.12	100.74
Mg#	85.62	84.19	86.49	86.49	83.46	84.74	83.82	83.82	83.98	87.3	84.51	85.03
Rehomogenized MI compositions												
SiO_2 (wt.%)		41.57	41.03	42.52		41.59	43.37	43.37	39.89	42.37	42.65	42.12
TiO_2		3.96	3.81	3.36		3.61	2.60	2.60	4.01	3.35	3.01	3.35
Al_2O_3		13.14	12.71	14.00		12.61	12.80	12.80	13.57	14.83	15.29	14.20
Cr_2O_3		0.00	0.27	0.28		0.41	0.11	0.11	0.29	0.09	0.29	0.51
FeO		14.82	15.50	14.08		14.47	16.61	16.61	12.72	10.33	15.70	16.14
MnO		0.25	0.26	0.23		0.21	0.38	0.38	0.19	0.16	0.36	0.30
MgO		8.13	6.60	6.03		11.03	7.02	7.02	10.93	9.88	4.05	6.97
CaO		12.09	12.25	12.62		10.19	8.98	8.98	11.88	12.77	8.65	6.74
Na_2O		2.81	2.47	2.58		2.40	3.21	3.21	3.15	2.73	4.17	5.30
K_2O		0.80	0.79	0.81		1.12	0.99	0.99	0.86	0.78	1.18	1.28
P_2O_5		0.37	0.29	0.18		0.44	0.43	0.43	0.41	0.33	0.70	0.62
NiO		0.02	0.02	0.05		0.01	0.06	0.06	0.04	0.02	0.00	0.00
F		0.10	0.03	0.14		0.01	0.24	0.24	0.01	0.00	0.13	0.00
Cl		0.03	0.06	0.05		0.06	0.07	0.07	0.05	0.03	0.08	0.07
S		0.48	0.30	0.31		0.10	0.19	0.19	0.24	0.26	0.11	0.18
Total		98.58	96.39	97.23		98.24	97.06	97.06	98.24	97.94	96.37	97.79
CO_2 (ppm)	194 (140)	694 (20)	721 (42)	933 (889)	908 (18)	99 (102)	580 (13)	194 (0)	184 (344)	440 (52)	238 (97)	252 (123)
H2O (wt. %)	1.18 (0.06)	1.46 (0.08)	1.58 (0.08)	1.49 (0.08)	1.89 (0.1)	0.45 (0.03)	3.15 (0.18)	0.84 (0)	0.77 (0.05)	1.05 (0.06)	1.36 (0.07)	1.53 (0.08)
F (ppm)	605 (16)	790 (21)	901 (24)	703 (22)	858 (23)	705 (19)	992 (35)	542 (0)	653 (19)	593 (16)	1311 (34)	1265 (33)
S (ppm)	635 (20)	2089 (64)	1681 (51)	1522 (47)	2705 (83)	561 (17)	991 (31)	1069 (0)	1062 (34)	1302 (40)	735 (22)	822 (25)
Cl (ppm)	489 (16)	359 (11)	389 (11)	398 (13)	464 (14)	481 (14)	644 (21)	382 (0)	400 (12)	348 (10)	587 (17)	531 (16)
PEC-Corrected MI Compositions												
PEC (% ol)		12.50	24.90	22.93		5.08	18.97	19.31	0.00	3.85	28.37	21.21
SiO_2 (wt.%)		40.72	40.66	41.71		41.23	41.82	42.60	39.66	42.20	41.61	41.02
TiO_2		3.41	2.86	2.58		3.40	2.06	2.10	3.99	3.21	2.16	2.60
Al_2O_3		11.31	9.55	10.75		11.89	10.15	10.34	13.49	14.23	10.97	11.02
Fe_2O_3		2.04	2.09	1.94		1.93	2.22	2.26	1.87	1.44	2.15	2.13
FeO		14.82	15.64	14.48		14.53	16.58	16.89	12.67	10.45	16.76	16.16
MnO		0.22	0.20	0.18		0.20	0.30	0.31	0.19	0.15	0.26	0.23
MgO		12.39	15.73	14.56		12.67	13.49	13.74	10.87	11.28	14.36	14.42
CaO		10.41	9.21	9.69		9.61	7.12	7.26	11.81	12.25	6.21	5.23
Na_2O		2.42	1.86	1.98		2.26	2.55	2.59	3.13	2.62	2.99	4.11
K_2O		0.69	0.59	0.62		1.06	0.79	0.80	0.86	0.75	0.85	0.99
P_2O_5		0.32	0.22	0.14		0.41	0.34	0.35	0.41	0.32	0.50	0.48
Cr_2O_3		0.00	0.20	0.22		0.39	0.09	0.09	0.29	0.09	0.21	0.40
H_2O		1.26	1.19	1.14		0.42	2.50	0.68	0.77	1.01	0.98	1.19
Total		100.01	100.00	99.99		100.00	100.01	100.01	100.01	100.00	100.01	99.98
CO_2 (ppm)		608 (20)	542 (42)	719 (889)		94 (102)	470 (13)	157 (0)	184 (344)	423 (52)	171 (97)	199 (123)
H_2O (wt. %)		1.27 (0.08)	1.19 (0.08)	1.15 (0.08)		0.43 (0.03)	2.55 (0.18)	0.68 (0)	0.77 (0.05)	1.01 (0.06)	0.98 (0.07)	1.2 (0.08)
F (ppm)		691 (21)	677 (24)	542 (22)		669 (19)	804 (35)	437 (0)	653 (19)	570 (16)	939 (34)	997 (33)
S (ppm)		1828 (64)	1263 (51)	1173 (47)		533 (17)	803 (31)	863 (0)	1062 (34)	1252 (40)	527 (22)	648 (25)
Cl (ppm)		315 (11)	292 (11)	306 (13)		457 (14)	522 (21)	308 (0)	400 (12)	334 (10)	421 (17)	419 (16)

Table 3-1: Major oxide and volatile species compositions of MIs and host olivines (continued)

	Northern Victoria Land											
Locality	The Pleiades											
Host Lava	12-19-01-3	12-19-01-3	12-19-01-3	12-19-01-3	12-19-01-3	12-19-01-3	12-19-01-3	12-19-01-3	12-19-01-3	12-19-01-3	12-19-01-3	12-19-01-3
Sample ID	12-19-01-3_4	12-19-01-3_5	12-19-01-3_6	12-19-01-3_7	12-19-01-3_8	12-19-01-3_9	12-19-01-3_10	12_12-14_1_1_48	5.05-12_1_1_41	5.05-12_1_2_42	05-12_	05-12_
Host Olivines												
SiO_2 (wt.%)	39.63	39.63	39.76	39.56	39.56	39.52	39.70	39.68	39.44		39.76	39.76
TiO_2	0.00	0.00	0.00	0.01	0.01	0.00	0.00	0.01	0.02		0.02	0.02
Al_2O_3	0.04	0.04	0.05	0.05	0.05	0.02	0.02	0.05	0.04		0.01	0.01
FeO	13.23	13.23	13.22	13.60	13.60	12.25	13.49	13.02	13.16		13.17	13.17
MnO	0.18	0.18	0.16	0.21	0.21	0.15	0.19	0.17	0.15		0.16	0.16
MgO	47.28	47.28	47.42	46.84	46.84	47.94	47.21	46.75	47.26		46.94	46.94
CaO	0.25	0.25	0.25	0.26	0.26	0.23	0.24	0.26	0.27		0.22	0.22
NiO	0.15	0.15	0.15	0.14	0.14	0.22	0.24	0.17	0.19		0.22	0.22
Total	100.76	100.76	101.01	100.65	100.65	100.32	101.09	100.09	100.51		100.50	100.50
Mg#	86.43	86.43	86.48	86	86	87.46	86.18	86.49	86.49		86.41	86.41
Rehomogenized MI compositions												
SiO_2 (wt.%)	43.29	43.51	43.86	41.68		43.70	43.32	44.67	44.56		44.59	43.79
TiO_2	2.94	2.83	2.76	2.57		2.94	2.64	2.75	2.71		2.26	2.52
Al_2O_3	14.81	13.48	15.41	12.20		13.07	12.94	13.75	15.49		13.00	13.27
Cr_2O_3	0.58	0.13	0.74	0.63		0.40	0.12	0.05	0.37		0.15	0.08
FeO	11.38	11.46	10.48	12.88		11.54	10.04	8.94	10.31		15.22	16.46
MnO	0.15	0.13	0.14	0.15		0.17	0.13	0.13	0.16		0.31	0.39
MgO	7.13	7.21	6.26	10.53		10.17	12.53	11.75	9.04		10.64	8.01
CaO	12.46	12.79	12.27	11.28		11.59	11.07	12.22	9.89		5.97	5.51
Na_2O	3.35	4.22	3.14	2.70		2.76	3.00	3.25	3.52		3.64	4.01
K_2O	0.66	0.42	0.58	0.57		0.72	0.67	0.61	0.77		1.62	1.83
P_2O_5	0.39	0.34	0.30	0.21		0.26	0.28	0.42	0.40		0.61	0.58
NiO	0.00	0.00	0.00	0.00		0.00	0.00	0.02	0.02		0.03	0.05
F	0.00	0.00	0.00	0.00		0.00	0.00	0.00	0.00		0.16	0.00
Cl	0.04	0.15	0.08	0.02		0.04	0.04	0.07	0.06		0.06	0.08
S	0.24	0.45	0.25	0.24		0.15	0.22	0.14	0.28		0.09	0.10
Total	97.42	97.12	96.27	95.67		97.51	96.99	98.77	97.57		98.35	96.68
CO_2 (ppm)	255 (84)	183 (91)	1897 (303)	1015 (16)	917 (30)	885 (83)	4680 (52)	284 (204)	240 (407)	468 (1692)	353 (1543)	265 (561)
H2O (wt. %)	1.24 (0.07)	1.16 (0.06)	1.01 (0.06)	1.71 (0.09)	1.85 (0.1)	1 (0.06)	1.11 (0.06)	0.87 (0.05)	1.33 (0.08)	1.29 (0.08)	1.55 (0.09)	1.47 (0.09)
F (ppm)	586 (15)	1516 (40)	646 (17)	587 (15)	612 (16)	630 (17)	563 (15)	556 (19)	591 (21)	823 (29)	972 (34)	986 (34)
S (ppm)	1286 (39)	2203 (67)	1171 (36)	1549 (47)	1532 (47)	735 (22)	1321 (41)	758 (24)	1613 (51)	1502 (48)	589 (19)	457 (14)
Cl (ppm)	343 (10)	1476 (43)	617 (18)	331 (10)	336 (10)	488 (14)	348 (10)	315 (10)	443 (14)	567 (18)	704 (23)	720 (23)
PEC-Corrected MI Compositions												
PEC (% ol)	12.23	11.86	12.70	5.63		7.07	0.00	0.00	4.14		12.82	23.16
SiO_2 (wt.%)	42.82	43.29	43.91	41.97		43.43	43.60	44.34	44.34		43.28	42.66
TiO_2	2.58	2.51	2.45	2.45		2.73	2.66	2.73	2.60		1.93	1.93
Al_2O_3	12.98	11.95	13.65	11.62		12.14	13.02	13.65	14.83		11.13	10.15
Fe_2O_3	1.66	1.84	1.53	1.86		1.64	1.46	1.31	1.41		2.01	2.18
FeO	11.72	11.70	11.15	13.06		11.63	10.16	8.89	10.51		14.90	16.24
MnO	0.13	0.12	0.12	0.14		0.16	0.13	0.13	0.15		0.27	0.30
MgO	11.73	11.70	11.21	12.60		12.74	12.61	11.66	10.57		14.89	16.22
CaO	10.92	11.34	10.87	10.75		10.77	11.14	12.13	9.47		5.11	4.22
Na_2O	2.94	3.74	2.78	2.57		2.56	3.02	3.23	3.37		3.12	3.07
K_2O	0.58	0.37	0.51	0.54		0.67	0.67	0.61	0.74		1.39	1.40
P_2O_5	0.34	0.30	0.27	0.20		0.24	0.28	0.42	0.38		0.52	0.44
Cr_2O_3	0.51	0.12	0.66	0.60		0.37	0.12	0.05	0.35		0.13	0.06
H_2O	1.09	1.03	0.89	1.63		0.93	1.12	0.86	1.27		1.33	1.12
Total	100.00	100.01	100.00	99.99		100.01	99.99	100.01	99.99		100.01	99.99
CO_2 (ppm)	224 (84)	161 (91)	1656 (303)	958 (16)		822 (83)	4680 (52)	284 (204)	230 (407)		307 (1543)	203 (561)
H_2O (wt. %)	1.09 (0.07)	1.02 (0.06)	0.88 (0.06)	1.61 (0.09)		0.93 (0.06)	1.11 (0.06)	0.87 (0.05)	1.27 (0.08)		1.36 (0.09)	1.13 (0.09)
F (ppm)	514 (15)	1336 (40)	564 (17)	554 (15)		585 (17)	563 (15)	556 (19)	566 (21)		848 (34)	758 (34)
S (ppm)	1129 (39)	1942 (67)	1022 (36)	1462 (47)		683 (22)	1321 (41)	758 (24)	1546 (51)		513 (19)	351 (14)
Cl (ppm)	301 (10)	1301 (43)	539 (18)	313 (10)		453 (14)	348 (10)	315 (10)	425 (14)		614 (23)	554 (23)

Table 3-1: Major oxide and volatile species compositions of MIs and host olivines (continued)

	Northern Victoria Land											
Locality	The Pleiades											
Host Lava	12-19-01-3	12-19-01-3	12-19-01-3	12-19-01-3	12-19-01-3	12-19-01-3	12-19-01-3	12-19-01-3	12-19-01-3	12-19-01-3	12-19-01-3	12-19-01-3
Sample ID	05-12_	12-19-01_1_44	12-19-01_1_45	12-19-01_2_46	12-19-01_3_47	12-19-01_4_48	12-19-01_5_50	12-19-01_6_51	12-19-01_7_53	12-19-01_8_54	12-19-01_9_57	12-19-01_10_58
Host Olivines												
SiO_2 (wt.%)	39.26	39.44	39.44	39.87	39.87	39.67	39.93	38.86	39.83	39.90	40.39	39.86
TiO_2	0.00	0.00	0.00	0.00	0.00	0.00	0.01	0.06	0.01	0.00	0.00	0.00
Al_2O_3	0.09	0.04	0.04	0.04	0.04	0.02	0.04	0.12	0.00	0.07	0.07	0.02
FeO	15.13	14.64	14.64	13.23	13.23	14.06	13.47	21.42	13.61	13.42	13.41	13.11
MnO	0.21	0.22	0.22	0.18	0.18	0.18	0.17	0.39	0.18	0.16	0.19	0.19
MgO	45.46	46.26	46.26	47.12	47.12	46.79	47.01	40.79	47.13	47.15	46.75	47.30
CaO	0.24	0.19	0.19	0.26	0.26	0.28	0.27	0.22	0.27	0.28	0.26	0.25
NiO	0.19	0.19	0.19	0.26	0.26	0.19	0.22	0.10	0.18	0.22	0.22	0.21
Total	100.58	100.99	100.99	101.02	101.02	101.24	101.16	102.00	101.24	101.26	101.35	101.00
Mg#	84.27	84.92	84.92	86.39	86.39	85.58	86.15	77.24	86.06	86.24	86.14	86.54
Rehomogenized MI compositions												
SiO_2 (wt.%)	43.37	44.59	44.59	37.60	46.10	44.54	42.49	40.72	43.52	43.67	43.39	44.83
TiO_2	3.13	2.34	2.34	3.12	2.77	2.82	3.18	3.45	3.31	3.38	3.41	2.97
Al_2O_3	13.08	16.81	16.81	20.22	14.94	14.03	14.77	15.73	14.68	15.78	14.13	14.63
Cr_2O_3	0.23	0.23	0.23	5.61	0.14	0.03	0.06	0.43	0.16	0.05	0.00	0.07
FeO	15.24	10.91	10.91	12.40	10.20	14.64	10.48	16.46	11.71	10.14	11.18	9.47
MnO	0.32	0.12	0.12	0.17	0.15	0.29	0.16	0.32	0.15	0.15	0.17	0.13
MgO	10.10	11.03	11.03	8.51	11.43	10.13	9.24	6.67	9.13	8.43	10.18	8.75
CaO	6.39	6.03	6.03	9.78	6.09	6.93	13.66	7.59	12.67	13.14	11.63	12.70
Na_2O	3.17	5.66	5.66	2.75	4.68	3.84	3.15	5.60	2.70	2.89	3.84	5.19
K_2O	1.73	2.01	2.01	0.95	2.05	1.63	0.87	1.29	0.84	0.92	0.71	0.54
P_2O_5	0.65	0.53	0.53	0.49	0.99	0.95	0.42	0.48	0.54	0.41	0.54	0.46
NiO	0.04	0.00	0.00	0.03	0.00	0.01	0.01	0.00	0.00	0.01	0.00	0.03
F	0.18											
Cl	0.05											
S	0.07											
Total	97.75	100.24	100.24	101.63	99.52	99.82	98.47	98.74	99.41	98.95	99.18	99.76
CO_2 (ppm)	273 (255)	282 (1057)	4612 (2619)	133 (72)	721 (2563)	6411 (355)	5458 (64)	1599 (35)	2287 (21)	73599 (33)	887 (996)	390 (2277)
H2O (wt. %)	1.41 (0.09)	0.63 (0.02)	0.64 (0.02)	0.54 (0.01)	0.49 (0.01)	0.51 (0.01)	0.71 (0.02)	0.4 (0.01)	0.98 (0.03)	0.95 (0.03)	0.55 (0.01)	0.57 (0.02)
F (ppm)	958 (33)	763 (20)	795 (20)	698 (18)	964 (25)	788 (20)	565 (15)	542 (24)	551 (14)	680 (14)	647 (18)	566 (17)
S (ppm)	390 (12)	543 (15)	550 (16)	1004 (29)	1116 (34)	584 (17)	2420 (70)	1562 (14)	1522 (44)	1519 (44)	769 (43)	419 (22)
Cl (ppm)	586 (19)	1222 (37)	1233 (38)	408 (13)	670 (21)	492 (15)	415 (13)	438 (15)	389 (13)	763 (12)	572 (23)	337 (18)
PEC-Corrected MI Compositions												
PEC (% ol)	8.51	0.00	0.00	11.63	0.00	10.24	2.76	6.40	6.48	4.54	2.06	1.77
SiO_2 (wt.%)	42.62	43.49	43.49	36.59	45.39	43.06	42.11	39.74	42.44	43.08	42.72	44.04
TiO_2	2.83	2.28	2.28	2.65	2.73	2.47	3.07	3.16	3.03	3.19	3.29	2.87
Al_2O_3	11.84	16.40	16.39	17.19	14.71	12.28	14.25	14.40	13.44	14.91	13.64	14.14
Fe_2O_3	1.95	1.54	1.54	1.36	1.47	1.91	1.59	2.71	1.62	1.45	1.66	1.59
FeO	15.30	10.70	10.70	12.50	10.08	14.42	10.43	16.12	11.66	10.21	11.04	9.19
MnO	0.29	0.12	0.12	0.14	0.15	0.25	0.15	0.29	0.14	0.14	0.16	0.13
MgO	12.88	10.76	10.76	12.46	11.25	13.44	10.19	8.59	11.31	10.05	10.78	9.28
CaO	5.78	5.88	5.88	8.31	6.00	6.07	13.18	6.95	11.60	12.41	11.23	12.28
Na_2O	2.87	5.52	5.52	2.34	4.61	3.36	3.04	5.13	2.47	2.73	3.71	5.02
K_2O	1.57	1.96	1.96	0.81	2.02	1.43	0.84	1.18	0.77	0.87	0.69	0.52
P_2O_5	0.59	0.52	0.52	0.42	0.97	0.83	0.41	0.44	0.49	0.39	0.52	0.44
Cr_2O_3	0.21	0.22	0.22	4.77	0.14	0.03	0.06	0.39	0.15	0.05	0.00	0.07
H_2O	1.28	0.61	0.62	0.46	0.48	0.45	0.69	0.90	0.87	0.52	0.55	0.43
Total	100.01	100.00	100.00	100.00	100.00	100.00	100.01	100.00	99.99	100.00	99.99	100.00
CO_2 (ppm)	250 (255)	282 (1057)	4612 (2619)	118 (72)	721 (2563)	5755 (355)	5307 (64)	1497 (35)	2139 (21)	70255 (33)	869 (996)	383 (2277)
H_2O (wt. %)	1.29 (0.09)	0.63 (0.02)	0.64 (0.02)	0.48 (0.01)	0.49 (0.01)	0.46 (0.01)	0.69 (0.02)	0.38 (0.01)	0.92 (0.03)	0.91 (0.03)	0.54 (0.01)	0.56 (0.02)
F (ppm)	876 (33)	763 (20)	795 (20)	617 (18)	964 (25)	708 (20)	549 (15)	508 (24)	515 (14)	649 (14)	633 (18)	556 (17)
S (ppm)	356 (12)	543 (15)	550 (16)	887 (29)	1116 (34)	524 (17)	2353 (70)	1462 (14)	1423 (44)	1450 (44)	753 (43)	412 (22)
Cl (ppm)	536 (19)	1222 (37)	1233 (38)	361 (13)	670 (21)	441 (15)	403 (13)	410 (15)	364 (13)	729 (12)	561 (23)	331 (18)

Table 3-1: Major oxide and volatile species compositions of MIs and host olivines (continued)

	Northern Victoria Land											
Locality	The Pleiades					Shield Nunatak						
Host Lava	12-19-01-3	12-19-01-3	12-19-01-3	12-19-01-3	12-19-01-3	NV-13A	NV-13A	NV-13A	NV-13A	NV-13A	NV-13A	NV-13A
Sample ID	12-19-01_11_60	12-19-01_12_61	12-19-01_13_88	12-19-01_14_89	12-19-01_15_90	NV13A_1_62	NV13A_2_63	NV13A_3_64	NV13A_4_66	NV13A_5_67	NV13A_6_68	NV13A_7_72
Host Olivines												
SiO_2 (wt.%)	39.74	39.92	39.76	39.80	39.79	39.97	39.63	39.99	39.62	39.62	39.99	39.84
TiO_2	0.00	0.00	0.00	0.00	0.00	0.00	0.00	0.00	0.00	0.00	0.02	0.01
Al_2O_3	0.03	0.07	0.05	0.04	0.05	0.02	0.05	0.02	0.03	0.03	0.06	0.00
FeO	14.24	13.01	12.91	13.67	13.24	14.85	14.71	14.10	14.91	14.91	14.42	15.00
MnO	0.21	0.17	0.20	0.20	0.17	0.20	0.20	0.19	0.21	0.21	0.19	0.19
MgO	46.31	46.98	47.09	46.56	46.98	45.68	45.92	46.29	45.63	45.63	46.09	45.50
CaO	0.22	0.24	0.26	0.27	0.29	0.31	0.25	0.20	0.30	0.30	0.24	0.28
NiO	0.23	0.25	0.24	0.20	0.18	0.21	0.29	0.30	0.19	0.19	0.25	0.20
Total	101.04	100.69	100.57	100.78	100.78	101.27	101.11	101.16	100.93	100.93	101.32	101.07
Mg#	85.29	86.55	86.67	85.86	86.35	84.58	84.77	85.41	84.51	84.51	85.07	84.39
Rehomogenized MI compositions												
SiO_2 (wt.%)	40.77	41.63	45.49	42.69	43.84	45.88	48.42	45.28	43.43	45.03	45.92	44.25
TiO_2	3.45	3.05	2.67	2.86	3.53	3.87	2.45	1.87	4.43	4.39	3.14	3.29
Al_2O_3	12.77	13.13	14.46	13.14	16.70	15.40	11.84	10.17	16.28	16.91	14.57	14.27
Cr_2O_3	0.01	0.22	0.23	0.36	0.26	0.32	0.50	0.07	0.28	0.43	0.31	0.33
FeO	10.43	12.70	10.11	12.15	10.32	11.41	12.85	10.46	12.40	11.71	9.97	10.90
MnO	0.17	0.18	0.15	0.16	0.15	0.18	0.22	0.12	0.17	0.17	0.13	0.15
MgO	9.90	10.97	10.37	12.80	6.60	6.73	7.71	24.02	6.44	5.09	9.17	10.22
CaO	14.38	9.44	11.54	12.27	12.70	13.17	14.08	6.19	13.28	13.20	11.75	11.31
Na_2O	4.51	5.18	3.26	2.48	3.10	2.07	2.09	1.83	2.04	1.83	2.81	2.62
K_2O	0.77	1.31	0.82	0.64	1.27	0.82	0.57	0.60	0.71	0.83	0.79	0.97
P_2O_5	0.20	0.60	0.45	0.33	0.63	0.40	0.38	0.41	0.76	0.94	0.46	1.07
NiO	0.03	0.04	0.03	0.03	0.01	0.01	0.03	0.04	0.06	0.00	0.01	0.00
F												
Cl												
S												
Total	97.38	98.45	99.59	99.89	99.10	100.27	101.14	101.06	100.28	100.53	99.04	99.37
CO_2 (ppm)	5195 (391)	367 (67)	1088 (249)	0 (23)	6582 (77)	89 (206)	90 (54)	70 (107)	69 (83)	76 (201)	105 (64)	87 (45)
H2O (wt. %)	0.44 (0.01)	0.8 (0.02)	0.84 (0.02)	0.54 (0.01)	1.28 (0.03)	0.41 (0.01)	0.53 (0.01)	0.47 (0.01)	0.46 (0.01)	0.46 (0.01)	0.5 (0.01)	0.37 (0.01)
F (ppm)	674 (15)	563 (17)	461 (15)	0 (12)	599 (15)	569 (15)	541 (14)	571 (15)	577 (15)	591 (15)	630 (16)	631 (16)
S (ppm)	1684 (12)	415 (49)	959 (12)	0 (27)	1860 (53)	978 (28)	877 (25)	794 (23)	1136 (32)	1145 (33)	768 (22)	956 (27)
Cl (ppm)	554 (10)	932 (17)	266 (29)	0 (8)	684 (21)	386 (12)	311 (10)	383 (12)	347 (11)	376 (12)	381 (12)	396 (12)
PEC-Corrected MI Compositions												
PEC (% ol)	0.00	4.95	0.00	0.00	10.52	9.19	9.86	0.00	12.50	14.93	0.00	0.00
SiO_2 (wt.%)	40.87	41.10	44.77	41.98	42.67	44.33	46.03	43.92	41.99	43.14	45.46	43.65
TiO_2	3.46	2.87	2.63	2.81	3.10	3.43	2.13	1.81	3.78	3.63	3.11	3.25
Al_2O_3	12.80	12.34	14.23	12.92	14.66	13.66	10.30	9.86	13.89	14.00	14.42	14.08
Fe_2O_3	1.89	1.96	1.45	1.69	1.47	1.60	1.91	1.96	1.65	1.58	1.45	1.55
FeO	10.16	12.46	9.99	12.04	10.58	11.59	12.61	9.75	12.70	12.31	9.90	10.82
MnO	0.17	0.17	0.15	0.16	0.13	0.16	0.19	0.12	0.15	0.14	0.13	0.15
MgO	9.92	12.59	10.21	12.59	10.51	9.98	11.03	23.30	10.88	10.55	9.08	10.08
CaO	14.42	8.87	11.36	12.07	11.15	11.68	12.25	6.00	11.33	10.93	11.63	11.16
Na_2O	4.52	4.87	3.21	2.44	2.72	1.84	1.82	1.77	1.74	1.51	2.78	2.58
K_2O	0.77	1.23	0.81	0.63	1.11	0.73	0.50	0.58	0.61	0.69	0.78	0.96
P_2O_5	0.20	0.56	0.44	0.32	0.55	0.35	0.33	0.40	0.65	0.78	0.46	1.06
Cr_2O_3	0.01	0.21	0.23	0.35	0.23	0.28	0.44	0.07	0.24	0.36	0.31	0.33
H_2O	0.80	0.79	0.53		1.12	0.36	0.46	0.46	0.39	0.38	0.49	0.36
Total	99.99	100.02	100.01	100.00	100.00	99.99	100.00	100.00	100.00	100.00	100.00	100.03
CO_2 (ppm)	5195 (391)	349 (67)	1088 (249)	0 (23)	5889 (77)	80 (206)	81 (54)	70 (107)	60 (83)	64 (201)	105 (64)	87 (45)
H_2O (wt. %)	0.44 (0.01)	0.76 (0.02)	0.84 (0.02)	0.54 (0.01)	1.15 (0.03)	0.37 (0.01)	0.48 (0.01)	0.47 (0.01)	0.4 (0.01)	0.39 (0.01)	0.5 (0.01)	0.37 (0.01)
F (ppm)	674 (15)	535 (17)	461 (15)	0 (12)	536 (15)	517 (15)	488 (14)	571 (15)	505 (15)	503 (15)	630 (16)	631 (16)
S (ppm)	1684 (12)	395 (49)	959 (12)	0 (27)	1664 (53)	888 (28)	791 (25)	794 (23)	994 (32)	974 (33)	768 (22)	956 (27)
Cl (ppm)	554 (10)	886 (17)	266 (29)	0 (8)	612 (21)	351 (12)	280 (10)	383 (12)	303 (11)	320 (12)	381 (12)	396 (12)

Table 3-1: Major oxide and volatile species compositions of MIs and host olivines (continued)

	Northern Victoria Land											
Locality	Shield Nunatak											
Host Lava	NV-13A	NV-13A	NV-13A	NV-13A	NV-13A	NV-13A	NV-13A	NV-13A	NV-13A	NV-13A	NV-13A	NV-13A
Sample ID	NV13A_8_73	NV13A_9_74	NV13A_10_75	NV13A_11_76	NV13A_12_78	NV13A_13_79	NV13A_14_80	NV13A_15_81	NV13A_16_82	NV13A_17_83	NV13A_18_84	NV13A_19_94
Host Olivines												
SiO_2 (wt.%)	39.84	39.72	39.70	38.59	38.55	39.42	39.37	38.33		38.93	38.93	39.08
TiO_2	0.01	0.03	0.00	0.03	0.03	0.04	0.01	0.04		0.02	0.02	0.03
Al_2O_3	0.00	0.01	0.02	0.07	0.04	0.05	0.03	0.05		0.02	0.02	0.09
FeO	15.00	14.99	15.07	19.44	19.01	16.32	16.15	21.18		18.54	18.54	18.03
MnO	0.19	0.20	0.19	0.24	0.25	0.24	0.21	0.34		0.27	0.27	0.25
MgO	45.50	45.45	45.27	42.02	42.58	44.69	44.48	41.05		42.94	42.94	43.55
CaO	0.28	0.25	0.29	0.28	0.27	0.31	0.32	0.28		0.26	0.26	0.28
NiO	0.20	0.24	0.22	0.09	0.13	0.14	0.13	0.12		0.09	0.09	0.07
Total	101.07	100.97	100.82	100.78	100.88	101.24	100.75	101.45		101.10	101.10	101.37
Mg#	84.39	84.39	84.26	79.39	79.97	83	83.08	77.55		80.51	80.51	81.15
Rehomogenized MI compositions												
SiO_2 (wt.%)		44.77	43.39	44.20	43.52	42.83	42.58	42.54		41.00	43.59	44.88
TiO_2		2.91	2.72	3.12	3.44	3.62	3.56	3.90		1.59	2.84	3.36
Al_2O_3		14.27	13.78	14.87	14.78	15.19	13.37	14.46		9.49	15.64	17.09
Cr_2O_3		0.28	0.27	0.16	0.54	0.07	0.00	0.08		0.31	0.43	0.03
FeO		11.34	21.76	15.87	21.99	12.90	15.40	19.25		15.58	14.80	13.62
MnO		0.17	0.42	0.24	0.43	0.18	0.29	0.36		0.20	0.22	0.24
MgO		11.11	4.97	8.12	4.07	8.76	10.10	5.26		23.42	10.26	7.12
CaO		11.31	7.77	10.70	7.37	12.32	10.07	9.34		4.86	9.34	11.09
Na_2O		2.14	3.41	2.29	2.81	2.48	2.87	3.37		1.32	1.58	2.74
K_2O		0.63	0.91	0.74	0.94	0.82	0.41	0.71		0.49	0.72	0.84
P_2O_5		0.39	0.75	0.60	0.47	0.66	0.53	0.60		0.56	0.90	0.63
NiO		0.03	0.01	0.00	0.02	0.03	0.02	0.03		0.00	0.00	0.02
F												
Cl												
S												
Total		99.34	100.15	100.91	100.38	99.85	99.21	99.90		98.81	100.32	101.66
CO_2 (ppm)	1834 (589)	78 (76)	142 (51)	115 (80)	176 (96)	188 (134)	119 (171)	115 (201)	165 (767)	75 (185)	86 (118)	58 (151)
H2O (wt. %)	0.36 (0.01)	0.52 (0.01)	0.43 (0.01)	0.51 (0.01)	0.47 (0.01)	0.43 (0.01)	0.51 (0.01)	0.31 (0.01)	0.59 (0.02)	0.5 (0.01)	0.58 (0.02)	0.52 (0.01)
F (ppm)	552 (14)	425 (11)	722 (19)	581 (15)	749 (19)	632 (16)	643 (17)	508 (14)	1361 (35)	579 (15)	621 (16)	623 (16)
S (ppm)	1018 (29)	814 (23)	781 (22)	1421 (40)	966 (28)	1525 (43)	1857 (53)	548 (18)	5062 (144)	1324 (38)	1280 (36)	1763 (50)
Cl (ppm)	397 (12)	319 (10)	281 (9)	365 (11)	137 (4)	364 (11)	239 (7)	153 (7)	932 (29)	414 (13)	382 (12)	426 (13)
PEC-Corrected MI Compositions												
PEC (% ol)		0.00	36.38	4.67	30.52	3.47	5.70	16.77		0.00	0.00	6.48
SiO_2 (wt.%)		44.10	40.61	42.41	40.60	41.83	41.62	40.72		40.33	42.29	42.81
TiO_2		2.87	1.66	2.87	2.29	3.42	3.29	3.15		1.56	2.76	3.02
Al_2O_3		14.06	8.43	13.66	9.85	14.35	12.36	11.67		9.33	15.17	15.34
Fe_2O_3		1.47	2.54	2.25	2.50	1.84	2.02	2.74		2.39	1.80	1.87
FeO		11.35	20.75	15.47	22.17	12.76	15.32	19.32		15.25	14.68	13.44
MnO		0.17	0.26	0.22	0.29	0.17	0.27	0.29		0.20	0.21	0.22
MgO		10.94	17.45	9.36	13.90	9.79	11.81	10.48		23.04	9.95	9.09
CaO		11.14	4.76	9.83	4.91	11.64	9.31	7.54		4.78	9.06	9.95
Na_2O		2.11	2.09	2.10	1.87	2.34	2.65	2.72		1.30	1.53	2.46
K_2O		0.62	0.56	0.68	0.63	0.77	0.38	0.57		0.48	0.70	0.75
P_2O_5		0.38	0.46	0.55	0.31	0.62	0.49	0.48		0.55	0.87	0.57
Cr_2O_3		0.28	0.17	0.15	0.36	0.07	0.00	0.06		0.30	0.42	0.03
H_2O		0.51	0.26	0.47	0.31	0.41	0.47	0.25		0.49	0.56	0.47
Total		100.00	100.00	100.02	99.99	100.01	99.99	99.99		100.00	100.00	100.02
CO_2 (ppm)		78 (76)	90 (51)	110 (80)	122 (96)	181 (134)	112 (171)	96 (201)		75 (185)	86 (118)	54 (151)
H_2O (wt. %)		0.52 (0.01)	0.28 (0.01)	0.49 (0.01)	0.33 (0.01)	0.42 (0.01)	0.48 (0.01)	0.26 (0.01)		0.5 (0.01)	0.58 (0.02)	0.49 (0.01)
F (ppm)		425 (11)	459 (19)	554 (15)	520 (19)	610 (16)	606 (17)	423 (14)		579 (15)	621 (16)	582 (16)
S (ppm)		814 (23)	497 (22)	1355 (40)	671 (28)	1472 (43)	1751 (53)	456 (18)		1324 (38)	1280 (36)	1649 (50)
Cl (ppm)		319 (10)	179 (9)	348 (11)	95 (4)	351 (11)	225 (7)	128 (7)		414 (13)	382 (12)	399 (13)

Table 3-1: Major oxide and volatile species compositions of MIs and host olivines (continued)

	Northern Victoria Land				Marie Byrd Land							
Locality	Shield Nunatak				Mount Berlin							
Host Lava	NV-13A	NV-13A	NV-13A	NV-13A	BN-14D	BN-14D	BN-14D	BN-14D	BN-14D	BN-14D	BN-14D	BN-14D
Sample ID	NV13A_20_95	NV13A_21_96	NV13A_22_97	16_NV-13_55	BN14D_1_91	BN14D_2_92	BN14D_3_98	BND14D_4_100	BND14D_5_101	BND14D_6_102	BND14D_7_103	BND14D_8_104
Host Olivines												
SiO_2 (wt.%)	39.08	39.68	39.50		39.96	37.37	36.38	37.53	38.64		37.39	39.45
TiO_2	0.03	0.03	0.02		0.01	0.07	0.17	0.04	0.04		0.07	0.02
Al_2O_3	0.09	0.06	0.02		0.05	0.11	0.16	0.07	0.04		0.14	0.07
FeO	18.03	14.88	15.48		13.12	27.35	34.83	27.68	21.39		28.42	17.05
MnO	0.25	0.20	0.22		0.18	0.36	0.75	0.36	0.32		0.38	0.22
MgO	43.55	45.58	45.28		46.91	35.75	29.73	35.91	40.79		35.13	43.99
CaO	0.28	0.31	0.30		0.26	0.15	0.31	0.09	0.11		0.17	0.10
NiO	0.07	0.15	0.20		0.18	0.13	0.04	0.06	0.14		0.13	0.27
Total	101.37	100.93	101.06		100.72	101.37	102.44	101.79	101.49		101.89	101.20
Mg#	81.15	84.52	83.91		86.44	69.97	60.34	69.81	77.27		68.78	82.14
Rehomogenized MI compositions												
SiO_2 (wt.%)	44.53	42.85	43.42		43.17	38.01	31.97	41.00	40.09		44.73	
TiO_2	3.49	3.75	2.86		3.87	2.06	0.91	0.67	3.77		5.12	
Al_2O_3	16.71	13.41	12.04		15.56	16.04	5.74	18.21	14.19		16.46	
Cr_2O_3	0.36	0.25	0.02		0.00	0.13	0.13	0.19	0.24		0.42	
FeO	14.99	11.59	11.95		10.74	23.97	21.41	22.25	13.89		18.22	
MnO	0.21	0.19	0.18		0.17	0.37	0.53	0.31	0.21		0.36	
MgO	5.24	9.07	13.94		7.94	5.35	8.82	6.78	10.95		2.93	
CaO	11.43	12.66	11.14		13.56	12.48	16.07	3.33	13.01		7.22	
Na_2O	2.27	2.29	2.19		2.83	2.47	2.41	2.46	3.09		4.22	
K_2O	0.81	0.79	0.72		0.94	0.07	0.65	3.59	0.26		1.48	
P_2O_5	0.64	0.59	1.52		0.53	0.05	10.93	1.82	0.13		0.83	
NiO	0.00	0.00	0.02		0.01	0.05	0.06	0.04	0.01		0.04	
F												
Cl												
S												
Total	100.68	97.44	99.99		99.32	101.05	99.60	100.64	99.83		102.04	
CO_2 (ppm)	2423 (75)	56 (82)	120 (613)	583 (58)	56 (250)	142 (149)	110 (128)	192 (78)	57 (106)	387 (32)	1057 (29)	61 (70)
H2O (wt. %)	0.61 (0.02)	0.45 (0.01)	0.4 (0.01)	1.45 (0.09)	0.47 (0.03)	0.65 (0.04)	0.77 (0.04)	0.79 (0.05)	0.68 (0.04)	0.47 (0.03)	0.45 (0.03)	0.43 (0.03)
F (ppm)	655 (17)	650 (17)	621 (16)	724 (25)	712 (19)	874 (23)	903 (24)	692 (18)	723 (19)	809 (28)	813 (28)	791 (28)
S (ppm)	1783 (51)	1143 (33)	877 (25)	874 (27)	1117 (34)	368 (11)	1362 (42)	1028 (31)	950 (29)	1181 (37)	1158 (36)	1027 (32)
Cl (ppm)	448 (14)	436 (13)	404 (12)	368 (12)	164 (5)	188 (6)	292 (9)	249 (7)	322 (9)	332 (11)	321 (10)	311 (10)
PEC-Corrected MI Compositions												
PEC (% ol)	15.44	2.55	0.00		8.04	11.56	0.00	4.78	0.00		10.08	
SiO_2 (wt.%)	42.33	42.93	42.50		42.20	36.19	30.68	39.07	39.13		41.75	
TiO_2	2.85	3.67	2.80		3.50	1.73	0.87	0.61	3.68		4.35	
Al_2O_3	13.64	13.12	11.79		14.05	13.46	5.51	16.56	13.85		13.99	
Fe_2O_3	2.01	1.76	1.64		1.52	3.99	6.10	3.17	1.98		4.59	
FeO	15.41	11.68	11.80		10.81	22.70	17.83	21.47	13.60		16.57	
MnO	0.17	0.19	0.18		0.15	0.31	0.51	0.28	0.20		0.31	
MgO	10.42	10.01	13.65		10.82	8.31	8.46	7.80	10.69		5.73	
CaO	9.33	12.38	10.90		12.25	10.47	15.42	3.03	12.70		6.14	
Na_2O	1.85	2.24	2.14		2.56	2.07	2.31	2.24	3.02		3.59	
K_2O	0.66	0.77	0.70		0.85	0.06	0.62	3.26	0.25		1.26	
P_2O_5	0.52	0.58	1.49		0.48	0.04	10.49	1.65	0.13		0.71	
Cr_2O_3	0.29	0.24	0.02		0.00	0.11	0.12	0.17	0.23		0.36	
H_2O	0.50	0.44	0.39		0.80	0.55	1.07	0.68	0.54		0.65	
Total	99.98	100.01	100.00		99.99	99.99	99.99	99.99	100.00		100.00	
CO_2 (ppm)	2049 (75)	55 (82)	120 (613)		486 (59)	40 (97)	260 (22)	1397 (72)	2620 (277)		87 (182)	
H_2O (wt. %)	0.51 (0.02)	0.44 (0.01)	0.4 (0.01)		0.81 (0.02)	0.59 (0.02)	1.11 (0.03)	0.72 (0.02)	0.55 (0.01)		0.69 (0.02)	
F (ppm)	554 (17)	634 (17)	621 (16)		507 (14)	320 (9)	881 (23)	745 (10)	930 (11)		346 (27)	
S (ppm)	1508 (51)	1114 (33)	877 (25)		1383 (43)	330 (11)	985 (28)	937 (13)	947 (18)		401 (26)	
Cl (ppm)	379 (14)	425 (13)	404 (12)		440 (15)	54 (2)	903 (28)	411 (36)	609 (7)		1050 (30)	

Table 3-1: Major oxide and volatile species compositions of MIs and host olivines (continued)

	Marie Byrd Land											
Locality	Mount Berlin					Mount Waesche						
Host Lava	BN-14D	BN-14D	BN-14D	BN-14D	BN-14D	39B	39B	39B	39B	39B	39B	39B
Sample ID	BND14D_9_105	BND14D_10_106	BN14D_11_108	BN14D_12_109	BN14D_13_110	39b_1_29	39b_2_30	39b_3_31	39b_4_32	39b_4_33	39b_5_35	39b_6_36
Host Olivines												
SiO_2 (wt.%)	39.45	39.45	40.13	40.13	37.37	38.86	39.03	39.03	38.82	38.82	38.98	38.98
TiO_2	0.02	0.02	0.00	0.00	0.06	0.03	0.03	0.02	0.01	0.01	0.02	0.02
Al_2O_3	0.07	0.07	0.02	0.02	0.11	0.04	0.06	0.02	0.03	0.03	0.04	0.04
FeO	17.05	17.05	11.48	11.48	27.68	18.48	17.30	17.06	16.21	16.21	18.32	18.32
MnO	0.22	0.22	0.15	0.15	0.38	0.29	0.29	0.26	0.25	0.25	0.27	0.27
MgO	43.99	43.99	48.75	48.75	35.92	42.87	43.81	43.91	44.98	44.98	43.08	43.08
CaO	0.10	0.10	0.25	0.25	0.11	0.31	0.31	0.31	0.30	0.30	0.30	0.30
NiO	0.27	0.27	0.27	0.27	0.13	0.11	0.11	0.09	0.12	0.12	0.11	0.11
Total	101.20	101.20	101.10	101.10	101.81	100.99	100.92	100.70	100.70	100.70	101.11	101.11
Mg#	82.14	82.14	88.34	88.34	69.82	80.53	81.86	82.11	83.19	83.19	80.74	80.74
Rehomogenized MI compositions												
SiO_2 (wt.%)	45.62	45.31	42.85	41.41	40.06	42.86	42.84	44.08	43.20		41.07	41.94
TiO_2	3.41	3.24	3.89	3.44	0.72	2.43	2.38	2.03	1.45		2.18	2.31
Al_2O_3	14.41	15.85	17.28	16.53	18.36	14.40	13.20	13.81	11.84		13.00	15.69
Cr_2O_3	0.40	0.15	0.29	0.17	0.07	0.05	0.02	0.03	0.00		0.10	0.12
FeO	15.97	13.85	9.59	12.38	20.59	14.85	15.91	13.74	12.08		16.31	14.17
MnO	0.30	0.28	0.11	0.20	0.24	0.25	0.30	0.22	0.20		0.26	0.22
MgO	5.04	5.97	4.51	5.43	7.48	9.06	9.73	11.13	17.09		8.87	5.48
CaO	8.82	6.79	14.26	10.05	3.52	10.72	9.95	10.72	8.35		10.39	10.98
Na_2O	3.61	4.54	3.32	4.66	3.28	3.36	2.80	3.17	2.91		2.96	3.61
K_2O	1.29	1.79	1.33	1.59	4.42	0.78	0.57	0.53	1.10		0.69	0.90
P_2O_5	0.71	0.82	0.45	0.71	2.72	0.25	0.38	0.17	0.23		0.20	0.24
NiO	0.00	0.00	0.02	0.01	0.00	0.04	0.03	0.03	0.01		0.03	0.03
F						0.04	0.00	0.02	0.00		0.17	0.03
Cl						0.07	0.03	0.05	0.05		0.05	0.06
S						0.19	0.27	0.20	0.10		0.21	0.24
Total	99.58	98.58	97.91	96.58	101.45	99.36	98.41	99.93	98.62		96.49	96.03
CO_2 (ppm)	45 (151)	946 (27)	98 (150)	1197 (210)	74 (409)	529 (59)	46 (97)	260 (22)	1467 (72)	2620 (277)	162 (1267)	97 (182)
H2O (wt. %)	0.54 (0.04)	0.55 (0.04)	0.24 (0.02)	0.65 (0.04)	0.56 (0.04)	0.89 (0.02)	0.66 (0.02)	1.11 (0.03)	0.75 (0.02)	0.55 (0.01)	0.71 (0.01)	0.77 (0.02)
F (ppm)	864 (30)	772 (27)	290 (10)	937 (33)	843 (29)	551 (14)	362 (9)	881 (23)	783 (10)	930 (11)	436 (24)	384 (27)
S (ppm)	1032 (32)	1096 (34)	456 (14)	1361 (43)	1110 (35)	1504 (43)	373 (11)	985 (28)	984 (13)	947 (18)	2985 (24)	446 (26)
Cl (ppm)	332 (11)	367 (12)	134 (4)	245 (8)	370 (12)	479 (15)	62 (2)	903 (28)	431 (36)	609 (7)	1308 (12)	1167 (30)
PEC-Corrected MI Compositions												
PEC (% ol)	19.90	12.50	19.72	25.57	0	1.74	4.99	0.00	0.00		5.97	12.42
SiO_2 (wt.%)	43.38	43.97	42.37	41.32	38.15	42.05	42.05	43.05	42.78		41.18	42.00
TiO_2	2.67	2.80	3.13	2.59	0.69	2.35	2.23	1.98	1.44		2.06	2.05
Al_2O_3	11.27	13.68	13.92	12.44	17.48	13.90	12.35	13.49	11.73		12.29	13.91
Fe_2O_3	2.23	2.00	1.44	1.81	3.28	2.23	2.18	1.91	1.91		2.39	2.19
FeO	16.44	14.25	10.49	12.99	19.3	14.59	15.84	13.51	11.86		16.51	14.93
MnO	0.23	0.24	0.09	0.15	0.23	0.24	0.28	0.21	0.20		0.25	0.20
MgO	11.88	10.30	12.48	15.45	7.12	9.48	11.23	10.87	16.93		10.87	9.83
CaO	6.90	5.86	11.49	7.56	3.35	10.35	9.31	10.47	8.27		9.83	9.74
Na_2O	2.82	3.92	2.67	3.51	3.12	3.24	2.62	3.10	2.88		2.80	3.20
K_2O	1.01	1.54	1.07	1.2	4.21	0.75	0.53	0.52	1.09		0.65	0.80
P_2O_5	0.56	0.71	0.36	0.53	2.59	0.24	0.36	0.17	0.23		0.19	0.21
Cr_2O_3	0.31	0.13	0.23	0.13	0.07	0.05	0.02	0.03	0.00		0.09	0.11
H_2O	0.30	0.60	0.25	0.34	0.4	0.53	1.00	0.69	0.69		0.88	0.84
Total	100.00	100.00	99.99	100.02	99.99	100.00	100.00	100.00	100.01		99.99	100.01
CO_2 (ppm)	391 (580)	88 (102)	369 (782)	86 (325)	76 (14)	203 (191)	200 (178)	55 (200)	586 (318)		110 (236)	101 (107)
H_2O (wt. %)	0.31 (0.01)	0.61 (0.01)	0.25 (0.02)	0.34 (0.01)	0.42 (0.02)	0.54 (0.03)	1.01 (0.06)	0.71 (0.04)	0.7 (0.04)		0.88 (0.05)	0.83 (0.05)
F (ppm)	732 (24)	911 (22)	473 (20)	685 (24)	846 (11)	804 (22)	859 (24)	787 (21)	1123 (30)		782 (22)	729 (22)
S (ppm)	663 (17)	798 (17)	283 (28)	436 (27)	604 (86)	1046 (32)	1677 (54)	1236 (38)	677 (21)		1022 (33)	1017 (35)
Cl (ppm)	310 (15)	848 (15)	245 (13)	358 (19)	499 (40)	358 (11)	304 (10)	212 (7)	246 (7)		329 (10)	328 (11)

Table 3-1: Major oxide and volatile species compositions of MIs and host olivines (continued)

	Marie Byrd Land											
Locality	Mount Waesche											
Host Lava	39B	39B	39B	39B	39B	39B	39B	39B	39B	39B	39B	39B
Sample ID	39b_7_37	39b_8_38	39b_9_39	39b_10_40	39b_11_41	39b_12_43	39b_13_44	39b_14_45	39b_15_46	39b_16_47	39b_17_50	39b_18_51
Host Olivines												
SiO_2 (wt.%)	38.84	38.87	38.87	38.87	38.87	38.66	38.80	38.80	38.61	39.01	39.00	39.11
TiO_2	0.01	0.01	0.01	0.01	0.01	0.02	0.03	0.03	0.02	0.01	0.02	0.03
Al_2O_3	0.04	0.02	0.02	0.05	0.05	0.03	0.05	0.05	0.05	0.02	0.04	0.04
FeO	17.22	16.37	16.37	18.14	18.14	17.36	17.53	17.53	17.74	16.65	16.33	18.24
MnO	0.29	0.26	0.26	0.30	0.30	0.27	0.30	0.30	0.30	0.27	0.26	0.31
MgO	44.05	44.70	44.70	43.45	43.45	44.08	43.79	43.79	44.01	44.85	44.73	43.14
CaO	0.31	0.29	0.29	0.30	0.30	0.30	0.30	0.30	0.32	0.27	0.29	0.28
NiO	0.13	0.13	0.13	0.12	0.12	0.13	0.13	0.13	0.12	0.15	0.13	0.13
Total	100.88	100.65	100.65	101.24	101.24	100.84	100.91	100.91	101.15	101.21	100.79	101.28
Mg#	82.01	82.96	82.96	81.02	81.02	81.91	81.66	81.66	81.56	82.77	83.01	80.83
Rehomogenized MI compositions												
SiO_2 (wt.%)	43.01	44.28		44.15	44.35	43.05		42.70	43.79	41.25	43.73	44.53
TiO_2	1.86	1.83		1.80	1.91	2.46		2.22	1.57	3.58	1.73	2.48
Al_2O_3	13.28	13.46		13.06	14.92	13.65		14.31	13.31	11.27	12.87	14.25
Cr_2O_3	0.00	0.01		0.00	0.03	0.03		0.05	0.03	0.03	0.04	0.07
FeO	13.20	12.57		14.32	13.95	14.31		14.96	13.27	17.49	13.63	13.17
MnO	0.22	0.19		0.22	0.22	0.23		0.24	0.21	0.36	0.21	0.18
MgO	13.49	13.36		12.74	8.43	9.88		8.46	14.22	9.06	12.80	10.20
CaO	9.73	9.82		9.27	9.62	10.84		11.16	9.45	9.85	10.01	10.17
Na_2O	2.94	2.97		3.32	3.74	2.90		3.20	2.79	4.51	3.27	3.36
K_2O	0.69	0.41		0.67	0.98	0.68		0.74	0.55	0.46	0.49	0.60
P_2O_5	0.29	0.23		0.45	0.49	0.30		0.32	0.16	0.41	0.28	0.43
NiO	0.05	0.02		0.02	0.02	0.01		0.05	0.02	0.05	0.07	0.03
F	0.00	0.00		0.05	0.00	0.01		0.04	0.03	0.17	0.04	0.04
Cl	0.05	0.04		0.03	0.06	0.05		0.05	0.04	0.05	0.05	0.01
S	0.23	0.23		0.28	0.34	0.20		0.24	0.17	0.21	0.21	0.20
Total	99.04	99.42		100.38	99.05	98.59		98.75	99.60	98.75	99.43	99.74
CO_2 (ppm)	88 (537)	488 (580)	100 (102)	460 (782)	115 (325)	76 (14)	207 (191)	210 (178)	55 (200)	586 (318)	1018 (3460)	117 (236)
H2O (wt. %)	0.45 (0.01)	0.39 (0.01)	0.7 (0.01)	0.31 (0.02)	0.45 (0.01)	0.42 (0.02)	0.55 (0.03)	1.07 (0.06)	0.71 (0.04)	0.7 (0.04)	0.71 (0.04)	0.93 (0.05)
F (ppm)	425 (15)	914 (24)	1041 (22)	589 (20)	920 (24)	846 (11)	818 (22)	904 (24)	787 (21)	1123 (30)	1127 (30)	832 (22)
S (ppm)	648 (11)	827 (17)	911 (17)	353 (28)	585 (27)	604 (86)	1064 (32)	1765 (54)	1236 (38)	677 (21)	681 (21)	1087 (33)
Cl (ppm)	234 (9)	387 (15)	969 (15)	305 (13)	481 (19)	499 (40)	365 (11)	320 (10)	212 (7)	246 (7)	247 (8)	350 (10)
PEC-Corrected MI Compositions												
PEC (% ol)	0.00	0.00		0.00	2.80	1.00		6.13	0.00	12.08	0.00	0.00
SiO_2 (wt.%)	42.44	43.57		43.02	43.55	42.51		41.87	42.92	40.36	43.00	43.70
TiO_2	1.84	1.80		1.75	1.83	2.41		2.05	1.54	3.09	1.70	2.43
Al_2O_3	13.10	13.25		12.73	14.28	13.35		13.22	13.05	9.73	12.65	13.98
Fe_2O_3	1.80	1.69		1.96	2.08	2.08		2.17	1.77	2.49	1.92	1.87
FeO	13.17	12.52		14.07	13.80	14.19		14.88	13.17	17.14	13.48	12.99
MnO	0.22	0.19		0.21	0.21	0.23		0.22	0.21	0.31	0.21	0.18
MgO	13.31	13.15		12.41	9.25	10.10		10.41	13.94	12.93	12.59	10.01
CaO	9.60	9.66		9.03	9.21	10.61		10.31	9.26	8.50	9.84	9.98
Na_2O	2.90	2.92		3.24	3.58	2.84		2.96	2.73	3.89	3.22	3.30
K_2O	0.68	0.40		0.65	0.94	0.67		0.68	0.54	0.40	0.48	0.59
P_2O_5	0.29	0.23		0.44	0.47	0.29		0.30	0.16	0.35	0.28	0.42
Cr_2O_3	0.00	0.01		0.00	0.03	0.03		0.05	0.03	0.03	0.04	0.07
H_2O	0.67	0.61		0.48	0.78	0.70		0.89	0.69	0.78	0.60	0.48
Total	100.02	100.00		99.99	100.01	100.01		100.01	100.01	100.00	100.01	100.00
CO_2 (ppm)	1928 (22)	468 (35)		54 (286)	703 (293)	58 (84)		549 (261)	67 (226)	144 (75)	99 (205)	74 (180)
H_2O (wt. %)	0.68 (0.04)	0.62 (0.04)		0.49 (0.03)	0.79 (0.05)	0.71 (0.04)		0.9 (0.05)	0.7 (0.04)	0.79 (0.05)	0.61 (0.04)	0.49 (0.03)
F (ppm)	666 (18)	633 (17)		743 (20)	774 (21)	803 (21)		781 (22)	682 (18)	877 (26)	521 (14)	758 (20)
S (ppm)	1052 (32)	1242 (38)		1563 (48)	1779 (56)	980 (30)		1061 (35)	915 (28)	959 (33)	940 (29)	1108 (34)
Cl (ppm)	313 (9)	151 (4)		264 (8)	337 (10)	362 (11)		378 (12)	277 (8)	294 (10)	204 (6)	243 (7)

Table 3-1: Major oxide and volatile species compositions of MIs and host olivines (continued)

	Marie Byrd Land											
Locality	Mount Waesche											
Host Lava	39B	39B	39B	39B	39B	39B	39B	39B	39B	39B	39B	39B
Sample ID	39b_19_52	39b_20_53	39b_21_54	39b_22_56	39b_23_57	39b_24_59	39b_25_60	39b_26_61	39b_27_62	39b_28_63	39b_29_64	39b_30_65
Host Olivines												
SiO_2 (wt.%)	39.20	38.12	38.88	39.32	39.32	39.13	38.78	39.42	39.22	39.00	39.00	38.66
TiO_2	0.03	0.05	0.03	0.01	0.01	0.02	0.02	0.02	0.03	0.02	0.02	0.05
Al_2O_3	0.06	0.12	0.03	0.04	0.04	0.08	0.07	0.04	0.02	0.01	0.01	0.05
FeO	16.73	24.40	17.26	16.52	16.52	17.38	19.38	16.41	16.62	16.07	16.07	21.16
MnO	0.27	0.46	0.28	0.25	0.25	0.28	0.29	0.25	0.26	0.24	0.24	0.33
MgO	44.36	38.04	43.75	44.48	44.48	43.56	41.98	44.73	44.36	44.71	44.71	40.83
CaO	0.30	0.33	0.31	0.29	0.29	0.29	0.29	0.31	0.29	0.32	0.32	0.32
NiO	0.13	0.10	0.11	0.15	0.15	0.12	0.11	0.12	0.13	0.16	0.16	0.09
Total	101.07	101.61	100.65	101.06	101.06	100.85	100.91	101.29	100.94	100.51	100.51	101.48
Mg#	82.54	73.54	81.88	82.76	82.76	81.71	79.43	82.93	82.63	83.22	83.22	77.48
Rehomogenized MI compositions												
SiO_2 (wt.%)	43.67	44.43	42.27	43.26	41.43	42.52	43.20	44.09	43.16	42.57	43.38	43.94
TiO_2	2.20	0.09	2.23	1.84	2.23	2.40	2.28	2.07	2.62	2.09	2.20	2.17
Al_2O_3	13.73	19.93	13.81	13.70	14.03	17.38	13.52	13.60	14.17	13.73	14.80	11.27
Cr_2O_3	0.02	0.00	0.05	0.00	0.00	0.07	0.05	0.00	0.02	0.07	0.03	0.09
FeO	12.32	14.03	15.23	13.03	13.84	11.43	14.95	13.51	13.06	12.58	13.13	15.20
MnO	0.18	0.22	0.23	0.18	0.21	0.15	0.24	0.18	0.23	0.21	0.25	0.22
MgO	13.20	9.70	8.07	13.59	10.20	6.23	10.79	11.63	11.26	10.79	8.16	12.64
CaO	10.16	9.56	11.14	9.93	12.45	10.48	9.88	10.67	11.23	11.98	12.35	9.11
Na_2O	3.11	1.84	2.99	2.74	2.75	4.00	3.39	2.88	2.95	3.13	3.35	3.49
K_2O	0.53	0.06	0.68	0.61	0.28	1.24	0.68	0.39	0.45	0.34	0.56	0.63
P_2O_5	0.47	0.00	0.52	0.20	1.08	0.24	0.58	0.17	0.65	1.97	0.70	0.50
NiO	0.02	0.04	0.02	0.04	0.06	0.04	0.02	0.05	0.02	0.02	0.04	0.02
F	0.00	0.00	0.21	0.06	0.08	0.01	0.13	0.20	0.08	0.03	0.00	0.00
Cl	0.04	0.00	0.04	0.05	0.02	0.05	0.03	0.02	0.02	0.04	0.06	0.02
S	0.16	0.00	0.24	0.26	0.32	0.18	0.26	0.20	0.22	0.08	0.32	0.21
Total	99.81	99.91	97.72	99.49	98.98	96.42	100.00	99.66	100.13	99.63	99.33	99.51
CO_2 (ppm)	116 (107)	1928 (22)	468 (35)	1115 (207)	54 (286)	723 (293)	58 (84)	444 (451)	585 (261)	67 (226)	164 (75)	99 (205)
H2O (wt. %)	0.95 (0.05)	0.68 (0.04)	0.62 (0.04)	0.83 (0.05)	0.49 (0.03)	0.81 (0.05)	0.72 (0.04)	0.46 (0.03)	0.96 (0.05)	0.7 (0.04)	0.9 (0.05)	0.61 (0.04)
F (ppm)	833 (22)	666 (18)	633 (17)	776 (20)	743 (20)	796 (21)	811 (21)	384 (11)	832 (22)	682 (18)	998 (26)	521 (14)
S (ppm)	1162 (35)	1052 (32)	1242 (38)	1762 (54)	1563 (48)	1830 (56)	990 (30)	623 (20)	1131 (35)	915 (28)	1091 (33)	940 (29)
Cl (ppm)	374 (11)	313 (9)	151 (4)	198 (6)	264 (8)	347 (10)	366 (11)	245 (9)	403 (12)	277 (8)	334 (10)	204 (6)
PEC-Corrected MI Compositions												
PEC (% ol)	0.00	0.00	8.48	0.00	0.83	5.59	0.00	0.00	0.00	0.00	6.12	0.00
SiO_2 (wt.%)	42.88	43.37	41.88	42.55	40.89	42.88	42.14	43.17	42.15	41.74	42.47	42.94
TiO_2	2.16	0.09	2.03	1.81	2.18	2.30	2.22	2.03	2.56	2.05	2.03	2.12
Al_2O_3	13.48	19.46	12.60	13.47	13.74	16.63	13.19	13.32	13.84	13.46	13.67	11.01
Fe_2O_3	1.66	1.36	2.20	1.72	1.99	1.79	2.13	1.82	1.78	1.83	1.94	2.20
FeO	12.24	14.32	15.38	12.99	13.73	11.85	14.63	13.38	12.88	12.35	13.07	14.88
MnO	0.18	0.21	0.21	0.18	0.21	0.14	0.23	0.18	0.22	0.21	0.23	0.21
MgO	12.96	9.47	10.92	13.37	10.35	8.31	10.53	11.39	11.00	10.58	10.19	12.35
CaO	9.98	9.33	10.16	9.77	12.19	10.03	9.64	10.45	10.97	11.75	11.40	8.90
Na_2O	3.05	1.80	2.73	2.69	2.69	3.83	3.31	2.82	2.88	3.07	3.09	3.41
K_2O	0.52	0.06	0.62	0.60	0.27	1.19	0.66	0.38	0.44	0.33	0.52	0.62
P_2O_5	0.46	0.00	0.47	0.20	1.06	0.23	0.57	0.17	0.63	1.93	0.65	0.49
Cr_2O_3	0.02	0.00	0.05	0.00	0.00	0.07	0.05	0.00	0.02	0.07	0.03	0.09
H_2O	0.42	0.54	0.74	0.65	0.70	0.75	0.69	0.90	0.63	0.64	0.71	0.77
Total	100.01	100.01	99.99	100.00	100.00	100.00	99.99	100.01	100.00	100.01	100.00	99.99
CO_2 (ppm)	39 (193)	21 (325)	76 (79)	51 (151)	60 (110)	66 (185)	56 (240)	61 (240)	56 (250)	142 (149)	103 (128)	192 (78)
H_2O (wt. %)	0.43 (0.03)	0.55 (0.03)	0.74 (0.05)	0.66 (0.04)	0.71 (0.04)	0.73 (0.04)	0.71 (0.04)	0.92 (0.05)	0.47 (0.03)	0.65 (0.04)	0.72 (0.04)	0.79 (0.05)
F (ppm)	632 (17)	65 (2)	748 (22)	669 (18)	831 (22)	729 (20)	834 (22)	770 (20)	712 (19)	874 (23)	848 (24)	692 (18)
S (ppm)	1014 (31)	7 (2)	1237 (41)	1078 (33)	1547 (48)	1085 (35)	1088 (33)	1124 (34)	1117 (34)	368 (11)	1279 (42)	1028 (31)
Cl (ppm)	172 (5)	2 (4)	278 (9)	244 (7)	235 (7)	433 (14)	290 (9)	221 (7)	164 (5)	188 (6)	274 (9)	249 (7)

Table 3-1: Major oxide and volatile species compositions of MIs and host olivines (continued)

	Marie Byrd Land								
Locality	Mount Waesche								
Host Lava	39B	39B	39B	39B	39B	39B	39B	39B	39B
Sample ID	39b_31_66	67-39b_1_43	67-39b_2_44	67-39b_3_45	67-39b_4_46	4_39b_3_49.asc	1-39b_2_61.asc	39b_4_62	39b_4_63
Host Olivines									
SiO_2 (wt.%)	39.17	38.52	38.52	38.52	38.52			38.85	38.85
TiO_2	0.00	0.04	0.04	0.04	0.04			0.02	0.02
Al_2O_3	0.03	0.06	0.06	0.06	0.06			0.04	0.04
FeO	16.81	18.52	18.52	18.52	18.52			17.99	17.99
MnO	0.27	0.31	0.31	0.31	0.31			0.31	0.31
MgO	44.42	42.39	42.39	42.39	42.39			43.57	43.57
CaO	0.28	0.32	0.32	0.32	0.32			0.30	0.30
NiO	0.16	0.13	0.13	0.13	0.13			0.12	0.12
Total	101.15	100.27	100.27	100.27	100.27			101.19	101.19
Mg#	82.49	80.32	80.32	80.32	80.32			81.19	81.19
Rehomogenized MI compositions									
SiO_2 (wt.%)	43.38	44.66	44.37	44.26	43.75			41.97	42.34
TiO_2	2.33	2.03	2.12	2.18	2.10			2.39	2.33
Al_2O_3	13.77	15.38	15.01	15.17	15.42			13.73	14.30
Cr_2O_3	0.00	0.00	0.02	0.05	0.00			0.08	0.05
FeO	12.99	11.59	11.90	11.19	11.54			12.87	12.44
MnO	0.20	0.17	0.17	0.16	0.20			0.21	0.20
MgO	11.86	10.29	9.96	10.61	9.63			10.66	9.76
CaO	10.34	10.33	10.56	10.08	11.08			11.80	10.97
Na_2O	3.23	3.56	3.34	3.47	3.70			3.14	3.59
K_2O	0.82	0.87	0.85	0.93	0.89			0.39	0.79
P_2O_5	0.18	0.50	0.47	0.57	0.51			1.26	0.47
NiO	0.05	0.03	0.01	0.03	0.03			0.02	0.03
F	0.01	0.01	0.02	0.06	0.10			0.00	0.00
Cl	0.04	0.04	0.03	0.03	0.05			0.05	0.06
S	0.18	0.23	0.21	0.20	0.21			0.25	0.18
Total	99.38	99.69	99.05	98.99	99.20			98.82	97.53
CO_2 (ppm)	74 (180)	39 (193)	21 (325)	83 (79)	51 (151)	60 (110)	70 (185)	56 (240)	61 (240)
H2O (wt. %)	0.49 (0.03)	0.43 (0.03)	0.55 (0.03)	0.81 (0.05)	0.66 (0.04)	0.71 (0.04)	0.78 (0.04)	0.71 (0.04)	0.92 (0.05)
F (ppm)	758 (20)	632 (17)	65 (2)	817 (22)	669 (18)	838 (22)	772 (20)	834 (22)	770 (20)
S (ppm)	1108 (34)	1014 (31)	7 (2)	1351 (41)	1078 (33)	1560 (48)	1150 (35)	1088 (33)	1124 (34)
Cl (ppm)	243 (7)	172 (5)	2 (4)	304 (9)	244 (7)	237 (7)	459 (14)	290 (9)	221 (7)
PEC-Corrected MI Compositions									
PEC (% ol)	0.00	0.00	0.00	0.00	0.00			0.00	0.00
SiO_2 (wt.%)	42.65	43.97	43.93	43.92	43.28			41.52	42.48
TiO_2	2.29	2.00	2.10	2.16	2.08			2.36	2.34
Al_2O_3	13.54	15.14	14.86	15.05	15.25			13.58	14.35
Fe_2O_3	1.80	1.62	1.69	1.56	1.69			1.88	1.90
FeO	12.87	11.50	11.86	11.21	11.43			12.76	12.46
MnO	0.20	0.17	0.17	0.16	0.20			0.21	0.20
MgO	11.66	10.13	9.86	10.53	9.53			10.55	9.79
CaO	10.17	10.17	10.46	10.00	10.96			11.67	11.01
Na_2O	3.18	3.50	3.31	3.44	3.66			3.11	3.60
K_2O	0.81	0.86	0.84	0.92	0.88			0.39	0.79
P_2O_5	0.18	0.49	0.47	0.57	0.50			1.25	0.47
Cr_2O_3	0.00	0.00	0.02	0.05	0.00			0.08	0.05
H_2O	0.67	0.46	0.45	0.43	0.53			0.64	0.56
Total	100.02	100.01	100.02	100.00	99.99			100.00	100.00
CO_2 (ppm)	57 (106)	387 (32)	1057 (29)	61 (70)	45 (151)			1197 (210)	74 (409)
H_2O (wt. %)	0.68 (0.04)	0.47 (0.03)	0.45 (0.03)	0.43 (0.03)	0.54 (0.04)			0.65 (0.04)	0.56 (0.04)
F (ppm)	723 (19)	809 (28)	813 (28)	791 (28)	864 (30)			937 (33)	843 (29)
S (ppm)	950 (29)	1181 (37)	1158 (36)	1027 (32)	1032 (32)			1361 (43)	1110 (35)
Cl (ppm)	322 (9)	332 (11)	321 (10)	311 (10)	332 (11)			245 (8)	370 (12)

Table 3-2: Trace element compositions of MIs

	Northern Victoria Land													
Locality	Mount Morning													
Host Lava	C88-89	C88-89	C88-89	C88-89	C88-89	C88-89	C88-89	C88-89	C88-89	C88-89	C88-89	C88-89	C88-89	C88-89
Sample ID	c88-89_3_70	c88-89_4_71	c88-89_5_72	c88-89_8_76	c88-89_9_77	c88-89_11_79	c88-89_13_81	c88-89_15_84	c88-89_17_86	c88-89_18_87	c88-89_21_90	c88-89_23_92	c88-89_25_147	c88-89_26_148
Measured MI compositions														
Li (ppm)	15 (5)	85 (22)	11 (3)	19 (37)	123 (37)	7 (1)	12 (2)	102 (10)	15 (5)	13 (2)	13 (2)	81 (8)	10 (1)	
Ti	2420 (750)	17700 (1600)	18200 (1200)	14300 (6500)	21800 (4600)	23750 (630)	18440 (760)	19900 (970)	24500 (1500)	16230 (670)	25500 (1200)	23200 (7500)	3080 (110)	27800 (2100)
V	35 (12)	246 (17)	233 (21)	209 (96)	354 (3)	307 (8)	236 (13)	255 (16)	278 (40)	169 (6)	287 (14)	330 (130)	48 (6)	407 (34)
Cr	560 (270)	3120 (380)	834 (69)	2800 (1300)	7870 (560)	1511 (38)	1110 (52)	283 (16)	291 (85)	318 (10)	337 (24)	445 (90)	105 (22)	693 (46)
Ni	26 (10)	225 (57)	360 (150)	550 (180)	433 (23)	149 (8)	129 (7)	298 (16)	330 (120)	460 (310)	195 (49)	196 (87)	76 (22)	1078 (91)
Rb		13 (16)	13.1 (3.5)	19 (17)	8.3 (4.9)	19.2 (1.4)	12.1 (1.5)	10.4 (1.3)	20 (4.4)	12.6 (1.3)	17.7 (2.7)	22 (18)	3.1 (0.22)	20.4 (2.8)
Sr	68 (25)	476 (73)	572 (41)	580 (260)	712 (55)	799 (22)	557 (22)	604 (32)	759 (48)	527 (24)	787 (35)	390 (130)	122 (4.6)	765 (65)
Y	3.7 (1.4)	25.6 (4.1)	26.4 (1.6)	20 (9.5)	21 (4.9)	26.9 (1.2)	27.5 (1.8)	22.7 (2)	33.3 (4.7)	25.2 (1.1)	32 (2)	28 (11)	4.1 (0.25)	32.1 (3.2)
Zr	33 (12)	186 (29)	164.9 (8.3)	156 (69)	161 (21)	193 (6.2)	172.5 (8.2)	153.9 (8)	234 (15)	167.8 (9.6)	220 (11)	234 (80)	37.5 (1.6)	209 (22)
Nb	6.8 (2.8)	49.4 (4.7)	26.3 (2.5)	35 (18)	40 (6.3)	46.8 (1.7)	32 (1.8)	31.3 (2.7)	43.9 (6.2)	32.4 (1.5)	44.1 (2.5)	44 (28)	10.4 (0.44)	45.5 (4.5)
Ba	36 (12)	231 (37)	166 (24)	320 (100)	300 (170)	298 (13)	179 (9)	214 (12)	283 (32)	173 (11)	283 (20)	212 (76)	73 (4)	303 (35)
La	5.7 (2)	34.3 (5.3)	22.7 (2.1)	28 (13)	19.8 (1.2)	34.9 (2)	25.8 (1.5)	22.6 (1.5)	32.3 (3.9)	24.7 (1.2)	34 (2.3)	29 (10)	7 (0.44)	31.6 (3.7)
Ce	10.5 (3.5)	67 (10)	44.1 (5.3)	53 (25)	58.6 (0.76)	69 (3.5)	51.5 (2.4)	48.2 (2.6)	63.6 (6.2)	48.8 (2.3)	74.3 (5.1)	74 (30)	13.2 (0.76)	74.9 (7.1)
Pr	1.3 (0.6)	8.1 (1.3)	7 (1.5)	6.3 (3.4)	8.6 (1.1)	9.4 (0.53)	7 (0.55)	6.6 (0.62)	9.8 (2.1)	6.7 (0.55)	9.8 (0.98)	8.7 (3)	1.6 (0.14)	9.4 (1.5)
Nd	5.1 (2.2)	36 (6.5)	27 (3.9)	33 (15)	32.3 (5.5)	39.8 (3)	30.8 (2.5)	27.9 (3.4)	38.4 (7.3)	28.8 (2)	39.9 (8.4)	40 (15)	6.7 (0.51)	38.5 (4)
Sm	0.9 (0.65)	6.5 (1.4)	5.1 (1.1)	7.4 (4.9)	8.2 (0.92)	7.5 (1.2)	5.5 (1.3)	6.3 (1.7)	7 (3.3)	6 (1)	8 (2.5)	8.7 (3.3)	1.3 (0.29)	7.7 (2.9)
Eu	0.5 (0.29)	1.8 (0.49)	2.2 (0.55)	1.5 (1)	1.9 (2.6)	2.4 (0.34)	2.4 (0.49)	1.7 (0.38)	2.9 (1.3)	2 (0.38)	2.5 (0.59)	2.2 (0.87)	0.4 (0.09)	2.4 (0.28)
Gd	1.1 (0.62)	6.6 (1.9)	7.7 (3.3)	4.7 (2.8)	5.3 (2.7)	7.1 (1.1)	7.4 (1.1)	5.1 (1.1)	5.6 (3.4)	6.3 (1.3)	9.1 (2.7)	7.7 (3.9)	1 (0.26)	9.8 (3.4)
Tb	0.1 (0.07)	0.9 (0.29)	0.9 (0.28)	0.8 (0.48)	0.2 (0.39)	1 (0.16)	1.1 (0.17)	0.6 (0.14)	1.4 (0.52)	1 (0.18)	1.2 (0.31)	1.1 (0.42)	0.1 (0.04)	0.9 (0.44)
Dy	1.2 (0.46)	5.7 (1.6)	3.7 (1)	4.1 (2.7)	4.6 (0.81)	5.8 (0.83)	6.2 (0.83)	4.6 (1.1)	7.5 (3.3)	5.6 (0.77)	6.6 (1.8)	5.3 (2.3)	0.8 (0.18)	6.9 (2.3)
Ho	0.2 (0.1)	0.8 (0.24)	1.1 (0.29)	0.8 (0.54)	0.8 (0.42)	1.1 (0.2)	1.1 (0.19)	0.6 (0.2)	1 (0.43)	1.1 (0.19)	1.3 (0.34)	0.7 (0.38)	0.1 (0.03)	1.2 (0.51)
Er	0.5 (0.44)	2.4 (0.82)	3.3 (0.93)	1.6 (1)	3.8 (7.5)	2.3 (0.34)	2.6 (0.49)	1.9 (0.56)	2.8 (2.2)	2.7 (0.76)	3.9 (1.1)	3.8 (2.2)	0.4 (0.14)	3.9 (0.76)
Tm	0 (0.05)	0.2 (0.07)	0.2 (0.16)	0.2 (0.17)	0 (0)	0.4 (0.1)	0.3 (0.09)	0.4 (0.15)	0.3 (0.24)	0.3 (0.12)	0.4 (0.13)	0.5 (0.33)	0.1 (0.02)	0.3 (0.2)
Yb	0.4 (0.39)	2.3 (1)	3.8 (2.1)	1.9 (1.3)	4 (0.45)	2 (0.61)	2.5 (0.82)	2 (0.87)	2.2 (1.2)	1.5 (0.52)	2.4 (0.93)	3 (3.1)	0.3 (0.12)	2 (0.45)
Lu	0.1 (0.06)	0.3 (0.13)	0.4 (0.28)	0.1 (0.16)	0.2 (0.36)	0.3 (0.1)	0.3 (0.12)	0.2 (0.13)	0.5 (0.13)	0.3 (0.1)	0.3 (0.12)	0.3 (0.25)	0.1 (0.02)	0.1 (0.15)
Hf	0.7 (0.42)	4.3 (0.94)	4.5 (2.8)	4.4 (2.6)	2.5 (1.3)	3.6 (0.65)	4.1 (0.77)	3.4 (1.1)	5.6 (2.9)	4.2 (0.8)	5.2 (1.4)	7.8 (4.1)	0.9 (0.17)	7.7 (2.1)
Ta	0.5 (0.2)	3.1 (0.69)	1.8 (0.45)	2.9 (1.4)	2.2 (2.2)	3 (0.3)	1.9 (0.38)	1.9 (0.4)	3.6 (0.87)	2.3 (0.26)	3.5 (0.65)	2.8 (1.2)	0.6 (0.1)	2.9 (0.82)
W	0.2 (0.14)	0.6 (0.38)	0.4 (0.33)	1.7 (1.3)	1.9 (3.7)	0.6 (0.2)	0.1 (0.11)	0.3 (0.26)	0.2 (0.29)	0.3 (0.18)	0.5 (0.29)	1.1 (0.66)	0.5 (0.12)	0.7 (0.51)
Pb	0.8 (0.33)	5 (1.1)	1.9 (1.2)	5.9 (2.6)	8.5 (4.9)	1.4 (0.22)	1.3 (0.32)	2.1 (0.4)	1.3 (0.49)	1.5 (0.29)	2 (0.67)	4.4 (1.7)	0.6 (0.11)	1.9 (0.81)
Th	0.6 (0.21)	3.1 (0.5)	1.9 (0.34)	2.8 (1.3)	2.4 (0.18)	3.4 (0.16)	2.6 (0.18)	2.2 (0.19)	3.5 (0.49)	2.6 (0.18)	3.8 (0.31)	2.5 (0.87)	0.7 (0.05)	3.5 (0.49)
U	0.1 (0.05)	0.8 (0.15)	0.4 (0.09)	0.7 (0.4)	0.6 (0.12)	0.8 (0.06)	0.6 (0.07)	0.5 (0.06)	0.7 (0.19)	0.6 (0.06)	0.7 (0.13)	0.8 (0.28)	0.2 (0.01)	0.9 (0.17)
PEC-corrected MI compositions														
Li (ppm)	15 (5)	85 (22)	10 (3)	18 (37)	114 (37)	6 (1)	11 (2)	102 (10)	12 (5)	10 (2)	10 (2)	71 (8)	10 (1)	
Ti	2420 (750)	17700 (1600)	17340 (1200)	13427 (6500)	20292 (4600)	21460 (630)	16915 (760)	19900 (970)	19850 (1500)	12369 (670)	20174 (1200)	20127 (7500)	3080 (110)	24326 (2100)
V	35 (12)	246 (17)	222 (21)	196 (96)	329 (3)	277 (8)	216 (13)	255 (16)	225 (40)	129 (6)	227 (14)	286 (130)	48 (6)	356 (34)
Cr	560 (270)	3120 (380)	795 (69)	2629 (1300)	7325 (560)	1365 (38)	1018 (52)	283 (16)	236 (85)	242 (10)	267 (24)	386 (90)	105 (22)	606 (46)
Ni	26 (10)	225 (57)	343 (150)	516 (180)	403 (23)	134 (8)	119 (7)	298 (16)	267 (120)	351 (310)	154 (49)	170 (87)	76 (22)	943 (91)
Rb		13 (16)	12.5 (3.5)	17.8 (17)	7.7 (4.9)	17.3 (1.4)	11.1 (1.5)	10.4 (1.3)	16.2 (4.4)	9.6 (1.3)	14 (2.7)	19.1 (18)	3.1 (0.22)	17.9 (2.8)
Sr	68 (25)	476 (73)	545 (41)	545 (260)	663 (55)	722 (22)	511 (22)	604 (32)	615 (48)	402 (24)	623 (35)	338 (130)	122 (4.6)	669 (65)
Y	3.7 (1.4)	25.6 (4.1)	25.2 (1.6)	18.8 (9.5)	19.5 (4.9)	24.3 (1.2)	25.2 (1.8)	22.7 (2)	27 (4.7)	19.2 (1.1)	25.3 (2)	24.3 (11)	4.1 (0.25)	28.1 (3.2)
Zr	33 (12)	186 (29)	157.1 (8.3)	146.5 (69)	149.9 (21)	174.4 (6.2)	158.2 (8.2)	153.9 (8)	189.6 (15)	127.9 (9.6)	174 (11)	203 (80)	37.5 (1.6)	182.9 (22)
Nb	6.8 (2.8)	49.4 (4.7)	25.1 (2.5)	32.9 (18)	37.2 (6.3)	42.3 (1.7)	29.4 (1.8)	31.3 (2.7)	35.6 (6.2)	24.7 (1.5)	34.9 (2.5)	38.2 (28)	10.4 (0.44)	39.8 (4.5)
Ba	36 (12)	231 (37)	158 (24)	300 (100)	279 (170)	269 (13)	164 (9)	214 (12)	229 (32)	132 (11)	224 (20)	184 (76)	73 (4)	265 (35)
La	5.7 (2)	34.3 (5.3)	21.6 (2.1)	26.3 (13)	18.4 (1.2)	31.5 (2)	23.7 (1.5)	22.6 (1.5)	26.2 (3.9)	18.8 (1.2)	26.9 (2.3)	25.2 (10)	7 (0.44)	27.7 (3.7)
Ce	10.5 (3.5)	67 (10)	42 (5.3)	49.8 (25)	54.6 (0.76)	62.3 (3.5)	47.2 (2.4)	48.2 (2.6)	51.5 (6.2)	37.2 (2.3)	58.8 (5.1)	64.2 (30)	13.2 (0.76)	65.5 (7.1)
Pr	1.3 (0.6)	8.1 (1.3)	6.7 (1.5)	5.9 (3.4)	8 (1.1)	8.5 (0.53)	6.4 (0.55)	6.6 (0.62)	7.9 (2.1)	5.1 (0.55)	7.8 (0.98)	7.5 (3)	1.6 (0.14)	8.2 (1.5)
Nd	5.1 (2.2)	36 (6.5)	25.7 (3.9)	31 (15)	30.1 (5.5)	36 (3)	28.3 (2.5)	27.9 (3.4)	31.1 (7.3)	21.9 (2)	31.6 (8.4)	34.7 (15)	6.7 (0.51)	33.7 (4)
Sm	0.9 (0.65)	6.5 (1.4)	4.9 (1.1)	6.9 (4.9)	7.7 (0.92)	6.8 (1.2)	5 (1.3)	6.3 (1.7)	5.7 (3.3)	4.6 (1)	6.3 (2.5)	7.5 (3.3)	1.3 (0.29)	6.7 (2.9)
Eu	0.5 (0.29)	1.8 (0.49)	2.1 (0.55)	1.4 (1)	1.8 (2.6)	2.2 (0.34)	2.2 (0.49)	1.7 (0.38)	2.3 (1.3)	1.5 (0.38)	2 (0.59)	1.9 (0.87)	0.4 (0.09)	2.1 (0.28)
Gd	1.1 (0.62)	6.6 (1.9)	7.3 (3.3)	4.4 (2.8)	4.9 (2.7)	6.4 (1.1)	6.8 (1.1)	5.1 (1.1)	4.5 (3.4)	4.8 (1.3)	7.2 (2.7)	6.7 (3.9)	1 (0.26)	8.6 (3.4)
Tb	0.1 (0.07)	0.9 (0.29)	0.8 (0.28)	0.8 (0.48)	0.2 (0.39)	0.9 (0.16)	1 (0.17)	0.6 (0.14)	1.1 (0.52)	0.8 (0.18)	0.9 (0.31)	1 (0.42)	0.1 (0.04)	0.8 (0.44)
Dy	1.2 (0.46)	5.7 (1.6)	3.5 (1)	3.8 (2.7)	4.3 (0.81)	5.2 (0.83)	5.6 (0.83)	4.6 (1.1)	6.1 (3.3)	4.2 (0.77)	5.2 (1.8)	4.6 (2.3)	0.8 (0.18)	6 (2.3)
Ho	0.2 (0.1)	0.8 (0.24)	1 (0.29)	0.8 (0.54)	0.8 (0.42)	1 (0.2)	1 (0.19)	0.6 (0.2)	0.8 (0.43)	0.8 (0.19)	1 (0.34)	0.6 (0.38)	0.1 (0.03)	1.1 (0.51)
Er	0.5 (0.44)	2.4 (0.82)	3.1 (0.93)	1.5 (1)	3.5 (7.5)	2.1 (0.34)	2.4 (0.49)	1.9 (0.56)	2.3 (2.2)	2.1 (0.76)	3.1 (1.1)	3.3 (2.2)	0.4 (0.14)	3.4 (0.76)
Tm	0 (0.05)	0.2 (0.07)	0.2 (0.16)	0.2 (0.17)	0 (0)	0.4 (0.1)	0.2 (0.09)	0.4 (0.15)	0.2 (0.24)	0.3 (0.12)	0.3 (0.13)	0.5 (0.33)	0.1 (0.02)	0.3 (0.2)
Yb	0.4 (0.39)	2.3 (1)	3.6 (2.1)	1.8 (1.3)	3.7 (0.45)	1.8 (0.61)	2.3 (0.82)	2 (0.87)	1.8 (1.2)	1.2 (0.52)	1.9 (0.93)	2.6 (3.1)	0.3 (0.12)	1.8 (0.45)
Lu	0.1 (0.06)	0.3 (0.13)	0.4 (0.28)	0.1 (0.16)	0.2 (0.36)	0.3 (0.1)	0.3 (0.12)	0.2 (0.13)	0.4 (0.13)	0.2 (0.1)	0.3 (0.12)	0.3 (0.25)	0.1 (0.02)	0.1 (0.15)
Hf	0.7 (0.42)	4.3 (0.94)	4.3 (2.8)	4.1 (2.6)	2.3 (1.3)	3.2 (0.65)	3.7 (0.77)	3.4 (1.1)	4.5 (2.9)	3.2 (0.8)	4.1 (1.4)	6.8 (4.1)	0.9 (0.17)	6.7 (2.1)
Ta	0.5 (0.2)	3.1 (0.69)	1.8 (0.45)	2.7 (1.4)	2 (2.2)	2.7 (0.3)	1.7 (0.38)	1.9 (0.4)	2.9 (0.87)	1.7 (0.26)	2.8 (0.65)	2.4 (1.2)	0.6 (0.1)	2.6 (0.82)
W	0.2 (0.14)	0.6 (0.38)	0.3 (0.33)	1.6 (1.3)	1.8 (3.7)	0.5 (0.2)	0.1 (0.11)	0.3 (0.26)	0.2 (0.29)	0.2 (0.18)	0.4 (0.29)	1 (0.66)	0.5 (0.12)	0.6 (0.51)
Pb	0.8 (0.33)	5 (1.1)	1.8 (1.2)	5.5 (2.6)	7.9 (4.9)	1.3 (0.22)	1.2 (0.32)	2.1 (0.4)	1.1 (0.49)	1.2 (0.29)	1.6 (0.67)	3.8 (1.7)	0.6 (0.11)	1.7 (0.81)
Th	0.6 (0.21)	3.1 (0.5)	1.8 (0.34)	2.6 (1.3)	2.2 (0.18)	3.1 (0.16)	2.3 (0.18)	2.2 (0.19)	2.8 (0.49)	2 (0.18)	3 (0.31)	2.1 (0.87)	0.7 (0.05)	3.1 (0.49)
U	0.1 (0.05)	0.8 (0.15)	0.4 (0.09)	0.6 (0.4)	0.5 (0.12)	0.7 (0.06)	0.5 (0.07)	0.5 (0.06)	0.5 (0.19)	0.4 (0.06)	0.6 (0.13)	0.7 (0.28)	0.2 (0.01)	0.7 (0.17)

Table 3-2: Trace element compositions of MIs (continued)

Northern Victoria Land													
Locality	Mount Morning	The Pleiades											
Host Lava	C88-89	12-19-01-3	12-19-01-3	12-19-01-3	12-19-01-3	12-19-01-3	12-19-01-3	12-19-01-3	12-19-01-3	12-19-01-3	12-19-01-3	12-19-01-3	12-19-01-3
Sample ID	c88-89_28_150	12-19-01-3_3	12-19-01-3_4	12-19-01-3_7	12-19-01-3_9	12-19-01-3_10	12_12-14_1_1_48	05-12_	05-12_	12-19-01_3_47	12-19-01_5_50	12-19-01_7_53	12-19-01_8_54
Li (ppm)	21 (2)			1 (0)	1 (0)	1 (0)	6 (1)	70 (5)	80 (9)	0 (0)	0 (0)	0 (0)	0 (0)
Ti	21700 (1800)	23400 (1800)	16690 (790)	1859 (90)	2023 (50)	1969 (45)	18170 (590)	13930 (410)	15200 (1300)	16390 (540)	18900 (1300)	18580 (840)	18660 (740)
V	268 (14)	320 (41)	275 (21)	29 (3)	27 (1)	30 (1)	220 (11)	118 (4)	103 (11)	120 (5)	311 (24)	295 (13)	318 (15)
Cr	1830 (130)	7600 (1100)	2080 (220)	1000 (480)	284 (7)	102 (4)	818 (37)	555 (24)	171 (41)	1512 (68)	494 (59)	970 (49)	943 (60)
Ni	407 (74)	1080 (140)	1730 (200)	45 (6)	33 (9)	18 (1)	71 (5)	127 (5)	153 (17)	106 (5)	192 (26)	502 (37)	551 (73)
Rb	22.2 (2.9)	35 (6.2)	6 (1.5)	1.7 (0.15)	2 (0.14)	1.9 (0.17)	13.1 (1.1)	39.9 (2.2)	40.7 (6.2)	41.4 (2.1)	16.2 (1.5)	16.4 (0.93)	16.6 (1.3)
Sr	743 (37)	963 (66)	643 (27)	66 (4.4)	89 (2.3)	75 (2.3)	714 (29)	947 (37)	987 (48)	833 (30)	664 (55)	704 (28)	706 (28)
Y	29.3 (1.9)	36.1 (3.3)	28.2 (3.1)	3 (0.19)	3.1 (0.13)	3.2 (0.17)	25.4 (1.5)	30.4 (1.8)	36.1 (3.8)	29.9 (1.5)	25.3 (2)	25.6 (2.4)	26.6 (1.7)
Zr	208 (11)	396 (37)	216 (18)	18.6 (0.99)	21.2 (0.62)	22.8 (0.74)	173.1 (8.8)	268 (10)	312 (25)	303.6 (9.4)	165 (13)	184 (10)	184.6 (9.2)
Nb	41 (2.8)	119 (11)	36.1 (4)	3.8 (0.28)	4.6 (0.18)	4.4 (0.17)	34.2 (2.7)	103.7 (4.9)	137 (21)	110.7 (5.9)	41.9 (4.3)	41.6 (2.5)	39.5 (2.8)
Ba	260 (18)	694 (60)	223 (20)	23 (2)	29 (1)	26 (1)	213 (23)	809 (37)	854 (75)	768 (35)	253 (25)	269 (18)	254 (13)
La	33.1 (1.6)	65.9 (5.8)	25.8 (3.5)	3 (0.24)	3.7 (0.16)	3.4 (0.13)	26.1 (1.7)	64.6 (3.4)	80.3 (7.2)	60.6 (2.7)	26.8 (1.9)	28.8 (1.3)	29.1 (1.5)
Ce	65.6 (3.3)	131 (13)	54 (3.9)	6.2 (0.59)	7.2 (0.25)	6.5 (0.24)	57.1 (5.5)	122.8 (6.2)	148 (15)	116.9 (5.9)	58.9 (5.4)	58.6 (2.7)	58.5 (3.6)
Pr	8.6 (0.94)	14.9 (2.4)	6.2 (1.2)	0.8 (0.07)	0.9 (0.05)	0.9 (0.06)	6.7 (0.74)	13.5 (0.96)	15.8 (1.6)	13.6 (0.84)	6.9 (0.91)	8.1 (0.75)	7.6 (0.66)
Nd	36.6 (4.1)	54.4 (8.1)	22.6 (5.8)	3.1 (0.39)	3.9 (0.31)	3.9 (0.24)	30.8 (4)	53.9 (3.9)	60 (7.1)	51.2 (3.2)	29.8 (4.8)	30.3 (3.2)	33.7 (3.5)
Sm	8.1 (1.8)	12.1 (4)	4.8 (2.7)	0.6 (0.12)	0.7 (0.1)	0.9 (0.13)	6.4 (1.6)	9.2 (1.4)	11.7 (2.9)	9.3 (1.5)	7.2 (1.3)	8.7 (2.2)	6.3 (1.6)
Eu	2.6 (0.69)	2.5 (0.83)	2.6 (0.4)	0.3 (0.06)	0.3 (0.05)	0.2 (0.04)	2.2 (0.42)	2.5 (0.35)	3 (0.66)	2.8 (0.32)	1.6 (0.25)	2.2 (0.48)	2.4 (0.55)
Gd	7.9 (2.1)	9.8 (3.1)	11.8 (5)	0.6 (0.16)	0.8 (0.13)	0.8 (0.12)	6.1 (1.4)	7.3 (0.89)	8.3 (2.5)	7.8 (1.2)	8 (1.7)	7.5 (2)	8.1 (2.2)
Tb	1 (0.19)	0.9 (0.4)	1 (0.46)	0.1 (0.03)	0.1 (0.03)	0.1 (0.03)	0.8 (0.18)	1.1 (0.13)	1.2 (0.33)	1.2 (0.22)	0.9 (0.31)	1 (0.24)	0.9 (0.25)
Dy	6 (1.4)	0 (1.7)	5.1 (2.1)	0.5 (0.14)	0.5 (0.09)	0.6 (0.1)	4.9 (0.74)	6.3 (0.96)	8.3 (2.8)	6.9 (1.2)	4.9 (1.3)	4.2 (0.94)	4 (0.99)
Ho	1.3 (0.26)	1.3 (0)	1.2 (0.54)	0.1 (0.03)	0.2 (0.02)	0.2 (0.03)	1 (0.14)	0.9 (0.11)	1.1 (0.35)	1.2 (0.15)	0.9 (0.21)	0.9 (0.2)	1.3 (0.26)
Er	3.7 (1.1)	2.8 (1.9)	4.2 (0.62)	0.2 (0.07)	0.3 (0.06)	0.3 (0.07)	2.4 (0.58)	3 (0.49)	3.1 (1)	2.8 (0.53)	2.7 (0.7)	1.9 (0.71)	3.8 (0.96)
Tm	0.4 (0.15)	0.4 (0)	0.2 (0.18)	0.1 (0.02)	0 (0.02)	0 (0.01)	0.3 (0.14)	0.4 (0.08)	0.5 (0.23)	0.3 (0.12)	0.3 (0.18)	0.5 (0.13)	0.2 (0.12)
Yb	2.6 (0.96)	3.7 (2)	2.2 (0.58)	0.3 (0.08)	0.3 (0.07)	0.3 (0.08)	2.6 (0.8)	2.7 (0.62)	3.2 (1.1)	2.6 (0.52)	1.6 (0.6)	1.6 (0.79)	1.8 (0.71)
Lu	0.3 (0.12)	0.1 (0.14)	0.4 (0.27)	0 (0.01)	0 (0.01)	0 (0.01)	0.4 (0.11)	0.4 (0.11)	0.9 (0.37)	0.4 (0.14)	0.3 (0.12)	0.3 (0.12)	0.5 (0.14)
Hf	6.2 (1.1)	7.3 (2.9)	6.4 (2.9)	0.6 (0.14)	0.5 (0.07)	0.6 (0.11)	5 (1.1)	5.8 (0.81)	5.1 (1.2)	5.7 (0.98)	4.4 (1.4)	4.2 (1)	4.6 (1.1)
Ta	2.6 (0.33)	6.9 (1.4)	2.7 (0.78)	0.3 (0.05)	0.3 (0.03)	0.3 (0.03)	2.2 (0.37)	5.5 (0.44)	7.3 (1.2)	6 (0.4)	2.7 (0.45)	2.5 (0.47)	2.7 (0.43)
W	0.5 (0.32)	2.8 (1.2)	1.9 (1.1)	0 (0.02)	0.1 (0.02)	0 (0.02)	1.1 (0.33)	0.9 (0.27)	1.2 (0.49)	1.1 (0.32)	0.4 (0.32)	0.5 (0.25)	0.3 (0.21)
Pb	1.7 (0.38)	8.7 (0)	3.1 (1.1)	0.2 (0.05)	0.2 (0.03)	0.2 (0.05)	2 (0.38)	4.3 (0.55)	5.5 (0.9)	5.8 (0.72)	1.6 (0.52)	1.2 (0.37)	1.8 (0.45)
Th	3.5 (0.22)	8.2 (0.96)	3 (0.57)	0.3 (0.02)	0.4 (0.02)	0.3 (0.02)	2.6 (0.28)	7 (0.53)	9.3 (1.9)	6.7 (0.51)	2.9 (0.33)	3 (0.24)	3.2 (0.21)
U	0.8 (0.1)	2.1 (0.27)	0.7 (0.13)	0.1 (0.01)	0.1 (0.01)	0.1 (0.01)	0.6 (0.12)	1.4 (0.09)	1.9 (0.64)	1.6 (0.11)	0.7 (0.11)	0.7 (0.08)	0.7 (0.08)
Li (ppm)	16 (2)			1 (0)	1 (0)	1 (0)	6 (1)	61 (5)	61 (9)	0 (0)	0 (0)	0 (0)	0 (0)
Ti	16724 (1800)	18437 (1800)	14648 (790)	1754 (90)	1880 (50)	1969 (45)	18170 (590)	12144 (410)	11679 (1300)	16390 (540)	18378 (1300)	17376 (840)	17812 (740)
V	207 (14)	252 (41)	241 (21)	27 (3)	25 (1)	30 (1)	220 (11)	103 (4)	79 (11)	120 (5)	302 (24)	276 (13)	304 (15)
Cr	1410 (130)	5988 (1100)	1826 (220)	944 (480)	264 (7)	102 (4)	818 (37)	484 (24)	131 (41)	1512 (68)	480 (59)	907 (49)	900 (60)
Ni	314 (74)	851 (140)	1518 (200)	42 (6)	30 (9)	18 (1)	71 (5)	111 (5)	118 (17)	106 (5)	187 (26)	469 (37)	526 (73)
Rb	17.1 (2.9)	27.6 (6.2)	5.3 (1.5)	1.6 (0.15)	1.9 (0.14)	1.9 (0.17)	13.1 (1.1)	34.8 (2.2)	31.3 (6.2)	41.4 (2.1)	15.8 (1.5)	15.4 (0.93)	15.8 (1.3)
Sr	573 (37)	759 (66)	564 (27)	62 (4.4)	82 (2.3)	75 (2.3)	714 (29)	826 (37)	758 (48)	833 (30)	646 (55)	658 (28)	674 (28)
Y	22.6 (1.9)	28.4 (3.3)	24.8 (3.1)	2.9 (0.19)	2.9 (0.13)	3.2 (0.17)	25.4 (1.5)	26.5 (1.8)	27.7 (3.8)	29.9 (1.5)	24.6 (2)	23.9 (2.4)	25.4 (1.7)
Zr	160.3 (11)	312 (37)	189.6 (18)	17.6 (0.99)	19.7 (0.62)	22.8 (0.74)	173.1 (8.8)	233.6 (10)	239.7 (25)	303.6 (9.4)	160.4 (13)	172.1 (10)	176.2 (9.2)
Nb	31.6 (2.8)	93.8 (11)	31.7 (4)	3.5 (0.28)	4.3 (0.18)	4.4 (0.17)	34.2 (2.7)	90.4 (4.9)	105.3 (21)	110.7 (5.9)	40.7 (4.3)	38.9 (2.5)	37.7 (2.8)
Ba	200 (18)	547 (60)	196 (20)	22 (2)	27 (1)	26 (1)	213 (23)	705 (37)	656 (75)	768 (35)	246 (25)	252 (18)	242 (13)
La	25.5 (1.6)	51.9 (5.8)	22.6 (3.5)	2.9 (0.24)	3.4 (0.16)	3.4 (0.13)	26.1 (1.7)	56.3 (3.4)	61.7 (7.2)	60.6 (2.7)	26.1 (1.9)	26.9 (1.3)	27.8 (1.5)
Ce	50.6 (3.3)	103.2 (13)	47.4 (3.9)	5.9 (0.59)	6.7 (0.25)	6.5 (0.24)	57.1 (5.5)	107.1 (6.2)	113.7 (15)	116.9 (5.9)	57.3 (5.4)	54.8 (2.7)	55.8 (3.6)
Pr	6.6 (0.94)	11.7 (2.4)	5.4 (1.2)	0.7 (0.07)	0.8 (0.05)	0.9 (0.06)	6.7 (0.74)	11.8 (0.96)	12.1 (1.6)	13.6 (0.84)	6.7 (0.91)	7.6 (0.75)	7.3 (0.66)
Nd	28.2 (4.1)	42.9 (8.1)	19.8 (5.8)	2.9 (0.39)	3.6 (0.31)	3.9 (0.24)	30.8 (4)	47 (3.9)	46.1 (7.1)	51.2 (3.2)	29 (4.8)	28.3 (3.2)	32.2 (3.5)
Sm	6.2 (1.8)	9.5 (4)	4.2 (2.7)	0.6 (0.12)	0.6 (0.1)	0.9 (0.13)	6.4 (1.6)	8 (1.4)	9 (2.9)	9.3 (1.5)	7 (1.3)	8.1 (2.2)	6 (1.6)
Eu	2 (0.69)	2 (0.83)	2.3 (0.4)	0.2 (0.06)	0.3 (0.05)	0.2 (0.04)	2.2 (0.42)	2.2 (0.35)	2.3 (0.66)	2.8 (0.32)	1.5 (0.25)	2.1 (0.48)	2.3 (0.55)
Gd	6.1 (2.1)	7.7 (3.1)	10.4 (5)	0.6 (0.16)	0.7 (0.13)	0.8 (0.12)	6.1 (1.4)	6.4 (0.89)	6.4 (2.5)	7.8 (1.2)	7.8 (1.7)	7 (2)	7.7 (2.2)
Tb	0.7 (0.19)	0.7 (0.4)	0.9 (0.46)	0.1 (0.03)	0.1 (0.03)	0.1 (0.03)	0.8 (0.18)	0.9 (0.13)	0.9 (0.33)	1.2 (0.22)	0.9 (0.31)	0.9 (0.24)	0.9 (0.25)
Dy	4.6 (1.4)	0 (1.7)	4.5 (2.1)	0.5 (0.14)	0.5 (0.09)	0.6 (0.1)	4.9 (0.74)	5.4 (0.96)	6.4 (2.8)	6.9 (1.2)	4.8 (1.3)	3.9 (0.94)	3.8 (0.99)
Ho	1 (0.26)	1 (0)	1.1 (0.54)	0.1 (0.03)	0.2 (0.02)	0.2 (0.03)	1 (0.14)	0.7 (0.11)	0.8 (0.35)	1.2 (0.15)	0.8 (0.21)	0.8 (0.2)	1.3 (0.26)
Er	2.9 (1.1)	2.2 (1.9)	3.7 (0.62)	0.2 (0.07)	0.3 (0.06)	0.3 (0.07)	2.4 (0.58)	2.6 (0.49)	2.4 (1)	2.8 (0.53)	2.6 (0.7)	1.8 (0.71)	3.6 (0.96)
Tm	0.3 (0.15)	0.3 (0)	0.1 (0.18)	0 (0.02)	0 (0.02)	0 (0.01)	0.3 (0.14)	0.3 (0.08)	0.3 (0.23)	0.3 (0.12)	0.3 (0.18)	0.4 (0.13)	0.2 (0.12)
Yb	2 (0.96)	2.9 (2)	1.9 (0.58)	0.3 (0.08)	0.3 (0.07)	0.3 (0.08)	2.6 (0.8)	2.4 (0.62)	2.5 (1.1)	2.6 (0.52)	1.6 (0.6)	1.5 (0.79)	1.7 (0.71)
Lu	0.2 (0.12)	0.1 (0.14)	0.3 (0.27)	0 (0.01)	0 (0.01)	0 (0.01)	0.4 (0.11)	0.4 (0.11)	0.7 (0.37)	0.4 (0.14)	0.3 (0.12)	0.2 (0.12)	0.4 (0.14)
Hf	4.8 (1.1)	5.8 (2.9)	5.6 (2.9)	0.5 (0.14)	0.4 (0.07)	0.6 (0.11)	5 (1.1)	5.1 (0.81)	3.9 (1.2)	5.7 (0.98)	4.3 (1.4)	3.9 (1)	4.4 (1.1)
Ta	2 (0.33)	5.4 (1.4)	2.4 (0.78)	0.3 (0.05)	0.3 (0.03)	0.3 (0.03)	2.2 (0.37)	4.8 (0.44)	5.6 (1.2)	6 (0.4)	2.6 (0.45)	2.3 (0.47)	2.6 (0.43)
W	0.4 (0.32)	2.2 (1.2)	1.7 (1.1)	0 (0.02)	0 (0.02)	0 (0.02)	1.1 (0.33)	0.8 (0.27)	0.9 (0.49)	1.1 (0.32)	0.4 (0.32)	0.4 (0.25)	0.2 (0.21)
Pb	1.3 (0.38)	6.9 (0)	2.7 (1.1)	0.2 (0.05)	0.2 (0.03)	0.2 (0.05)	2 (0.38)	3.7 (0.55)	4.2 (0.9)	5.8 (0.72)	1.5 (0.52)	1.1 (0.37)	1.7 (0.45)
Th	2.7 (0.22)	6.4 (0.96)	2.7 (0.57)	0.3 (0.02)	0.3 (0.02)	0.3 (0.02)	2.6 (0.28)	6.1 (0.53)	7.1 (1.9)	6.7 (0.51)	2.8 (0.33)	2.8 (0.24)	3 (0.21)
U	0.6 (0.1)	1.7 (0.27)	0.6 (0.13)	0.1 (0.01)	0.1 (0.01)	0.1 (0.01)	0.6 (0.12)	1.2 (0.09)	1.5 (0.64)	1.6 (0.11)	0.7 (0.11)	0.6 (0.08)	0.7 (0.08)

Table 3-2: Trace element compositions of MIs (continued)

Northern Victoria L	Northern Victoria Land							Marie Byrd Land					
Locality	The Pleiades			Shield Nunatak				Mount Berlin					
Host Lava	12-19-01-3	12-19-01-3	12-19-01-3	NV-13A	NV-13A	NV-13A	NV-13A	BN-14D	BN-14D	BN-14D	BN-14D	39B	39B
Sample ID	12-19-01_11_60	12-19-01_13_88	12-19-01_14_89	NV13A_9_74	NV13A_14_80	NV13A_20_95	NV13A_22_97	BN14D_1_91	BN14D_2_92	BN14D_3_98	BND14D_5_101	39b_1_29	39b_14_45
Li (ppm)	0 (0)	0 (0)	0 (0)	0 (0)	0 (0)	0 (0)	0 (0)	0 (0)	0 (0)	0 (0)	0 (0)	35 (25)	28 (15)
Ti	20020 (720)	2100 (150)	17110 (950)	17370 (870)	21400 (1200)	18900 (1300)	18300 (1300)	22100 (1000)	12280 (610)	5400 (240)	22200 (1300)	12400 (1900)	11100 (1800)
V	330 (18)	35 (2)	295 (17)	249 (14)	224 (18)	223 (19)	253 (20)	343 (24)	260 (14)	28 (2)	461 (25)	313 (58)	342 (90)
Cr	1051 (45)	326 (21)	2200 (140)	2990 (120)	164 (12)	85 (12)	174 (17)	1280 (110)	348 (20)	19 (2)	1750 (120)	660 (350)	1100 (510)
Ni	271 (29)	57 (7)	147 (8)	453 (47)	233 (34)	1680 (120)	149 (11)	956 (89)	729 (38)	315 (21)	120 (8)	6000 (3100)	7000 (4800)
Rb	12.7 (0.8)	2.4 (0.32)	15.4 (1.3)	14 (1.6)	9.6 (1)	16.3 (2.4)	17.8 (2.1)	18.2 (1.6)	0.8 (0.36)	12.1 (1.2)	2.4 (0.39)	26.6 (5.4)	30 (11)
Sr	310 (13)	80 (4.7)	488 (24)	472 (22)	1083 (79)	543 (39)	470 (26)	758 (32)	206 (11)	575 (22)	292 (14)	334 (72)	337 (71)
Y	28.8 (1.9)	3 (0.25)	19.9 (1.5)	21.5 (1.8)	34.5 (2.1)	25.5 (2.7)	23.7 (1.6)	26.9 (2.3)	22 (1.8)	135 (6.5)	23.7 (1.4)	19.6 (4.3)	18.3 (3.9)
Zr	167.4 (6.3)	25.4 (1.4)	148.4 (7.5)	164.5 (8.6)	220 (11)	189 (17)	152.8 (9.6)	199 (11)	254 (13)	148.7 (9)	101.3 (6.2)	137 (31)	115 (28)
Nb	24.2 (1.4)	5 (0.28)	30.3 (2)	41.9 (2.6)	63 (5.2)	48.2 (5.3)	45.8 (3.7)	45.8 (3.2)	12.7 (1.3)	25.2 (1.6)	19.5 (1.1)	33.9 (7.4)	35 (5.9)
Ba	173 (9)	35 (3)	217 (17)	201 (15)	237 (22)	241 (20)	269 (17)	306 (22)	30 (4)	365 (24)	147 (8)	207 (39)	176 (42)
La	19.8 (1.2)	3.9 (0.24)	21.9 (1.4)	26.1 (1.7)	59.8 (4.4)	31.3 (3.1)	44.5 (3)	31.7 (1.9)	18.8 (1.1)	200.6 (9.7)	18 (1.2)	21.1 (5.1)	19.2 (4.8)
Ce	41.9 (2.3)	8.8 (0.65)	50.4 (2.7)	55.3 (4.7)	89.3 (8.1)	59.3 (4.9)	93.5 (7.2)	64.9 (4.1)	48.4 (2.8)	473 (27)	33.9 (2.2)	44.7 (9.6)	45.5 (9.9)
Pr	6.2 (0.51)	1 (0.09)	5.6 (0.34)	6.6 (0.59)	10.6 (1.1)	7 (1.2)	9.5 (0.73)	7.8 (0.67)	4.5 (0.64)	72.1 (4)	4.4 (0.43)	5.5 (1.4)	4.7 (1.4)
Nd	24.7 (3)	3.9 (0.37)	24.3 (2.1)	26.6 (2.9)	43.9 (6)	28.5 (5.3)	35 (2.8)	33 (4.2)	31.8 (4.8)	337 (22)	19.7 (2.3)	21.7 (6)	19.1 (5.8)
Sm	4.9 (0.92)	0.9 (0.19)	4.4 (0.73)	5.2 (1.1)	7.4 (1.9)	7.2 (2.7)	7 (1.4)	6.5 (1.9)	5.6 (1.4)	64.4 (4.2)	4.4 (1)	5.1 (1.7)	3.9 (1.7)
Eu	2.4 (0.23)	0.3 (0.07)	1.9 (0.28)	2 (0.48)	2.6 (0.59)	2.7 (1)	1.7 (0.29)	2 (0.63)	1.6 (0.27)	19.5 (1.5)	1.6 (0.34)	1.3 (0.57)	1.2 (0.44)
Gd	7.4 (1.9)	1 (0.18)	4.8 (1.1)	6.7 (1.5)	8.1 (1.9)	8.9 (3.8)	5.5 (1.5)	5.7 (1.4)	6.1 (2.4)	61.3 (5.6)	5.9 (1.4)	4.9 (2.1)	4.4 (1.7)
Tb	1 (0.28)	0.1 (0.03)	0.8 (0.18)	0.7 (0.17)	1.3 (0.4)	0.7 (0.35)	1 (0.19)	0.8 (0.36)	0.8 (0.26)	7.7 (0.74)	1 (0.22)	0.6 (0.2)	0.6 (0.27)
Dy	4.5 (0.96)	0.5 (0.14)	34.6 (0.82)	10 (1)	7.4 (1.2)	4.7 (2.1)	5 (1.1)	7 (1.5)	4.3 (1.2)	6 (2.7)	4.5 (0.73)	4.5 (1.4)	2.6 (1)
Ho	1.1 (0.21)	0.1 (0.04)	0.7 (0.68)	0.7 (0.52)	1.5 (0.34)	0.7 (0.26)	0.8 (0.21)	0.7 (0.28)	0.8 (0.27)	5.4 (0.3)	1.1 (0.24)	0.7 (0.35)	0.6 (0.23)
Er	3.6 (0.95)	0.3 (0.12)	1.9 (0.54)	1.9 (0.76)	2.9 (1.3)	2.3 (1.6)	2.6 (0.52)	2.2 (1.2)	2.5 (0.62)	11.4 (1.7)	2.8 (0.63)	1.4 (0.67)	1.5 (0.79)
Tm	0.3 (0.12)	0 (0.02)	0.2 (0.26)	0.3 (0.21)	0.3 (0.14)	0.2 (0.18)	0.3 (0.1)	0.4 (0.22)	0.5 (0.23)	1.2 (0.17)	0.3 (0.12)	0.3 (0.14)	0.2 (0.13)
Yb	1.1 (0.82)	0.1 (0.07)	1.7 (0.58)	1.4 (0.63)	2 (0.86)	1.7 (1.6)	2.4 (0.91)	0.6 (0.66)	3.2 (0.56)	5.3 (1.1)	1.6 (0.59)	1.8 (0.94)	1.5 (0.86)
Lu	0.3 (0.12)	0 (0.03)	0.3 (0.12)	0.2 (0.12)	0.5 (0.18)	0.6 (0.38)	0.2 (0.1)	0.4 (0.2)	0.3 (0.15)	0.9 (0.26)	0.3 (0.08)	0.3 (0.24)	0.1 (0.08)
Hf	5.2 (1)	0.6 (0.13)	3.8 (0.94)	4.2 (1.1)	5.6 (1.3)	5 (2.1)	3 (0.77)	4.7 (1.3)	7.9 (1.3)	3.4 (0.75)	2.8 (0.69)	3.3 (1.1)	3.2 (1.1)
Ta	1.9 (0.31)	0.3 (0.06)	2.1 (0.34)	2.5 (0.32)	4.1 (0.64)	3.6 (0.95)	3.1 (0.43)	2.8 (0.51)	0.8 (0.23)	1.5 (0.36)	1.2 (0.22)	1.9 (0.64)	1.6 (0.67)
W	0.2 (0.15)	0 (0.02)	0.2 (0.1)	0.9 (0.49)	1.2 (0.58)	0.9 (0.74)	0.3 (0.18)	0.3 (0.19)	0.7 (0.31)	0.3 (0.18)	0.2 (0.19)	0.2 (0.13)	0.3 (0.2)
Pb	1.4 (0.37)	0.3 (0.05)	1.6 (0.42)	1.1 (1.4)	2.7 (1.1)	1.9 (0.37)	1.5 (0.36)	2.4 (0.76)	1.8 (0.79)	3.6 (0.76)	3.2 (0.42)	1.4 (0.66)	1.2 (0.9)
Th	1.8 (0.13)	0.4 (0.04)	2.3 (0.18)	3.1 (0.26)	4.7 (0.51)	3.4 (0.48)	3.7 (0.29)	3.4 (0.33)	1.2 (0.17)	9.6 (0.47)	1.3 (0.14)	2.5 (0.66)	1.9 (0.57)
U	0.3 (0.05)	0.1 (0.01)	0.6 (0.07)	0.7 (0.1)	1.3 (0.16)	0.7 (0.15)	0.9 (0.09)	0.9 (0.12)	0.2 (0.06)	1.8 (0.13)	0.4 (0.04)	0.6 (0.15)	0.6 (0.16)
Li (ppm)	0 (0)	0 (0)	0 (0)	0 (0)	0 (0)	0 (0)	0 (0)	0 (0)	0 (0)	0 (0)	0 (0)	34 (25)	26 (15)
Ti	20020 (720)	2100 (150)	17110 (950)	17370 (870)	20180 (1200)	15982 (1300)	18300 (1300)	20324 (1000)	10861 (610)	5400 (240)	22200 (1300)	12185 (1900)	10419 (1800)
V	330 (18)	35 (2)	295 (17)	249 (14)	211 (18)	189 (19)	253 (20)	315 (24)	230 (14)	28 (2)	461 (25)	308 (58)	321 (90)
Cr	1051 (45)	326 (21)	2200 (140)	2990 (120)	155 (12)	72 (12)	174 (17)	1177 (110)	308 (20)	19 (2)	1750 (120)	649 (350)	1033 (510)
Ni	271 (29)	57 (7)	147 (8)	453 (47)	220 (34)	1421 (120)	149 (11)	879 (89)	645 (38)	315 (21)	120 (8)	5896 (3100)	6571 (4800)
Rb	12.7 (0.8)	2.4 (0.32)	15.4 (1.3)	14 (1.6)	9.1 (1)	13.8 (2.4)	17.8 (2.1)	16.7 (1.6)	0.7 (0.36)	12.1 (1.2)	2.4 (0.39)	26.1 (5.4)	28.2 (11)
Sr	310 (13)	80 (4.7)	488 (24)	472 (22)	1021 (79)	459 (39)	470 (26)	697 (32)	182 (11)	575 (22)	292 (14)	328 (72)	316 (71)
Y	28.8 (1.9)	3 (0.25)	19.9 (1.5)	21.5 (1.8)	32.5 (2.1)	21.6 (2.7)	23.7 (1.6)	24.7 (2.3)	19.5 (1.8)	135 (6.5)	23.7 (1.4)	19.3 (4.3)	17.2 (3.9)
Zr	167.4 (6.3)	25.4 (1.4)	148.4 (7.5)	164.5 (8.6)	207.5 (11)	159.8 (17)	152.8 (9.6)	183 (11)	224.7 (13)	148.7 (9)	101.3 (6.2)	134.6 (31)	107.9 (28)
Nb	24.2 (1.4)	5 (0.28)	30.3 (2)	41.9 (2.6)	59.4 (5.2)	40.8 (5.3)	45.8 (3.7)	42.1 (3.2)	11.2 (1.3)	25.2 (1.6)	19.5 (1.1)	33.3 (7.4)	32.9 (5.9)
Ba	173 (9)	35 (3)	217 (17)	201 (15)	223 (22)	204 (20)	269 (17)	281 (22)	27 (4)	365 (24)	147 (8)	203 (39)	165 (42)
La	19.8 (1.2)	3.9 (0.24)	21.9 (1.4)	26.1 (1.7)	56.4 (4.4)	26.5 (3.1)	44.5 (3)	29.2 (1.9)	16.6 (1.1)	200.6 (9.7)	18 (1.2)	20.7 (5.1)	18 (4.8)
Ce	41.9 (2.3)	8.8 (0.65)	50.4 (2.7)	55.3 (4.7)	84.2 (8.1)	50.1 (4.9)	93.5 (7.2)	59.7 (4.1)	42.8 (2.8)	473 (27)	33.9 (2.2)	43.9 (9.6)	42.7 (9.9)
Pr	6.2 (0.51)	1 (0.09)	5.6 (0.34)	6.6 (0.59)	10 (1.1)	5.9 (1.2)	9.5 (0.73)	7.1 (0.67)	4 (0.64)	72.1 (4)	4.4 (0.43)	5.4 (1.4)	4.4 (1.4)
Nd	24.7 (3)	3.9 (0.37)	24.3 (2.1)	26.6 (2.9)	41.4 (6)	24.1 (5.3)	35 (2.8)	30.3 (4.2)	28.1 (4.8)	337 (22)	19.7 (2.3)	21.3 (6)	17.9 (5.8)
Sm	4.9 (0.92)	0.9 (0.19)	4.4 (0.73)	5.2 (1.1)	7 (1.9)	6.1 (2.7)	7 (1.4)	6 (1.9)	5 (1.4)	64.4 (4.2)	4.4 (1)	5 (1.7)	3.7 (1.7)
Eu	2.4 (0.23)	0.3 (0.07)	1.9 (0.28)	2 (0.48)	2.4 (0.59)	2.3 (1)	1.7 (0.29)	1.8 (0.63)	1.4 (0.27)	19.5 (1.5)	1.6 (0.34)	1.3 (0.57)	1.1 (0.44)
Gd	7.4 (1.9)	1 (0.18)	4.8 (1.1)	6.7 (1.5)	7.6 (1.9)	7.5 (3.8)	5.5 (1.5)	5.2 (1.4)	5.4 (2.4)	61.3 (5.6)	5.9 (1.4)	4.8 (2.1)	4.1 (1.7)
Tb	1 (0.28)	0.1 (0.03)	0.8 (0.18)	0.7 (0.17)	1.2 (0.4)	0.6 (0.35)	1 (0.19)	0.8 (0.36)	0.7 (0.26)	7.7 (0.74)	1 (0.22)	0.5 (0.2)	0.5 (0.27)
Dy	4.5 (0.96)	0.5 (0.14)	34.6 (0.82)	10 (1)	7 (1.2)	4 (2.1)	5 (1.1)	6.4 (1.5)	3.8 (1.2)	6 (2.7)	4.5 (0.73)	4.4 (1.4)	2.4 (1)
Ho	1.1 (0.21)	0.1 (0.04)	0.7 (0.68)	0.7 (0.52)	1.4 (0.34)	0.6 (0.26)	0.8 (0.21)	0.7 (0.28)	0.7 (0.27)	5.4 (0.3)	1.1 (0.24)	0.7 (0.35)	0.6 (0.23)
Er	3.6 (0.95)	0.3 (0.12)	1.9 (0.54)	1.9 (0.76)	2.7 (1.3)	1.9 (1.6)	2.6 (0.52)	2 (1.2)	2.2 (0.62)	11.4 (1.7)	2.8 (0.63)	1.4 (0.67)	1.4 (0.79)
Tm	0.3 (0.12)	0 (0.02)	0.2 (0.26)	0.3 (0.21)	0.3 (0.14)	0.1 (0.18)	0.3 (0.1)	0.3 (0.22)	0.4 (0.23)	1.2 (0.17)	0.3 (0.12)	0.2 (0.14)	0.2 (0.13)
Yb	1.1 (0.82)	0.1 (0.07)	1.7 (0.58)	1.4 (0.63)	1.9 (0.86)	1.4 (1.6)	2.4 (0.91)	0.5 (0.66)	2.8 (0.56)	5.3 (1.1)	1.6 (0.59)	1.7 (0.94)	1.4 (0.86)
Lu	0.3 (0.12)	0 (0.03)	0.3 (0.12)	0.2 (0.12)	0.4 (0.18)	0.5 (0.38)	0.2 (0.1)	0.4 (0.2)	0.3 (0.15)	0.9 (0.26)	0.3 (0.08)	0.3 (0.24)	0.1 (0.08)
Hf	5.2 (1)	0.6 (0.13)	3.8 (0.94)	4.2 (1.1)	5.3 (1.3)	4.2 (2.1)	3 (0.77)	4.3 (1.3)	7 (1.3)	3.4 (0.75)	2.8 (0.69)	3.2 (1.1)	3 (1.1)
Ta	1.9 (0.31)	0.3 (0.06)	2.1 (0.34)	2.5 (0.32)	3.8 (0.64)	3.1 (0.95)	3.1 (0.43)	2.5 (0.51)	0.7 (0.23)	1.5 (0.36)	1.2 (0.22)	1.8 (0.64)	1.5 (0.67)
W	0.2 (0.15)	0 (0.02)	0.2 (0.1)	0.9 (0.49)	1.1 (0.58)	0.8 (0.74)	0.3 (0.18)	0.2 (0.19)	0.6 (0.31)	0.3 (0.18)	0.2 (0.19)	0.2 (0.13)	0.2 (0.2)
Pb	1.4 (0.37)	0.3 (0.05)	1.6 (0.42)	1.1 (1.4)	2.5 (1.1)	1.6 (0.37)	1.5 (0.36)	2.2 (0.76)	1.6 (0.79)	3.6 (0.76)	3.2 (0.42)	1.4 (0.66)	1.1 (0.9)
Th	1.8 (0.13)	0.4 (0.04)	2.3 (0.18)	3.1 (0.26)	4.4 (0.51)	2.8 (0.48)	3.7 (0.29)	3.1 (0.33)	1.1 (0.17)	9.6 (0.47)	1.3 (0.14)	2.5 (0.66)	1.8 (0.57)
U	0.3 (0.05)	0.1 (0.01)	0.6 (0.07)	0.7 (0.1)	1.2 (0.16)	0.6 (0.15)	0.9 (0.09)	0.8 (0.12)	0.2 (0.06)	1.8 (0.13)	0.4 (0.04)	0.6 (0.15)	0.6 (0.16)

Table 3-2: Trace element compositions of MIs (continued)

	Marie Byrd Land			
Locality	Mount Waesche			
Host Lava	39B	39B	39B	39B
Sample ID	39b_19_52	39b_27_62	67-39b_2_44	67-39b_3_45
Li (ppm)	5 (1)	6 (1)	6 (1)	4 (1)
Ti	13470 (260)	15600 (480)	13360 (380)	11960 (310)
V	164 (5)	191 (7)	231 (10)	208 (6)
Cr	107 (6)	133 (6)	79 (4)	74 (3)
Ni	102 (3)	125 (4)	117 (4)	121 (7)
Rb	10.5 (0.86)	10.8 (0.94)	19.6 (1.4)	17.5 (1)
Sr	340 (10)	358 (14)	532 (16)	495 (13)
Y	22.6 (1.5)	24.4 (1.5)	24.9 (1.2)	23.4 (1)
Zr	135.1 (5.2)	138.5 (6)	192.2 (7.1)	167.3 (4.9)
Nb	22.8 (1.2)	22 (1.2)	44 (2)	42.2 (2.1)
Ba	222 (10)	188 (8)	345 (17)	318 (12)
La	21.3 (0.98)	20.1 (1.1)	34.9 (1.2)	32.5 (1.4)
Ce	45.1 (2)	44.6 (2)	69.1 (2.8)	64.8 (2.3)
Pr	6.2 (0.61)	6.4 (0.46)	7.9 (0.46)	7.4 (0.35)
Nd	26.4 (2.4)	28.3 (2.1)	29 (2.1)	29 (1.9)
Sm	4.9 (1.3)	4.7 (1)	5.4 (0.92)	6.1 (1)
Eu	1.7 (0.44)	1.8 (0.25)	1.8 (0.33)	1.6 (0.23)
Gd	4.9 (0.66)	5.7 (0.9)	5.6 (1.2)	5.4 (0.86)
Tb	0.7 (0.14)	0.9 (0.15)	0.9 (0.13)	0.8 (0.13)
Dy	4.4 (0.85)	4.5 (0.65)	4.5 (0.7)	4.4 (0.62)
Ho	0.9 (0.16)	0.8 (0.17)	0.9 (0.18)	0.9 (0.12)
Er	2.2 (0.5)	2.4 (0.47)	2.4 (0.44)	2.8 (0.44)
Tm	0.3 (0.11)	0.5 (0.13)	0.3 (0.08)	0.3 (0.08)
Yb	2.1 (0.69)	2.1 (0.56)	2.2 (0.64)	2.6 (0.66)
Lu	0.3 (0.13)	0.3 (0.1)	0.3 (0.08)	0.3 (0.07)
Hf	3.4 (0.68)	2.9 (0.54)	3.2 (0.46)	4.1 (0.58)
Ta	1.4 (0.23)	1.4 (0.16)	2.7 (0.26)	2.5 (0.27)
W	0.2 (0.15)	0.1 (0.091)	0.5 (0.2)	0.4 (0.16)
Pb	1.5 (0.34)	1.4 (0.28)	1.9 (0.36)	1.9 (0.3)
Th	1.8 (0.17)	1.5 (0.11)	2.9 (0.12)	2.9 (0.15)
U	0.4 (0.04)	0.4 (0.053)	0.7 (0.05)	0.7 (0.05)
Li (ppm)	5 (1)	6 (1)	6 (1)	4 (1)
Ti	13470 (260)	15600 (480)	13360 (380)	11960 (310)
V	164 (5)	191 (7)	231 (10)	208 (6)
Cr	107 (6)	133 (6)	79 (4)	74 (3)
Ni	102 (3)	125 (4)	117 (4)	121 (7)
Rb	10.5 (0.86)	10.8 (0.94)	19.6 (1.4)	17.5 (1)
Sr	340 (10)	358 (14)	532 (16)	495 (13)
Y	22.6 (1.5)	24.4 (1.5)	24.9 (1.2)	23.4 (1)
Zr	135.1 (5.2)	138.5 (6)	192.2 (7.1)	167.3 (4.9)
Nb	22.8 (1.2)	22 (1.2)	44 (2)	42.2 (2.1)
Ba	222 (10)	188 (8)	345 (17)	318 (12)
La	21.3 (0.98)	20.1 (1.1)	34.9 (1.2)	32.5 (1.4)
Ce	45.1 (2)	44.6 (2)	69.1 (2.8)	64.8 (2.3)
Pr	6.2 (0.61)	6.4 (0.46)	7.9 (0.46)	7.4 (0.35)
Nd	26.4 (2.4)	28.3 (2.1)	29 (2.1)	29 (1.9)
Sm	4.9 (1.3)	4.7 (1)	5.4 (0.92)	6.1 (1)
Eu	1.7 (0.44)	1.8 (0.25)	1.8 (0.33)	1.6 (0.23)
Gd	4.9 (0.66)	5.7 (0.9)	5.6 (1.2)	5.4 (0.86)
Tb	0.7 (0.14)	0.9 (0.15)	0.9 (0.13)	0.8 (0.13)
Dy	4.4 (0.85)	4.5 (0.65)	4.5 (0.7)	4.4 (0.62)
Ho	0.9 (0.16)	0.8 (0.17)	0.9 (0.18)	0.9 (0.12)
Er	2.2 (0.5)	2.4 (0.47)	2.4 (0.44)	2.8 (0.44)
Tm	0.3 (0.11)	0.5 (0.13)	0.3 (0.08)	0.3 (0.08)
Yb	2.1 (0.69)	2.1 (0.56)	2.2 (0.64)	2.6 (0.66)
Lu	0.3 (0.13)	0.3 (0.1)	0.3 (0.08)	0.3 (0.07)
Hf	3.4 (0.68)	2.9 (0.54)	3.2 (0.46)	4.1 (0.58)
Ta	1.4 (0.23)	1.4 (0.16)	2.7 (0.26)	2.5 (0.27)
W	0.2 (0.15)	0.1 (0.09)	0.5 (0.2)	0.4 (0.16)
Pb	1.5 (0.34)	1.4 (0.28)	1.9 (0.36)	1.9 (0.3)
Th	1.8 (0.17)	1.5 (0.11)	2.9 (0.12)	2.9 (0.15)
U	0.4 (0.04)	0.4 (0.05)	0.7 (0.05)	0.7 (0.05)

CHAPTER IV

GEOCHEMICAL PERSPECTIVES ON THE AFRICAN LITHOSPHERE DYNAMICS: INSIGHTS FROM MANTLE XENOLITHS

Abstract

Mantle xenoliths from contrasting geodynamic environments in the East African Rift System (EARS) provide new perspectives on mantle dynamics from plume to rift settings. This study presents new major oxide, trace element, and Sr-Nd-Hf-Pb isotopic data for mantle xenoliths from the southern Main Ethiopian Rift (Dillo and Megado), located at a key juncture between the MER, the Turkana Depression, and the Kenya Rift. Also reported are new Nd-Hf-Pb isotopic data for mantle xenolith clinopyroxene from Neogene-Quaternary alkaline lavas overlying the continental flood basalts of the Ethiopian Plateau (Injibara and Dedessa). Together, the xenolith suite testifies to complex, multistage development of the sub-continental lithospheric mantle (SCLM) beneath both environments. Lu-Hf isotopic systematics attest to ancient melt depletion events during continental assembly that have been variably overprinted by diverse metasomatic enrichment processes. In the southern MER, these metasomatic agents were likely subalkaline asthenospheric melts in Dillo and low-volume alkaline silicate and carbonatitic melts in Megado, and provide evidence for a new model of the development of high-μ (μ = U/Pb) Pb isotopic signatures in the southern MER and northern Kenya by carbonatitic metasomatism of SCLM during ancient subduction. In the Ethiopian Plateau, metasomatic agents were likely subalkaline melts related to CFB magmas of the Afar Plume. The preservation of heterogeneous

domains on both large and small (km) spatial scales strongly supports the view that the SCLM is an important long-lived reservoir of recycled components that contribute to rift development.

1. Introduction

Mantle xenoliths entrained in rising mafic magmas serve as a powerful tool for investigating the composition and evolution of the lithospheric mantle. Episodes of melt extraction, thermal perturbation, and metasomatic modification may be recorded in the mantle xenolith chemical, textural, and mineralogical suite, and numerous studies have established that ultramafic xenoliths from continental settings in particular testify to the complex tectonic and chemical histories of the uppermost mantle during continental evolution (e.g., among others, Pearson et al., 2003; Reisberg et al., 2004; Lee et al., 2010; Bodinier and Godard, 2013; Choi and Mukasa, 2014). Of various processes that may influence the upper mantle beneath continents, metasomatic modification has been identified as a key agent for fertilization of the mantle with volatiles and generation of chemically heterogeneous mantle domains characterized by lower solidus temperatures (Bailey, 1982; Hofmann, 1997; Pearson et al., 2003). In regions where continental magmatism is accompanied by lithospheric extension, understanding the xenolith record of the nature and provenance of easily fusible components is especially critical due to their unique perspective on volatile recycling within the solid Earth as a whole, as well as the ability of volatilized, metasomatized lithologies to enhance mantle melting (e.g., Hirschmann et al., 2003; Dasgupta et al., 2007; Pilet et al., 2008). Elucidating whether metasomatic silicate, carbonatitic, or aqueous fluids originate during ancient subduction or orogenic events, or are imposed from melts generated in the sublithospheric mantle, is therefore key to unraveling both the history and role of the sub-continental lithospheric mantle (SCLM) in the geodynamics of ongoing volcanic and tectonic activity in continental rifts.

The East African Rift System (EARS), one of the largest continental rift systems on Earth, is characterized by both depressed, narrow rift basins related to extensional tectonics and topographically high domes in Kenya and the Afar region of Ethiopia (Figure 4-1). In light of evidence for elevated mantle temperatures (Rooney et al., 2012a), flood basalt volcanism (Thorpe and Smith, 1974; Baker et al., 1996; Hofmann et al., 1997; Pik et al., 1999; Beccaluva et al., 2009; Natali et al., 2011; 2016), and anomalous low-density mantle structures that potentially extend beyond depths of 1100 km (Gurnis et al., 2000), one or more ascending mantle plumes have been implicated beneath East Africa as a major driving force behind ongoing tectonic and magmatic activity (Ebinger and Sleep, 1998; Rogers et al., 2006; Corti, 2009). Plume-linked magmatism has been better constrained in the northern parts of the rift system, where pre-rift eruption of continental flood basalts during the Oligocene are chronologically and isotopically consistent with active upwelling of geochemically distinct deep mantle material (Ebinger and Sleep, 1998; Pik et al., 1999; Corti, 2009). Plume-related magmas may mix with input from continental lithosphere and are subject to increasing interactions with normal mantle asthenosphere with distance from the plume head centered in the Afar region of Ethiopia (Ebinger and Sleep, 1998; Rooney et al., 2012a), and ambiguous geophysical links between deep plume structures and the lateral extent and depth of low-velocity mantle beneath more distal portions of the rift (e.g., Hansen et al., 2012) raise questions regarding the extent of deep plume influence in more southern reaches of the rift system. This study reports new geochemical data on mantle xenoliths from the southern portion of the Main Ethiopian Rift (MER), where a transition from dominantly deep mantle plume contributions to shallower mantle upwelling and alkaline metasomatic processes is believed to occur (Furman et al., 2004, 2006a; Beccaluva et al., 2011; Furman et al., 2016). Additionally, new Nd, Hf, and Pb isotopic data for xenoliths from

Injibara and Dedessa on the Ethiopian plateau are reported, and together provide new geochemical constraints on the processes affecting the SCLM in plume versus rift settings of the Afro-Arabian region.

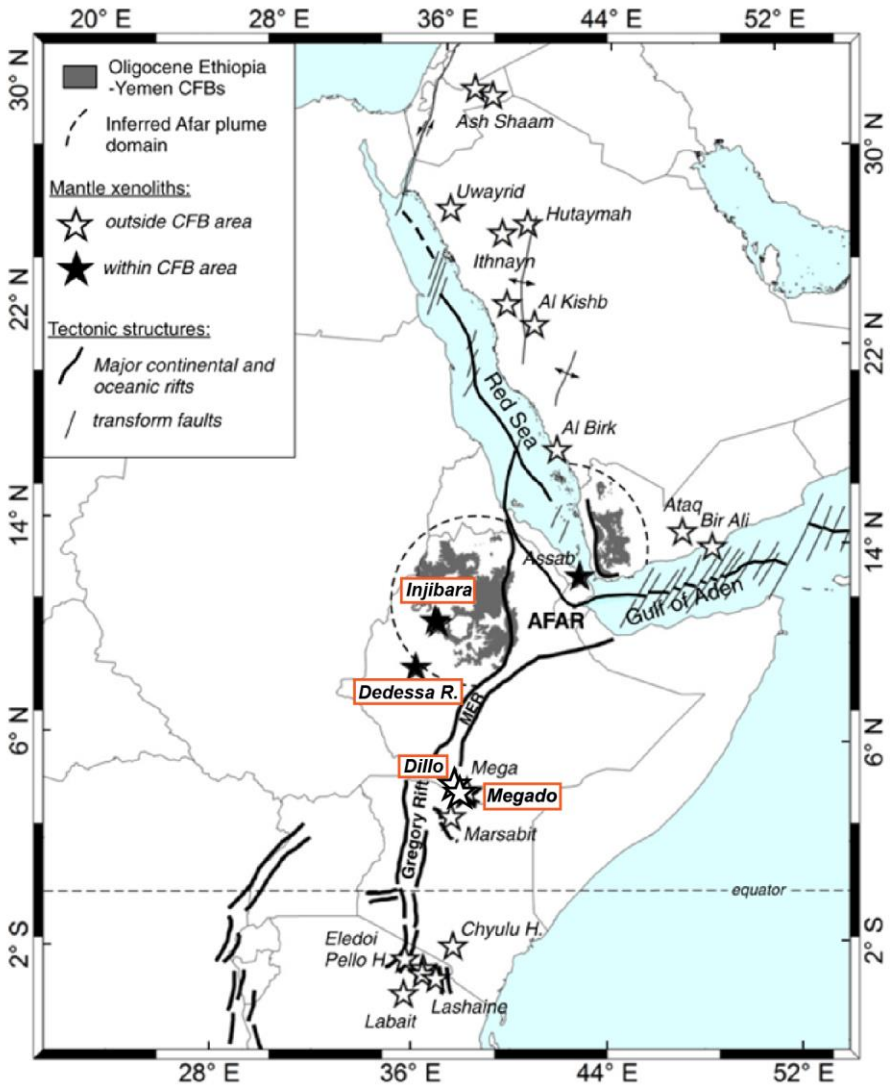

Figure 4-1. Regional sketch map of the East African Rift System (modified from Sgualdo et al., 2015) showing xenolith occurrences throughout the Afro-Arabian domain. Sample locations of rift (Dillo and Megado) and plateau (Injibara and Dedessa) xenoliths in this study are labeled in red outlined boxes. Other xenolith localities discussed in this study are shown for reference.

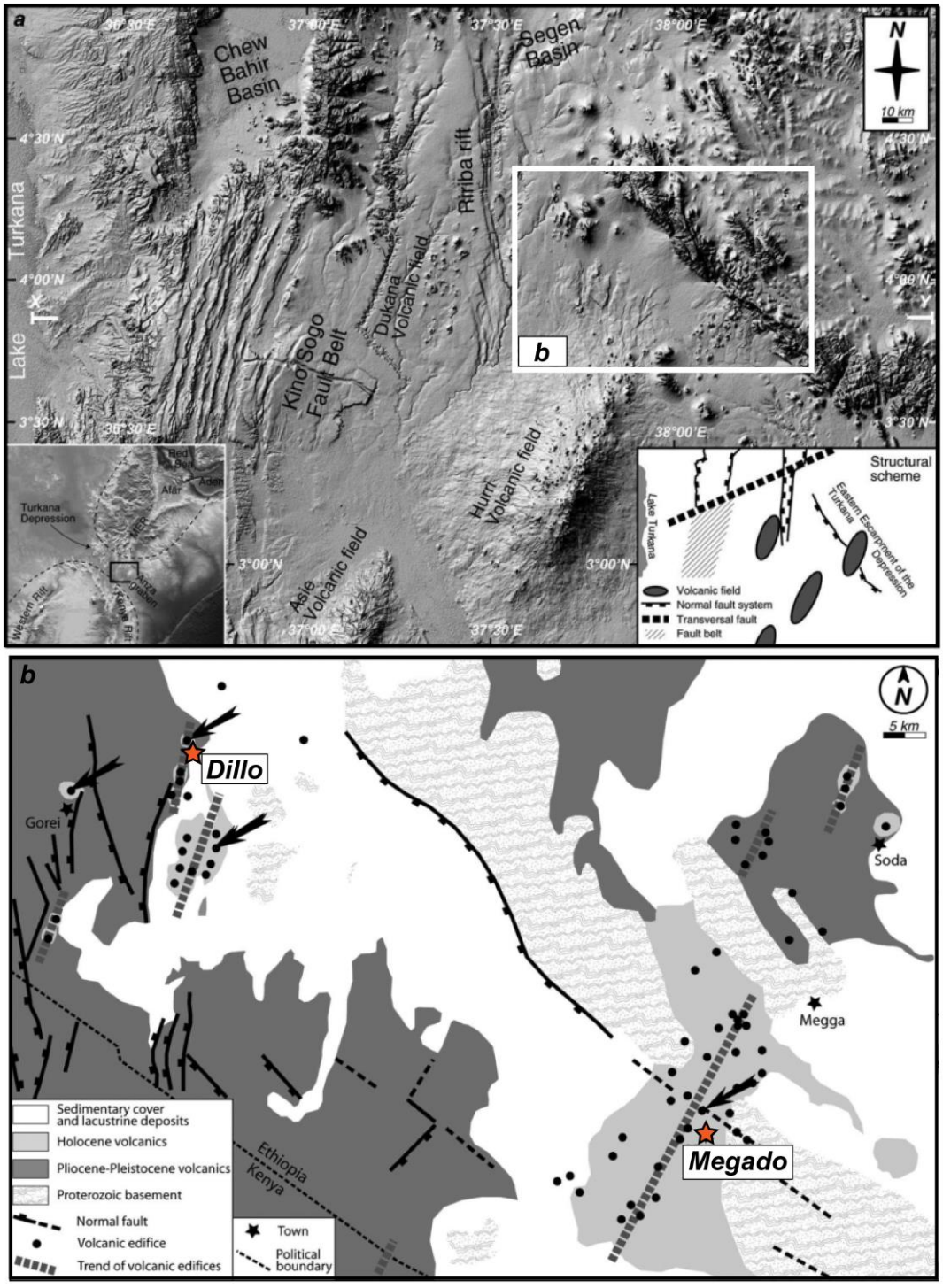

Figure 4-2. (**a**) Digital elevation model of the topography of the eastern Southern Main Ethiopian Rift (MER) and Turkana depression of the East African Rift System (modified from Orlando et al., 2006). Bottom left inset shows the Turkana depression in the larger context of the EARS, with the Ethiopian (northern) and Kenyan (southern) plume-related domes delineated by dashed lines. MER = Main Ethiopian Rift. (**b**) Schematic of the major structural features shown on the map and the locations of Dillo and Megado, marked by red stars.

Mantle xenoliths erupted in mafic lavas from two localities in the southern portion of the MER, Megado and Dillo, represent a key area at the junction between the southern Ethiopian Rift and the northern Kenya Rift (Figure 4-2). In this area, Pleistocene-Holocene volcanic products overlie ~1 Ma basaltic lava flows related to the Huri Hills volcanism in northern Kenya (Figure 4-2; Class et al., 1994; Orlando et al., 2006). The collected mantle xenoliths span the compositional range including spinel lherzolites, harzburgites, dunites, and olivine-websterites. A significant number samples contain amphibole – an important hydrous metasomatic phase – either disseminated in the peridotite matrix, interstitial to olivine and clinopyroxene, or associated with reaction rims. Previous geochemical investigations of peridotites from Megado and the neighboring volcanic province of Mega (e.g., Orlando et al., 2006; Beccaluva et al., 2011; Bianchini et al., 2014) found that, in contrast to more northern Ethiopian plateau xenoliths that have been pervasively metasomatized by subalkaline melts derived from the Afar plume, the trace elemental and isotopic affinities of the mantle beneath the southern MER indicate metasomatism by alkaline agents during passive mantle upwelling unrelated to the Afar plume. Orlando et al. (2006) argue that pyroxenite mantle xenoliths observed in Dillo likely represent crystal cumulates segregated from these metasomatizing alkaline melts on the basis of their major oxide and trace elemental compositions, but an alternative explanation invokes recycled subducted ocean lithosphere in the generation of pyroxenite in the Afro-Arabian domain (e.g., Sgualdo et al., 2015). Notably, heterogeneous Re-Os and Lu-Hf isotopic signatures have been observed in Mega peridotites (respectively Reisberg et al., 2004; Bianchini et al., 2014), and are interpreted to indicate that thermochemically unaltered sections of ancient (~2 Ga) lithospheric mantle persist beneath the southern MER, a key finding for the development of geodynamic

models of the East African mantle structure and evolution. Expanding the available isotopic information for Megado and Dillo, as well as plateau xenoliths from Injibara and Dedessa (previously studied by Beccaluva et al., 2011), is crucial to developing a time-integrated perspective on the thermochemical perturbations that have occurred during the long-term evolution of the mantle beneath the East Africa.

1.1 Geologic setting

Xenoliths hosted by Neogene-Quaternary alkaline lavas from distinct Ethiopian volcanic regions provide a diverse perspective of the nature of the sub-continental lithospheric mantle (SCLM) across ~1000 km of distance (Figure 4-2). Samples from the Northern Ethiopian Plateau (Gojam) or close to its southwestern border (Dedessa River) sample the boundary of a region dominated by voluminous continental flood basalts (CFB) extruded mainly during the Oligocene impingement of the Afar Plume to build up a topographically high plateau (Hofmann et al., 1997) extending into Yemen prior to dissection by the opening of the Red Sea and Gulf of Aden. Farther to the south, the Main Ethiopian Rift (MER) is a key tectonomagmatic province in the East African Rift System that connects the Afar Depression and the Red Sea - Gulf of Aden rifts to the north with the Turkana depression and the Kenya Rift to the south (Figures 4-1, 4-2). The MER region is characterized by a series of NE to SW-trending active rift segments accommodating E-W and ESE-WNW extension between the Nubian plate and Somalian protoplate (Chu and Gordon, 1999). Sample localities of Dillo and Megado are located in the Southern MER, where a broad, ~300-km-wide diffusely rifted zone characterized by basin and range topography occurs due to interactions between faults of the MER and the N-S trending faults of the Kenya Rift (Bonini et al., 2005). In this region, earlier Cretaceous – Paleogene NW-SE trending faults related to extension in the Anza graben (Vetel and LeGall, 2006) are

juxtaposed with Cenozoic N-S- faults of the EARS (Davidson and Rex, 1980; Ebinger et al., 2000), lending considerable structural complexity to the diffusely rifted zone.

The Southern MER hosts some of the oldest volcanic rocks recorded in the MER, and date back to an early phase of basaltic volcanic activity initiating at 45 Ma that was followed by a second basaltic phase beginning in the early Miocene (Ebinger et al., 1993). Volcanic activity occurs along NNE to NE-trending volcanic fields and edifices including maar craters and cinder cones. The volcanic products are dominantly alkaline basic basalts, and occurrences of entrained mantle xenolith are well-documented (e.g., Bedini et al., 1997; Orlando et al., 2006; Beccaluva et al., 2011). Both mantle xenoliths from Dillo and Megado were collected from pyroclastic deposits.

2. Samples and methods

To provide a new geochemical perspective on the contrasting processes that have affected the lithospheric mantle beneath the Ethiopian Plateau and the southern MER, this study presents new Nd-Hf-Pb isotopic data for Injibara and Dedessa plateau peridotites that have been previously investigated by Beccaluva et al. (2011), as well as whole rock and clinopyroxene geochemistry for new southern MER peridotite and pyroxenite localities in Dillo and Megado. A total of 64 mantle xenoliths from Dillo and 76 from Megado were processed for this study. Fresh, unaltered portions of each sample were crushed and powdered in an agate mill, then measured for major oxides and select trace elements (Ba, Co, Cr, Cu, Ga, Hf, La, Nb, Ni, Pb, Sc, Sr, V, Y, Zn, and Zr) using the ARL Advant'X X-ray fluorescence (XRF) spectrometer at the Department of Physics and Earth Sciences at the University of Ferrara using the procedures described in Sgualdo et al. (2015). Accuracy and precision are generally better than 10% for all elements above 10 ppm. Mineral compositions were obtained for thin sections at the CNR-IGG

Institute of Padova using a Cameca SX-50 electron microprobe fitted with three wavelength dispersive spectrometers, and following the techniques described in Sgualdo et al. (2015) and Natali et al. (2016). Analyses were carried out using a 15 kV accelerating voltage and a 20 nA current.

Of the total sample suite, 24 samples were selected for more detailed geochemical analysis of mantle xenolith clinopyroxene. Hand-picked clinopyroxene were mounted in epoxy and polished in preparation for Li-U trace element analyses, which were performed using a Photon Machines 193 nm Excimer laser ablation platform and a NuAttoM HR single-collector ICP-MS at the University of New Hampshire. Analyses were conducted with a 40µm spot size, 6.75 J/cm^2 fluence, and a 4 Hz rep rate. Raw data were processed in Iolite (Paton et al., 2011) using ^{43}Ca (as determined from electron microprobe CaO measurements) as an internal standard. Instrumental drift was corrected by bracketing unknowns with the ML3B-G glass standard using reference values from Jochum et al. (2005). Replicate measurements of glass standards KL2-G and StHs6/80g performed throughout analytical runs indicate that trace elements are accurate to 10% or better (Jochum et al., 2005). For Hf-Nd-Pb-Sr isotopic analyses, aliquots of 200 – 400 mg of picked clinopyroxene were leached in hot (120°C) 6N HCl to remove surface contamination (e.g., Wittig et al., 2006) following techniques described in Blichert-Toft and Albarede (2009). Subsequent leached residues were purified for Nd, Hf, and Pb using the procedures described in Sgualdo et al. (2015) and for Sr as described in Bryce et al. (2005). Sr, Nd, Hf, and Pb isotopic measurements for Dillo and Megado samples, as well as Sr for Injibara and Dedessa samples, were performed on the NuPlasma II multicollector inductively-coupled plasma mass spectrometer (MC-ICP-MS) at the University of New Hampshire. Standard reference materials JNdi, JMC-475, and NIST SRM 987 were performed throughout the Nd, Hf,

and Sr analytical runs to both monitor instrument performance and correct for instrumental drift (using the standard bracketing techniques described in Albarède et al., 2004), and yielded average values of $^{143}Nd/^{144}Nd = 0.512115 \pm 0.000008$ (2σ, n = 28), $^{176}Hf/^{177}Hf = 0.282163 \pm 0.000003$ (2σ, n = 12), and $^{87}Sr/^{86}Sr = 0.710249 \pm 0.000022$ (2σ, n = 18). Additional corrections for Rb and Kr interferences during the Sr isotope analyses were performed following the procedure adapted from Konter and Storm (2014). Procedural blanks were ~30 pg for Hf and Nd and ~400 pg for Sr, abundances irrelevant to the amount of material processes for analyses. Isotope standards for analyses conducted at UNH are reported in Appendix 3.

Injibara and Dedessa xenoliths received the same chemical treatment described above, but were measured for Pb, Nd, and Hf isotopes on the Nu Plasma 500 HR multiple-collector inductively coupled plasma mass spectrometer (MC-ICP-MS) at the École Normale Supérieure in Lyon. Instrumental mass fractionation was corrected relative to $^{179}Hf/^{177}Hf = 0.7325$ and $^{146}Nd/^{144}Nd = 0.7219$ using an exponential law, and instrument performance was assessed by analysis of the JMC-475 Hf and Rennes in-house Nd standards for Hf and Nd, respectively. The JMC-475 Hf standard, run throughout the analytical session (n= 16), yielded $^{176}Hf/^{177}Hf = 0.282166 \pm 0.000012$ (2σ), identical within error to the accepted value of 0.282163 ± 0.000009 (Blichert-Toft et al., 1997). Accordingly no corrections were applied to the Hf isotopic data. Total procedural Hf blanks were less than 30 pg. BCR-1 processed with the same chemical procedure gave 0.512646 ± 0.000011 (2σ), similar to the recommended value from the GEOREM database (Jochum et al., 2005). The Rennes in- house Nd standard run throughout the analytical session (n =16) gave $^{143}Nd/^{144}Nd=0.511968\pm0.000013$ (2σ), well within analytical uncertainty of previously reported means of 0.511961 ± 0.000013 (Chauvel and Blichert-Toft,

2001), thus requiring no further corrections to the Nd isotopic data. Total procedural Nd blanks were less than 30 pg.

Pb isotopic measurements also were carried out on the Nu Plasma 500 HR MC-ICP-MS at the Ecole Normale Supérieure in Lyon for Injibara and Dedessa xenolith clinopyroxene and on the NuPlasma II at UNH for the Dillo and Megado xenolith clinopyroxene. Instrumental mass fractionation was corrected via Tl normalization as described in White et al. (2000), and ratios were additionally adjusted for instrumental drift and accuracy using the sample-standard bracketing technique described in Albarède et al. (2004) and the NIST SRM values reported in Eisele et al. (2003). For the Lyon analytical runs, eight replicates of NIST SRM 981 run alongside samples yielded averages (with 2σ external precision) of $^{208}Pb/^{204}Pb = 36.728 \pm 0.024$, $^{207}Pb/^{204}Pb = 15.498 \pm 0.011$ and $^{206}Pb/^{204}Pb = 16.941 \pm 0.012$. Total procedural Pb blanks were less than 100 pg for the plateau samples. For the Dillo and Megado rift samples analyzed at UNH, 12 replicate measurements of NIST SRM-981 yielded average values of $^{208}Pb/^{204}Pb = 36.726 \pm 0.002$, $^{207}Pb/^{204}Pb = 15.498 \pm 0.001$ and $^{206}Pb/^{204}Pb = 16.941 \pm 0.001$, and procedural blanks were less than 50 pg.

3. Results

3.1 Petrographic features and mineral chemistry of mantle xenoliths

Xenoliths from plateau localities of Injibara and Dedessa are represented by mainly protogranular peridotites (sp-lherzolites and sp-harzburgites) and spinel-olivine websterites. Full details on their textural and mineralogical features are provided in Beccaluva et al. (2011). Rift xenoliths from Dillo and Megado are represented by spinel (sp)-lherzolites, sp-harzburgites, sp- and garnet pyroxenites (Figure 4-3). Using the nomenclature of Harte (1977), the Dillo peridotites generally exhibit medium- to coarse-grained, protogranular to equigranular textures,

with variable extents of recrystallization indicated by 120° triple junctions at grain boundaries (Figure 4-4). Olivines are typically coarse, with Fo between 89.4 and 89.9 in lherzolites, and do not show evidence for extensive deformation. Coarse orthopyroxenes (up to 2 mm in size) often have exsolution lamellae with clinopyroxene. Medium- to fine-grained clinopyroxene sometimes display orthopyroxene exsolution lamellae and have Mg# between 90.0 and 91.3 and Cr# between 5.4 and 7.9. Dark amphiboles are pargasitic in composition. Reaction rims with frothy textures consisting of secondary olivine and pyroxene microcrystals are present in some samples (Figure 4-4b). Brown, lobate spinels are often interstitial, and rare, medium- to fine-grained pleochroic amphiboles are observed. In contrast, Megado peridotites exhibit protogranular to porphyroclastic textures characterized by coarse, deformed olivines and undeformed smaller neoblasts. The large, lobate olivines have Fo contents between 88.9 and 89.6, and exhibit kink-banding in the most deformed samples (Figure 4-4c). Orthopyroxenes are coarse (up to 1 mm) and occasionally contain clinopyroxene exsolution lamellae. Clinopyroxene Mg# varies from 91.2 to 91.6 and Cr# from 6.5 to 7.0. Eroded, lobate spinels are often found concurrently with secondary olivine and pyroxene microcrystals. Among the Megado harzburgites, textures are typically protogranular and medium- to fine-grained, with rare interstitial clinopyroxene with Mg# ranging from 93.3 to 94.4 and Cr# between 12.5 and 17.9.

Pyroxenites from both rift sample localities are classified as olivine-websterites and websterites (Figure 4-3) and are largely coarse-grained and protogranular, and characterized by the paucity of olivine. Very large pyroxenes (up to 5 mm in diameter) often contain mutual exsolution lamellae between clinopyroxene and orthopyroxene, although these features are less common in the Megado pyroxenites. Among the Megado olivine-websterites, clinopyroxene exhibit a Mg# of 90.7, and Cr# ranges from 4.5 to 4.8, whereas orthopyroxenes range from 89.7

to 90.4 and 3.1, respectively. One unusual sample from Megado, MG3-15, is classified as an amphibole-gabbro and is characterized by the presence of plagioclase, clinopyroxene, hornblende, and rare phlogopite.

Thermobarometric estimates of existing studies of peridotite and pyroxenite mantle xenoliths from the same sample localities in the southern MER (Orlando et al., 2006; Meshesha et al., 2011; Alemayehu et al., 2016) indicate equilibration temperatures of 950 – 1020°C and pressures of 13 – 14 kbar and for Dillo peridotites and 10 – 13 kbar for Megado peridotites. Alemayehu et al. (2016) did not find evidence for a systematic pressure-temperature difference between harzburgite and lherzolite units, which argues against lithological stratification in this region. For xenoliths from the Ethiopian Plateau, pressures of 9 – 12.5 kbar and 930 – 1050°C have been calculated for large equilibrated phenocrysts (Beccaluva et al., 2011).

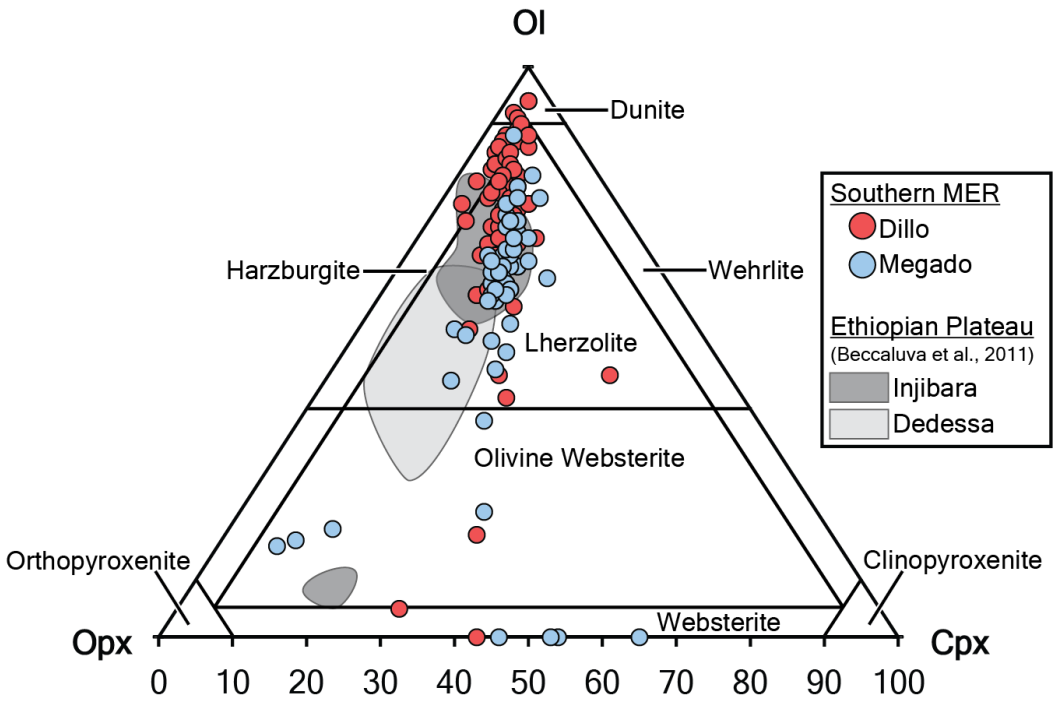

Figure 4-3. Modal classification diagram showing the composition of Dillo and Megado mantle xenoliths based on olivine-orthopyroxene-clinopyroxene modal abundances. Mineral modal abundances were obtained by least squares mass balance calculations between whole rock and mineral major oxide compositions given in Table 4-1. Grey fields indicate the compositions Injibara and Dedessa xenoliths (from Beccaluva et al., 2011).

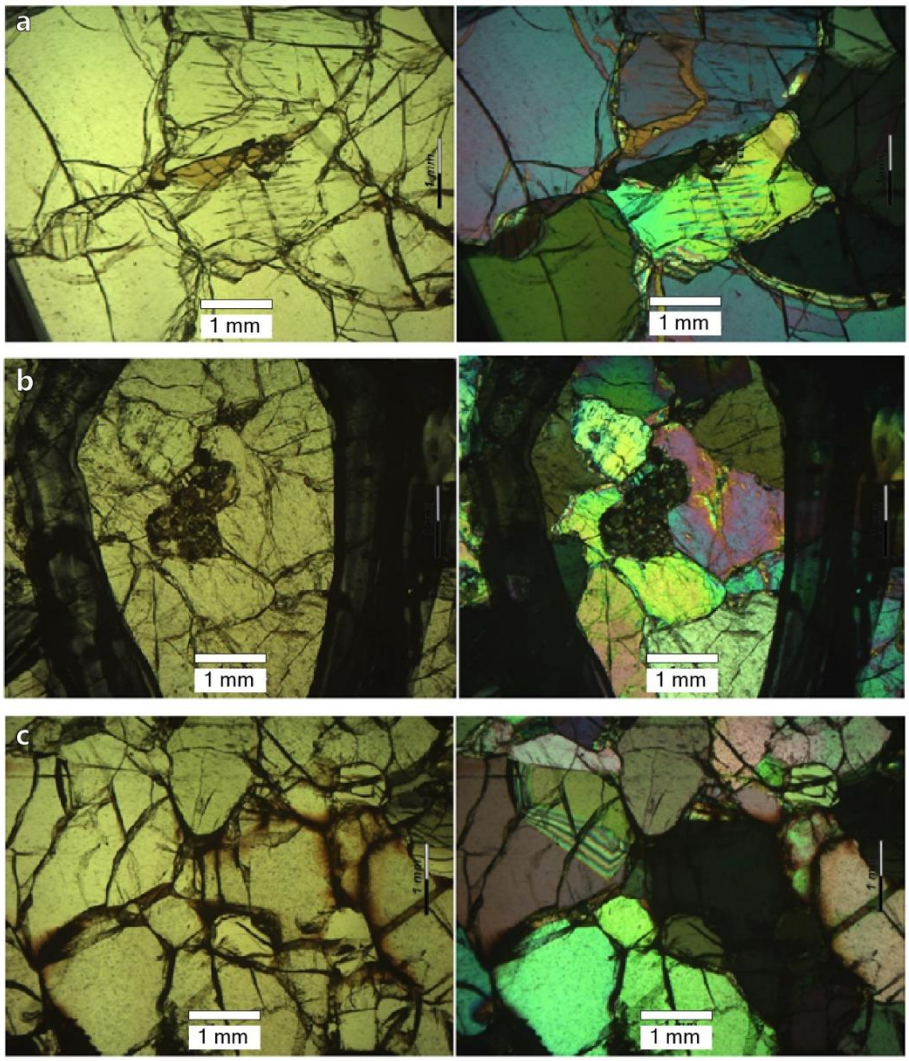

Figure 4-4. Photomicrographs of Dillo and Megado xenoliths (courtesy of Gianluca Bianchini) showing common petrographic textures. (a) Dillo lherzolite demonstrating partial metasomatic transformation of pyroxene into pargasitic amphibole. (b) Reaction patch in a Dillo lherzolite containing microcrystalline secondary olivine, spinel, and pyroxene. (c) Megado dunite with kink-banding in olivines that are altered to iddingsite at their borders.

3.2 Whole rock chemistry of xenoliths

The major oxide compositions of Dillo and Megado xenoliths exhibits marked compositional continuity, and are shown alongside the compositions of plateau xenoliths from Injibara and Dedessa studied by Beccaluva et al. (2011) in Figure 4-5. Peridotites from both southern MER sample localities define continuous trends of decreasing SiO_2, CaO, Al_2O_3, Na_2O, and TiO_2 with increasing MgO, Ni, and proportion of olivine, indicative of increasingly

refractory compositions. These overall trends correspond well with those expected for melt extraction (Niu, 1997) or, alternatively, re-fertilization by upwelling mantle melts (e.g., Le Roux et al., 2007; Bodinier and Godard, 2013). Superimposed on these relatively continuous trends are systematic compositional differences apparent between xenoliths from each locality. For example, Dillo peridotites generally occupy ranges lower in MgO and SiO_2, but higher in TiO_2, compared to those from Megado and the nearby Mega, as well as higher Al_2O_3 and CaO in comparison to the plateau xenoliths (Beccaluva et al., 2011). Additionally, pyroxenites from both southern MER localities are distinct from the peridotites, exhibiting higher Al_2O_3, SiO_2, CaO, TiO_2, and lower Ni. Their compositions generally agree with those of plateau pyroxenites (Beccaluva et al., 2011). For the limited whole rock trace element information available, distinctive trends in rare-earth element (REE) distribution patterns are apparent. Using La/Y to parameterize LREE/HREE enrichment, Megado peridotites exhibit a large range in values (La/Y = 2 – 40) that generally increase and exhibit greater La/Y variability with decreasing modal clinopyroxene, suggesting the degree of LREE enrichment increases as samples become increasingly refractory and progressively depleted in clinopyroxene. These observations are consistent with similar trends observed in Mega (Beccaluva et al., 2011) that have been attributed to enhanced permeability of refractory mantle domains to enriched metasomatizing agents (Toramaru and Fujii, 1986; Beccaluva et al., 2011). In contrast, Dillo peridotites and pyroxenites exhibit a more restricted and less enriched range of La/Y values (0.2 – 6) that do not appear to correlate with modal clinopyroxene.

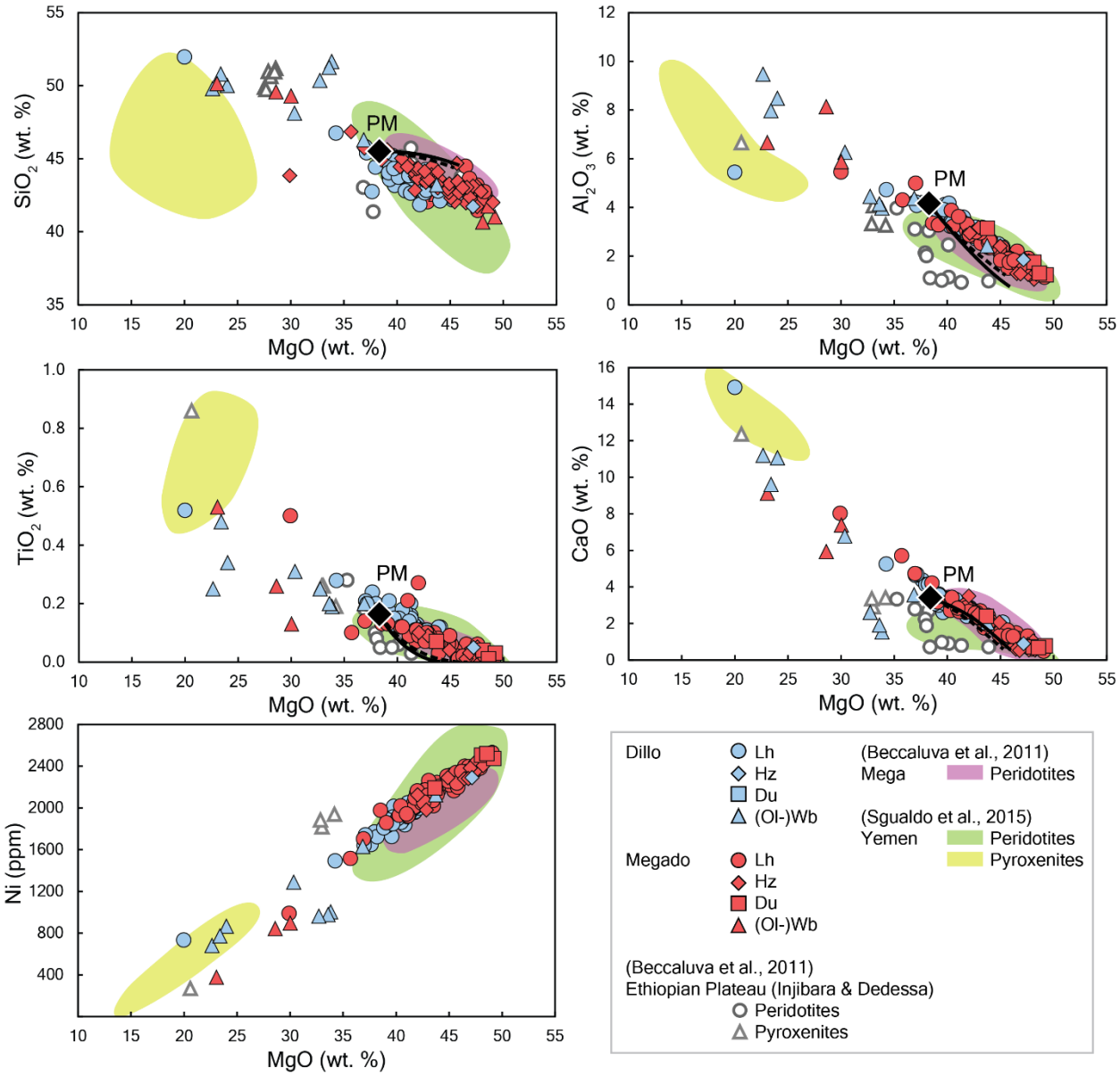

Figure 4-5. Whole rock variation diagrams of SiO_2, Al_2O_3, TiO_2, CaO, and Ni versus MgO for Dillo and Megado rift mantle xenoliths (this study) and Injibara and Dedessa plateau xenoliths (from Beccaluva et al., 2011). Shown for comparison are compositional fields for peridotites from Mega (purple; Beccaluva et al., 2011), and Yemen peridotites (green) and pyroxenites (yellow; Sgualdo et al., 2015). Black diamond indicates the composition of primitive mantle (PM), and black lines define batch (dashed) and fractional (solid) melting trends from Niu (1997).

3.3 Trace element systematics of xenolith clinopyroxene

Chondrite-normalized REE distribution patterns are shown in Figure 4-6. Among the Dillo and Megado xenoliths, two main types of peridotites can be identified on the basis of the clinopyroxene REE systematics. LREE-depleted clinopyroxene have $(La/Yb)_N < 1$ (0.02 – 0.47) and flat M- and HREE distribution patterns that are consistent with variable partial melting of mantle lherzolite (e.g., Shaw et al., 2007). LREE-enriched clinopyroxene exhibit higher $(La/Yb)_N$ between 1.2 and 12.6. Pyroxenites from both sample localities range to both LREE-enriched and -depleted, with $(La/Yb)_N$ between 0.3 and 5.9, but are distinct from peridotites in that several pyroxenites display concave-down patterns of M- and HREE that peak at Eu.

On the multi-element trace element diagrams (Figure 4-6), both LREE-enriched and LREE-depleted samples exhibit common features including negative Ba, Nb, and Ti anomalies. However, they differ in terms of the overall shapes of their distribution patterns, particularly with respect to the systematics of Th, U, Pb, Zr, and Ti. LREE-depleted clinopyroxene tend to be depleted in the most incompatible elements (Rb-Sm), with the exception of U and Pb, which exhibit variable positive excursions and have a pronounced negative Nb anomaly but mild Ti and Zr anomalies. The strong negative Nb signature is more prominent in Megado samples and is often accompanied by positive Pb anomalies. In contrast, LREE-enriched clinopyroxene display greater enrichments in Th-Sm and exhibit much stronger Th and U positive anomalies and negative Pb and Ti anomalies, and a much less pronounced Nb anomaly. One lherzolite from Dillo (DL2-5) exhibits instead a strong positive Ti anomaly.

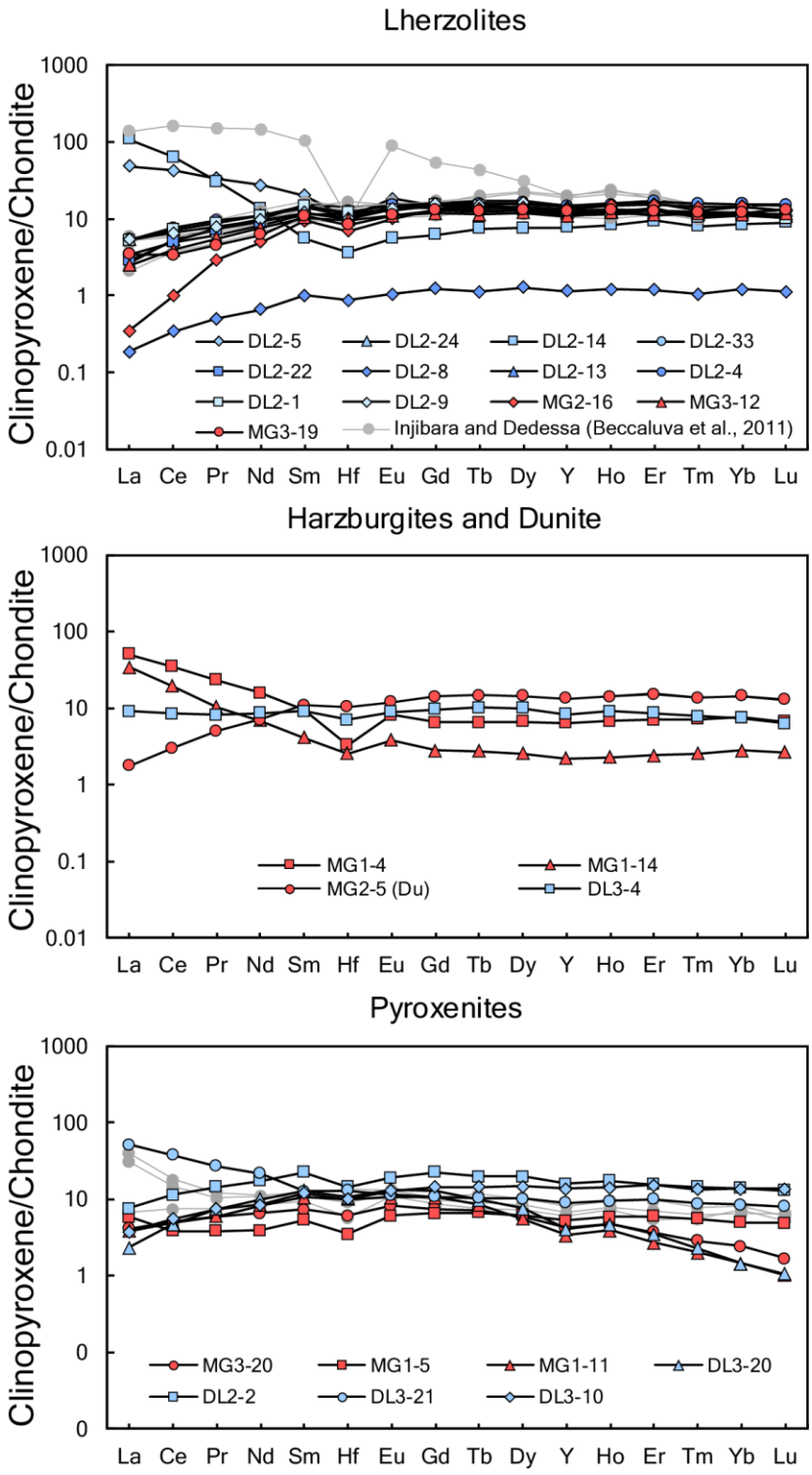

Figure 4-6. Clinopyroxene chondrite-normalized trace element (REE + Hf) distribution patterns for Dillo and Megado (**a**) lherzolites, (**b**) harzburgite and dunite, and (**c**) pyroxenite xenoliths, showing light rare-earth element (LREE) depletion in the majority of samples. Also shown are peridotite and pyroxenite xenoliths from Injibara and Dedessa (grey symbols; Beccaluva et al., 2011). Normalizing values are from Sun and McDonough (1989).

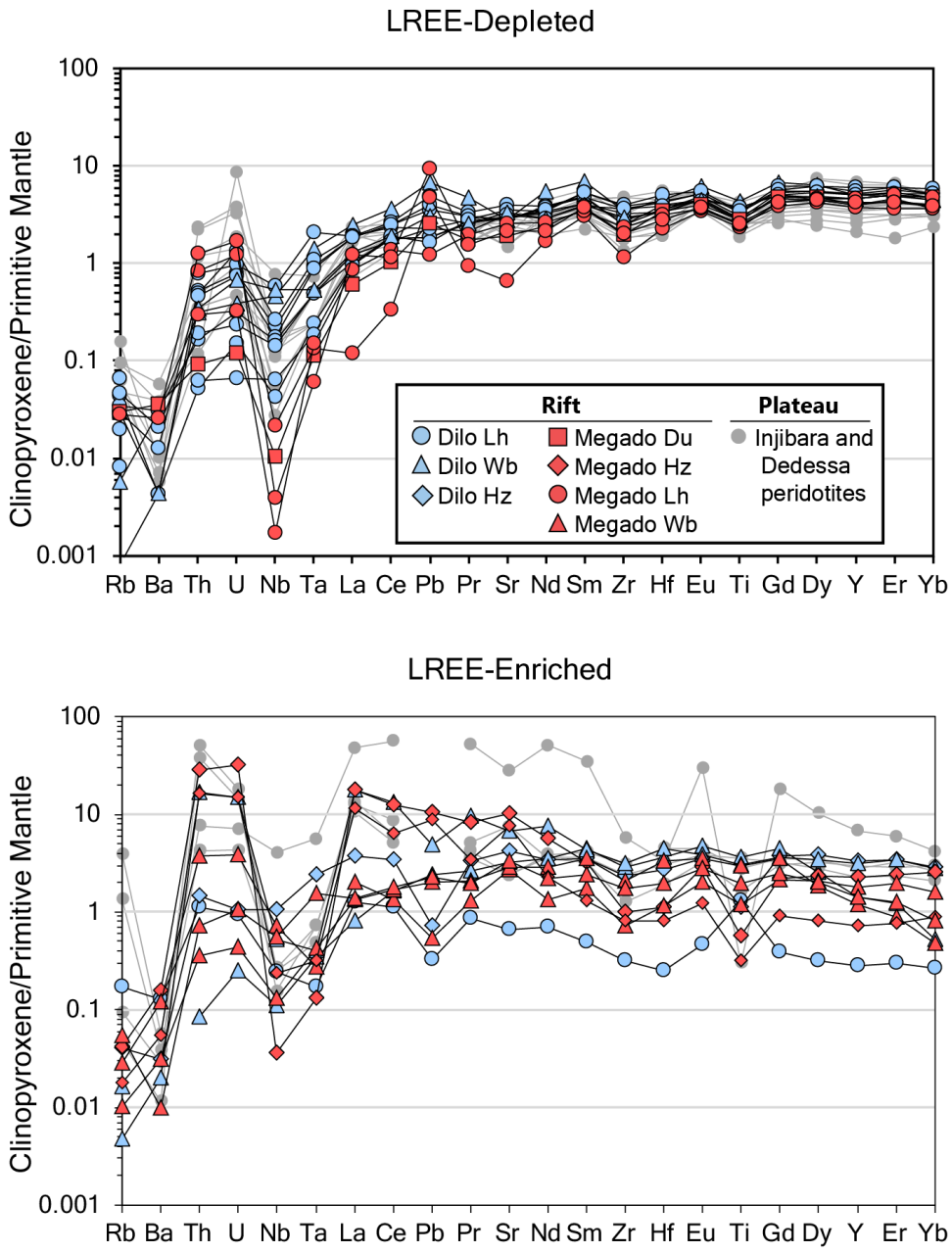

Figure 4-7. Clinopyroxene primitive mantle normalized trace element abundances for (**a**) LREE-enriched and (**b**) LREE-depleted (based on Chondrite-normalized La/Yb) Dillo and Megado xenoliths. Also shown are the clinopyroxene compositions of the Ethiopian Plateau xenoliths from Injibara and Dedessa (grey symbols; Beccaluva et al., 2011). Normalizing values from Sun and McDonough (1989).

3.4 Sr-Nd-Hf-Pb isotopic compositions of southern MER and Ethiopian Plateau xenoliths

Sr-Nd-Hf-Pb isotopic compositions of Dillo and Megado xenoliths clinopyroxene are given in Table 4-4. Also presented in this study are new Pb, Hf, and Nd isotopic data for Injibara and Dedessa xenolith clinopyroxene, complementing previously measured Sr isotopes on separate clinopyroxene separates by Beccaluva et al. (2011). Existing Nd isotopic data for the Injibara and Dedessa xenolith clinopyroxene agree well and overlap with the new data presented in this study (Beccaluva et al., 2011), in spite of the distinctive leaching protocols employed for the currently reported samples. For Southern MER xenoliths from Dillo and Megado, both LREE-depleted and LREE-enriched clinopyroxenes from peridotites encompass similar overlapping ranges of 0.70218 – 0.70337 for $^{87}Sr/^{86}Sr$, 0.512547 – 0.513624 for $^{143}Nd/^{144}Nd$, and 0.28290 - 0.28545 for $^{176}Hf/^{177}Hf$. The samples are characterized by relatively unradiogenic Sr isotopic compositions in comparison to plume-related basalts of the Ethiopian and Yemen plateaus (Natali et al., 2016). Varied Nd-Hf isotopic signatures in these samples complement findings in existing studies from Dillo, Megado, and nearby regions (Beccaluva et al., 2011; Bianchini et al., 2014; Alemayehu et al., 2016). Notably, two samples – a Megado harzburgite (MG1-14) and Dillo lherzolite (DL2-14) – record strongly elevated Hf isotopic compositions (ε_{Hf} =+94.7 and +53.5, respectively) that approach the suprachondritic values observed in Mega by Bianchini et al. (2014). The high degree of Hf and Nd isotopic variability exhibited in these samples is consistent with xenolith occurrences throughout the Afro-Arabian domain, including those studied in Yemen (Sgualdo et al., 2015) and Jordan (Shaw et al., 2007). With the exception of these very radiogenic values, significantly higher than commonly observed in continental and oceanic igneous rocks and falling above the ε_{Hf}-ε_{Nd} "mantle array" defined for oceanic basalts (Vervoort et al., 1999), Nd and Hf isotopes for the Dillo and Megado xenoliths are correlated and

fall close to, but generally below, the expected range for mantle values (Figure 4-9a). Plateau xenolith clinopyroxene from Injibara and Dedessa uniformly plot below the ε_{Hf}-ε_{Nd} mantle array and exhibit comparatively more restricted ranges for Hf ($^{176}Hf/^{177}Hf$ = 0.28283 - 0.28352) and Sr ($^{87}Sr/^{86}Sr$ = 0.702414 – 0.703536) isotopic signatures, but maintain a similar range in Nd ($^{143}Nd/^{144}Nd$ = 0.512967 - 0.513620) isotopic compositions as the southern MER xenoliths.

Lead isotopic variations are shown in Figure 4-8, and for Dillo and Megado xenoliths range to 17.56 - 20.05 for $^{206}Pb/^{204}Pb$, 15.49 - 15.70 for $^{207}Pb/^{204}Pb$, 37.37 - 40.15 for $^{208}Pb/^{204}Pb$. Using the nomenclature of Hart (1986) to define mantle endmembers, the xenoliths span the compositional array between DMM and high-μ (high $^{238}U/^{204}Pb$, HIMU) domains such as the C component (Hanan and Graham, 1996) or the extreme radiogenic HIMU endmember (Hart et al.,1992; 1986). Megado peridotites generally overlap with the Pb isotopic compositions of Mega peridotites (Bianchini et al., 2014) and are clustered at moderately high $^{206}Pb/^{204}Pb$ values that resemble C, which has been argued to be the composition of the Afar Plume (e.g., Rooney et al., 2012b), but range to even more radiogenic values for $^{206}Pb/^{204}Pb$ that overlap with HIMU-trending basalts from the Turkana Depression (Furman et al., 2006b). Additionally, the more radiogenic Megado peridotites and one pyroxenite sample fall below the Northern Hemisphere reference line (NHRL, defined Hart, 1984) in $^{208}Pb/^{204}Pb$-$^{206}Pb/^{204}Pb$ space, with negative vertical deviation from the NHRL (parameterized by -Δ8/4) increasing with increasing $^{206}Pb/^{204}Pb$. This trend indicates less thorogenic Pb (lower $^{208}Pb/^{204}Pb$) for a given uranogenic Pb ($^{206}Pb/^{204}Pb$) enrichment, and is accompanied by universally enriched $^{207}Pb/^{204}Pb$ (+Δ7/4) throughout both rift and plateau samples. In contrast, Megado pyroxenites and Dillo pyroxenites and peridotites fall near or above the NHRL (i.e., exhibit +Δ8/4) in $^{208}Pb/^{204}Pb$-$^{206}Pb/^{204}Pb$ space and encompass a larger range in $^{206}Pb/^{204}Pb$ that approaches the depleted mantle endmember at

the unradiogenic extreme of the sample distribution. Plateau xenoliths from Gojam (Injibara) also exhibit elevated $^{208}Pb/^{204}Pb$ at a given $^{206}Pb/^{204}Pb$, which is consistent with elevated Δ8/4 observed in northwest Ethiopian continental flood basalts (CFB) associated with activity of the Afar Plume (Pik, 1999; Natali et al., 2016). Whereas high Δ8/4 values in CFB lavas have been interpreted to indicate the involvement of an enriched mantle component such as continental crust or Pan-African lithosphere (Figure 4-8), in the mantle xenoliths it is possible that the high Δ8/4 is due to overprinting of $^{206}Pb/^{204}Pb$ by young uranogenic Pb.

3.5 Relationships between trace elements and radiogenic isotopes

Useful trace element ratios for indications of metasomatic interaction include high La/Yb, imparted by metasomatic agents and fluids enriched in highly incompatible LREE, and high Zr/Hf coupled with low Ti/Eu associated with carbonatitic metasomatism. These diagnostic ratios display some systematic relationships with the Pb isotopic compositions of the Dillo, Megado, and Gojam xenolith clinopyroxene, and, to a lesser extent, Hf isotopic compositions (Figure 4-11). Generally, LREE-depleted clinopyroxene follow relatively well-defined linear trends that show negative relationships for $(La/Yb)_N$ and Zr/Hf versus $^{206}Pb/^{204}Pb$, and flat trends for Zr/Hf and Ti/Eu versus $^{176}Hf/^{177}Hf$. In contrast, LREE-enriched clinopyroxene exhibit considerably more variable trace element ratios at a given range for $^{206}Pb/^{204}Pb$, as well as for a larger range in $^{176}Hf/^{177}Hf$. The observation that low Ti/Eu is associated with Megado harzburgites that range to high $^{176}Hf/^{177}Hf$ and $(La/Yb)_N$ agrees well with trends expected for carbonatitic metasomatism (e.g., Dupuy et al., 1991, 1992; Rudnick et al., 1993). However, Zr/Hf values do not show concomitant increasing trends with $^{176}Hf/^{177}Hf$ expected for carbonatitic metasomatism, which may indicate that relatively recent metasomatism (< 100 Myr ago) has affected the Zr/Hf signature without allowing enough elapsed time to evolve a

characteristic Hf isotopic signature. Interestingly, Pb isotopes exhibit diverging trends with respect to $(La/Yb)_N$, in which LREE-depleted samples show a negative correlation with $^{206}Pb/^{204}Pb$, whereas enriched samples range to higher and more variable $(La/Yb)_N$ with increasing $^{206}Pb/^{204}Pb$.

Less robust correlations between Hf and Nd isotopes and these diagnostic trace element ratios (not shown) suggest that the Hf and Nd isotopic systems have not been as affected by metasomatic interaction and, especially with consideration of significant Hf isotopic variation (Figure 4-9) preserved in the sample suite, may reflect pre-metasomatic mantle signatures. These observations suggest that the metasomatic agents were poor in Hf, and in some cases also Nd, are consistent with the general observation that these two isotopic systems are more resistant to metasomatic overprinting than the Pb isotopic system (Vervoort and Blichert-Toft, 1999; Wittig et al., 2006; Bianchini et al., 2014; Choi and Mukasa, 2014).

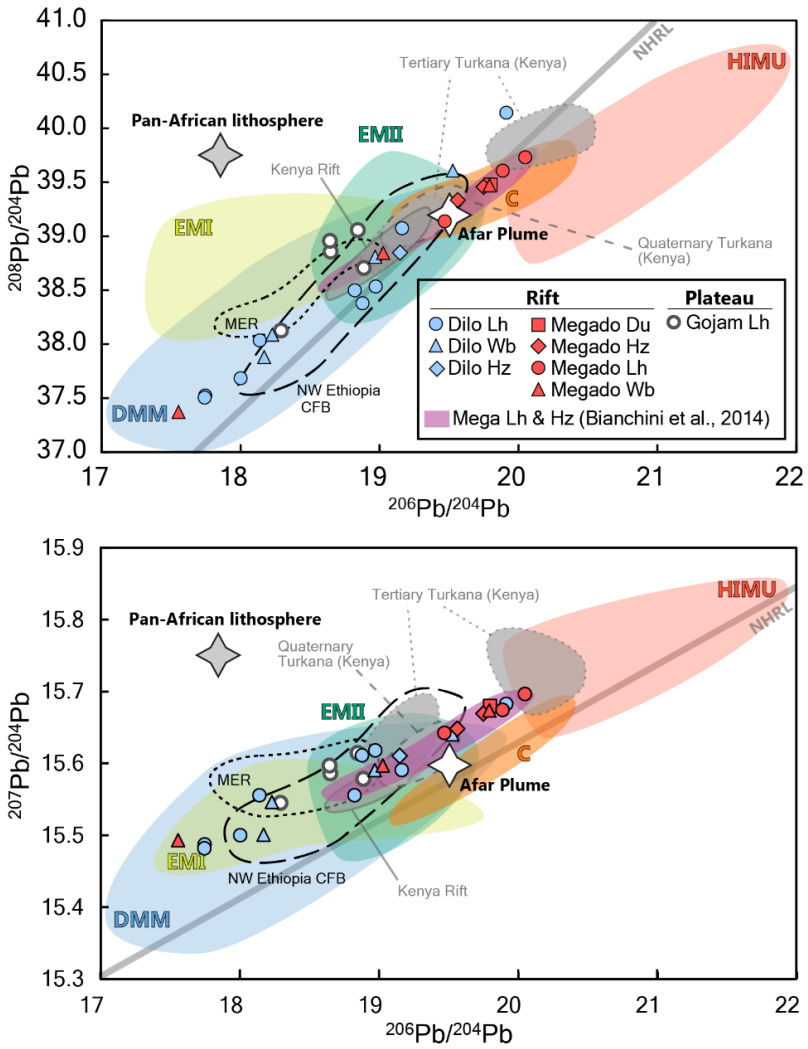

Figure 4-8. Pb isotopic diagram showing the compositions of Dillo and Megado rift and Injibara and Dedessa plateau xenolith clinopyroxene. Also shown are compositions of plume-related continental flood basalts (CFB) from NW Ethiopia (Pik, 1999; Nelson et al., 2012; Natali et al., 2016) and lavas from the Main Ethiopian Rift (MER; Furman et al., 2006a), the Kenya Rift (Class et al., 1994), and Quaternary and Tertiary lavas from Turkana (Furman et al., 2004; 2006b). Colored fields indicate mantle end-member populations defined by Hart (1986) for DMM (blue), EMI (yellow), EMII (green) and HIMU (red), using the compilation by Stracke et al. (2005). Orange field indicates the C component (Hanan and Graham, 1996) using data from the Cook-Austral islands of Ruturu (Chauvel et al., 1992) and Raivavae (Lassiter et al., 2003). Grey line is the Northern Hemisphere reference line (NHRL; Hart, 1984). Grey and white stars indicate end-member compositions for the Afar plume (white) and the Pan African Lithosphere (dark grey) given in Rooney et al. (2012b).

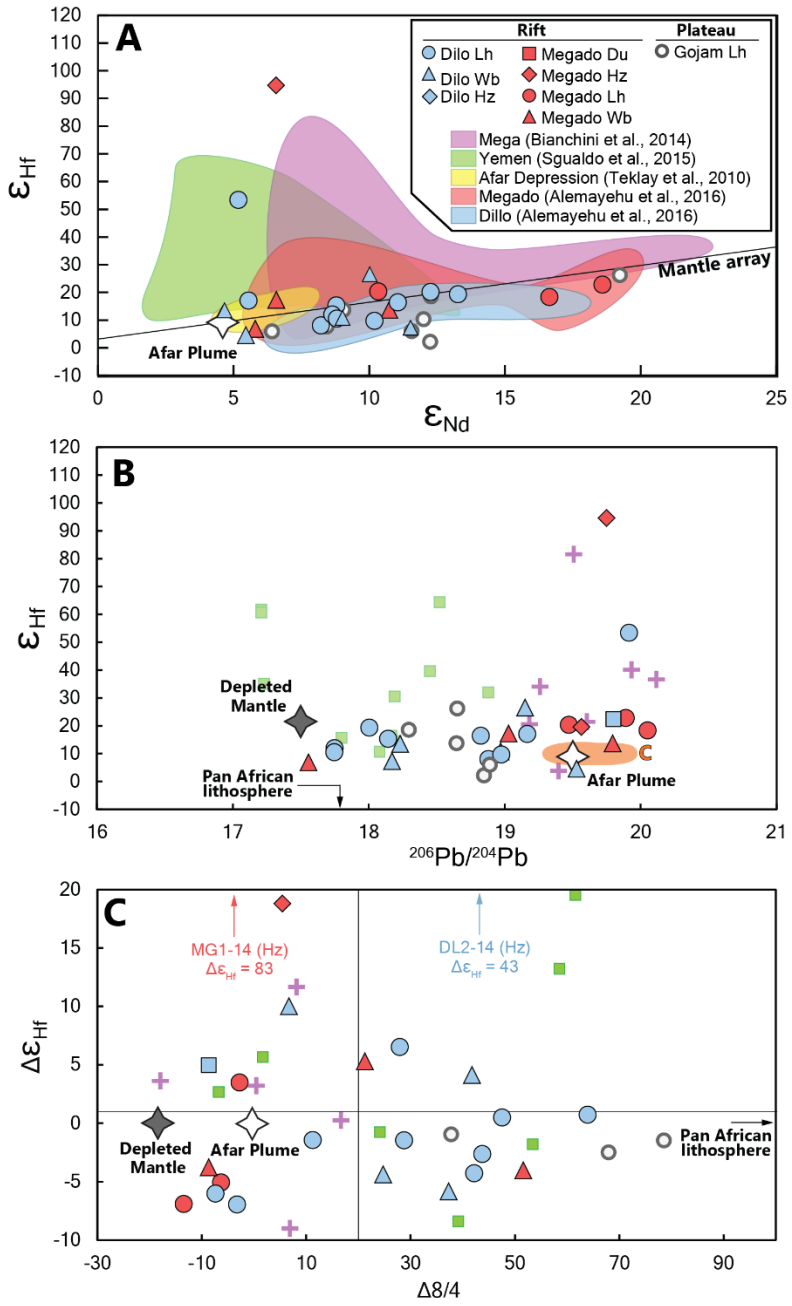

Figure 4-9. The compositions of Dillo and Megado rift and Gojam plateau xenolith clinopyroxene in (**a**) ε_{Hf}-ε_{Nd} space and (**b**) ε_{Hf}-$^{206}Pb/^{204}Pb$ space. Shown for comparison are mantle clinopyroxene compositions from Yemen (green field and square symbols; Sgualdo et al., 2015), Mega (purple field and crosses; Bianchini et al., 2014), and the Afar Depression (yellow field; Teklay et al., 2010). The Afar Plume and C end-member compositions are the same as in Figure 4-8. Black line indicates the 'mantle array' (given by $\varepsilon_{Hf} = 1.33*\varepsilon_{Nd} + 3.19$) from Vervoort et al. (1999). (**c**) Diagram showing $\Delta\varepsilon_{Hf}$ (vertical displacement from the mantle array in ε_{Hf}-ε_{Nd} space) versus $\Delta 8/4$ (vertical displacement from the NHRL in $^{208}Pb/^{204}Pb$-$^{206}Pb/^{204}Pb$ space).

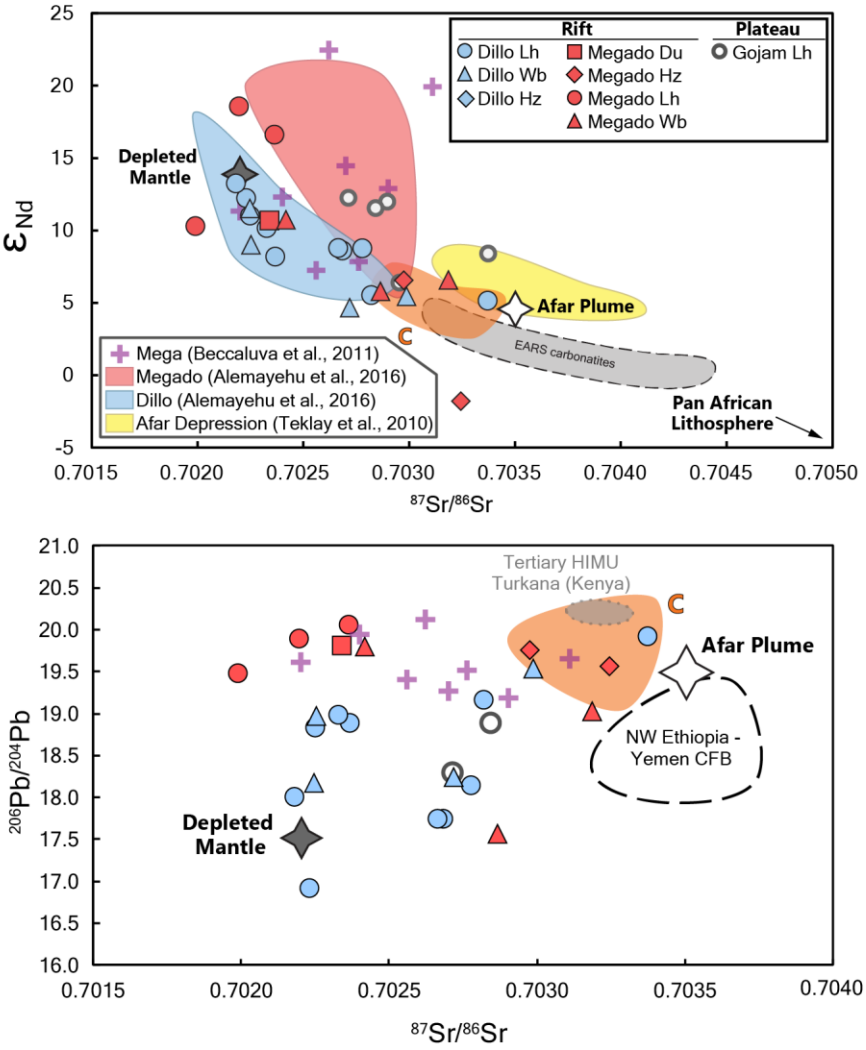

Figure 4-10. Nd-Sr (**a**) and Pb-Sr (**b**) isotopic compositions of Dillo and Megado rift and Gojam plateau xenolith clinopyroxene. Shown for comparison are mantle xenolith clinopyroxene compositions from the same sample localities by Alemayehu et al. (2016), from Mega (Beccaluva et al., 2011), and from the Afar Depression (Teklay et al., 2010). Also shown are the compositions of carbonatitic lavas studied throughout the EARS (Bell and Tilton, 2001), CFB lavas from Ethiopia and Yemen (Natali et al., 2016), and HIMU Tertiary mafic lavas from Turkana (Furman et al., 2006b). The Afar Plume, Depleted Mantle, Pan-African Lithosphere, and C end-member compositions are the same as in Figure 4-8.

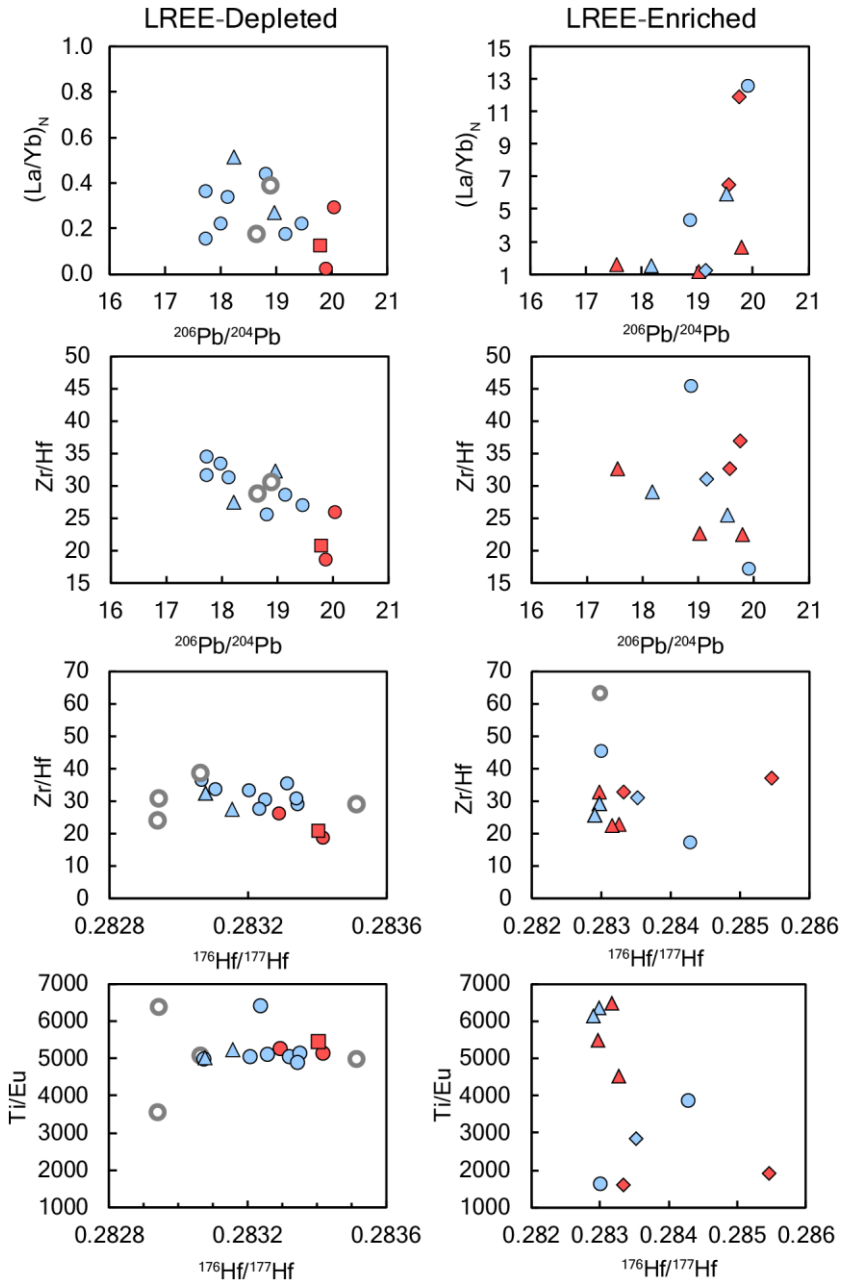

Figure 4-11. $(La/Yb)_N$, Zr/Hf, and Ti/Eu versus $^{206}Pb/^{204}Pb$ and $^{176}Hf/^{177}Hf$ for LREE-depleted and LREE-enriched clinopyroxene from Dillo and Megado rift xenoliths and Injibara and Dedessa plateau xenoliths. Normalizing values from Sun and McDonough (1989)**.** Symbols as described in Figures 4-5 to 4-10.

4. Discussion

4.1 Partial melting and metasomatic enrichment of the Dillo and Megado mantle

The chemical systematics of Dillo and Megado rift xenoliths suggest that a complex, multistage history involving both melt depletion and metasomatic enrichment events has affected the southern Ethiopian sub-continental lithospheric mantle (SCLM), and that the events have likely impacted the region heterogeneously on a remarkably small scale, such that locations separated by only tens of kilometers (and even xenoliths within the same region) sample mantle domains that record diverse histories. The Dillo and Megado xenoliths exhibit variable mineral modes ranging from websterites to fertile lherzolites and refractory harzburgites, which are accompanied by covariations in bulk rock and clinopyroxene compositions. The continuous linear trends in bulk rock MgO, Al_2O_3, and CaO shown in Figure 4-5 are consistent with the extraction of basaltic melts from primitive upper mantle (e.g., Pearson et al., 2003; Canil, 2004), and the simple, flat chondrite-normalized M- and HREE distribution patterns of clinopyroxene (Figure 4-6) are easily explained by melt extraction and preferential removal of the most incompatible LREE. In contrast, the fractionated M- and HREE observed in some pyroxenite xenolith clinopyroxene, as evidenced by concave-down distribution patterns for Sm-Lu that peak at Eu, likely reflect stabilization in the garnet facies (Pearson et al., 2003; and references therein).

Although the bulk rock major oxide trends and certain aspects of the clinopyroxene REE distribution patterns can be attributed to melt depletion processes, the many of the petrographic features and clinopyroxene incompatible element systematics exhibited by Dillo and Megado xenoliths suggest that they do not simply constitute partial melting residues, and require that significant metasomatic re-enrichment has occurred after the original melt depletion. Variable deformation and recrystallization textures, prevalent reaction patches and rims containing

secondary minerals such as microcrystalline olivine, pyroxene, and spinel, and the occurrence of amphibole in both reaction patches and disseminated in the peridotite matrix all attest to widespread metasomatic processes, the evidence for which has also been observed by other studies in the MER. Among several authors who report the presence of metasomatic ilmenite, amphibole, apatite, and phlogopite (e.g., Dawson, 2002; Orlando et al., 2006; Beccaluva et al., 2011; Bianchini et al., 2014), Bedini et al. (1997) observe that modal metasomatism – in this case apatite-bearing – is more prevalent in less recrystallized, deformed clinopyroxene-poor lherzolites and harzburgites from Mega that exhibit LILE enrichment and HFSE (Nb, Ta, Zr, Hf, and Ti) depletion, but absent in the most recrystallized granular peridotites lacking these LILE and HFSE features. The authors further argue for variable enrichment by a spatially and compositionally evolving melt volume, in which both small-volume, low-degree melts impart their enriched LILE signatures on deformed peridotite domains without causing significant recrystallization, and large-volume, high-degree melts with depleted incompatible element budgets trigger extensive recrystallization. Both of these processes may have been related to the impingement of the Afar plume, during which the initial small-degree melts may have been triggered by reactive porous flow at the base of the lithosphere in response to thermo-mechanical erosion by the rising plume head, and later high-degree melts may be linked to extensive subalkaline basaltic magmatism that emplaced the Ethiopian Plateau flood basalts. Alternatively, it has also been argued that the metasomatic agents were low-volume alkaline silicate melts, possibly containing a carbonatitic component, generated during the Cenozoic development of the MER, and that fractionation of trace element signatures occurred by reactive porous flow of alkaline melts triggered by lithospheric extension (e.g., Le Roux et al., 2007; Beccaluva et al., 2011; Bianchini et al., 2014).

In order to better constrain the metasomatic processes affecting the Dillo and Megado mantle, calculations of the melt compositions in equilibrium with peridotite clinopyroxene were performed to elucidate the possible metasomatic agents involved in the mantle enrichment processes. Two clinopyroxene-melt partition coefficients were utilized, $D_{cpx\text{-}silicate\ melt}$ and $D_{cpx\text{-}carbonatite}$ in an attempt to assess the different possible metasomatic agents. The results of this modeling are shown in Figure 4-12a-b, and illustrate several key features. Rather than representing the product of a unique metasomatic agent, it is more likely that both carbonatitic and mafic silicate metasomatism have occurred to impart positive Th and U and slight HFSE enrichment exhibited by the modeled equilibrium melts for the most enriched modeled melts (Downes, 2001). Existing investigations of Dillo and Megado xenoliths (Orlando et al., 2006; Alemayehu et al., 2016) have argued in support of the role of both silicate and carbonatitic metasomatism, and that multiple episode of both types of metasomatism have occurred on a small (km) scale via progressive solidification and melt infiltration into the lithospheric mantle during successive melt-rock interactions (e.g., Bedini et al., 1997). The melt infiltration process, during which liquids evolve down the chemical gradient from basalts to volatile-rich, low-T, small volume carbonatite melts, is supported in the Dillo and Megado xenoliths by the presence of spongy microcrystalline reaction patches and borders associated with clinopyroxene.

Excluding Dillo and Megado equilibrium melts with the greatest overall enrichments, the majority of the calculated melts are characterized by more modest enrichments in in the most incompatible elements. Dillo equilibrium melts lack strong Nb anomalies and are a reasonably good match with silicate melts shown in Figure 4-12b. Considering that, with the exception of two Dillo lherzolites (DL2-5 and DL2-14), the majority of Dillo clinopyroxenes exhibit flat or depleted REE patterns, it is likely that the causative metasomatic agents were subalkaline silicate

melts. Megado equilibrium melts are characterized by stronger negative Nb anomalies and variable negative Ti anomalies. The Nb anomaly can be explained by stabilization in the presence of rutile or Ti-oxides (e.g., Bedini et al., 1999). In general, the Megado xenoliths trace element compositions resemble those of xenoliths from Mega, which have been argued have undergone re-fertilization by low-volume alkaline melts with a carbonatitic component (Bianchini et al., 2014). This may explain equilibrium melts calculated for LREE-enriched Dillo and Megado xenoliths, which have positive Th, U, La, and Ce anomalies. In contrast, similar trace element modeling performed by Beccaluva et al. (2011) for the Injibara and Dedessa xenoliths has found that plateau equilibrium melts are only moderately enriched in incompatible elements, have negative Th anomalies, and lack HFSE depletions. On this basis, the authors argue convincingly that a subalkaline metasomatic agent highly resembling Ethiopian plateau CFB can be identified, which supports interpretations that the Pb isotopic signatures of the plateau xenoliths have been largely overprinted (see discussion in section 4.2) by plume-related melts.

Clinopyroxene $(La/Yb)_N$ and Ti/Eu additionally serve as useful discriminators for the different types of metasomatic agents because silicate metasomatism is associated with elevated HFSE and moderate to low enrichment in LREE, whereas carbonatitic metasomatism is characterized by extreme LILE enrichment and HFSE (particularly Ti) depletion. Lherzolites and pyroxenites from both the southern MER and Ethiopian plateau largely exhibit low $(La/Yb)_N$ and high Ti/Eu that plot in the field indicating silicate metasomatism, with the exception of two LREE-enriched Dillo lherzolites (DL2-5 and DL2-14), which have more transitional compositions (Figure 4-12c). The low Ti/Eu and high $(La/Yb)_N$ exhibited by LREE-enriched Megado harzburgites is consistent with carbonatitic metasomatism, and is also observed in Mega

peridotites and, more rarely, in one plateau peridotite from Dedessa (WOL2, Beccaluva et al., 2011), in line with observations from xenoliths throughout the Afro-Arabian domain (e.g., Shaw et al., 2007) that suggest that carbonated metasomatic agents have impacted the African SCLM on a wide regional scale.

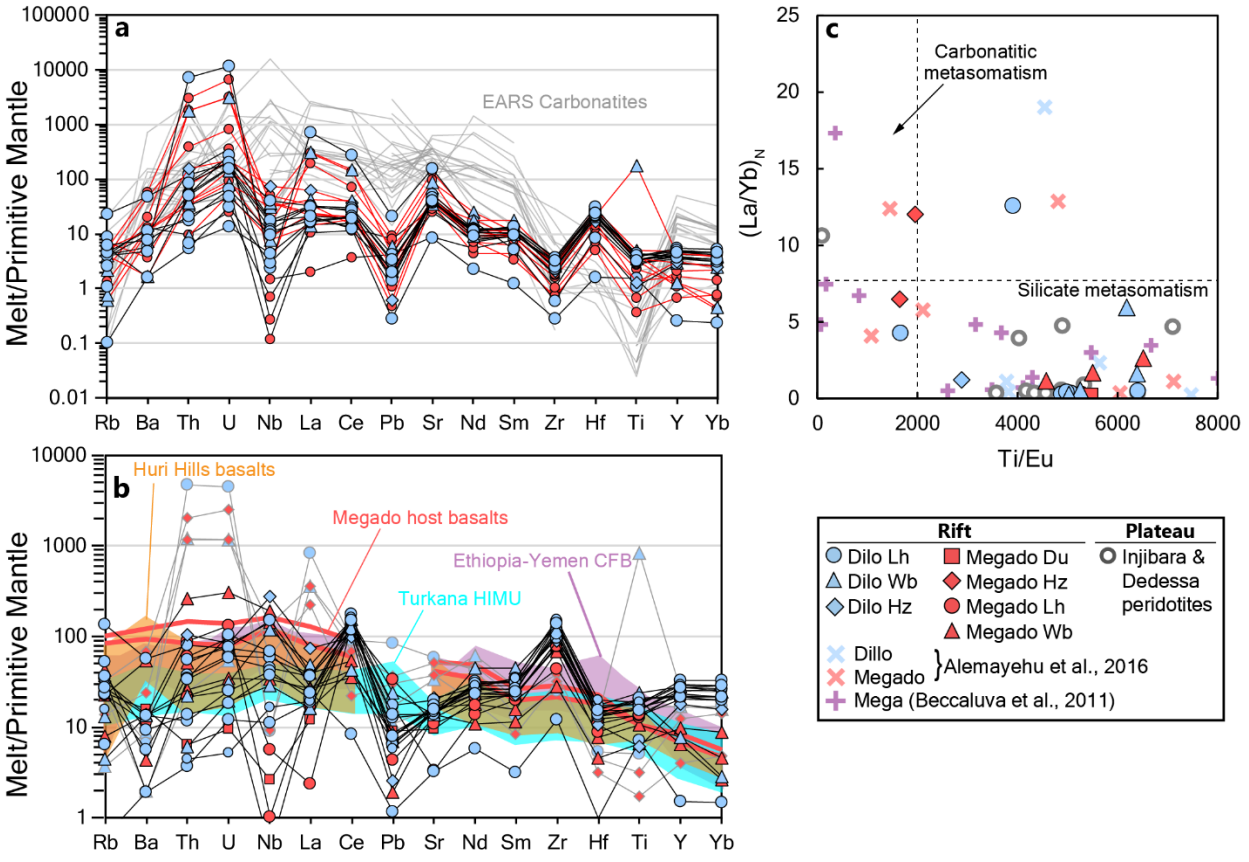

Figure 4-12. Primitive mantle-normalized trace element compositions of Dillo and Megado potential (**a**) carbonatitic and (**b**) silicate metasomatizing melts in equilibrium with xenolith clinopyroxene. Calculations were performed using cpx-carbonatite and cpx-silicate melt partition coefficients from Blundy and Dalton (2000) for Rb, Ba, Nb, La, Pb, Sr, Nd, Sm, Zr, Ti, Yb, and Y, from Hauri et al. (1994) for Th and U, and from Zack and Brumm (1998) for Ce and Hf. Shown for comparison are the compositions of EARS carbonatitic lavas (grey lines; Bizimis et al., 2003), Huri Hills alkaline basalts (orange field; Class et al., 1994), Turkana HIMU basalts (teal field; Furman et al., 2006b), and Ethiopia-Yemen CFB lavas (purple field; Natali et al., 2016). Normalizing values from Sun and McDonough (1989). In (**b**), grey outlined symbols and lines indicate unusual samples that exhibit carbonatitic melt affinities. (**c**) Chondrite-normalized La/Yb versus Ti/Eu discrimination diagram for carbonatitic and silicate metasomatism of xenolith clinopyroxene. Shown for comparison are Southern MER xenoliths from Dillo and Megado (Alemayehu et al., 2016) and Mega (Beccaluva et al., 2011). Carbonatite metasomatism and silicate metasomatism fields are after Yaxley et al. (1991) and Coltorti et al. (1999).

4.2 Sr-Nd-Hf-Pb isotopic variability of the SCLM beneath Ethiopian plateau and rift environments

The ranges of radiogenic isotopic ratios exhibited by the Dillo and Megado rift xenoliths reflect time-integrated ingrowth of parent-daughter ratios (i.e., U,Th/Pb, Sm/Nd, Lu/Hf, and Rb/Sr) that have been fractionated by melt depletion and/or re-equilibration with isotopically distinct metasomatic agents. Generally, the Megado and Dillo rift xenoliths have correlated Hf and Nd isotopic signatures that plot within ±15 ε_{Hf} units of the mantle array, consistent with the signatures of rocks formed in the convecting mantle (Figure 4-9a). The Gojam plateau xenoliths also plot close to the mantle array, but typically fall below it. Positive correlations between $^{143}Nd/^{144}Nd$ and $^{176}Hf/^{177}Hf$ in mantle-derived oceanic basalts (MORB and OIB) are well-documented, and defines the mantle array on the Nd-Hf isotope diagram shown in Figure 4-9a. (Patchett and Tatsumoto, 1980; Salters and Hart, 1991; Vervoort and Blichert-Toft, 1999; Vervoort et al., 1999; Bouvier et al., 2008). The coherency of the two isotopic systems is due to similar fractionation of more compatible parent (Lu and Sm) and less compatible daughter (Hf and Nd) species during partial melting (Patchett and Tatsumoto, 1980; Johnson and Beard, 1993; Patchett, 1983). The notable exceptions are two samples (DL2-14 and MG1-14) that exhibit extremely radiogenic Hf, with ε_{Hf} of +53 and +95, respectively. High ε_{Hf} that deviates significantly from the mantle array has been widely observed in peridotites from the SCLM throughout the Afro-Arabian domain (e.g., Shaw et al., 2007; Bianchini et al., 2014; Sgualdo et al., 2015), and has commonly been attributed to fractionation of the two isotopic systems during melt depletion followed by long-term isolation from the convecting mantle (Lapen et al., 2005; Wittig et al., 2006; Bizimis et al., 2007).

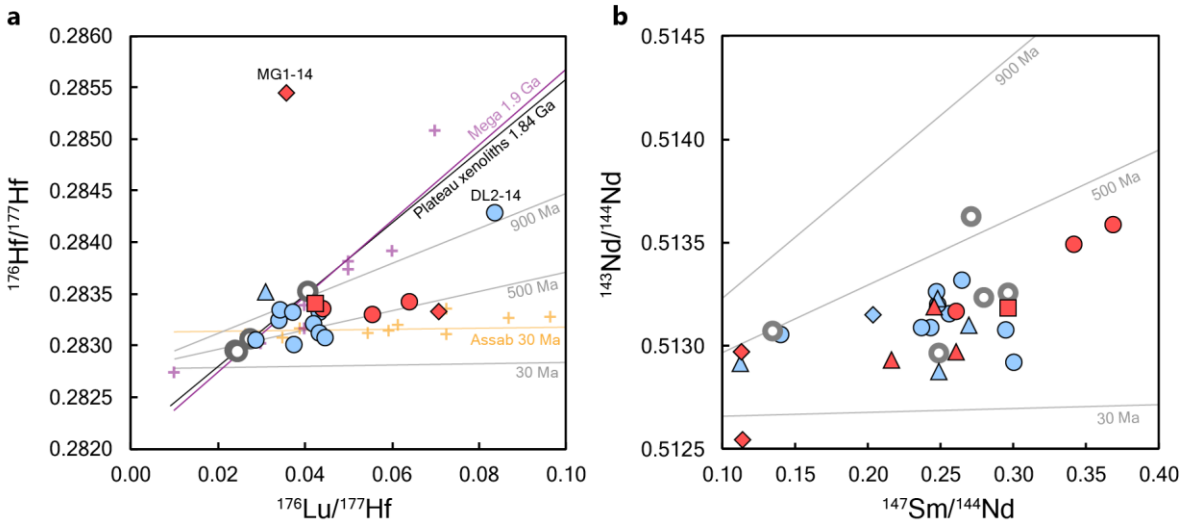

Figure 4-13. (**a**) $^{176}Lu/^{177}Hf$-$^{176}Hf/^{177}Hf$ and (**b**) $^{147}Sm/^{144}Nd$-$^{143}Nd/^{144}Nd$ relationships in Dillo and Megado rift peridotite and Gojam plateau peridotite clinopyroxene. Xenolith symbols as defined in figure 4-9, with the addition of Assab xenoliths as orange crosses. Black line indicates the pseudo-isochron for the plateau xenoliths calculated from measured Lu/Hf and $^{176}Hf/^{177}Hf$, which gives an apparent age of 1.84 Ga. Also shown are apparent isochrons for 1.9 Ga peridotites from Mega (Bianchini et al., 2014) and 30 Ma peridotites from Assab, in the Afar Depression (Teklay et al., 2010). Grey lines are CHUR reference isochrons for 500 and 900 Ma, calculated using parameters from Vervoort (2014).

The studied xenolith clinopyroxene with extremely radiogenic Hf isotopic signatures do not also bear extremely radiogenic Nd isotopic compositions, the latter of which exhibit only mildly to moderately suprachondritic values. Such strong decoupling of the Hf-Nd isotopic systems can be generated during late stage metasomatism due to the greater resistance of the Lu-Hf isotopic system to metasomatic overprinting compared to the Sm-Nd isotopic (e.g., Bedini et al., 2004; Stracke et al., 2011). This multi-stage process of ancient melt depletion, long-term isolation, and subsequent metasomatism has been invoked to explain highly radiogenic Hf that is decoupled from Nd in both the Afro-Arabian domain (e.g., Shaw et al., 2007; Bianchini et al., 2014; Sgualdo et al., 2015) and in xenoliths sampling SCLM globally (e.g., among others, Wittig et al., 2006; Bizimis et al., 2007; Choi and Mukasa, 2014). The significant Hf isotopic variability

observed in the Dillo and Megado rift xenoliths is in stark contrast to the relatively homogeneous Hf isotopic signatures of the Gojam plateau xenoliths (cf. Figure 4-9b) and the even more restricted range in Hf-Nd isotopic signatures of Afar Depression xenoliths (Teklay et al., 2010), where it is likely that increased thermochemical perturbation provided by the Afar plume has led to enhanced resetting of both isotopic systems (e.g., Bedini et al., 2004).

The preservation of highly radiogenic Hf in one Megado harzburgite (MG1-14; ε_{Hf} = +95) and one Dillo lherzolite (DL2-14; ε_{Hf} = +53) is concurrent with significant enrichment in LREE (chondrite-normalized La/Yb ~ 12) and LILE, but depletion in HFSE (Ti/Eu < 3900), chemical signatures that testify for metasomatism by carbonatitic agents (e.g., Wittig et al., 2007). These metasomatic fluids would have insufficiently abundant Hf to accomplish significant isotopic overprinting of Hf. The remaining peridotites in the sample suite, however, are too enriched in Hf (up to 1.5 ppm) and other HFSE for carbonatite liquids to be the dominant metasomatic mechanism. Xenoliths that are characterized by only moderate, rather than extreme LREE and LILE enrichment suggest that alkaline silicate melts also serve as important metasomatic agents beneath the MER. These alkaline silicate metasomatic liquids may also be capable of similarly fractionating the Sm-Nd and Lu-Hf isotopic systems via porous flow though the peridotite matrix due to their differing incompatibilities (Le Roux et al., 2009; Bianchini et al., 2014).

The Pb isotopic signatures of xenoliths are variable and also record multiple episodes and types of chemical overprinting. The most radiogenic $^{206}Pb/^{204}Pb$ signatures (> 19.5) are associated with simultaneously the least and most LREE-enriched samples. In contrast, the remaining samples (mostly Dillo lherzolites) have Pb isotopic signatures that trend toward DM (Figure 4-8), supporting the interpretation that they have been re-fertilized by subalkaline melts

with a MORB-like affinity. Because previous (ancient) melt depletions are expected to result in substantively less radiogenic Pb ingrowth over time, the highly radiogenic Pb isotopic ratios are at odds with the ancient depleted mantle components established by the Hf-Nd isotopic systematics, especially considering that the xenoliths with the highest ε_{Hf} also have very radiogenic Pb. These Pb signatures are the result of radiogenic ingrowth of precursor material with elevated U/Pb (= μ), and similar high-μ isotopic compositions are observed also in Mega peridotites (Bianchini et al., 2014). As shown in Figures 4-8 and 4-11, high-μ-type Megado lherzolites and harzburgites (including sample MG1-14 with ε_{Hf} = +95) are LREE-depleted and enriched, respectively, exhibit Pb anomalies that vary from slightly negative to significantly positive on the incompatible element abundance diagram that do not correlate with $(La/Yb)_N$ (Figure 4-11), and plot very near or below the ^{208}Pb NHRL. In contrast, the high-μ Dillo lherzolite with ε_{Hf} = +53 is LREE-enriched and plots well above the NHRL. The observation that the high-μ signature is associated with distinct trace element compositions suggests that it may be characteristic of more than one sublithospheric metasomatic component affecting the MER mantle (Aulbach et al., 2011; Beccaluva et al., 2011; Bianchini et al., 2014), possibly linked to signatures generated during pre-Paleozoic subduction cycles (Stern et al., 2012; Thomas et al., 2013).

Separate pathways of enrichment to explain the Pb isotopic signatures is reasonable considering that subduction zone processing can generate in the mantle both carbonatitic components associated with the devolatilization of the entire lithosphere + sediment package is devolatilized as well as mafic silicate components derived from the eclogite (Weaver et al., 1991). Additionally, the fact that the LREE-enriched high-μ Megado harzburgites and Dillo lherzolite have $^{87}Sr/^{86}Sr$ isotopic compositions that trend toward the composition of C and the

Afar plume (Figure 4-10) suggests that the plume is associated with at least one of the high-μ components, but this not necessarily in conflict with a subduction origin for the trace element and isotopic features of the xenoliths given the increasing evidence that high-μ domains in general require subduction zone processing of precursor materials (e.g., Stracke et al., 2005; Castillo et al., 2015). In fact, recent work has argued that high-μ domains may be generated by delamination and recycling of SCLM that has been pervasively metasomatized by subduction-related carbonatitic fluids (Weiss et al., 2016), fortifying the links between metasomatized SCLM, high- μ, and the recycling of ancient continental roots into the convecting mantle. These events could have occurred during Pan African or older geodynamic cycles. The remaining Dillo lherzolites, as well as pyroxenites from both localities, plot near or above the ^{208}Pb NHRL, with compositions exhibiting MORB-like affinities signifying overprinting by subalkaline asthenospheric melts. Plateau peridotites plot further above the NHRL, suggesting the role of enriched mantle (EM) components that have been recognized throughout the EARS as representative of a pre-Cenozoic metasomatic signature residing in the lithosphere (Beccaluva et al., 2011; Bianchini et al., 2014).

Geochemical and isotope signatures in Megado lherzolites and harzburgites illustrate that refractory domains in the SCLM have been altered by high-μ silicate and/or carbonatitic fluids that have re-set the Pb isotopic signatures (Figure 4-9c), while leaving suprachondritic Hf isotopic signatures intact. The observation that these samples plot near or below the NHRL (i.e., have $\Delta 8/4 < 10$) and extend to subchondritic Hf isotopic ratios ($\Delta\varepsilon_{Hf}$ as low as -7) is consistent with metasomatism of ancient upper mantle residua by a high-μ component similar to C, the proposed composition of the Afar Plume (Hanan et al., 2004; Rooney et al., 2012b). This high- μ component is arguably comprised of ancient SCLM metasomatized by carbonatitic fluids related

to Proterozoic Pan-African or older continental assembly that, after isolation at the base of the of the continental crust, is foundered and entrained in the convecting mantle before upwelling as a mantle plume (e.g., Furman et al., 2016). Although several of the Dillo lherzolites fall in the SW (low $\Delta\varepsilon_{Hf}$ and $\Delta 8/4$) quadrant of the Figure 4-9c, the majority exhibit a wide range in $\Delta\varepsilon_{Hf}$ but are displaced toward significantly higher $\Delta 8/4$ (> 20), implying the Dillo xenoliths record variable contamination of the upper mantle by continental lithospheric mantle material through plume-related thermochemical erosion and/or detachment and foundering of continental material into the asthenosphere (e.g., Rooney et al., 2012b; Furman et al., 2016), or that the Pb isotopic signature has been partially re-set by metasomatizing agents characterized by young uranogenic $^{206}Ph/^{204}Pb$. Mantle xenoliths from Gojam, on the Ethiopian Plateau, range to similarly high $\Delta 8/4$ but are restricted to relatively low $\Delta\varepsilon_{Hf}$ (< 0), suggesting that the plume environment may have caused some degree of thermochemical reset with respect to even robust isotopic systems such as Lu-Hf. The latest metasomatic overprinting, therefore, may be linked to the percolation of melts related to Oligocene CFB that carry significant EM-type contributions.

4.3 The timing of thermochemical events in the East African SCLM

Because the Lu-Hf and Sm-Nd systematics of the southern MER and Ethiopian Plateau xenoliths have clearly been obscured by late-stage metasomatism (see discussion in sections 4.1 and 4.2), calculations of meaningful pseudo-isochrons or model ages render a spectrum of approximate ages of the ancient melt depletion events. Lu-Hf pseudo-isochrons (Figure 4-13a) demonstrate that, consistent with the findings of Alemayehu et al. (2016), the majority of Megado and Dillo peridotites plot between 500 – 900 Ma CHUR reference isochrons. As illustrated in Figure 4-13b, Sm-Nd isotopic data are scattered to apparent ages younger than 500 Ma, indicating that they have been affected by late-stage metasomatism. The 900-500 Ma

apparent ages on the Lu-Hf diagram are meaningful because they coincide with the timing of Pan African continental assembly. During this protracted orogenic cycle accompanied by multiple phases of tectonic and magmatic activity, significant melt extraction is likely to have occurred (e.g., Kröner and Stern, 2004, and references therein). The negative slope of the apparent isochron for Megado peridotites (both with and without the very radiogenic sample MG1-14) yields a negative age, which likely demonstrates recent isotopic exchange with a metasomatic agent low in $^{176}Hf/^{177}Hf$ (Choi and Mukasa, 2014). In contrast to the somewhat poorly defined Dillo and Megado isochrons, plateau peridotites from Gojam define a tight linear correlation that yields an apparent age of 1.84 Ga, similar to the 1.9 Ga Lu-Hf apparent age defined for Mega peridotites (Bianchini et al., 2014) that was found to be in reasonable agreement with Re-Os ages for the same locality (Reisberg et al., 2004). This indicates that the ancient melt depletion history that extends possibly into the Neoarchean-Paleoproterozoic argued for the southern MER lithospheric mantle is shared by the plateau mantle. The oldest recorded events pre-date the earliest continental collisions related to Gondwana assembly during the Pan African orogenic cycle, and illustrate that lithospheric sections preserve a record of Grenvillian (or Kibaran in Africa; Kröner and Stern, 2004) orogenic events that has remained intact throughout East Africa (Rino et al., 2008).

4.4 Xenolith perspective on the dynamic development of East African SCLM

The Ethiopian Plateau and Southern MER clinopyroxene radiogenic isotope systematics presented in this work, particularly with respect to Pb and Hf isotopes, provide an important perspective on the dynamic evolution of the East African SCLM that is involved with ongoing rift tectonomagmatic activity. In the history summarized in Figure 4-14, subduction and continental accretion during Kibaran and Pan African supercontinent assembly and subsequent

breakup released volatiles that triggered both flux melting and the extraction of lavas to produce depleted mantle residua, as well as generated metasomatized, recycled components in the upper mantle and SCLM (top panel). Subduction-related carbonatitic metasomatism SCLM, in particular, generated domains with elevated (U, Th)/Pb and serve as long-lived precursors necessary for the development of high-μ Pb isotopic signatures observed in mantle xenoliths and mafic lavas in the southern MER and northern Kenya (e.g., Furman et al., 2006b; Beccaluva et al., 2011; Bianchini et al., 2014). Subsequent detachment and foundering of the dense, metasomatized SCLM recycled material into the convecting mantle, generating additional melts (e.g., Furman et al., 2016), many of which served as later-stage metasomatic agents percolating through the thinned SCLM (middle panel). At 30 Ma, the developing Afar Plume at the base of the northern Ethiopia SCLM supplied heat to facilitate thermal erosion of the continental root, and generated voluminous melts to build the Ethiopian Plateau (Baker et al. 1996; Hofmann et al., 1997; Pik et al., 1999). Most recently (bottom panel), ongoing rifting and decompression melting sample heterogeneous recycled domains in the SCLM and upper mantle. The small spatial scale of these heterogeneities is evidenced by the record of diverse metasomatic processes (e.g., subalkaline silicate, alkaline silicate, and carbonatitic) in southern MER sample localities including Dillo, Megado, and Mega (Bianchini et al., 2014).

5. Conclusions

New radiogenic isotope and trace element information on mantle xenolith clinopyroxene sampled from the Ethiopian plateau and the southern Main Ethiopian Rift provide constraints on the contrasting nature and histories of the SCLM beneath distinct provinces of the EARS. On a wide scale, the EARS SCLM, as represented by southern MER and Ethiopian Plateau xenoliths, preserves a Hf isotopic record of ancient Pan-African melt depletion that has been variably

overprinted by multiple isotopically distinct events or episodes of metasomatism. Late-stage metasomatism involved alkaline silicate and carbonatitic agents, as well as depleted asthenospheric inputs in the Southern MER, but was characterized by distinctly subalkaline affinities in the Ethiopian Plateau mantle, where pervasive percolation of CFB magmas related to the Afar Plume is recorded in the trace element and isotopic systematics of Injibara and Dedessa peridotites (e.g., Beccaluva et al., 2011). Recent perspectives on the formation of high-μ mantle domains from ancient, subduction-related carbonatitic metasomatism of the SCLM are in agreement with the tectonic history of East Africa and the isotopic signatures observed in mantle xenoliths and mafic lavas from the southern MER and northern Kenya. These findings strongly support the view that the rifted, metasomatized SCLM serves as an extremely heterogeneous, long-lived reservoir for recycled continental materials that contribute to petrogenesis through multiple stages of continental evolution.

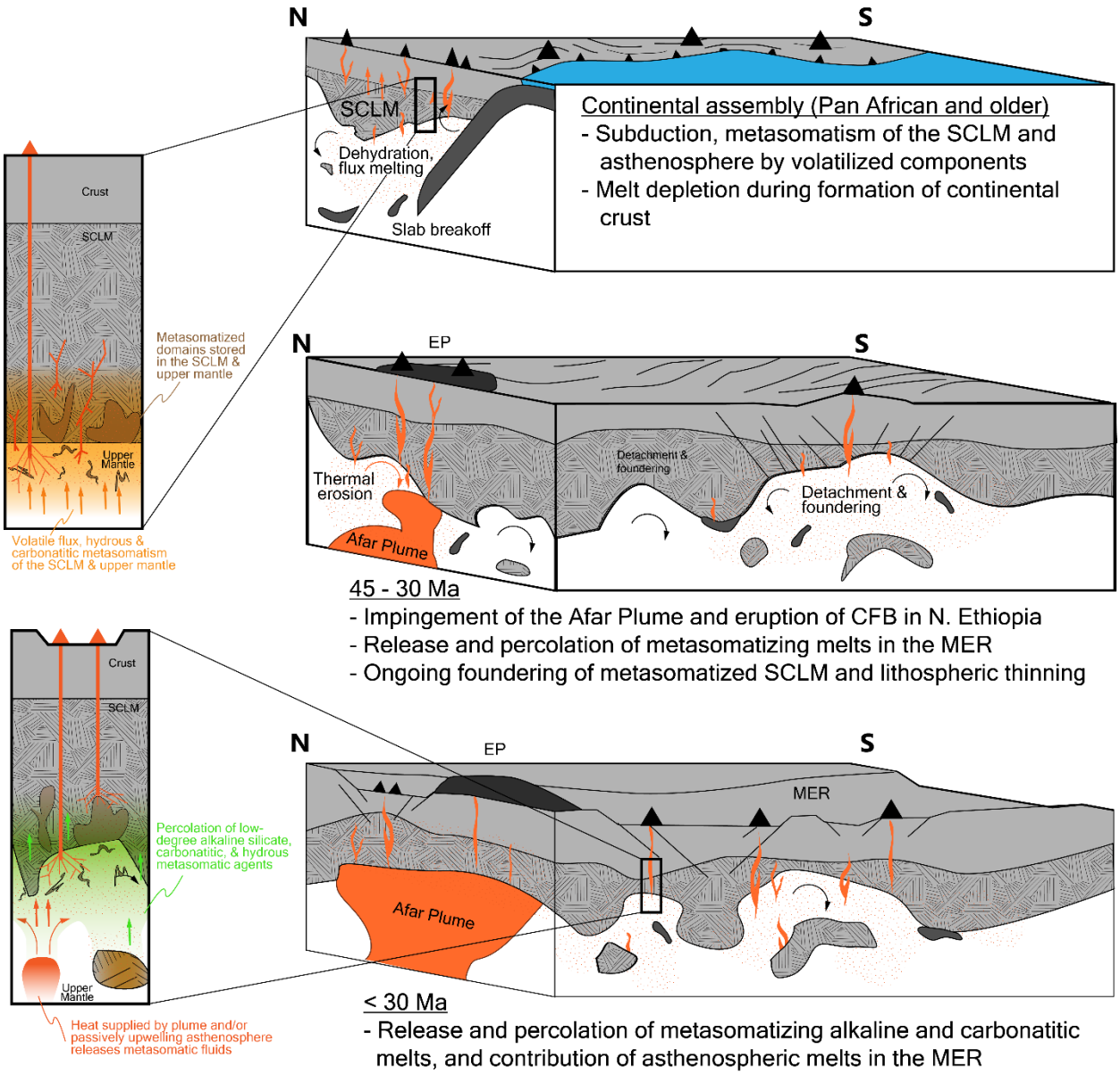

Figure 4-14. Summary schematic of the multiple stages of melt depletion and metasomatic processes contributing to the Ethiopian Plateau and southern MER SCLM. Subduction during Pan African continental assembly released volatiles that triggered both flux melting and the extraction of arc lavas, as well as generated metasomatized, recycled components in the SCLM and upper mantle (top panel). Subsequent detachment and foundering of the dense, metasomatized SCLM recycled material into the convecting mantle, generating additional melts, many of which serve as later-stage metasomatic agents percolating through the thinned SCLM (middle panel). The developing Afar Plume at the base of the northern Ethiopia SCLM supplied heat to facilitate thermal erosion of the continental root, and generated voluminous melts that build the Ethiopian Plateau. Most recently (bottom panel), ongoing rifting and decompression melting sample heterogeneous recycled domains in the SCLM and asthenosphere.

Table 4-1. Whole rock compositions of Dillo and Megado xenoliths

Locality	Dillo														
Sample	DL1-1	DL2-1	DL2-2	DL2-3	DL2-4	DL2-5	DL2-6	DL2-7	DL2-8	DL2-9	DL2-10	DL2-11	DL2-12	DL2-13	DL2-14
Tyle	Lh	Lh	Wb	Lh	Lh	Lh	Lh	Lh	Lh	Lh	Lh	Ol-Wb	Lh	Lh	Lh
SiO_2 (wt. %)	43.84	43.77	49.8	43.19	43.29	44.44	43.1	43.37	43.25	42.82	43.31	43.22	46.76	43.49	42.2
TiO_2	0.12	0.16	0.25	0.15	0.14	0.2	0.11	0.2	0.16	0.17	0.13	0.07	0.28	0.14	0.04
Al_2O_3	3.04	3.87	9.47	4.12	3.37	4.14	2.95	3.15	3.19	3.34	2.9	2.43	4.73	3.52	2.39
FeO	8.41	8.94	5.67	9.02	8.88	8.82	8.68	9.12	8.97	9.36	8.79	8.33	8.32	9.05	7.86
MnO	0.14	0.15	0.13	0.16	0.14	0.14	0.14	0.14	0.15	0.15	0.14	0.13	0.14	0.15	0.13
MgO	41.37	39.64	22.64	39.76	41	37.96	42.17	41.22	41.26	40.77	41.82	43.74	34.24	40.1	45.21
CaO	2.95	3.35	11.2	3.12	3.07	4.14	2.79	2.72	2.96	3.32	2.85	2.05	5.27	3.43	2.07
Na_2O	0.06	0.09	0.77	0.29	0.07	0.13	0.05	0.06	0.05	0.06	0.05	0.03	0.24	0.09	0.07
K_2O	0.01	0	0.03	0.13	0.01	0.01	0.02	0.01	0	0.01	0.01	0	0	0.01	0.02
P_2O_5	0.03	0.01	0.01	0.04	0	0.02	0	0.01	0	0	0	0	0.01	0.01	0.01
LOI	0	0	0	0	0	0	0	0	0	0	0	0	0	0	0
Total	100	100	100	100	100	100	100	100	100	100	100	100	100	100	100
Mg#	0.9	0.89	0.88	0.89	0.89	0.89	0.9	0.89	0.89	0.89	0.9	0.9	0.88	0.89	0.91
Ba	2	4	1	52	1	3	nd	3	nd	2	nd	nd	5	nd	4
Co	110	110	57	110	109	103	113	111	112	110	110	114	94	105	119
Cr	2392	2404	1974	2513	2422	2528	2516	2525	2082	2190	2198	2725	2719	2436	3036
Cu	18	14	36	23	12	16	14	11	9	10	9	11	19	14	7
Ga	4	5	9	5	4	5	4	4	5	5	4	3	7	5	3
Hf	2	3	2	2	3	2	3	2	2	3	3	2	3	3	2
La	4	nd	2	5	nd	1	nd	nd	nd	6	nd	4	1	1	5
Nb	1	2	2	3	2	1	2	1	2	2	2	2	2	2	1
Ni	1991	1880	679	2016	1918	1770	2045	1940	1959	1925	2046	2126	1495	1868	2316
Pb	2	3	2	3	2	2	1	2	1	1	2	nd	1	1	2
Sc	13	16	39	14	14	19	13	13	13	15	15	10	21	14	9
Sr	13	16	46	95	19	20	16	18	16	17	19	13	27	25	35
V	64	81	158	69	68	85	60	70	75	78	63	52	117	71	45
Y	1	2	4	2	2	3	1	1	1	1	2	1	5	1	nd
Zn	41	53	38	63	45	50	41	47	41	42	40	46	52	47	54
Zr	4	7	11	7	6	8	4	6	4	4	6	3	12	5	1
Cpx	14	16	54	17	20	13	13	14	15	13	10	25	16	10	14
Opx	20	22	46	17	25	16	19	18	15	17	16	37	19	9	24
Ol	66	61	0	66	56	71	68	68	69	70	74	38	65	82	62
Total	100	100	100	100	100	100	100	100	100	100	100	100	100	100	100

Ol = olivine, Cpx = clinopyroxene, Opx = orthopyroxene

Table 4-1. Whole rock compositions of Dillo and Megado xenoliths (continued)

Locality	Dillo														
Sample	DL2-15	DL2-16	DL2-17	DL2-18	DL2-19	DL2-20	DL2-21	DL2-22	DL2-23	DL2-24	DL2-25	DL2-26	DL2-27	DL2-28	DL2-29
Tyle	Lh	Lh	Lh	Lh	Lh	Lh	Lh	Lh	Lh	Lh	Lh	Lh	Lh	Lh	Lh
SiO_2 (wt. %)	44.45	45.21	43.38	43.63	43.18	43.45	43.34	44.29	42.75	44.4	44.26	44.14	42.83	43.54	44.11
TiO_2	0.14	0.13	0.15	0.15	0.12	0.12	0.17	0.13	0.24	0.15	0.09	0.14	0.12	0.13	0.13
Al_2O_3	3.14	3.84	3.69	3.51	3.02	3.4	3.46	3.23	4.2	4.04	2.72	3.56	3.22	3.6	3.28
FeO	8.37	8.4	8.8	8.81	9.07	8.55	9.06	8.75	10.45	8.63	7.67	8.2	9.1	8.19	8.67
MnO	0.14	0.14	0.14	0.14	0.15	0.14	0.15	0.14	0.18	0.15	0.12	0.13	0.15	0.13	0.14
MgO	40.82	39.58	40.44	40.45	41.72	41.66	40.67	40.29	37.63	39.17	42.68	40.71	41.78	41.5	40.48
CaO	2.86	2.62	3.3	3.2	2.69	2.6	3.07	3.1	4.38	3.02	2.42	3.01	2.73	2.83	3.12
Na_2O	0.07	0.06	0.09	0.07	0.05	0.06	0.06	0.07	0.13	0.24	0.04	0.07	0.06	0.07	0.07
K_2O	0	0	0.01	0.02	0	0.01	0	0	0.02	0.12	0	0.01	0.01	0	0
P_2O_5	0.01	0.01	0	0.01	0	0	0.01	0	0.01	0.06	0	0.02	0	0.01	0
LOI	0	0	0	0	0	0	0	0	0	0.01	0	0	0	0	0
Total	100	100	100	100	100	100	100	100	100	100	100	100	100	100	100
Mg#	0.9	0.89	0.89	0.89	0.89	0.9	0.89	0.89	0.87	0.89	0.91	0.9	0.89	0.9	0.89
Ba	nd	2	2	3	nd	1	nd	nd	4	38	2	14	2	1	nd
Co	108	104	111	112	111	114	112	106	92	109	115	111	111	116	106
Cr	3756	3246	3033	2731	2437	2757	2414	2282	2190	2770	3238	2758	2496	2913	2612
Cu	5	6	10	6	9	10	9	12	22	23	10	8	10	13	7
Ga	5	5	5	5	4	5	5	4	5	4	4	5	4	5	5
Hf	3	3	3	2	3	3	3	3	3	2	2	2	2	2	3
La	3	5	2	5	3	nd	2	nd	nd	5	3	2	2	4	5
Nb	1	2	1	1	2	2	2	2	2	6	1	2	2	1	1
Ni	1838	1727	1905	1907	1959	1998	1891	1874	1650	1886	2072	1953	1967	1996	1863
Pb	1	nd	2	2	2	2	1	nd	2	nd	1	2	2	1	2
Sc	16	14	19	17	13	14	13	15	17	17	13	16	11	15	15
Sr	26	16	18	20	16	17	14	17	22	78	18	25	13	18	17
V	72	71	76	76	62	68	81	69	81	75	62	75	62	74	72
Y	1	1	2	2	1	1	1	2	3	2	nd	2	1	1	2
Zn	52	50	52	48	44	50	49	42	45	59	47	52	48	51	42
Zr	7	5	6	6	5	4	4	5	10	12	3	5	4	5	6
Cpx	13	16	15	13	13	14	15	21	16	11	14	13	14	15	22
Opx	33	19	20	17	20	19	23	16	25	22	24	16	21	22	31
Ol	54	65	65	70	67	66	62	63	59	67	62	71	66	63	48
Total	100	100	100	100	100	100	100	100	100	100	100	100	100	100	100

Ol = olivine, Cpx = clinopyroxene, Opx = orthopyroxene

Table 4-1. Whole rock compositions of Dillo and Megado xenoliths (continued)

Locality	Dillo														
Sample	DL2-30	DL2-31	DL2-32	DL2-33	DL3-1	DL3-2	DL3-3	DL3-4	DL3-5	DL3-6	DL3-7	DL3-9	DL3-10	DL3-11A	DL3-11B
Tyle	Lh	Lh	Lh	Lh	Wb	Lh	Lh	Hz	Lh	Lh	Lh	Lh	Ol-Wb	Lh	Wb
SiO_2 (wt. %)	45.83	41.87	43.21	43.04	46.29	51.97	43.74	41.73	44.34	42.8	43.84	45.43	48.12	45.27	50.02
TiO_2	0.21	0.11	0.11	0.08	0.2	0.52	0.15	0.05	0.15	0.12	0.14	0.2	0.31	0.18	0.34
Al_2O_3	4.23	3.06	2.83	2.39	4.37	5.45	4.18	1.85	3.91	2.36	3.39	4.09	6.26	4.11	8.48
FeO	7.78	9.7	8.52	8.3	8.4	6.11	8.53	8.17	8.55	8.49	8.47	8.1	7.63	7.84	5.29
MnO	0.13	0.16	0.14	0.13	0.14	0.14	0.14	0.13	0.14	0.13	0.13	0.14	0.14	0.13	0.13
MgO	36.99	42.13	42.79	44.05	36.87	19.97	40.13	47.16	39.68	43.86	41.09	37.11	30.35	38.2	24.01
CaO	4.64	2.88	2.33	1.97	3.57	14.93	3.04	0.9	3.12	2.19	2.87	4.71	6.78	4.16	11.07
Na_2O	0.16	0.05	0.04	0.03	0.11	0.66	0.07	0	0.08	0.03	0.06	0.14	0.38	0.1	0.63
K_2O	0.01	0.02	0.03	0	0.03	0.03	0.01	0.01	0.02	0.01	0.01	0.03	0.02	0.01	0.03
P_2O_5	0.02	0.01	0	0.01	0.01	0.01	0.01	0.01	0.01	0.01	0	0.05	0.01	0	0
LOI	0	0	0	0	0	0.2	0	0	0	0	0	0	0	0	0
Total	100	100	100	100	100	100	100	100	100	100	100	100	100	100	100
Mg#	0.9	0.89	0.9	0.91	0.89	0.85	0.89	0.91	0.89	0.9	0.9	0.89	0.88	0.9	0.89
Ba	3	4	5	nd	17	22	15	nd	19	5	2	65	17	7	22
Co	96	108	117	123	100	55	112	123	106	121	116	104	84	100	58
Cr	2153	2466	2452	2341	3294	5042	3614	2444	2800	2572	2323	2814	2416	3032	3459
Cu	11	13	8	7	12	81	13	6	11	9	16	18	35	5	15
Ga	5	4	4	4	5	8	5	2	4	4	4	4	7	5	9
Hf	2	3	2	2	3	1	2	2	3	2	2	2	2	2	2
La	nd	nd	nd	nd	3	6	5	5	8	6	nd	3	2	2	5
Nb	2	1	1	1	3	3	1	2	2	2	1	2	2	1	2
Ni	1642	2000	2043	2192	1631	735	1899	2289	1848	2209	2050	1744	1287	1726	866
Pb	2	1	2	2	2	nd	2	nd	2	2	2	3	2	1	2
Sc	22	15	13	12	18	45	15	10	16	11	14	20	30	21	41
Sr	28	16	13	9	30	65	29	9	53	22	17	39	37	19	45
V	101	58	61	53	91	240	80	33	75	52	70	88	134	83	172
Y	4	1	1	nd	2	5	2	nd	2	nd	2	3	6	2	8
Zn	42	47	45	40	48	15	62	45	48	47	47	43	54	54	61
Zr	7	4	4	3	9	15	5	2	6	5	5	8	12	8	15
Cpx	13	11	9	9	65	17	15	4	15	10	14	22	33	19	53
Opx	10	17	15	15	35	38	24	8	26	13	22	28	45	29	47
Ol	77	72	75	75	0	44	61	88	59	77	65	50	22	52	0
Total	100	100	100	100	100	100	100	100	100	100	100	100	100	100	100

Ol = olivine, Cpx = clinopyroxene, Opx = orthopyroxene

Table 4-1. Whole rock compositions of Dillo and Megado xenoliths (continued)

Locality	Dillo														
Sample	DL3-12	DL3-13	DL3-14	DL3-15	DL3-16	DL3-17	DL3-18	DL3-19	DL3-20	DL3-21	DL3-22	DL3-23	DL3-24	DL3-25	DL3-26
Tyle	Lh	Lh	Lh	Ol-Wb	Ol-Wb	Lh	Lh	Lh	Wb	Ol-Wb	Lh	Lh	Lh	Lh	Lh
SiO_2 (wt. %)	42.97	42.44	43.91	51.66	51.26	43.85	42.66	43.59	50.8	50.36	45.38	44.5	42.67	42.13	44.09
TiO_2	0.08	0.07	0.15	0.19	0.2	0.17	0.15	0.17	0.48	0.25	0.15	0.13	0.11	0.12	0.12
Al_2O_3	3.18	2.51	3.72	3.97	4.14	3.84	3.48	4	7.97	4.45	3.9	3.5	3.2	2.65	3.15
FeO	7.99	8.2	8.86	8.6	8.65	9.05	9.49	9.2	6.83	9.29	8.37	8.17	8.71	8.89	8.63
MnO	0.13	0.13	0.14	0.15	0.15	0.15	0.15	0.15	0.16	0.17	0.14	0.13	0.14	0.14	0.14
MgO	43.31	44.79	39.72	33.84	33.6	39.19	41.26	39.3	23.4	32.73	38.83	40.41	42.62	44.03	41.08
CaO	2.23	1.83	3.38	1.53	1.91	3.62	2.73	3.44	9.61	2.6	3.1	3.06	2.51	1.98	2.73
Na_2O	0.06	0.02	0.08	0.05	0.07	0.09	0.04	0.11	0.68	0.13	0.11	0.08	0.04	0.02	0.06
K_2O	0.04	0.01	0.01	0	0.01	0.02	0.02	0.02	0.04	0.02	0.01	0.01	0	0.02	0
P_2O_5	0.01	0	0.02	0	0	0.02	0.02	0.01	0.02	0.01	0.01	0.01	0	0.01	0
LOI	0	0	0	0	0	0	0	0	0.01	0	0	0	0	0	0
Total	100	100	100	100	100	100	100	100	100	100	100	100	100	100	100
Mg#	0.91	0.91	0.89	0.88	0.87	0.89	0.89	0.88	0.86	0.86	0.89	0.9	0.9	0.9	0.9
Ba	28	nd	4	3	4	34	5	1	30	16	4	5	nd	14	nd
Co	125	121	112	71	68	103	112	105	53	66	110	113	116	125	117
Cr	2832	2776	2614	3703	3772	2659	2570	2605	2991	3936	3028	2961	2636	2733	2448
Cu	8	9	9	8	7	14	10	21	20	8	30	13	11	10	12
Ga	4	3	5	6	6	5	4	5	9	7	5	4	4	3	5
Hf	2	2	2	3	4	3	3	3	2	4	2	2	3	3	3
La	4	4	4	nd	8	nd	1	2	nd	nd	nd	1	1	6	3
Nb	2	1	2	1	2	1	2	1	2	2	2	2	2	1	2
Ni	2232	2251	1914	1003	977	1832	1954	1869	772	962	1809	1930	2109	2187	1970
Pb	1	1	1	3	3	nd	2	nd	1	2	2	2	1	1	2
Sc	11	11	13	20	18	17	14	19	32	20	15	15	13	12	14
Sr	24	8	25	9	12	24	21	20	50	28	22	18	13	23	18
V	57	51	75	91	94	76	63	77	175	95	79	73	64	56	69
Y	1	nd	2	nd	nd	2	1	2	7	nd	2	2	1	nd	1
Zn	51	58	52	39	36	47	49	49	18	37	47	51	52	67	48
Zr	3	2	7	2	4	6	6	7	18	5	6	4	5	4	3
Cpx	11	9	16	8	10	17	13	17	46	14	15	15	12	9	13
Opx	16	12	22	75	73	22	17	22	54	68	32	25	15	12	23
Ol	73	79	62	16	17	61	70	62	0	19	53	60	73	79	64
Total	100	100	100	100	100	100	100	100	100	100	100	100	100	100	100

Ol = olivine, Cpx = clinopyroxene, Opx = orthopyroxene

Table 4-1. Whole rock compositions of Dillo and Megado xenoliths (continued)

Locality	Dillo				Megado										
Sample	DL3-27	DL3-28	DL3-29	DL4-1	MG1-1	MG1-2	MG1-3	MG1-4	MG1-5	MG1-6	MG1-7	MG1-9	MG1-11	MG1-12	MG1-13
Tyle	Lh	Lh	Lh	Lh	Hz	Lh	Lh	Hz	Ol-Wb	Lh	Lh	Lh	Ol-Wb	Lh	Lh
SiO_2 (wt. %)	42.85	44.05	43.82	43.79	41.72	42.84	43.96	42.93	49.29	43.47	43.01	44.45	49.57	43.79	43.12
TiO_2	0.11	0.21	0.18	0.11	0.05	0.11	0.1	0.02	0.13	0.1	0.08	0.12	0.26	0.07	0.01
Al_2O_3	2.97	3.75	3.39	3.09	1.64	3.08	3.05	1.2	5.87	2.46	2.49	3.85	8.14	3.28	1.41
FeO	8.76	8.98	8.96	8.58	8.17	9.49	8.3	7.5	6.9	8.53	7.88	8.34	7.03	7.89	7.07
MnO	0.14	0.14	0.14	0.14	0.12	0.14	0.13	0.12	0.13	0.14	0.13	0.14	0.15	0.14	0.12
MgO	42.76	39.2	40.47	41.83	47.53	41.68	41.7	47.68	30.02	43.46	43.83	40.28	28.6	41.73	47.5
CaO	2.35	3.56	2.95	2.41	0.76	2.6	2.71	0.53	7.38	1.75	2.42	2.7	5.93	3	0.71
Na_2O	0.05	0.11	0.08	0.05	0	0.05	0.06	0	0.28	0.06	0.09	0.08	0.27	0.09	0.03
K_2O	0.01	0	0	0	0	0	0	0.01	0	0.02	0.06	0.03	0.02	0.01	0.03
P_2O_5	0	0	0	0	0	0	0	0	0	0.01	0.01	0.01	0.02	0	0.01
LOI	0	0	0	0	0	0	0	0	0	0	0	0	0	0	0
Total	100	100	100	100	100	100	100	100	100	100	100	100	100	100	100
Mg#	0.9	0.89	0.89	0.9	0.91	0.89	0.9	0.92	0.89	0.9	0.91	0.9	0.88	0.9	0.92
Ba	nd	2	2	nd	nd	nd	nd	nd	2	10	18	8	6	17	15
Co	119	110	112	113	128	122	118	126	69	124	122	110	64	115	124
Cr	2465	2619	2358	2433	1807	2184	2563	2514	3954	2734	3310	3280	4008	3213	3640
Cu	11	19	13	17	7	8	9	3	8	21	9	13	9	14	8
Ga	4	5	4	4	3	4	4	2	6	3	3	5	10	4	2
Hf	3	3	3	2	2	3	2	2	2	2	2	3	3	2	2
La	4	nd	4	1	nd	nd	3	1	nd	1	4	nd	3	3	8
Nb	1	2	1	2	1	2	2	1	2	1	2	2	2	3	2
Ni	2053	1888	1935	2011	2389	2055	2011	2369	896	2072	2245	1932	842	2004	2363
Pb	2	2	3	1	2	1	nd	2	1	4	2	nd	2	2	2
Sc	12	18	15	13	6	15	16	7	28	13	12	14	35	16	6
Sr	11	20	18	13	4	7	6	11	28	25	59	18	30	47	39
V	61	81	75	66	34	69	68	31	120	58	51	78	173	68	33
Y	nd	2	2	1	nd	nd	1	nd	1	nd	nd	2	6	1	nd
Zn	45	50	51	45	44	56	47	42	47	46	60	54	37	48	49
Zr	4	9	8	4	1	1	2	2	3	2	5	4	9	3	nd
Cpx	11	17	14	12	4	12	13	3	34	9	12	13	30	14	4
Opx	16	23	22	22	7	16	21	12	48	19	12	27	65	19	13
Ol	73	60	64	67	89	71	66	85	18	73	76	59	5	67	83
Total	100	100	100	100	100	100	100	100	100	100	100	100	100	100	100

Ol = olivine, Cpx = clinopyroxene, Opx = orthopyroxene

Table 4-1. Whole rock compositions of Dillo and Megado xenoliths (continued)

Locality	Megado														
Sample	MG1-14	MG1-15	MG1-16	MG1-17	MG1-19	MG1-20	MG1-21	MG1-22	MG1-23	MG1-25	MG1-26	MG1-27	MG1-28	MG1-29	MG1-30
Tyle	Hz	Lh	Lh	Du	Lh	Lh	Hz	Hz	Lh	Lh	Hz	Lh	Lh	Hz	Lh
SiO_2 (wt. %)	42.07	42.87	42	42.57	46.85	44.68	42.16	43.47	41.97	43.12	42.88	45.73	42.36	42.66	43.66
TiO_2	0.09	0.02	0.01	0.07	0.1	0	0.02	0.1	0.06	0.02	0.02	0.14	0.03	0.02	0.07
Al_2O_3	3.14	1.42	1.1	3.12	4.27	1.47	1.48	2.9	2.17	1.42	1.81	4.96	1.75	1.01	2.65
FeO	9.1	7.47	7.26	8.03	7.08	7.08	7.91	7.8	7.61	7.39	7.21	7.09	7.8	7.06	7.75
MnO	0.15	0.13	0.12	0.13	0.12	0.12	0.12	0.13	0.12	0.12	0.12	0.12	0.13	0.12	0.13
MgO	42.87	46.93	49.04	43.66	35.68	45.63	47.63	42.03	46.48	47.15	47.2	36.93	46.84	48.07	43.37
CaO	2.5	1.06	0.46	2.37	5.71	1.02	0.63	3.48	1.46	0.76	0.72	4.73	0.97	1.01	2.31
Na_2O	0.04	0.03	0	0.04	0.17	0	0.02	0.08	0.04	0	0.02	0.22	0.04	0.01	0.04
K_2O	0	0.05	0.01	0	0.01	0	0.02	0.02	0.08	0.02	0.02	0.03	0.06	0.03	0
P_2O_5	0.04	0.02	0	0	0	0	0	0	0.01	0	0	0.05	0.02	0.01	0.01
LOI	0	0	0	0	0	0	0.01	0	0	0	0	0	0	0	0
Total	100	100	100	100	100	100	100	100	100	100	100	100	100	100	100
Mg#	0.89	0.92	0.92	0.91	0.9	0.92	0.92	0.91	0.92	0.92	0.92	0.9	0.92	0.92	0.91
Ba	2	23	nd	nd	5	nd	17	2	20	2	nd	86	14	7	nd
Co	116	124	135	126	98	119	128	115	129	127	128	101	126	133	114
Cr	2634	3517	2392	2862	2923	3363	3354	2478	3490	4369	2980	3865	2451	2497	3114
Cu	7	6	12	11	12	4	4	24	9	5	5	17	6	9	12
Ga	4	2	2	4	5	2	2	4	3	2	2	5	2	2	3
Hf	2	2	2	2	2	2	2	2	2	2	2	2	2	2	2
La	4	3	1	nd	8	3	2	5	4	nd	2	12	8	5	nd
Nb	2	5	1	1	2	1	1	1	3	2	1	3	4	1	1
Ni	1981	2298	2532	2190	1516	2220	2404	2124	2401	2337	2344	1705	2397	2449	2110
Pb	2	1	1	2	2	3	1	2	nd	1	2	3	1	4	nd
Sc	12	11	4	10	22	12	4	16	7	7	8	20	6	7	14
Sr	10	52	7	5	27	7	31	17	54	17	21	104	42	23	9
V	60	33	25	63	99	47	36	75	40	38	34	101	29	28	60
Y	1	nd	nd	nd	nd	nd	nd	2	nd	nd	nd	4	nd	nd	nd
Zn	52	47	48	58	41	43	57	46	67	58	55	68	59	45	50
Zr	2	3	nd	1	2	nd	1	2	5	1	1	10	7	1	1
Cpx	4	12	5	2	11	26	5	3	16	7	4	23	5	5	11
Opx	13	12	11	6	14	32	22	9	14	7	14	31	10	8	18
Ol	83	76	84	92	75	42	73	88	70	85	82	46	85	87	71
Total	100	100	100	100	100	100	100	100	100	100	100	100	100	100	100

Ol = olivine, Cpx = clinopyroxene, Opx = orthopyroxene

Table 4-1. Whole rock compositions of Dillo and Megado xenoliths (continued)

Locality	Megado														
Sample	MG1-31	MG1-32	MG1-33	MG1-34	MG1-35	MG1-36	MG1-37	MG1-38	MG1-40	MG1-41	MG1-42	MG1-43	MG1-44	MG1-45	MG2-1
Tyle	Hz	Lh	Hz	Lh	Hz	Lh	Lh	Lh	Lh	Lh	Lh	Hz	Lh	Lh	Lh
SiO_2 (wt. %)	42.57	44.05	41.47	42.05	42.29	42.32	44.52	43.91	42.69	43.54	43.62	43.22	42.69	43.26	44.92
TiO_2	0.03	0.07	0.04	0.04	0.02	0.06	0.07	0.07	0.08	0.08	0.27	0.01	0.01	0.08	0.13
Al_2O_3	1.22	2.53	1.76	1.96	1.35	2.31	2.51	2.78	2.12	2.78	2.89	1.22	1.86	2.5	3.32
FeO	7.24	7.43	8.18	9.14	7.42	8.24	7.29	7.57	8.48	8.42	8.08	7.16	8.05	8.06	8.6
MnO	0.11	0.12	0.13	0.15	0.12	0.14	0.12	0.12	0.14	0.14	0.13	0.11	0.13	0.13	0.14
MgO	48.28	43.42	47.58	45.43	48.23	45.06	43.32	43.25	44.86	42.41	41.96	47.51	45.81	43.51	38.53
CaO	0.53	2.34	0.82	1.19	0.53	1.76	2.11	2.25	1.58	2.56	2.82	0.77	1.28	2.41	4.21
Na_2O	0	0.04	0	0.02	0	0.05	0.03	0.04	0.02	0.04	0.1	0	0.09	0.03	0.12
K_2O	0.01	0	0.01	0.01	0.03	0.03	0.01	0	0.01	0	0.11	0.01	0.05	0	0.02
P_2O_5	0.01	0	0.01	0.01	0.01	0.03	0.01	0.01	0	0.01	0.01	0	0.02	0	0.01
LOI	0	0	0	0	0	0	0	0	0	0.01	0	0	0.01	0.01	0
Total	100	100	100	100	100	100	100	100	100	100	100	100	100	100	100
Mg#	0.92	0.91	0.91	0.9	0.92	0.91	0.91	0.91	0.9	0.9	0.9	0.92	0.91	0.91	0.89
Ba	nd	nd	2	22	6	9	1	nd	2	nd	17	nd	43	1	4
Co	133	118	132	116	131	122	118	116	126	112	117	131	121	118	117
Cr	2602	2987	1745	2387	1950	2580	2820	3409	1483	2650	3461	3388	3121	2673	2447
Cu	3	12	4	3	11	7	13	14	13	8	20	4	7	9	14
Ga	2	3	3	3	2	3	3	4	3	4	4	2	2	4	4
Hf	2	2	2	3	2	2	2	2	2	2	2	2	2	2	2
La	4	nd	1	10	nd	6	2	3	nd	1	5	1	40	36	34
Nb	1	1	2	1	2	2	2	2	1	1	3	1	2	1	2
Ni	2447	2131	2451	2167	2494	2221	2128	2113	2308	2046	2150	2442	2200	2021	1979
Pb	3	3	2	1	1	nd	3	2	2	3	2	2	2	2	2
Sc	6	13	5	7	5	8	12	13	9	13	15	9	8	12	20
Sr	10	8	10	46	26	52	12	11	9	6	62	6	65	8	18
V	27	61	32	37	26	46	59	62	45	59	72	39	35	62	77
Y	nd	nd	nd	nd	nd	nd	nd	nd	nd	nd	2	nd	nd	0	1
Zn	47	46	47	46	55	58	51	52	39	44	58	51	63	47	46
Zr	1	2	1	2	2	2	2	2	2	1	9	nd	nd	1	3
Cpx	3	11	4	6	3	8	10	11	8	12	14	4	7	11	19
Opx	10	20	6	11	9	11	23	20	13	18	17	13	11	15	23
Ol	87	69	90	84	89	81	67	69	79	70	70	83	82	73	57
Total	100	100	100	100	100	100	100	100	100	100	100	100	100	100	100

Ol = olivine, Cpx = clinopyroxene, Opx = orthopyroxene

Table 4-1. Whole rock compositions of Dillo and Megado xenoliths (continued)

Locality	Megado														
Sample	MG2-2	MG2-4	MG2-5	MG2-6	MG2-8	MG2-9	MG2-10	MG2-11	MG2-12	MG2-13	MG2-14	MG2-15	MG2-16	MG3-1	MG3-2
Tyle	Lh	Hz	Du	Lh	Lh	Lh	Lh	Lh	Lh	Lh	Hz	Lh	Lh	Lh	Lh
SiO_2 (wt. %)	43.28	42.88	40.67	44.31	43.65	43.53	42.94	43.28	43.64	43.42	42.75	43.84	44.65	43.25	44.35
TiO_2	0.09	0.02	0.04	0.11	0.1	0.08	0.06	0.07	0.06	0.02	0.01	0.5	0.09	0.06	0.09
Al_2O_3	1.8	1.52	1.72	3.27	3.01	2.5	2.23	2.32	2.6	1.85	1.26	5.42	3.41	2.52	2.83
FeO	8.44	7.69	8.69	7.45	7.76	7.89	8.29	8.14	7.39	7.21	6.88	11.72	7.89	8.31	7.9
MnO	0.12	0.11	0.13	0.12	0.13	0.13	0.13	0.13	0.12	0.12	0.11	0.17	0.13	0.12	0.13
MgO	44.92	47.01	48.06	41.79	42.83	43.07	44.79	43.97	43.99	45.64	48.21	29.9	41.11	43.78	41.99
CaO	1.31	0.71	0.69	2.84	2.41	2.68	1.51	2.02	2.13	1.62	0.69	8.03	2.64	1.93	2.65
Na_2O	0.01	0.03	0	0.09	0.06	0.05	0.03	0.03	0.04	0	0.02	0.3	0.06	0.03	0.05
K_2O	0.01	0.02	0	0.01	0.04	0.05	0.01	0.02	0.02	0.04	0.04	0.07	0	0	0
P_2O_5	0.02	0.01	0.01	0	0.01	0.02	0	0.02	0	0.07	0.03	0.04	0.01	0	0
LOI	0	0	0	0	0	0	0	0	0	0	0	0	0	0	0
Total	100	100	100	100	100	100	100	100	100	100	100	100	100	100	100
Mg#	0.91	0.92	0.91	0.91	0.91	0.91	0.91	0.91	0.91	0.92	0.93	0.82	0.9	0.9	0.91
Ba	nd	25	nd	2	23	2	5	9	nd	4	10	34	nd	2	1
Co	128	134	138	118	123	124	127	122	121	125	127	107	116	122	117
Cr	2517	2414	1818	3016	3147	2082	2141	1934	2948	2765	2797	1244	3112	3231	2480
Cu	8	3	5	9	24	19	12	18	19	6	6	39	10	13	16
Ga	4	2	3	4	4	3	3	4	3	3	2	8	4	4	3
Hf	2	2	2	2	2	2	2	2	2	2	2	3	2	2	2
La	33	37	38	37	33	34	35	34	35	32	44	54	34	38	38
Nb	1	2	1	2	1	1	1	2	2	1	2	5	1	1	1
Ni	2256	2383	2507	2097	2187	2263	2307	2164	2208	2339	2406	990	1925	2176	2165
Pb	2	1	4	3	2	2	2	2	2	1	3	2	nd	1	1
Sc	10	5	4	14	10	15	12	12	11	10	4	29	16	10	13
Sr	11	39	4	20	28	13	11	12	16	17	77	60	5	7	6
V	53	28	32	68	68	64	47	52	63	46	27	159	77	56	69
Y	nd	nd	nd	1	1	1	nd	nd	nd	nd	nd	4	1	nd	1
Zn	64	59	53	49	51	43	42	35	44	44	42	66	51	62	49
Zr	1	1	nd	3	3	1	1	2	1	nd	nd	16	1	1	1
Cpx	6	4	3	14	12	12	7	9	10	7	3	38	13	9	12
Opx	17	13	3	22	19	15	15	16	18	15	10	16	27	17	22
Ol	77	84	93	64	69	72	78	75	72	78	86	46	61	74	65
Total	100	100	100	100	100	100	100	100	100	100	100	100	100	100	100

Ol = olivine, Cpx = clinopyroxene, Opx = orthopyroxene

Table 4-1. Whole rock compositions of Dillo and Megado xenoliths (continued)

Locality	Megado														
Sample	MG3-3	MG3-4	MG3-5	MG3-6	MG3-7	MG3-8	MG3-9	MG3-10	MG3-11	MG3-12	MG3-13	MG3-14	MG3-15	MG3-16	MG3-17
Tyle	Hz	Lh	Lh	Hz	Lh	Lh	Hz	Lh	Lh	Lh	Lh	Du	Gb	Du	Lh
SiO_2 (wt. %)	42.98	42.75	43.01	44.5	44.45	44.14	43.65	43.57	44.1	45.62	43.45	41.02	52.21	41.75	43.39
TiO_2	0.04	0.04	0.02	0.01	0.21	0.07	0.03	0.09	0.03	0.13	0.01	0.03	0.72	0.01	0.1
Al_2O_3	2.37	1.26	1.8	1.25	3.59	2.96	1.23	3.08	2.62	3.25	1.71	1.2	10.79	1.27	3
FeO	7.54	7.34	7.6	7.08	7.49	7.51	7.64	7.79	7.19	8.53	7.67	7.5	6.83	7.6	8.03
MnO	0.12	0.11	0.12	0.11	0.13	0.12	0.12	0.13	0.12	0.14	0.12	0.12	0.2	0.12	0.13
MgO	44.89	47.91	46.18	46.45	40.97	42.6	46.81	43.01	43.86	39.07	45.72	49.21	8.24	48.57	42.72
CaO	2.04	0.58	1.27	0.57	2.82	2.55	0.5	2.29	2.04	3.16	1.32	0.76	18.11	0.66	2.58
Na_2O	0.02	0	0	0	0.1	0.04	0	0.04	0.03	0.08	0	0.03	1.81	0	0.04
K_2O	0	0.01	0.01	0.01	0.08	0	0.01	0	0	0.01	0	0.03	0.44	0.01	0.01
P_2O_5	0	0	0	0.01	0.01	0	0	0	0	0	0	0.1	0.63	0	0
LOI	0	0	0	0	0.15	0	0	0	0	0	0	0	0.01	0	0
Total	100	100	100	100	100	100	100	100	100	100	100	100	100	100	100
Mg#	0.91	0.92	0.92	0.92	0.91	0.91	0.92	0.91	0.92	0.89	0.91	0.92	0.68	0.92	0.91
Ba	nd	nd	nd	15	26	nd	nd	4	nd	nd	nd	33	57	nd	1
Co	128	125	128	125	112	114	129	120	111	109	118	137	18	128	122
Cr	2857	2546	2406	2970	3617	3733	3281	2702	4054	2629	3311	1462	81	2127	2131
Cu	4	4	10	6	12	14	6	10	15	11	7	9	13	7	9
Ga	3	2	3	2	4	4	2	4	3	4	3	2	17	2	4
Hf	2	2	2	2	2	2	2	2	2	3	2	2	1	2	2
La	38	35	37	40	41	36	30	37	37	31	27	47	38	39	38
Nb	1	2	1	1	3	1	1	1	1	1	1	4	22	1	1
Ni	2289	2383	2349	2280	1944	2057	2281	2139	2129	1860	2238	2474	52	2521	2173
Pb	1	nd	1	3	nd	1	2	2	nd	1	nd	nd	15	1	3
Sc	14	3	8	4	18	11	8	12	12	17	8	2	16	2	14
Sr	5	7	8	19	39	10	6	8	17	11	4	115	388	16	13
V	48	30	43	31	79	64	34	68	52	74	45	18	137	23	68
Y	nd	nd	nd	nd	2	1	nd	nd	nd	1	nd	2	16	nd	1
Zn	45	43	43	45	53	54	53	50	53	44	45	54	98	46	49
Zr	nd	nd	nd	2	7	2	2	1	nd	4	nd	2	68	nd	3
Cpx	3	9	6	3	14	12	3	11	10	15	6	3	72	3	12
Opx	11	14	14	21	25	21	17	20	21	31	16	3	28	6	18
Ol	86	77	80	76	61	67	81	69	69	54	78	94	0	91	70
Total	100	100	100	100	100	100	100	100	100	100	100	100	100	100	100

Ol = olivine, Cpx = clinopyroxene, Opx = orthopyroxene

Table 4-1. Whole rock compositions of Dillo and Megado xenoliths (continued

Locality	Megado				
Sample	MG3-18	MG3-19	MG3-20	MG3-21	MG3-22
Tyle	Lh	Lh	Wb	Lh	Lh
SiO_2 (wt. %)	43.03	45.02	50.14	43.59	41.73
TiO_2	0.02	0.12	0.53	0.08	0.06
Al_2O_3	1.62	3.19	6.66	2.92	1.88
FeO	7.41	7.6	9.94	7.91	7.34
MnO	0.12	0.13	0.19	0.13	0.12
MgO	46.58	40.43	23.06	42.99	47.54
CaO	1.17	3.41	9.12	2.31	1.3
Na_2O	0.01	0.09	0.34	0.04	0.02
K_2O	0.02	0.01	0	0.01	0.02
P_2O_5	0.01	0	0.01	0.01	0
LOI	0	0	0	0	0
Total	100	100	100	100	100
Mg#	0.92	0.91	0.81	0.91	0.92
Ba	62	nd	16	nd	52
Co	124	113	64	119	132
Cr	2670	2870	1999	2737	7613
Cu	8	16	16	10	8
Ga	2	4	11	4	3
Hf	2	2	3	2	2
La	47	34	37	40	41
Nb	3	1	2	1	1
Ni	2348	2019	377	2122	2403
Pb	3	2	2	2	1
Sc	7	19	50	12	8
Sr	38	12	33	8	22
V	38	80	259	66	54
Y	nd	2	7	1	nd
Zn	48	48	48	47	67
Zr	3	3	17	1	3
Cpx	6	16	43	11	6
Opx	13	25	57	19	6
Ol	81	59	0	70	88
Total	100	100	100	100	100

Ol = olivine, Cpx = clinopyroxene, Opx = orthopyroxene

Table 4-2. Representative mineral compositions of Dillo and Megado xenoliths

Sample	DL2-15					DL2-8					DL2-9				DL3-10		
Type	Lh					Lh					Lh				Ol-Wb		
Mineral	Ol	Cpx	Opx	Amph	Sp	Ol	Cpx	Opx	Amph	Sp	Ol	Cpx	Opx	Amph	Cpx	Opx	Sp
No. of analyses	3	6	2	5	3	3	3	3	2	2	3	1	2	2	3	2	3
SiO_2	40.81	52.23	55.72	43.00		40.70	51.71	55.60	42.65		40.67	51.34	55.37	42.69	51.66	55.07	
TiO_2	0.00	0.70	0.10	2.57	0.12	0.01	0.85	0.12	3.42	0.09	0.01	0.86	0.13	3.51	0.62	0.10	0.12
Al_2O_3	0.00	6.57	3.49	14.54	54.98	0.00	6.49	3.42	14.36	59.60	0.01	6.81	3.70	14.30	6.81	4.36	61.36
FeO	10.22	2.63	6.32	3.93	11.05	10.49	2.64	6.69	4.20	11.62	10.48	2.69	6.74	4.27	3.06	7.82	10.98
MnO	0.15	0.09	0.13	0.06	0.07	0.14	0.09	0.17	0.05	0.09	0.14	0.03	0.12	0.09	0.09	0.17	0.11
MgO	49.88	14.99	34.16	17.64	0.39	49.57	14.85	34.07	17.34	0.42	49.60	14.67	33.71	17.21	15.39	32.77	0.38
CaO	0.05	19.97	0.48	10.35		0.04	21.05	0.37	11.11		0.03	21.05	0.77	11.11	20.30	0.52	
Na_2O	0.01	2.06	0.08	4.04		0.01	1.90	0.04	3.95		0.00	1.90	0.09	3.89	1.77	0.09	
K_2O		0.01	0.01	0.18			0.00	0.01	0.13			0.00	0.00	0.10	0.00	0.01	
Cr_2O_3	0.01	0.78	0.24	1.02	12.46	0.00	0.55	0.16	0.68	7.20	0.00	0.71	0.23	0.66	0.37	0.17	5.08
NiO	0.35			0.12		0.41			0.10		0.40			0.12			
Total	101.48	100.02	101.82	97.44	99.52	101.37	100.13	101.68	97.99	100.00	101.33	100.06	100.87	97.95	100.06	101.08	98.22

Sample	DL2-19					DL2-13			DL2-33					DL2-28			
Type	Lh					Lh			Lh					Lh			
Mineral	Ol	Cpx	Opx	Amph	Sp	Ol	Cpx	Amph	Ol	Cpx	Opx	Amph	Sp	Ol	Cpx	Opx	Sp
No. of analyses	2	2	2	3	2	2	4	3	2	3	2	3	1	4	6	4	2
SiO_2	40.76	52.05	55.91	42.86		40.33	52.38	43.08	41.00	52.40	56.08	43.30		40.90	52.03	55.47	
TiO_2	0.01	0.72	0.12	3.52	0.08	0.01	0.66	3.17	0.01	0.56	0.10	2.53	0.05	0.01	0.60	0.12	0.13
Al_2O_3	0.00	6.85	3.58	14.16	59.04	0.00	6.40	14.32	0.01	6.20	3.52	14.60	57.47	0.03	6.38	3.82	58.31
FeO	10.17	2.58	6.70	4.23	11.12	10.48	2.70	4.01	10.26	2.58	6.67	3.96	11.65	10.07	2.70	6.41	10.31
MnO	0.16	0.07	0.14	0.07	0.10	0.14	0.07	0.03	0.14	0.04	0.12	0.06	0.00	0.16	0.07	0.11	0.00
MgO	49.56	14.59	34.17	17.16	0.44	49.36	15.02	17.61	49.97	15.04	34.19	17.55	0.43	50.10	15.83	34.21	0.43
CaO	0.02	20.61	0.38	10.92		0.02	20.58	10.87	0.03	20.72	0.40	10.97		0.07	20.20	0.58	
Na_2O	0.00	2.14	0.03	4.01		0.02	1.98	3.76	0.00	1.95	0.04	3.57		0.01	1.59	0.09	
K_2O		0.01	0.01	0.22			0.00	0.30		0.00	0.00	0.62			0.00	0.00	
Cr_2O_3	0.03	0.70	0.24	0.75	8.20	0.01	0.55	0.67	0.02	0.75	0.25	0.83	9.60	0.02	0.63	0.25	9.78
NiO	0.41			0.10		0.39		0.11	0.42			0.10		0.34			
Total	101.10	100.32	101.29	98.01	100.01	100.76	100.34	97.93	101.85	100.24	101.34	98.08	100.06	101.72	100.02	101.07	100.42

Ol = olivine, Cpx = clinopyroxene, Opx = orthopyroxene, Amph = amphibole, Sp = spinel

Table 4-2. Representative mineral compositions of Dillo and Megado xenoliths (continued)

Sample	MG3-20		MG3-19				MG3-12				MG2-16				MG2-5			
Type	Wb		Lh				Lh				Lh				Du			
Mineral	Cpx	Opx	Ol	Cpx	Opx	Sp	Ol	Cpx	Opx	Sp	Ol	Cpx	Opx	Sp	Ol	Cpx	Opx	Sp
No. of analyses	3	4	3	2	2	2	3	3	3	2	3	3	2	3	3	4	5	2
SiO_2	48.91	52.14	40.78	52.14	55.54		40.49	52.08	55.19		40.55	52.08	54.90		40.75	52.14	55.35	
TiO_2	1.15	0.14	0.00	0.61	0.10	0.11	0.00	0.57	0.11	0.13	0.01	0.50	0.13	0.06	0.00	0.60	0.13	0.16
Al_2O_3	8.50	6.62	0.01	6.39	4.16	58.65	0.02	6.44	4.13	58.41	0.00	6.53	4.50	58.56	0.02	6.42	4.12	56.93
FeO	4.53	12.07	10.35	2.56	6.43	10.61	11.03	2.68	6.80	10.72	10.58	2.49	6.63	10.92	10.26	2.70	6.39	10.64
MnO	0.09	0.23	0.14	0.05	0.16	0.00	0.14	0.07	0.15	0.00	0.13	0.09	0.19	0.00	0.13	0.07	0.14	0.00
MgO	13.33	29.33	49.78	15.36	33.89	0.38	49.72	15.55	33.93	0.42	49.62	15.18	33.48	0.39	50.05	15.66	33.91	0.37
CaO	21.53	0.34	0.08	20.47	0.48		0.03	20.14	0.50		0.03	20.91	0.69		0.06	19.99	0.61	
Na_2O	1.33	0.02	0.01	1.80	0.07		0.00	1.81	0.09		0.00	1.69	0.08		0.01	1.79	0.09	
K_2O	0.00	0.00		0.00	0.00			0.00	0.00			0.00	0.00			0.00	0.00	
Cr_2O_3	0.30	0.21	0.02	0.66	0.25	9.18	0.01	0.72	0.28	9.13	0.02	0.67	0.36	9.10	0.02	0.82	0.33	10.90
NiO			0.35				0.41				0.40				0.38			
Total	99.68	101.10	101.53	100.04	101.08	100.21	101.84	100.04	101.18	99.98	101.34	100.14	100.96	99.93	101.67	100.20	101.07	100.23

Sample	MG1-14			MG1-1				MG1-4				MG1-11			MG1-5		
Type	Hz			Hz				Hz				Ol-Wb			Ol-Wb		
Mineral	Ol	Cpx	Opx	Ol	Cpx	Opx	Sp	Ol	Cpx	Opx	Sp	Cpx	Opx	Sp	Cpx	Opx	Sp
No. of analyses	6	4	6	4	6	4	3	5	5	4	4	5	4	3	7	3	3
SiO_2	41.02	53.67	56.36	40.86	53.07	56.16		41.20	53.68	56.80		51.71	54.99		52.03	54.83	
TiO_2	0.00	0.05	0.03	0.01	0.29	0.09	0.13	0.01	0.08	0.04	0.10	0.63	0.13	0.10	0.25	0.06	0.08
Al_2O_3	0.01	4.20	2.86	0.00	3.94	3.20	49.22	0.01	3.17	2.27	34.04	6.88	4.54	61.60	6.37	4.94	60.74
FeO	8.96	2.12	5.59	9.14	2.16	5.70	10.53	8.55	2.18	5.27	12.97	2.85	6.74	10.31	3.11	6.34	9.90
MnO	0.15	0.10	0.15	0.14	0.07	0.14	0.12	0.12	0.07	0.13	0.21	0.08	0.12	0.07	0.10	0.15	0.08
MgO	51.00	16.73	35.01	50.77	16.82	35.00	0.30	50.84	17.35	35.23	0.21	15.58	33.07	0.45	16.94	33.46	0.34
CaO	0.04	20.60	0.56	0.03	22.36	0.42		0.04	21.53	0.56		19.98	0.62		19.50	0.97	
Na_2O	0.00	1.66	0.08	0.00	0.90	0.02		0.01	1.04	0.06		1.60	0.11		1.39	0.12	
K_2O		0.01	0.00		0.00	0.01			0.01	0.01		0.01	0.01		0.01	0.00	
Cr_2O_3	0.01	1.26	0.43	0.00	0.84	0.38	19.48	0.04	1.03	0.44	35.65	0.48	0.22	6.58	0.48	0.24	6.90
NiO	0.40			0.38				0.41									
Total	101.60	100.38	101.06	101.32	100.44	101.12	99.47	101.25	100.14	100.81	99.95	99.80	100.55	100.02	100.19	101.11	100.09

Ol = olivine, Cpx = clinopyroxene, Opx = orthopyroxene, Amph = amphibole, Sp = spinel

Table 4-3. Dillo and Megado clinopyroxene major oxide and trace element compositions

Locality	Dillo														
Sample	DL2-1	DL2-2	DL2-4	DL2-5	DL2-8	DL2-9	DL2-13	DL2-14	DL2-22	DL2-24	DL2-33	DL3-4	DL3-10	DL3-20	DL3-21
Type	Lh	Wb	Lh	Lh	Lh	Lh	Lh	Lh	Lh	Lh	Lh	Hz	Wb	Wb	Wb
TiO_2 (wt. %)	0.81	0.94	0.71	0.28	0.71	0.63	0.82	0.20	0.66	0.74	0.60	0.24	0.61	0.79	0.65
SiO_2	52.16	49.48	52.40	52.75	52.19	52.43	51.96	53.34	52.15	51.83	52.02	51.80	52.15	51.64	51.92
K_2O	0.00	0.01	0.00	0.00	0.00	0.00	0.00	0.00	0.00	0.00	0.00	0.00	0.00	0.01	0.00
MnO	0.08	0.12	0.07	0.10	0.08	0.08	0.08	0.07	0.09	0.09	0.09	0.10	0.07	0.07	0.08
Na_2O	1.90	1.29	2.07	2.00	2.04	2.07	1.91	2.85	1.83	2.10	2.09	1.13	2.02	2.25	1.92
Cr_2O_3	0.55	0.35	0.67	0.75	0.55	0.61	0.59	1.13	0.31	0.52	0.79	1.32	0.65	0.54	0.97
Al_2O_3	6.38	8.18	6.63	6.28	6.89	6.48	6.50	6.19	7.03	6.88	6.30	5.77	6.45	7.64	6.28
CaO	20.96	21.37	20.57	18.81	20.21	20.66	20.97	18.67	20.30	20.02	20.33	17.95	20.46	19.55	19.64
FeO	2.60	4.68	2.54	3.19	2.77	2.57	2.70	2.45	3.01	2.84	2.53	3.27	2.45	2.95	3.00
MgO	14.92	13.49	15.00	15.92	15.08	14.92	14.90	14.79	14.92	14.84	14.89	18.41	14.76	14.53	15.49
Total	100.37	99.91	100.65	100.09	100.53	100.45	100.42	99.70	100.28	99.86	99.62	99.99	99.62	99.98	99.95
No. of Analyses	8	5	8	5	8	7	8	8	7	5	8	8	12	5	8
Li	1.36	1.78	1.26	1.68	0.10	1.63	1.40	1.61	1.23	1.23	1.19	0.86	1.24	1.46	1.20
Sc	75.34	75.60	75.41	66.62	5.34	76.74	74.79	80.98	55.56	73.36	83.55	57.86	72.18	32.02	71.86
V	314.18	357.82	271.75	224.00	18.71	304.97	297.41	247.14	251.71	262.08	255.50	197.63	250.79	285.22	265.05
Cr	6457.13	2402.60	5762.50	5574.00	292.63	11675.71	4716.25	8257.50	2275.29	3974.00	5957.50	9613.75	5392.50	3936.00	6836.25
Mn	678.13	1053.40	663.75	746.60	46.71	831.29	666.88	556.25	724.57	648.00	609.50	714.13	583.33	567.60	635.38
Co	30.13	28.38	20.80	23.04	1.37	57.66	19.63	16.21	19.96	18.48	15.81	27.03	18.60	18.88	22.23
Cu	0.82	0.62	1.17	1.45	0.10	1.60	0.76	1.50	1.58	2.54	0.91	1.86	1.21	1.41	1.11
Zn	57.16	11.76	17.78	14.84	0.76	150.99	12.49	8.80	8.64	7.94	5.48	14.59	16.87	7.40	10.64
Rb	0.02	0.00	0.03	1.40	0.00	0.04	0.01	0.02	0.02	0.01	0.03	0.02	0.03	0.01	0.00
Sr	59.24	61.82	82.14	183.30	4.08	72.56	59.34	220.44	62.56	57.64	65.03	76.13	71.39	66.38	137.60
Y	18.10	25.01	23.24	17.39	1.80	22.21	19.00	12.22	17.58	23.44	22.31	12.91	21.30	6.38	14.01
Zr	27.76	40.24	39.68	48.62	2.77	35.20	28.59	6.46	30.50	42.86	39.45	22.42	32.86	31.50	34.14
Nb	0.16	0.36	0.18	2.33	0.00	0.40	0.12	0.02	0.11	0.04	0.10	0.65	0.39	0.08	0.37
Ba	0.09	0.22	0.03	11.98	0.00	-0.16	-0.05	0.10	0.22	-0.07	0.14	0.19	0.07	-0.05	0.14
La	1.26	1.80	1.26	11.50	0.04	1.27	1.28	25.61	0.67	0.63	0.82	2.17	0.90	0.55	12.11
Ce	4.37	6.93	4.63	26.15	0.21	4.02	4.43	39.19	3.09	3.27	2.98	5.17	3.38	2.86	22.93
Pr	0.84	1.37	0.90	3.18	0.05	0.75	0.86	2.89	0.70	0.72	0.59	0.77	0.71	0.70	2.58
Nd	5.16	8.06	5.15	12.78	0.31	4.50	5.20	6.37	4.23	4.60	3.82	3.99	3.95	4.69	10.14
Sm	2.18	3.32	2.08	2.96	0.15	1.76	2.13	0.82	1.73	2.28	1.67	1.34	1.76	1.93	1.88
Eu	0.75	1.08	0.85	1.03	0.06	0.75	0.79	0.31	0.81	0.87	0.71	0.50	0.73	0.75	0.64
Gd	3.02	4.42	3.17	3.00	0.25	3.15	3.06	1.24	2.73	3.21	2.96	1.91	2.87	2.57	2.14
Tb	0.52	0.72	0.57	0.48	0.04	0.54	0.52	0.27	0.47	0.62	0.57	0.37	0.52	0.35	0.37
Dy	3.31	4.89	3.99	3.19	0.31	3.95	3.55	1.87	3.17	4.29	3.86	2.44	3.62	1.86	2.49
Ho	0.67	0.94	0.84	0.62	0.07	0.82	0.69	0.45	0.64	0.87	0.83	0.50	0.78	0.25	0.52
Er	2.18	2.48	2.68	1.93	0.19	2.55	2.14	1.50	2.02	2.80	2.45	1.39	2.42	0.56	1.60
Tm	0.266	0.368	0.403	0.273	0.027	0.322	0.285	0.203	0.275	0.387	0.362	0.199	0.339	0.058	0.223
Yb	1.78	2.25	2.50	1.80	0.19	2.33	1.96	1.36	1.87	2.43	2.50	1.20	2.22	0.23	1.36
Lu	0.249	0.317	0.377	0.267	0.027	0.320	0.268	0.221	0.251	0.379	0.361	0.154	0.339	0.026	0.198
Hf	1.24	1.47	1.28	1.04	0.09	1.03	1.12	0.38	1.05	1.48	1.19	0.72	1.03	1.10	1.34
Ta	0.038	0.060	0.044	0.093	0.001	0.084	0.039	0.010	0.020	0.007	0.019	0.085	0.022	0.014	0.016
Pb	0.25	0.50	0.34	0.31	0.01	0.16	0.29	1.54	0.13	0.11	0.16	0.04	0.23	0.17	0.34
Th	0.044	0.028	0.040	1.266	0.000	0.065	0.041	4.993	0.013	0.005	0.016	0.106	0.029	0.007	1.397
U	0.016	0.009	0.027	0.272	0.000	0.020	0.016	1.059	0.006	0.001	0.005	0.019	0.014	0.005	0.306

Table 4-3. Dillo and Megado clinopyroxene major oxide and trace element compositions (continued)

Locality	Megado								
Sample	MG1-4	MG1-5	MG1-11	MG1-14	MG2-5	MG2-16	MG3-12	MG3-19	MG3-20
Type	Hz	Wb	Wb	Hz	Du	Lh	Lh	Lh	Wb
TiO_2 (wt. %)	0.12	0.26	0.65	0.07	0.61	0.50	0.53	0.55	0.42
SiO_2	52.93	51.80	51.73	53.82	51.76	52.11	52.31	52.20	52.22
K_2O	0.01	0.00	0.00	0.00	0.01	0.00	0.00	0.00	0.00
MnO	0.08	0.10	0.07	0.07	0.08	0.07	0.08	0.09	0.07
Na_2O	1.61	1.43	1.69	1.04	1.83	1.61	1.81	1.85	2.29
Cr_2O_3	1.16	0.56	0.53	1.04	0.80	0.67	0.67	0.69	0.15
Al_2O_3	4.65	6.60	6.82	2.93	6.34	6.19	6.39	6.53	7.18
CaO	20.73	19.60	19.90	21.52	20.04	21.17	20.01	20.20	20.46
FeO	2.12	3.03	2.88	2.20	2.69	2.45	2.72	2.50	2.58
MgO	16.45	16.52	15.66	17.50	15.74	15.47	15.46	15.40	14.66
Total	99.87	99.89	99.92	100.20	99.89	100.24	99.98	100.01	100.04
No. of Analyses	8	8	10	8	8	7	5	5	5
Li	1.24	0.71	1.45	0.68	1.24	1.65	1.32	1.41	1.53
Sc	92.13	56.69	40.87	101.51	86.31	73.34	64.96	73.94	51.66
V	227.28	208.01	318.58	216.68	262.48	257.17	234.76	253.70	194.44
Cr	8946.25	4172.50	3586.50	7870.00	5805.00	5845.71	6204.00	5714.00	1140.00
Mn	591.25	643.00	581.70	584.00	652.13	719.71	652.60	670.00	558.60
Co	19.68	24.68	21.87	20.16	20.50	24.57	23.32	20.76	16.59
Cu	1.15	3.25	1.57	1.21	1.62	1.19	1.43	1.37	1.11
Zn	12.63	15.41	8.89	9.76	9.36	26.97	20.04	16.66	2.95
Rb	0.03	0.02	0.01	0.01	0.02	-0.01	0.00	0.02	0.03
Sr	208.41	57.79	60.46	164.55	40.16	14.12	52.54	44.46	71.56
Y	10.05	8.24	5.34	3.47	20.88	20.98	16.76	19.99	6.61
Zr	10.94	8.14	23.24	9.60	22.12	13.14	25.38	23.24	19.35
Nb	0.02	0.52	0.09	0.17	0.01	0.01	0.00	0.00	0.40
Ba	1.06	0.86	0.22	0.40	0.25	-0.03	-0.13	0.18	0.07
La	11.86	1.39	0.91	8.11	0.42	0.08	0.59	0.82	0.97
Ce	21.49	2.35	2.99	11.90	1.84	0.60	2.40	2.06	3.17
Pr	2.19	0.36	0.57	0.99	0.48	0.28	0.53	0.43	0.56
Nd	7.38	1.83	3.85	3.24	3.30	2.30	3.54	2.89	3.04
Sm	1.39	0.79	1.56	0.61	1.62	1.41	1.53	1.63	1.09
Eu	0.46	0.34	0.59	0.21	0.68	0.56	0.62	0.62	0.46
Gd	1.30	1.30	2.10	0.56	2.79	2.61	2.33	2.55	1.47
Tb	0.24	0.24	0.31	0.10	0.53	0.49	0.41	0.45	0.26
Dy	1.64	1.52	1.37	0.63	3.57	3.49	2.98	3.16	1.45
Ho	0.37	0.32	0.21	0.13	0.77	0.82	0.67	0.72	0.25
Er	1.12	0.95	0.43	0.39	2.43	2.43	1.79	2.03	0.60
Tm	0.182	0.141	0.051	0.065	0.346	0.361	0.301	0.311	0.073
Yb	1.22	0.80	0.23	0.45	2.33	2.34	1.81	1.93	0.39
Lu	0.165	0.120	0.025	0.066	0.318	0.317	0.287	0.322	0.041
Hf	0.34	0.36	1.03	0.26	1.07	0.71	1.00	0.86	0.62
Ta	0.005	0.011	0.018	0.013	0.005	0.006	0.006	0.002	0.064
Pb	0.71	0.04	0.14	0.64	0.18	0.35	0.08	0.64	0.16
Th	2.319	0.316	0.031	1.454	0.008	0.072	0.025	0.105	0.062
U	0.645	0.082	0.009	0.326	0.003	0.026	0.007	0.035	0.022

Table 4-4. Sr-Nd-Hf-Pb isotopic compositions of clinopyroxene

Sample Name	Type	Fraction analyzed	$^{208}Pb/^{204}Pb$	$^{207}Pb/^{204}Pb$	$^{206}Pb/^{204}Pb$	$^{143}Nd/^{144}Nd$	2σ	ε_{Nd}	$^{176}Hf/^{177}Hf$	2σ	ε_{Hf}	$^{87}Sr/^{86}Sr$	2σ
Dillo													
DL2-1	Lh	Cpx	38.54	15.62	18.97	0.513160	0.000005	10.2	0.283049	0.000018	9.8	0.702325	0.000010
DL2-2	Wb	Cpx	38.09	15.55	18.23	0.512878	0.000009	4.7	0.283155	0.000016	13.5	0.702718	0.000007
DL2-4	Lh	Cpx	38.04	15.56	18.14	0.513089	0.000006	8.8	0.283207	0.000008	15.4	0.702777	0.000007
DL2-5	Lh	Cpx	38.38	15.61	18.88	0.513059	0.000008	8.2	0.283001	0.000003	8.1	0.702365	0.000007
DL2-8	Lh	Cpx	37.52	15.49	17.75	0.513081	0.000007	8.6	0.283113	0.000018	12.0	0.702683	0.000007
DL2-9	Lh	Cpx	37.50	15.48	17.74	0.513089	0.000005	8.8	0.283072	0.000012	10.6	0.702663	0.000006
DL2-13	Lh	Cpx	38.50	15.56	18.82	0.513205	0.000007	11.1	0.283237	0.000004	16.5	0.702247	0.000009
DL2-14	Lh	Cpx	40.15	15.68	19.91	0.512903	0.000007	5.2	0.284284	0.000019	53.5	0.703370	0.000006
DL2-22	Lh	Cpx				0.513266	0.000008	12.3	0.283344	0.000009	20.2	0.702228	0.000006
DL2-24	Lh	Cpx	39.08	15.59	19.16	0.512922	0.000008	5.5	0.283256	0.000004	17.1	0.702820	0.000006
DL2-33	Lh	Cpx	37.68	15.50	18.00	0.513318	0.000007	13.3	0.283320	0.000013	19.4	0.702180	0.000006
DL3-4	Hz	Cpx	38.85	15.61	19.15	0.513152	0.000005	10.0	0.283522	0.000017	26.5	0.702715	0.000006
DL3-10	Wb	Cpx	38.81	15.59	18.97	0.513100	0.000006	9.0	0.283078	0.000006	10.8	0.702252	0.000008
DL3-20	Wb	Cpx	37.88	15.50	18.17	0.513229	0.000007	11.5	0.282978	0.000006	7.3	0.702246	0.000006
DL3-21	Wb	Cpx	39.61	15.64	19.53	0.512918	0.000007	5.5	0.282902	0.000005	4.6	0.702987	0.000007
Megado													
MG1-4	Hz	Cpx	39.34	15.65	19.56	0.512547	0.000008	-1.8	0.283327	0.000112	19.6	0.703244	0.000005
MG1-5	Wb	Cpx	38.85	15.60	19.03	0.512975	0.000008	6.6	0.283260	0.000010	17.3	0.703185	0.000006
MG1-11	Wb	Cpx	39.47	15.67	19.79	0.513189	0.000006	10.7	0.283160	0.000007	13.7	0.702417	0.000006
MG1-14	Hz	Cpx	39.46	15.67	19.75	0.512975	0.000008	6.6	0.285449	0.000017	94.7	0.702974	0.000007
MG2-5	Du	Cpx	39.48	15.68	19.80	0.513187	0.000007	10.7	0.283405	0.000004	22.4	0.702338	0.000006
MG2-16	Lh	Cpx	39.61	15.67	19.89	0.513591	0.000009	18.6	0.283419	0.000008	22.9	0.702195	0.000010
MG3-12	Lh	Cpx	39.14	15.64	19.47	0.513167	0.000007	10.3	0.283349	0.000007	20.4	0.701989	0.000006
MG3-19	Lh	Cpx	39.73	15.70	20.05	0.513491	0.000006	16.6	0.283293	0.000004	18.4	0.702361	0.000008
MG3-20	Wb	Cpx	37.37	15.49	17.56	0.512936	0.000007	5.8	0.282967	0.000005	6.9	0.702864	0.000006
Dedessa													
WOL2	cpx-poor lh	Cpx				0.513070	0.000014	8.4	0.282990	0.000020	7.7		
Injibara													
GOJ2	Lh	Cpx	38.96	15.60	18.65	0.513102	0.000010	9.0	0.283161	0.000009	13.8		
GOJ4	cpx-poor lh	Cpx	38.71	15.58	18.89	0.513231	0.000006	11.6	0.282942	0.000007	6.0		
GOJ7	Lh	Cpx	39.06	15.61	18.85	0.513266	0.000007	12.3	0.282834	0.000010	2.2		
GOJ19	cpx-poor lh	Cpx				0.513253	0.000014	12.0	0.283064	0.000009	10.3		
GOJ26	Lh	Cpx	38.12	15.54	18.29	0.513267	0.000009	12.3	0.283297	0.000009	18.6		
GOJ29	Lh	Cpx	38.86	15.59	18.65	0.513624	0.000005	19.2	0.283515	0.000011	26.3		
GOJ31B	Lh	Cpx				0.512967	0.000008	6.4	0.282940	0.000009	5.9		

CHAPTER V

CONCLUSIONS

The work reported in this dissertation addresses three facets of rift petrogenesis in two of Earth's major active continental rift systems, the West Antarctic Rift System (WARS) and the East African Rift System (EARS). The primary aims of this work were to investigate, in regions where the mantle plume hypothesis may fail as an encompassing model for rift-wide petrogenesis, the validity of alternative models that highlight the role of passive decompression melting of volatilized, easily fusible components in the underlying upper mantle beneath both rifts. In Chapter II, submarine and subaerial lavas from the Ross Embayment of the West Antarctic Rift System exhibit major oxide, trace element, and Sr-Nd-Pb-Hf isotopic affinities for subduction-recycled domains hosted in the sub-continental lithospheric mantle (SCLM) and upper mantle. The occurrence of key easily-fusible components including volatilized peridotite and pyroxenite can be linked to long-lived subduction during the Paleozoic and Mesozoic, when West Antarctica and its constituent tectonic blocks were part of the paleo-Pacific active margin of Gondwana. The hydrated and carbonated source lithologies are confirmed in Chapter III, in which olivine-hosted melt inclusions record high H_2O and CO_2 linked to pervasive metasomatism by hydrous and carbonatitic fluids during subduction. These results suggest that volatile-rich metasomatic domains in the SCLM and upper mantle can be long-lived, and continue to contribute to tectonomagmatic activity well after subduction cessation. A new model for WARS rift petrogenesis that reconciles these findings with evolving regional geophysical frameworks is presented in Chapter II.

In Chapter IV, mantle xenoliths from contrasting environments (both plume-dominated and passive rift-dominated) in the East African SCLM document the complex, multistage history of the continental lithosphere involving ancient melt depletion events during Pan African continental assembly or older. These ancient melt depletions, signified by large Hf isotopic variations, are accompanied by high-μ Pb isotopic compositions, which may be reconciled by a new model for the production of high-μ domains by ancient metasomatism of the residual SCLM by subduction-related carbonatitic fluids. Late stage metasomatism by percolating alkaline and carbonatitic fluids in the southern portions of the rift contrast with the subalkaline plume-related magmas serving as metasomatizing agents on plateau xenoliths, supporting the interpretation that the dynamics of rift environments more distal to the plume head are more strongly linked with passive decompression melting. In these passive rift environments, kilometer-scale (or less) chemical heterogeneities are observed in the xenolith suite.

Collectively, these chapters fortify links between tectonic history, the production of chemically heterogeneous domains in the SCLM and sublithospheric convecting mantle, and continental rift evolution. They have important implications not only for understanding rift petrogenesis in East Africa and West Antarctica, but also for understanding other areas of intraplate magmatism that occur in the absence of significant thermal anomalies. The presented studies also illustrate that the sub-continental lithospheric mantle serves as an important long-lived host of heterogeneous recycled chemical components that continue to contribute to dynamic evolution of the continents over many cycles of accretion and breakup.

APPENDICES

APPENDIX 1

SUPPORTING INFORMATION FOR CHAPTER II

A1.1. Analytical Methods

A1.1.1. Electron microprobe analyses

Mineral compositions were determined on diamond-polished thin sections analyzed with a Cameca SX 100 electron microprobe at the University of Michigan Electron Microbeam Analysis Laboratory (EMAL) using a beam power of 15 kV and a current of 60 μA. Typical counting times were 20 seconds for major oxides and 30 seconds for minor elements. Diopside was used as a standard to generate a calibration for Ca and Si, enstatite for Mg, almandine for Fe and Al, albite for Na, rhodonite for Mn, uvaroite for Cr, and geikite for Ti. Ferrous and ferric iron concentrations in pyroxene were approximated by charge balancing to six oxygen atoms. Two separate analyses were performed for each sample to assess reproducibility of the calculations.

A1.1.2. Major oxide and trace element analyses

Sample chips for detailed chemical analyses were washed ultrasonically in deionized water and soaked in dilute (2.5N) HCl before crushing to < 150 μm grain size and pulverization. Major oxides, Rb, Sr, and Zr were analyzed by x-ray fluorescence (XRF), and trace elements were obtained on the same glass disks by laser ablation inductively coupled plasma mass spectrometer (LA-ICP-MS) at Michigan State University using the techniques described by Deering et al. (2008) and Rooney et al. (2012). Reproducibility using these techniques is typically better than 5% for trace elements based on standard analyses (Vogel et al., 2006). Three sample replicates were measured at the Washington State University Geoanalytical Laboratory

following the methods of Knaack at al. (1994) and Johnson et al. (2004) to assess reproducibility. Major elements and most trace elements agreed within 10%, and Rb, Ho, V, Cr, and Nb varied within 15%. Lead concentrations were also determined by isotope dilution during isotopic analyses for six samples for comparison with ICP-MS and XRF analyses. Major oxides and most trace elements agreed within 10%, Rb, Ho, V, Cr, and Nb varied within 15%, and Pb showed up to 23% variation. Samples were sorted by major-oxide data, removing those with low totals (less than 96 wt. %, inferred to indicate high LOI) from further consideration in the isotopic analyses that followed.

A1.2. Major Oxide Variations of West Antarctic Lavas

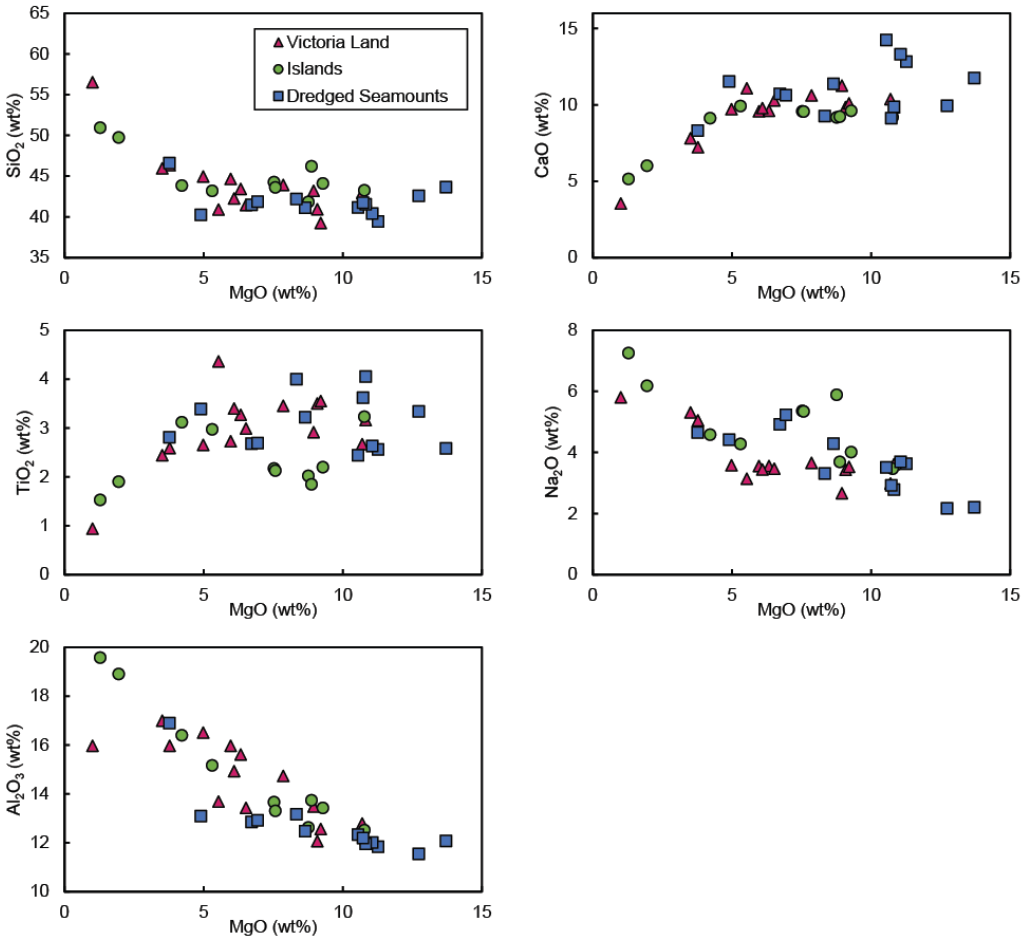

Figure A1.2.1. Variation diagrams versus MgO (wt. %) for WARS lavas, showing well-defined trends for fractional crystallization.

APPENDIX 2

SUPPORTING INFORMATION FOR CHAPTER III

A2.1. Sample selection and re-homogenization

Olivine crystals larger than 0.5 mm were picked from crushed and sieved host basanite lavas. Each crystal was examined under binocular microscope while submerged in isopropyl alcohol to verify the presence of amber-colored melt inclusions. At this stage, inclusions that contained abundant oxides or those that appeared to be associated with internal fractures within the olivine host were excluded from further study. Melt inclusions were rehomogenized at the Piston Cylinder Laboratory at Rensselaer Polytechnic Institute following the procedures described in Stefano et al. (2012) and Cabato et al. (2015), using experimental cell and capsule designs modified from Trail et al. (2012) and Ayers et al. (1992). Olivine phenocrysts were packed in graphite powder inside graphite capsules and equilibrated in a NaCl pressure medium to a temperature of 1300°C and a pressure of 6 kBar for 10 minutes, then rapidly quenched. Olivine phenocrysts recovered from the experimental capsules were again checked for inclusions free from cracks, then mounted in epoxy and polished to a 0.1 µm optical finish.

A2.2. Analytical techniques

Olivine phenocrysts with inclusions exposed on the surface were transferred to an indium mount in preparation for volatile analyses. Prior to loading in the sample chamber, the indium mounts were dried in a vacuum oven at 110°C for at least 12 hours, then coated in gold. Measurements of H_2O, CO_2, S, F, and Cl were performed at Woods Hole Oceanographic Institution on a Cameca 1280 IMS secondary ion mass spectrometer (SIMS) using the methods described in Helo et al. (2011). Measurements were conducted using a $^{133}Cs+$ primary beam and

a 500 nA current rastered to a 20 µm-diameter spot. Secondary ions of ^{12}C, $^{16}O^{1}H$, ^{19}F, ^{30}Si, ^{32}S, and ^{35}Cl were monitored for a uniform ion image with the highest intensity signal centered on the field aperture. Individual measurements were collected after 240 seconds of pre-sputter, and then counted for a minimum of 10 cycles. Calibration curves were produced by repeat measurements of nine standard glasses (Alvin 519-4-1, D51-3, D52-5, 6001, 1654-3, JD17H, D20-3, NS-1, and 46D) of known volatile species abundances. Replicate measurements of standard glass Alvin 519-4-1 were conducted to monitor instrument performance and yielded relative error of 8.2% or better for C, F, S, and Cl, and 12.6% for H_2O. Data quality for unknowns was assessed during the analysis by monitoring the signal stability for each analytical run, and inclusions that exhibited instability were flagged and removed from the figures and discussion in the main text, but are reported in Table 1 of Chapter II. The CO_2 measurements were particularly affected due to their generally low abundances.

Olivine major-oxide compositions were measured on the JEOL-JXA-8200 Superprobe at the Massachusetts Institute of Technology (MIT) Electron Microprobe Facility using a 15 kV accelerating voltage, 4 nA beam current, and a ~1µm focused beam. Melt-inclusion major-oxide compositions were measured at MIT using the same analytical conditions as host olivine grains, but with a 10 µm unfocused beam. Counting times were 5s for Na and 40s for all other elements. Replicate analyses (n=10) of the standard Alvin 1690-20 yielded relative error of 1.72% for CaO, 0.19% for SiO_2, 0.11% for Al_2O_3, 1.50% for FeO, 0.89% for MgO, and 7.47% for K_2O (Grove et al., 1992), and are available in Table A2.2.1.

Abundances of Li-U trace elements in MIs were determined on a laser ablation inductively coupled plasma mass spectrometer (ICP-MS) employing a Photon Machines 193 nm Excimer laser ablation platform plumbed into a NuAttoM high resolution single-collector ICP-

MS at the University of New Hampshire. Analyses were conducted with a 25µm spot size, 5.40 J/cm2 fluence, and a 4 Hz rep rate. Raw data were processed in Iolite (Paton et al., 2011) using ^{43}Ca (obtained from electron microprobe CaO measurements) as the internal standard. Instrumental drift was corrected by bracketing unknowns with the KL2-G glass standard using reference values from Jochum et al. (2005). Replicate measurements (n = 15) of glass standard ML3-BG run as an unknown standard throughout analytical runs indicate that trace elements are accurate to ±11% for U, to ± 8% or better for Li, V, Ni, Rb, and Sm, and to ±5% or better for all other elements (Jochum et al., 2005), and are available in Table S1. Owing to the very small size of some melt inclusions, analytical uncertainties for some measurements are high due to ablation of host olivine or limited availability of material during the measurement, particularly for very shallow inclusions.

Table A2.2.1. Average values for replicate measurements of standard reference glasses during ICP-MS and electron microprobe analyses. Analytical parameters are described in section A2.2.

	ML3-BG Average (n = 15)	**SD**
Li (ppm)	4.8	1
Ti	12719	398
V	290	16
Cr	175	10
Ni	114	5
Rb	6.2	0.3
Sr	314	10
Y	24.4	1.2
Zr	126	4.7
Nb	8.8	0.4
Ba	81	3.5
La	8.9	0.37
Ce	23.2	1.07
Pr	3.5	0.18
Nd	17	1.04
Sm	4.4	0.54
Eu	1.7	0.09
Gd	5.3	0.55
Tb	0.9	0.1
Dy	4.7	0.38
Ho	0.9	0.09
Er	2.4	0.35
Tm	0.3	0.05
Yb	2	0.39
Lu	0.3	0.06
Hf	3.1	0.37
Ta	0.5	0.06
Pb	1.4	0.12
Th	0.5	0.04
U	0.4	0.03
	1690-20 Average (n = 10)	**SD**
CaO	10.63	0.12
Al_2O_3	15.49	0.21
P_2O_5	0.19	0.02
MnO	0.18	0.01
Na_2O	3.2	0.11
TiO_2	1.67	0.03
SiO_2	49.99	0.35
SO_3	0.23	0.02
FeO	9.77	0.08
MgO	7.61	0.06
Cr_2O_3	0.06	0.02
K_2O	0.13	0.01
NiO	0.001	0.002

A2.3. Comparison of measured versus PEC-corrected H_2O and CO_2 concentrations of olivine-hosted melt inclusions.

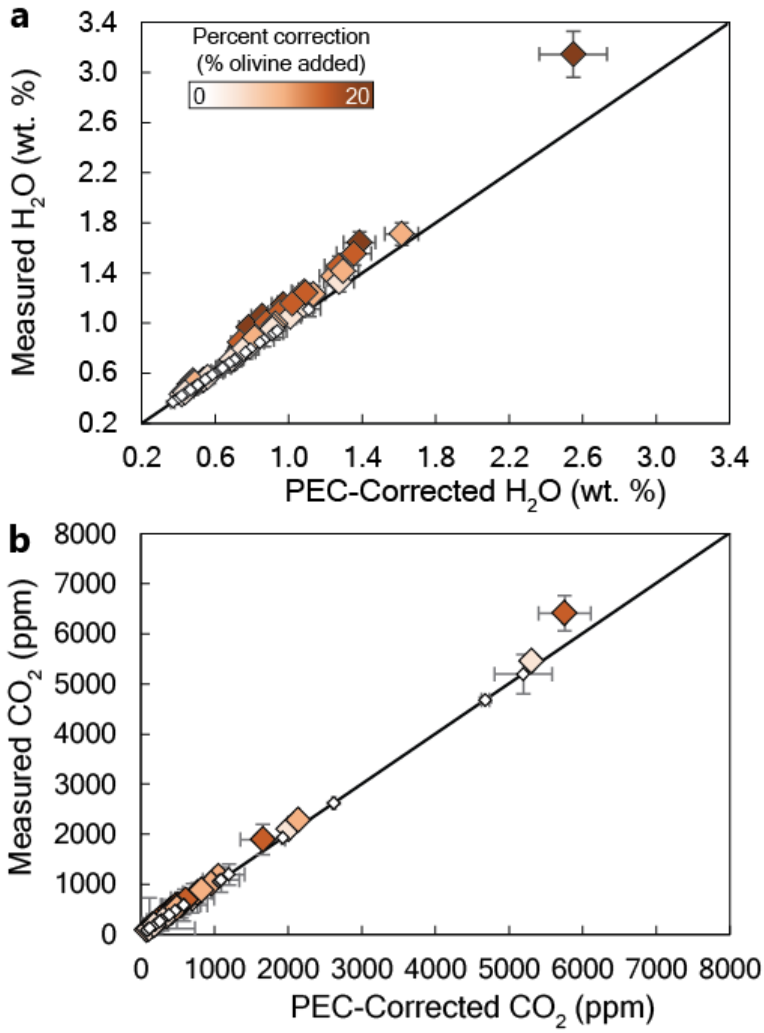

Figure A.2.3.1. Plots of measured (a) H_2O and (b) CO_2 versus PEC-corrected abundances for each volatile species. PEC corrections were carried out using Petrolog3 (Danyushevsky and Plechov, 2011), using model parameters described in Chapter III of the main text. Data points are colored by the amount of correction applied, with darker colors indicating more correction. Solid line represents the zero-correction line, at which measured and PEC-corrected volatile abundances are equivalent. Error bars are 2σ from the SIMS volatile analyses.

APPENDIX 3

SUPPORTING INFORMATION FOR CHAPTER IV

Table A3.1. Average values for replicate measurements of standard reference glasses during LA-ICP-MS analyses of mantle xenolith clinopyroxene. Measurements were conducted using a 40µm spot size, 6.75 J/cm^2 fluence, and a 4 Hz rep rate. See main text in Chapter IV for complete analytical details.

	KL2G Average (n = 23)	**SD**	**StHs6/80g Average (n = 29)**	**SD**
Li (ppm)	5.42	0.46	19.3	6.6
V	296	7	76.6	15.1
Cr	302	11	13.3	21.2
Ni	111	3	12.1	8.2
Cu	94	3	20.6	13.2
Zn	112	8	37.4	9.9
Rb	9.14	0.34	63.2	5.6
Sr	354	12	29.3	4.5
Y	26	1.5	468	3
Zr	154	7	11.3	0.9
Nb	15.2	0.6	115	2
Cs	0.14	0.04	6.56	5.55
Ba	121	3	295	1
La	13.1	0.4	11.5	4.4
Ce	32	1	25.3	3.1
Pr	4.60	0.16	3.06	4.24
Nd	21.9	0.9	12.3	5
Sm	5.68	0.5	2.61	6.13
Eu	1.94	0.14	0.91	4.99
Gd	6.19	0.41	2.57	0.93
Tb	0.89	0.07	0.38	1.82
Dy	5.40	0.38	2.15	3.17
Ho	0.98	0.1	0.41	1.74
Er	2.65	0.24	1.17	0.55
Tm	0.35	0.03	0.17	3.19
Yb	2.17	0.23	1.17	3.59
Lu	0.29	0.03	0.17	1.16
Hf	3.99	0.29	2.96	3.71
Ta	0.99	0.06	0.42	0.92
W	0.50	0.12	0.51	7.87
Pb	2.22	0.19	10.9	5.5
Th	1.04	0.05	2.23	2.24
U			1.02	0.98

Table A3.2. Average values for replicate measurements the NIST SRM987 500 ppb Sr isotopic standard during MC-ICP-MS analyses of mantle xenolith clinopyroxene. See main text in Chapter IV for complete analytical details.

	$^{87}Sr/^{86}Sr$ (Measured)	$^{87}Sr/^{86}Sr$ (Bracket corrected)
1	0.710226	0.710259
2	0.710206	0.710231
3	0.710220	0.710245
4	0.710238	0.710262
5	0.710229	0.710242
6	0.710231	0.710246
7	0.710238	0.710257
8	0.710226	0.710240
9	0.710230	0.710246
10	0.710240	0.710261
11	0.710223	0.710236
12	0.710230	0.710252
13	0.710227	0.710247
14	0.710263	0.710260
15	0.710253	0.710229
16	0.710281	0.710273
17	0.710258	0.710241
18	0.710251	0.710245
Average	0.710237	0.710249
2SE	0.000035	0.000022

Table A3.2. Average values for replicate measurements the JNdi 50 ppb Nd isotopic standard during MC-ICP-MS analyses of mantle xenolith clinopyroxene. See main text in Chapter IV for complete analytical details.

	$^{143}Nd/^{144}Nd$ (Measured)	$^{143}Nd/^{144}Nd$ (Bracket corrected)
1	0.512089	0.512117
2	0.512080	0.512109
3	0.512082	0.512120
4	0.512075	0.512113
5	0.512071	0.512109
6	0.512079	0.512118
7	0.512082	0.512118
8	0.512080	0.512117
9	0.512073	0.512108
10	0.512079	0.512125
11	0.512066	0.512107
12	0.512068	0.512113
13	0.512074	0.512119
14	0.512073	0.512116
15	0.512069	0.512111
16	0.512073	0.512118
17	0.512073	0.512117
18	0.512069	0.512111
19	0.512073	0.512119
20	0.512079	0.512111
21	0.512081	0.512118
22	0.512078	0.512115
23	0.512075	0.512115
24	0.512073	0.512115
25	0.512083	0.512111
26	0.512086	0.512117
27	0.512086	0.512115
28	0.512084	0.512115
Average	0.512077	0.512115
2SE	0.000012	0.000008

Table A3.3. Average values for replicate measurements the JMC475 50 ppb and 3.5 ppb Hf isotopic standard during MC-ICP-MS analyses of mantle xenolith clinopyroxene. See main text in Chapter IV for complete analytical details.

50 ppb Hf	**$^{176}Hf/^{177}Hf$ (Measured)**	**$^{176}Hf/^{177}Hf$ (Bracket corrected)**
1	0.282135	0.282165
2	0.282134	0.282161
3	0.282136	0.282163
4	0.282138	0.282164
5	0.282139	0.282164
6	0.282138	0.282164
7	0.282135	0.282159
8	0.282139	0.282165
9	0.282139	0.282162
10	0.282140	0.282164
11	0.282140	0.282165
12	0.282136	0.282164
Average	0.282137	0.282163
2SE	0.000004	0.000003
3.5 ppb Hf	**$^{176}Hf/^{177}Hf$ (Measured)**	**$^{176}Hf/^{177}Hf$ (Bracket corrected)**
1	0.282124	0.282161
2	0.282123	0.282165
3	0.282118	0.282168
4	0.282104	0.282150
5	0.282115	0.282170
6	0.282113	0.282164
7	0.282109	0.282155
8	0.282120	0.282160
9	0.282138	0.282203
10	0.282076	0.282100
Average	0.282114	0.282160
2SE	0.000031	0.000048

Table A3.3. Average values for replicate measurements the NIST SRM981 20 ppb Pb isotopic standard during MC-ICP-MS analyses of mantle xenolith clinopyroxene. Standard runs are corrected using the bracketing method described in Chapter IV of the main text.

	$^{208}Pb/^{204}Pb$	$^{207}Pb/^{204}Pb$	$^{206}Pb/^{204}Pb$
1	36.727	15.498	16.941
2	36.727	15.498	16.941
3	36.726	15.497	16.941
4	36.725	15.497	16.941
5	36.725	15.497	16.940
6	36.726	15.498	16.941
7	36.727	15.498	16.941
8	36.726	15.497	16.940
9	36.727	15.498	16.942
10	36.727	15.498	16.941
11	36.725	15.497	16.941
12	36.727	15.498	16.941
Average	36.726	15.498	16.941
2SE	0.002	0.001	0.001

LIST OF REFERENCES

Albarede, F., & Beard, B. (2004). Analytical Methods for Non-Traditional Isotopes. Reviews in Mineralogy and Geochemistry, 55, 113–152. doi:10.2138/gsrmg.55.1.113

Alemayehu, M., Zhang, H.-F., & Sakyi, P. A. (2016). Nature and evolution of lithospheric mantle beneath the southern Ethiopian rift zone: evidence from petrology and geochemistry of mantle xenoliths. *International Journal of Earth Sciences*. doi:10.1007/s00531-016-1342-z

Armienti, P., Civetta, L., Innocenti, F., Manetti, P., Tripodo, A., Villari, L. T., & Vita, G. (1991). New petrological and geochemical data on Mt. Melbourne volcanic field, northern Victoria Land, Antarctica (II Italian Antarctic expedition). *Memorie della Società Geologica Italiana, 46*, 397-424.

Asimow, P. D. (1998). Algorithmic modifications extending MELTS to calculate subsolidus phase relations. *American Mineralogist*, *83*(1), 1127–1132.

Asimow, P. D., & Langmuir, C. H. (2003). The importance of water to oceanic mantle melting regimes. *Nature*, *421*(6925), 815–20. doi:10.1038/nature01429

Asimow, P. D., Dixon, J. E., & Langmuir, C. H. (2004). A hydrous melting and fractionation model for mid-ocean ridge basalts: Application to the Mid-Atlantic Ridge near the Azores. *Geochemistry, Geophysics, Geosystems*, *5*(1), n/a-n/a. doi:10.1029/2003GC000568

Aulbach, S., Rudnick, R. L., & Mcdonough, W. F. (2011). Evolution of the lithospheric mantle beneath the East African Rift in Tanzania and its potential signatures in rift magmas. *America Special Paper*, *478*(June), 105–12510. doi:10.1130/2011.2478(06)

Aviado, K. B., Rilling-Hall, S., Bryce, J. G., & Mukasa, S. B. (2015). Submarine and subaerial lavas in the West Antarctic Rift System: Temporal record of shifting magma source components from the lithosphere and asthenosphere. *Geochemistry, Geophysics, Geosystems*, pp. 1541–1576. doi:10.1002/2015GC006076

Ayers, J. C., J. B. Brenan, E. B. Watson, D. A. Wark, and W. G. Minarik (1992), A new capsule technique for hydrothermal experiments using the piston-cylinder apparatus, Am. Mineral., 77(9-10), 1080–1086.

Bailey, D. K. (1982). Mantle metasomatism—continuing chemical change within the Earth. *Nature*, *296*(5857), 525–530. doi:10.1038/296525a0

Baker, J., Chazot, G., Menzies, M., & Thirlwall, M. (1998). Metasomatism of the shallow mantle beneath Yemen by the Afar plume—implications for mantle plumes, flood volcanism, and intraplate volcanism. *Geology*, (5), 431–434. Retrieved from http://geology.gsapubs.org/content/26/5/431.short

Baker, J., Snee, L., & Menzies, M. (1996). A brief Oligocene period of flood volcanism in Yemen: Implications for the duration and rate of continental flood volcanism at the Afro-

Arabian triple junction. *Earth and Planetary Science Letters*, *138*(1–4), 39–55. Retrieved from https://pubs.er.usgs.gov/publication/70019397

Bastow, I. D., Nyblade, a. a., Stuart, G. W., Rooney, T. O., & Benoit, M. H. (2008). Upper mantle seismic structure beneath the Ethiopian hot spot: Rifting at the edge of the African low-velocity anomaly. *Geochemistry, Geophysics, Geosystems*, *9*. doi:10.1029/2008GC002107

Bayer, B., Geissler, W. H., Eckstaller, A., & Jokat, W. (2009). Seismic imaging of the crust beneath Dronning Maud Land, East Antarctica. *Geophysical Journal International*, *178*(2), 860–876. doi:10.1111/j.1365-246X.2009.04196.x

Beccaluva, L., Bianchini, G., Ellam, R., Natali, C., Santato, A., Siena, F., & Stuart, F. (2011). Peridotite xenoliths from Ethiopia: inferences on mantle processes from Plume to Rift settings. *Geological Society of America Special Papers*, *478*, 77–104. doi:10.1130/2011.2478(05)

Beccaluva, L., Bianchini, G., Natali, C., & Siena, F. (2009). Continental flood basalts and mantle plumes: A case study of the Northern Ethiopian Plateau. *Journal of Petrology*, *50*(7), 1377–1403. doi:10.1093/petrology/egp024

Bedini, R. M., Bodinier, J.-L., Dautria, J.-M., & Morten, L. (1997). Evolution of LILE-enriched small melt fractions in the lithospheric mantle: a case study from the East African Rift. *Earth and Planetary Science Letters*, *153*, 67–83. doi:10.1016/S0012-821X(97)00167-2

Bedini, R.-M., Blichert-Toft, J., Boyet, M., & Albarede, F. (2004). Isotopic constraints on the cooling of the continental lithosphere. *Earth and Planetary Science Letters*, *223*(1–2), 99–111. doi:10.1016/j.epsl.2004.04.012

Behrendt, C., Damaske, D., Mccafferty, A., Finn, C. A., & Bell, R. E. (1996). Patterns of late Cenozoic volcanic and tectonic activity in the West Antarctic rift system revealed by aeromagnetic surveys Results of Aeromagnetic Surveys, *15*(2), 660–676.

Behrendt, J. (1999). Crustal and lithospheric structure of the West Antarctic Rift System from geophysical investigations -€" a review. *Global and Planetary Change*, *23*(1–4), 25–44. doi:10.1016/S0921-8181(99)00049-1

Behrendt, J. C., Blankenship, D. D., Finn, C. A., Bell, R. E., Sweeney, R. E., Hodge, S. M., & Brozena, J. M. (1994). CASERTZ aeromagnetic data reveal late Cenozoic flood basalts(?) in the West Antarctic rift system. *Geology*, *22*(6), 527. doi:10.1130/0091-7613(1994)022<0527:CADRLC>2.3.CO;2

Behrendt, J. C., Cooper, A., Survey, U. S. G., Road, M., & Park, M. (1991). Evidence of rapid Cenozoic uplift of the shoulder escarpment of the Cenozoic West Antarctic rift system and a speculation on possible climate forcing, (April), 315–319.

Behrendt, J., & LeMasurier, W. (1991). Geophysical studies of the West Antarctic Rift System. *Tectonics*, *10*(6), 1257–1273. Retrieved from http://www.agu.org/pubs/crossref/1991/91TC00868.shtml

Bell, K., & Tilton, G. R. (2001). Nd, Pb and Sr Isotopic Compositions of East African Carbonatites: Evidence for Mantle Mixing and Plume Inhomogeneity. *Journal of Petrology*, *42*(10), 1927–1945. doi:10.1093/petrology/42.10.1927

Benoit, M. H., Nyblade, A. A., & Vandecar, J. C. (2006). Upper mantle P-wave speed variations beneath Ethiopia and the origin of the Afar hotspot, (5), 329–332. doi:10.1130/G22281.1

Berg, J. H., Moscati, R. J., & Herz, D. L. (1989). A petrologic geotherm from a continental rift in Antarctica. *Earth and Planetary Science Letters*, *93*(1), 98–108. doi:10.1016/0012-821X(89)90187-8

Bianchini, G., Bryce, J. G., Blichert-Toft, J., Beccaluva, L., & Natali, C. (2014). Mantle dynamics and secular variations beneath the East African Rift: Insights from peridotite xenoliths (Mega, Ethiopia). *Chemical Geology*, *386*, 49–58. doi:10.1016/j.chemgeo.2014.07.024

Birt, C. S., Maguire, P. K. H., Khan, M. A., Thybo, H., Keller, G. R., & Patel, J. (1997). The influence of pre-existing structures on the evolution of the southern Kenya Rift Valley — evidence from seismic and gravity studies. *Tectonophysics*, *278*(1–4), 211–242. doi:10.1016/S0040-1951(97)00105-4

Bizimis, M., Salters, V. J. M., & Dawson, J. B. (2003). The brevity of carbonatite sources in the mantle: Evidence from Hf isotopes. *Contributions to Mineralogy and Petrology*, *145*(3), 281–300. doi:10.1007/s00410-003-0452-3

Blichert-Toft, J., & Albarède, F. (2009). Mixing of isotopic heterogeneities in the Mauna Kea plume conduit. *Earth and Planetary Science Letters*, *282*(1–4), 190–200. doi:10.1016/j.epsl.2009.03.015

Blundy, J., & Dalton, J. (2000). Experimental comparison of trace element partitioning between clinopyroxene and melt in carbonate and silicate systems, and implications for mantle metasomatism. *Contributions to Mineralogy and Petrology*, *139*, 356–371. doi:10.1007/s004100000139

Bodinier, J. L., & Godard, M. (2013). *Orogenic, Ophiolitic, and Abyssal Peridotites*. *Treatise on Geochemistry: Second Edition* (Vol. 3). doi:10.1016/B978-0-08-095975-7.00204-7

Bonini, M., Corti, G., Innocenti, F., Manetti, P., Mazzarini, F., Abebe, T., & Pecskay, Z. (2005). Evolution of the Main Ethiopian Rift in the frame of Afar and Kenya rifts propagation. *Tectonics*, *24*(1), n/a-n/a. doi:10.1029/2004TC001680

Bouvier, A., Vervoort, J. D., & Patchett, P. J. (2008). The Lu–Hf and Sm–Nd isotopic composition of CHUR: Constraints from unequilibrated chondrites and implications for the bulk composition of terrestrial planets. *Earth and Planetary Science Letters*, *273*(1–2), 48–57. doi:10.1016/j.epsl.2008.06.010

Bradshaw, J. D. (1989). Cretaceous geotectonic patterns in the New Zealand Region. *Tectonics*, *8*(4), 803–820. doi:10.1029/TC008i004p00803

Brown, B., Gaina, C., & Müller, R. D. (2006). Circum-Antarctic palaeobathymetry: Illustrated examples from Cenozoic to recent times. *Palaeogeography, Palaeoclimatology, Palaeoecology*, *231*(1–2), 158–168. doi:10.1016/j.palaeo.2005.07.033

Brown, B., Gaina, C., & Müller, R. D. (2006). Circum-Antarctic palaeobathymetry: Illustrated examples from Cenozoic to recent times. *Palaeogeography, Palaeoclimatology, Palaeoecology*, *231*(1–2), 158–168. doi:10.1016/j.palaeo.2005.07.033

Bryce, J. G., & DePaolo, D. J. (2004). Pb isotopic heterogeneity in basaltic phenocrysts. *Geochimica et Cosmochimica Acta*, *68*(21), 4453–4468. doi:10.1016/j.gca.2004.01.016

Bucholz, C. E., Gaetani, G. a., Behn, M. D., & Shimizu, N. (2013). Post-entrapment modification of volatiles and oxygen fugacity in olivine-hosted melt inclusions. *Earth and Planetary Science Letters*, *374*, 145–155. doi:10.1016/j.epsl.2013.05.033

Cabato, J. A., Stefano, C. J., & Mukasa, S. B. (2015). Volatile concentrations in olivine-hosted melt inclusions from the Columbia River flood basalts and associated lavas of the Oregon Plateau: Implications for magma genesis. *Chemical Geology*, *392*, 59–73. doi:10.1016/j.chemgeo.2014.11.015

Cande, S. C., & Stock, J. M. (2004). Pacific-Antarctic-Australia motion and the formation of the Macquarie Plate. *Geophysical Journal International*, *157*(1), 399–414. doi:10.1111/j.1365-246X.2004.02224.x

Cande, S. C., Stock, J. M., Müller, R. D., & Ishihara, T. (2000). Cenozoic motion between East and West Antarctica. *Nature*, *404*(6774), 145–150. doi:10.1038/35004501

Canil, D. (2004). Mildly incompatible elements in peridotites and the origins of mantle lithosphere. *Lithos*, *77*(1–4 SPEC. ISS.), 375–393. doi:10.1016/j.lithos.2004.04.014

Cartigny, P., Pineau, F., Aubaud, C., & Javoy, M. (2008). Towards a consistent mantle carbon flux estimate: Insights from volatile systematics (H_2O/Ce, δD, CO_2/Nb) in the North Atlantic mantle (14° N and 34° N). *Earth and Planetary Science Letters*, *265*(3–4), 672–685. doi:10.1016/j.epsl.2007.11.011

Castillo, P. R. (2015). The recycling of marine carbonates and sources of HIMU and FOZO ocean island basalts. *Lithos*, *216–217*, 254–263. doi:10.1016/j.lithos.2014.12.005

Chaffey, D. J., Cliff, R. A., & Wilson, B. M. (1989). Characterization of the St Helena magma source. *Geological Society, London, Special Publications*, *42*(1), 257–276. doi:10.1144/GSL.SP.1989.042.01.16

Chauvel, C., & Blichert-Toft, J. (2001). A hafnium isotope and trace element perspective on melting of the depleted mantle. *Earth and Planetary Science Letters*, *190*(3–4), 137–151. doi:10.1016/S0012-821X(01)00379-X

Chauvel, C., Hofmann, A. W., & Vidal, P. (1992). HIMU-EM: The French Polynesian connection. *Earth and Planetary Science Letters*, *110*(1–4), 99–119. doi:10.1016/0012-821X(92)90042-T

Chauvel, C., Lewin, E., Carpentier, M., Arndt, N. T., & Marini, J.-C. (2008). Role of recycled oceanic basalt and sediment in generating the Hf–Nd mantle array. *Nature Geoscience*, *1*(JANUARY), 64–67. doi:10.1038/ngeo.2007.51

Chauvel, C., McDonough, W., Guille, G., Maury, R., & Duncan, R. (1997). Contrasting old and young volcanism in Rurutu Island, Austral chain. *Chemical Geology*, *139*(97), 125–143. doi:10.1016/S0009-2541(97)00029-6

Choi, S. H., & Mukasa, S. B. (2014). Lu – Hf and Sm – Nd isotope systematics of Korean spinel peridotites: A case for metasomatically induced Nd – Hf decoupling. *Lithos*, *154*(December 2012), 263–276. doi:10.1016/j.lithos.2012.07.017

Choi, S., Mukasa, S., Andronikov, A., Osanai, Y., Harley, S., & Kelly, N. (2006). Lu–Hf systematics of the ultra-high temperature Napier Metamorphic Complex in Antarctica: Evidence for the early Archean differentiation of Earth's mantle. *Earth and Planetary Science Letters*, *246*(3–4), 305–316. doi:10.1016/j.epsl.2006.04.012

Chu, D., & Gordon, R. G. (1998). Current plate motions across the Red Sea. *Geophysical Journal International*, *135*(2), 313–328. doi:10.1046/j.1365-246X.1998.00658.x

Class, C., Altherr, R., Volker, F., Eberz, G., & McCulloch, M. T. (1994). Geochemistry of Pliocene to Quaternary alkali basalts from the Huri Hills, northern Kenya. *Chemical Geology*, *113*, 1–22. doi:10.1016/0009-2541(94)90002-7

Coltorti, M., Beccaluva, L., Bonadiman, C., Faccini, B., Ntaflos, T., & Siena, F. (2004). Amphibole genesis via metasomatic reaction with clinopyroxene in mantle xenoliths from Victoria Land, Antarctica. *Lithos*, *75*, 115–139. doi:10.1016/j.lithos.2003.12.021

Coltorti, M., Bonadiman, C., Hinton, R. W., Siena, F., & Upton, B. G. J. (1999). Carbonatite Metasomatism of the Oceanic Upper Mantle: Evidence from Clinopyroxenes and Glasses in Ultramafic Xenoliths of Grande Comore, Indian Ocean. *Journal of Petrology*, *40*(1), 133–165. doi:10.1093/petroj/40.1.133

Cooper, A. F., Adam, L. J., Coulter, R. F., Eby, G. N., & McIntosh, W. C. (2007). Geology, geochronology and geochemistry of a basanitic volcano, White Island, Ross Sea, Antarctica. *Journal of Volcanology and Geothermal Research*, *165*(3–4), 189–216. doi:10.1016/j.jvolgeores.2007.06.003

Corti, G. (2009). Continental rift evolution: From rift initiation to incipient break-up in the Main Ethiopian Rift, East Africa. *Earth-Science Reviews*, *96*(1–2), 1–53. doi:10.1016/j.earscirev.2009.06.005

Dalziel, I. W. D., & Elliot, D. H. (1982). West Antarctica: Problem child of Gondwanaland. *Tectonics*, *1*(1), 3–19. doi:10.1029/TC001i001p00003

Dalziel, I. W. D., Helper, M. A., Hutson, F. E., & Grimes, S.W. (1994). Geologic investigations in the Shackleton Range and Coats Land nunataks, Antarctica. *Antarct. J. US*, *29*, 4-6

Danyushevsky, L. V, McNeill, A. W., & Sobolev, A. V. (2002). Experimental and petrological studies of melt inclusions in phenocrysts from mantle-derived magmas: an overview of techniques, advantages and complications. *Chemical Geology*, *183*(1–4), 5–24. doi:10.1016/S0009-2541(01)00369-2

Danyushevsky, L. V., & Plechov, P. (2011). Petrolog3: Integrated software for modeling crystallization processes. *Geochemistry, Geophysics, Geosystems*, *12*(7). doi:10.1029/2011GC003516

Dasgupta, R., & Hirschmann, M. M. (2006). Melting in the Earth's deep upper mantle caused by carbon dioxide. *Nature*, *440*(7084), 659–662. doi:10.1038/nature04612

Dasgupta, R., Hirschmann, M. M., & Smith, N. D. (2007a). Partial melting experiments of peridotite + CO_2 at 3 GPa and genesis of alkalic ocean island basalts. *Journal of Petrology*, *48*(11), 2093–2124. doi:10.1093/petrology/egm053

Dasgupta, R., Hirschmann, M. M., & Smith, N. D. (2007b). Water follows carbon: CO_2 incites deep silicate melting and dehydration beneath mid-ocean ridges. *Geology*, *35*(2), 135–138. doi:10.1130/G22856A.1

Davidson, A., & Rex, D. C. (1980). Age of volcanism and rifting in southwestern Ethiopia. *Nature*, *283*(5748), 657–658. doi:10.1038/283657a0

Dawson, J. B. (2002). Metasomatism and Partial Melting in Upper-Mantle Peridotite Xenoliths from the Lashaine Volcano, Northern Tanzania. *Journal of Petrology*, *43*(9), 1749–1777. doi:10.1093/petrology/43.9.1749

Debayle, E., Lévêque, J. J., & Cara, M. (2001). Seismic evidence for a deeply rooted low-velocity anomaly in the upper mantle beneath the northeastern Afro/Arabian continent. *Earth and Planetary Science Letters*, *193*(3–4), 423–436. doi:10.1016/S0012-821X(01)00509-X

Deering, C. D., Cole, J. W., & Vogel, T. A. (2008). A Rhyolite Compositional Continuum Governed by Lower Crustal Source Conditions in the Taupo Volcanic Zone, New Zealand. *Journal of Petrology*, *49*(12), 2245–2276. doi:10.1093/petrology/egn067

DiVenere, V. J., Kent, D. V, & Dalziel, I. W. D. (1994). Mid-Cretaceous paleomagnetic results from Marie Byrd Land, West Antarctica: A test of post-100 Ma relative motion between East and West Antarctica. *Journal of Geophysical Research: Solid Earth*, *99*(B8), 15115–15139. doi:10.1029/94JB00807

Downes, H. (2001). Formation and Modification of the Shallow Sub-continental Lithospheric Mantle: a Review of Geochemical Evidence from Ultramafic Xenolith Suites and Tectonically Emplaced Ultramafic Massifs of Western and Central Europe. *Journal of Petrology*, *42*(1), 233–250. doi:10.1093/petrology/42.1.233

Dupuy, C., Mevel, C., Bodinier, J. L., & Savoyant, L. (1991). Zabargad peridotite: evidence for multistage metasomatism during Red Sea rifting. *Geology*, *19*(7), 722–725. doi:10.1130/0091-7613(1991)019<0722:ZPEFMM>2.3.CO

Dupuy, C., Liotard, J. ., & Dostal, J. (1992). Zr/Hf fractionation in intraplate basaltic rocks: Carbonate metasomatism in the mantle source. *Geochimica et Cosmochimica Acta*, *56*(6), 2417–2423. doi:10.1016/0016-7037(92)90198-R

Eagles, G., Gohl, K., & Larter, R. D. (2004). High-resolution animated tectonic reconstruction of the South Pacific and West Antarctic Margin. *Geochemistry, Geophysics, Geosystems*, *5*(7). doi:10.1029/2003GC000657

Ebinger, C. (2005). Continental break-up: The East African perspective. *Astronomy and Geophysics*, *46*(July), 2.16-2.21. doi:10.1111/j.1468-4004.2005.46216.x

Ebinger, C. J., Jackson, J. A., Foster, A. N., & Hayward, N. J. (1999). Extensional basin geometry and the elastic lithosphere. *Philosophical Transactions of the Royal Society A: Mathematical, Physical and Engineering Sciences*, *357*(1753), 741–765. doi:10.1098/rsta.1999.0351

Ebinger, C. J., Yemane, T., Harding, D. J., Tesfaye, S., Kelley, S., & Rex, D. C. (2000). Rift deflection, migration, and propagation: Linkage of the Ethiopian and Eastern rifts, Africa. *Geological Society of America Bulletin*, *112*(2), 163–176. doi:10.1130/0016-7606(2000)112<163:RDMAPL>2.0.CO;2

Ebinger, C. J., Yemane, T., Woldegabriel, G., Aronson, J. L., & Walter, R. C. (1993). Late Eocene-Recent volcanism and faulting in the southern main Ethiopian rift. *Journal of the Geological Society*, *150*(1), 99–108. doi:10.1144/gsjgs.150.1.0099

Ebinger, C., & Sleep, N. (1998). Cenozoic magmatism throughout east Africa resulting from impact of a single plume. *Nature*, *395*(October), 788–791.

Ebinger, C., Yemane, T., Harding, D., Tesfaye, S., Kelley, S., & Rex, D. (2000). Rift deflection, migration, and propagation: Linkage of the Ethiopian and Eastern rifts, Africa. *Geological Society of America Bulletin*, *112*(2), 163–176. Retrieved from http://gsabulletin.gsapubs.org/content/112/2/163.short

Eisele, J., Abouchami, W., Galer, S. J. G., & Hofmann, A. W. (2003). The 320 kyr Pb isotope evolution of Mauna Kea lavas recorded in the HSDP-2 drill core. *Geochemistry, Geophysics, Geosystems*, *4*(5), n/a-n/a. doi:10.1029/2002GC000339

Elkins-Tanton, L. T. (2007). Continental magmatism, volatile recycling, and a heterogeneous mantle caused by lithospheric gravitational instabilities. *Journal of Geophysical Research*, *112*(B3), B03405. doi:10.1029/2005JB004072

Elliot, D. H., & Fleming, T. H. (2000). Weddell triple junction: The principal focus of Ferrar and Karoo magmatism during initial breakup of Gondwana. *Geology*, *28*(1989), 539–542. doi:10.1130/0091-7613(2000)28<539:WTJTPF>2.0.CO;2

Emry, E. L., Nyblade, A. A., Julià, J., Anandakrishnan, S., Aster, R. C., Wiens, D. A., … Wilson, T. J. (2015). The mantle transition zone beneath West Antarctica: Seismic evidence for hydration and thermal upwellings. *Geochemistry, Geophysics, Geosystems*, *16*, 40–58. doi:10.1002/2014GC005588

Esser, R. P., Kyle, P. R., & McIntosh, W. C. (2004). 40Ar/39Ar dating of the eruptive history of Mount Erebus, Antarctica: volcano evolution. *Bulletin of Volcanology*, *66*(8), 671–686. doi:10.1007/s00445-004-0354-x

Finn, C. a., Müller, R. D., & Panter, K. S. (2005). A Cenozoic diffuse alkaline magmatic province (DAMP) in the southwest Pacific without rift or plume origin. *Geochemistry, Geophysics, Geosystems*, *6*(2), n/a-n/a. doi:10.1029/2004GC000723

Fitzgerald, P. G., Sandiford, M., Barrett, P. J., & Gleadow, A. J. W. (1986). Asymmetric extension associated with uplift and subsidence in the Transantarctic Mountains and Ross Embayment. *Earth and Planetary Science Letters*, *81*, 67–78. doi:10.1016/0012-821X(86)90101-9

Furman, T., & Graham, D. (1999). Erosion of lithospheric mantle beneath the East African Rift system: Geochemical evidence from the Kivu volcanic province. *Lithos*, *48*(1–4), 237–262. doi:10.1016/S0024-4937(99)00031-6

Furman, T., Bryce, J. G., Karson, J., & Iotti, A. (2004). East African Rift System (EARS) Plume Structure: Insights from Quaternary Mafic Lavas of Turkana, Kenya. *Journal of Petrology*, *45*(5), 1069–1088. doi:10.1093/petrology/egh004

Furman, T., Bryce, J., Rooney, T., Hanan, B., Yirgu, G., & Ayalew, D. (2006a). Heads and tails: 30 million years of the Afar plume. *Geological Society, London, Special Publications*, *259*(1), 95–119. doi:10.1144/GSL.SP.2006.259.01.09

Furman, T., Kaleta, K. M., Bryce, J. G., & Hanan, B. B. (2006b). Tertiary mafic lavas of Turkana, Kenya: Constraints on East African plume structure and the occurrence of high-μ volcanism in Africa. *Journal of Petrology*, *47*(6), 1221–1244. doi:10.1093/petrology/egl009

Furman, T., Nelson, W. R., & Elkins-Tanton, L. T. (2016). Evolution of the East African rift: Drip magmatism, lithospheric thinning and mafic volcanism. *Geochimica et Cosmochimica Acta*, *185*, 418–434. doi:10.1016/j.gca.2016.03.024

Gaetani, G. a., O'Leary, J. a., Shimizu, N., Bucholz, C. E., & Newville, M. (2012). Rapid reequilibration of H_2O and oxygen fugacity in olivine-hosted melt inclusions. *Geology*, *40*(SEPTEMBER), 915–918. doi:10.1130/G32992.1

Gerbode, C., & Dasgupta, R. (2010). Carbonate-fluxed melting of MORB-like pyroxenite at 2·9 GPa and genesis of HIMU ocean Island basalts. *Journal of Petrology*, *51*(10), 2067–2088. doi:10.1093/petrology/egq049

Ghiorso, M. S., & Sack, R. O. (1995). Chemical mass transfer in magmatic processes IV. A revised and internally consistent thermodynamic model for the interpolation and extrapolation of liquid-solid equilibria in magmatic systems at elevated temperatures and pressures. *Contributions to Mineralogy and Petrology*, *119*(2–3), 197–212. doi:10.1007/BF00307281

Graw, J. H., Adams, a. N., Hansen, S. E., Wiens, D. a., Hackworth, L., & Park, Y. (2016). Upper mantle shear wave velocity structure beneath northern Victoria Land, Antarctica: Volcanism and uplift in the northern Transantarctic Mountains. *Earth and Planetary Science Letters*, *449*, 48–60. doi:10.1016/j.epsl.2016.05.026

Green, D. H. (1973). Experimental melting studies on a model upper mantle composition at high pressure under water-saturated and water-undersaturated conditions. *Earth and Planetary Science Letters*, *19*(May 2016), 37–53. doi:10.1016/0012-821X(73)90176-3

Grove, T. L., R. J. R. J. Kinzler, and W. B. W. Bryan (1992), Fractionation of mid-ocean ridge basalt (MORB), Gephysical Monogr. Geophys. Union, 71, 281–310, doi:10.1029/GM071p0281.

Grove, T. L., Chatterjee, N., Parman, S. W., & Médard, E. (2006). The influence of H_2O on mantle wedge melting. *Earth and Planetary Science Letters*, *249*, 74–89. doi:10.1016/j.epsl.2006.06.043

Gualda, G. a R., & Ghiorso, M. S. (2015). MELTS_Excel: A Microsoft Excel-based MELTS interface for research and teaching of magma properties and evolution. *Geochemistry,Geophysics,Geosystems*, *16*, 315–324. doi:10.1002/2014GC005545.Received

Gurenko, A. a., Sobolev, A. V., Hoernle, K. a., Hauff, F., & Schmincke, H.-U. (2009). Enriched, HIMU-type peridotite and depleted recycled pyroxenite in the Canary plume: A mixed-up

mantle. *Earth and Planetary Science Letters*, *277*(3–4), 514–524. doi:10.1016/j.epsl.2008.11.013

Gurnis, M., Mitrovica, J. X., Ritsema, J., & van Heijst, H.-J. (2000). Constraining mantle density structure using geological evidence of surface uplift rates: The case of the African Superplume. *Geochemistry, Geophysics, Geosystems*, *1*(7). doi:10.1029/1999GC000035

Halliday, A., Lee, D., & Tommasini, S. (1995). Incompatible trace elements in OIB and MORB and source enrichment in the sub-oceanic mantle. *Earth and Planetary Science Letters*, *133*, 379–395. Retrieved from http://www.sciencedirect.com/science/article/pii/0012821X9500097V

Hanan, B. B., & Graham, D. W. (1996). Lead and Helium Isotope Evidence from Oceanic Basalts for a Common Deep Source of Mantle Plumes. *Science*, *272*, 991–995. doi:10.1126/science.272.5264.991

Hansen, S. E., Graw, J. H., Kenyon, L. M., Nyblade, A. A., Wiens, D. A., Aster, R. C., … Wilson, T. (2014). Imaging the Antarctic mantle using adaptively parameterized P-wave tomography: Evidence for heterogeneous structure beneath West Antarctica. *Earth and Planetary Science Letters*, *408*, 66–78. doi:10.1016/j.epsl.2014.09.043

Hansen, S. E., Nyblade, A. A., & Benoit, M. H. (2012). Mantle structure beneath Africa and Arabia from adaptively parameterized P-wave tomography : Implications for the origin of Cenozoic Afro-Arabian tectonism. *Earth and Planetary Science Letters*, *319–320*, 23–34. doi:10.1016/j.epsl.2011.12.023

Harrison, W. J., & Wood, B. J. (1980). An experimental investigation of the partitioning of REE between garnet and liquid with reference to the role of defect equilibria. *Contributions to Mineralogy and Petrology*, *72*(2), 145–155. doi:10.1007/BF00399474

Hart, S. R. (1984). A large-scale isotope anomaly in the Southern Hemisphere mantle. *Nature*, *309*(5971), 753–757. doi:10.1038/309753a0

Hart, S. R., &. Kyle, P. R. (1993). Geochemistry of McMurdo Group volcanic rocks, *Antarct. J. U.S., 8(5),* 14–16

Hart, S. R., Gerlach, D. C., & White, W. M. (1986). A possible new Sr-Nd-Pb mantle array and consequences for mantle mixing. *Geochimica et Cosmochimica Acta*, *50*(7), 1551–1557. doi:10.1016/0016-7037(86)90329-7

Hart, S. R., Hauri, E. H., Oschmann, L. A., & Whitehead, J. A. (1992). Mantle plumes and entrainment: isotopic evidence. *Science (New York, N.Y.)*, *256*(5056), 517–520. doi:10.1126/science.256.5056.517

Hart, S., Blijsztajn, J., & Craddock, C. (1995). Cenozoic volcanism in Antarctica: Jones Mountains and Peter I Island. *Geochimica et Cosmochimica Acta*, *59*(16). Retrieved from http://www.sciencedirect.com/science/article/pii/001670379500212I

Hart, S., Blusztajn, J., LeMasurier, W., & Rex, D. (1997). Hobbs Coast Cenozoic volcanism: implications for the West Antarctic rift system. *Chemical Geology*, *139*, 223–248. doi:10.1016/s0009-2541(97)00037-5

Harte, B., & Ben. (1977). Rock Nomenclature with Particular Relation to Deformation and Recrystallisation Textures in Olivine-Bearing Xenoliths. *The Journal of Geology*, *85*(3), 279–288. doi:10.1086/628299

Hartley, M. E., Neave, D. a., Maclennan, J., Edmonds, M., & Thordarson, T. (2015). Diffusive over-hydration of olivine-hosted melt inclusions. *Earth and Planetary Science Letters*, *425*, 168–178. doi:10.1016/j.epsl.2015.06.008

Hauri, E. H. (1996). Major-element variability in the Hawaiian mantle plume. *Nature*, *382*, 415–419. doi:10.1038/382415a0

Helo, C., M.-A. Longpré, N. Shimizu, D. a. Clague, and J. Stix (2011), Explosive eruptions at mid-ocean ridges driven by CO_2-rich magmas, Nat. Geosci., 4(4), 260–263, doi:10.1038/ngeo1104.

Hendrie, D. B., Kusznir, N. J., Morley, C. K., & Ebinger, C. J. (1994). Cenozoic extension in northern Kenya: a quantitative model of rift basin development in the Turkana region. *Tectonophysics*, *236*(1–4), 409–438. doi:10.1016/0040-1951(94)90187-2

Henjes-Kunst, F., Altherr, R., & Baumann, A. (1990). Evolution and composition of the lithospheric mantle underneath the western Arabian peninsula: constraints from Sr?Nd isotope systematics of mantle xenoliths. *Contributions to Mineralogy and Petrology*, *105*(4), 460–472. doi:10.1007/BF00286833

Herzberg, C. (2006). Petrology and thermal structure of the Hawaiian plume from Mauna Kea volcano. *Nature*, *444*(7119), 605–609. doi:10.1038/nature05254

Herzberg, C. (2011). Basalts as temperature probes of Earth's mantle. *Geology*. doi:10.1130/focus122011.1

Herzberg, C., & Asimow, P. D. (2008). Petrology of some oceanic island basalts: PRIMELT2.XLS software for primary magma calculation. *Geochemistry Geophysics Geosystems*, *9*(9). doi:10.1029/2008GC002057

Hirose, K. (1997). Partial melt compositions of carbonated peridotite at 3 GPa and role of CO_2 in alkali-basalt magma generation. *Geophysical Research Letters*. doi:10.1029/97GL02956

Hirose, K., & Kushiro, I. (1993). Partial melting of dry peridotites at high pressures: Determination of compositions of melts segregated from peridotite using aggregates of diamond. *Earth and Planetary Science Letters*. doi:10.1016/0012-821X(93)90077-M

Hirschmann, M. M., Kogiso, T., Baker, M. B., & Stolper, E. M. (2003). Alkalic magmas generated by partial melting of garnet pyroxenite. *Geology*, *31*(6), 481–484. doi:10.1130/0091-7613(2003)031<0481:AMGBPM>2.0.CO;2

Hoernle, K., White, J. D. L., van den Bogaard, P., Hauff, F., Coombs, D. S., Werner, R., … Cooper, a. F. (2006). Cenozoic intraplate volcanism on New Zealand: Upwelling induced by lithospheric removal. *Earth and Planetary Science Letters*, *248*, 335–352. doi:10.1016/j.epsl.2006.06.001

Hofmann, A. W. (1997). Mantle geochemistry: the message from oceanic volcanism. *Nature*, *385*, 219–229. doi:10.1038/385219a0

Hofmann, A. W., & White, W. M. (1982). Mantle plumes from ancient oceanic crust. *Earth and Planetary Science Letters*, *57*(2), 421–436. doi:10.1016/0012-821X(82)90161-3

Hofmann, C., Courtillot, V., Féraud, G., Rochette, P., Yirgu, G., Ketefo, E., & Pik, R. (1997). Timing of the Ethiopian flood basalt event and implications for plume birth and global change. *Nature*, *389*(6653), 838–841. doi:10.1038/39853

Hole, M. J. (1988). Post-subduction alkaline volcanism along the Antarctic Peninsula. *Journal of the Geological Society*, *145*(6), 985–998. doi:10.1144/gsjgs.145.6.0985

Hole, M. J., & LeMasurier, W. E. (1994). Tectonic controls on the geochemical composition of Cenozoic, mafic alkaline volcanic rocks from West Antarctica. *Contributions to Mineralogy and Petrology*, *117*(2), 187–202. doi:10.1007/BF00286842

Hudgins, T. R., Mukasa, S. B., Simon, a. C., Moore, G., & Barifaijo, E. (2015). Melt inclusion evidence for CO_2-rich melts beneath the western branch of the East African Rift: implications for long-term storage of volatiles in the deep lithospheric mantle. *Contributions to Mineralogy and Petrology*, *169*(October), 46. doi:10.1007/s00410-015-1140-9

Huerta, A. D., & Harry, D. L. (2007). The transition from diffuse to focused extension: Modeled evolution of the West Antarctic Rift system. *Earth and Planetary Science Letters*, *255*(1–2), 133–147. doi:10.1016/j.epsl.2006.12.011

Ibs-von Seht, M., Blumenstein, S., Wagner, R., Hollnack, D., & Wohlenberg, J. (2001). Seismicity, seismotectonics and crustal structure of the southern Kenya Rift-new data from the Lake Magadi area. *Geophysical Journal International*, *146*(2), 439–453. doi:10.1046/j.0956-540x.2001.01464.x

Ionov, D. A., & Hofmann, A. W. (1995). Nb-Ta-rich mantle amphiboles and micas: Implications for subduction-related metasomatic trace element fractionations. *Earth and Planetary Science Letters*, *131*(October 2015), 341–356. doi:10.1016/0012-821X(95)00037-D

Jackson, M. G., & Dasgupta, R. (2008). Compositions of HIMU, EM1, and EM2 from global trends between radiogenic isotopes and major elements in ocean island basalts. *Earth and Planetary Science Letters*, *276*, 175–186. doi:10.1016/j.epsl.2008.09.023

Jackson, M. G., Hart, S. R., Koppers, A. a. P., Staudigel, H., Konter, J., Blusztajn, J., … Russell, J. a. (2007). The return of subducted continental crust in Samoan lavas. *Nature*, *448*(August), 684–687. doi:10.1038/nature06048

Jennings, E. S., Gibson, S. A., Maclennan, J., & Heinonen, J. S. (2017). Deep mixing of mantle melts beneath continental flood basalt provinces: Constraints from olivine-hosted melt inclusions in primitive magmas. *Geochimica et Cosmochimica Acta*. doi:10.1016/j.gca.2016.09.015

Jochum, K. P., Stoll, B., Herwig, K., Willbold, M., Hofmiann, A. W., Amini, M., Aarburg, S., Abouchami, W., Hellebrand, E., Mocek, B., Raczek, I., Stracke, A., Alard, O., Bouman, C., Becker, S., Dücking, M., Brätz, H., Klemd, R., De Bruin, D., Canil, D., Cornell, D., De Hoog, C. J., Dalpé, C., Danyushevshy, L., Eisenhauer, A., Gao, Y., Snow, J. E., Groschopf, N., Günther, D., Latkoczy, C., Guillong, M., Hauri, E. H., Höfer, H. E., Lahaye, Y., Horz, K., Jacob, D. E., Kasemann, S., Kent, A. J. R., Ludwig, T., Zack, T., Mason, P., Meixner, A., Rosner, M., Misawa, K., Nash, B. P., Pfänder, J., Premo, W. R., Sun, W. D., Tiepolo, M., Vannucci, R., Vennemann, T., Wayne, D., & Woodhead, J. D. (2005). MPI-DING reference glasses for in situ microanalysis: New reference values for element concentrations and isotope ratios. *Geochemistry, Geophysics, Geosystems*, *7*. Doi:10.1029/2005GC001060

Johnson, C. M., & Beard, B. L. (1993). Evidence from hafnium isotopes for ancient sub-oceanic mantle beneath the Rio Grande rift. *Nature*, *362*(6419), 441–444. doi:10.1038/362441a0

Johnston, A. D., & Schwab, B. E. (2004). Constraints on clinopyroxene/melt partitioning of REE, Rb, Sr, Ti, Cr, Zr, and Nb during mantle melting: First insights from direct peridotite melting experiments at 1.0 GPa. *Geochimica et Cosmochimica Acta*, *68*(23), 4949–4962. doi:10.1016/j.gca.2004.06.009

Jull, M., & McKenzie, D. (1996). The effect of deglaciation on mantle melting beneath Iceland. *Journal of Geophysical Research*, *101*, 21,815-21,828. doi:10.1029/96JB01308

Kamp, P. J. J., & Fitzgerald, P. G. (1987). Geologic constraints on the Cenozoic Antarctica-Australia-Pacific relative plate motion circuit. *Geology*, *15*(8), 694. doi:10.1130/0091-7613(1987)15<694:GCOTCA>2.0.CO;2

Keller, T., & Katz, R. F. (2016). The role of volatiles in reactive melt transport in the asthenosphere. *Journal of Petrology*, *57*(6), 1073–1108. doi:10.1093/petrology/egw030

Kempton, P. D., Fitton, J. G., Hawkesworth, C. J., & Ormerod, D. S. (1991). Isotopic and trace element constraints on the composition and evolution of the lithosphere beneath the southwestern United States. *Journal of Geophysical Research: Solid Earth*, *96*(B8), 13713–13735. doi:10.1029/91JB00373

Kiseeva, E. S., Yaxley, G. M., Hermann, J., Litasov, K. D., Rosenthal, A., & Kamenetsky, V. S. (2012). An experimental study of carbonated eclogite at 3.5-5.5 GPa-implications for silicate and carbonate metasomatism in the cratonic mantle. *Journal of Petrology*, *53*(4), 727–759. doi:10.1093/petrology/egr078

Knaack, C., S. Cornelius, & Hooper, P.R. (1994). Trace element analysis of rocks and minerals by ICP-MS Open File Report, Department of Geology, Washington State University, Washington.

Kogiso, T., Hirose, K., & Takahashi, E. (1998). Melting experiments on homogeneous mixtures of peridotite and basalt: Application to the genesis of ocean island basalts. *Earth and Planetary Science Letters*, *162*, 45–61. doi:10.1016/S0012-821X(98)00156-3

Kogiso, T., Hirschmann, M. M., & Frost, D. J. (2003). High-pressure partial melting of garnet pyroxenite: Possible mafic lithologies in the source of ocean island basalts. *Earth and Planetary Science Letters*, *216*(4), 603–617. doi:10.1016/S0012-821X(03)00538-7

Konter, J. G., & Storm, L. P. (2014). High precision $^{87}Sr/^{86}Sr$ measurements by MC-ICP-MS, simultaneously solving for Kr interferences and mass-based fractionation. *Chemical Geology*, *385*, 26–34. doi:10.1016/j.chemgeo.2014.07.009

Kyle, P. R., & Rankin, P. C. (1976). Rare earth element geochemistry of late Cenozoic alcaline lava of the McMurdo Volcanic Group, Antarctica. *Geochimica et Cosmochimica Acta*, *40*, 1497–1507.

Kyle, P. R., Moore, J. A., & Thirlwall, M. F. (1992). Petrologic evolution of anorthoclase phonolite lavas at Mount Erebus, Ross island, Antarctica. *Journal of Petrology*, *33*(4), 849–875. doi:10.1093/petrology/33.4.849

Lapen, T. J., Medaris, L. G., Johnson, C. M., & Beard, B. L. (2005). Archean to Middle Proterozoic evolution of Baltica subcontinental lithosphere: evidence from combined Sm–Nd and Lu–Hf isotope analyses of the Sandvik ultramafic body, Norway. *Contributions to Mineralogy and Petrology*, *150*(2), 131–145. doi:10.1007/s00410-005-0021-z

Lassiter, J. C., Blichert-Toft, J., Hauri, E. H., & Barsczus, H. G. (2003). Isotope and trace element variations in lavas from Raivavae and Rapa, Cook-Austral islands: Constraints on the nature of HIMU- and EM-mantle and the origin of mid-plate volcanism in French Polynesia. *Chemical Geology*, *202*, 115–138. doi:10.1016/j.chemgeo.2003.08.002

Lawver, L. A., & Gahagan, L. M. (1994). Constraints on timing of extension in the Ross Sea region, *Terra Ant.*, *1(3)*, 545-552

Le Bas, M. J. (1989). Nephelinitic and Basanitic Rocks. *Journal of Petrology*, *30*(5), 1299–1312. doi:10.1093/petrology/30.5.1299

Le Bas, M. J., Le Maitre, R. W., Streckeisen, A., & Zanettin, B. (1986). A chemical classification of volcanic rocks based on the total alkali silica diagram. *Journal of Petrology*, *27*(3), 745–750. doi:10.1093/petrology/27.3.745

Le Roux, V., Bodinier, J. L., Tommasi, a., Alard, O., Dautria, J. M., Vauchez, a., & Riches, a. J. V. (2007). The Lherz spinel lherzolite: Refertilized rather than pristine mantle. *Earth and Planetary Science Letters*, *259*, 599–612. doi:10.1016/j.epsl.2007.05.026

Le Voyer, M., Kelley, K. a., Cottrell, E., & Hauri, E. H. (2017). Heterogeneity in mantle carbon content from CO_2-undersaturated basalts. *Nature Communications*, *8*, 14062. doi:10.1038/ncomms14062

Lee, C. A., Luffi, P., & Chin, E. J. (2010). Building and Destroying Continental Mantle, (December), 59–90. doi:10.1146/annurev-earth-040610-133505

LeMasurier, W. E., & Landis, C. a. (1996). Mantle-plume activity recorded by low-relief erosion surfaces in West Antarctica and New Zealand. *Bulletin of the Geological Society of America*, *108*(11), 1450–1466. doi:10.1130/0016-7606(1996)108<1450:MPARBL>2.3.CO;2

LeMasurier, W. E., & Rex, D. C. (1989). Evolution of linear volcanic ranges in Marie Byrd Land, West Antarctica. *Journal of Geophysical Research*, *94*, 7223. doi:10.1029/JB094iB06p07223

LeMasurier, W. E., & Thomson, J. W. (1990). Volcanoes of the Antarctic Plate and Southern Oceans. (W. E. LeMasurier, J. W. Thomson, P. E. Baker, P. R. Kyle, P. D. Rowley, J. L. Smellie, & W. J. Verwoerd, Eds.), *Antarctic Research Series*. Washington, D. C.: American Geophysical Union. doi:10.1029/AR048

LeMasurier, W. E., Choi, S. H., Hart, S. R., Mukasa, S., & Rogers, N. (2016). Reconciling the shadow of a subduction signature with rift geochemistry and tectonic environment in Eastern Marie Byrd Land, Antarctica. *Lithos*, *260*, 134–153. doi:10.1016/j.lithos.2016.05.018

LeMasurier, W. E., Futa, K., Hole, M., & Kawachi, Y. (2003). Polybaric evolution of phonolite, trachyte, and rhyolite volcanoes in eastern Marie Byrd Land, Antarctica: Controls on peralkalinity and silica saturation. *International Geology Review*, *45*(October 2015), 1055–1099. doi:10.2747/0020-6814.45.12.1055

LeMasurier, W. E., Harwood, D. M., & Rex, D. C. (1994, February). Geology of Mount Murphy Volcano: an 8-m.y. history of interaction between a rift volcano and the West Antarctic ice sheet. *Geological Society of America Bulletin*. Geological Society of America. doi:10.1130/0016-7606(1994)106<0265:GOMMVA>2.3.CO;2

Luyendyk, B. P., Sorlien, C. C., Wilson, D. S., Bartek, L. R., & Siddoway, C. S. (2001). Structural and tectonic evolution of the Ross Sea rift in the Cape Colbeck region, Eastern Ross Sea, Antarctica. *Tectonics*, *20*(6), 933–958. doi:10.1029/2000TC001260

Maclennan, J. (2017). Bubble formation and decrepitation control the CO 2 content of olivine-hosted melt inclusions. *Geochemistry, Geophysics, Geosystems*, 18(2), 597–616. doi:10.1002/2016GC006633

Mallik, A., & Dasgupta, R. (2014). Effect of variable CO_2 on eclogite-derived andesite and lherzolite reaction at 3 GPa - Implications for mantle source characteristics of alkalic ocean island basalts. *Geochemistry, Geophysics, Geosystems*, *15*, 1533–1557. doi:10.1002/2014GC005251

McDonough, W. F., & Sun, S. -s. (1995). The composition of the Earth. *Chemical Geology*, *120*(3–4), 223–253. doi:10.1016/0009-2541(94)00140-4

Mckenzie, D., & Bickle, M. J. (1988). The volume and composition of melt generated by extension of the lithosphere. *Journal of Petrology*, *29*(July 1987), 625–679. doi:10.1093/petrology/29.3.625

Mechie, J., Keller, G. R., Prodehl, C., Khan, M. a., & Gaciri, S. J. (1997). A model for the structure, composition and evolution of the Kenya rift. *Tectonophysics*, *278*, 95–119. doi:10.1016/S0040-1951(97)00097-8

Michael, P. (1995). Regionally distinctive sources of depleted MORB: Evidence from trace elements and H_2O. *Earth and Planetary Science Letters*, *131*, 301–320. doi:10.1016/0012-821X(95)00023-6

Moore, G., Vennemann, T., & Carmichael, I. S. E. (1998). An empirical model for the solubility of H 2 O in magmas to 3 kilobars. *American Mineralogist*, *83*(1–2), 36–42. https://doi.org/10.1016/j.jvolgeores.2004.09.019

Morgan, W. J. (1971). Convection Plumes in the Lower Mantle. *Nature*, *230*(5288), 42–43. doi:10.1038/230042a0

Mukasa, S. B., & Dalziel, I. W. D. (2000). Marie Byrd Land, West Antarctica: Evolution of Gondwana's Pacific margin constrained by zircon U-Pb geochronology and feldspar common-Pb isotopic compositions. *Bulletin of the Geological Society of America*, *112*(4), 611–627. doi:10.1130/0016-7606(2000)112<611:MBLWAE>2.0.CO;2

Mukasa, S. B., Shervais, J. W., Wilshire, H. G., & Nielson, J. E. (1991). Intrinsic Nd, Pb, and Sr Isotopic Heterogeneities Exhibited by the Lherz Alpine Peridotite Massif, French Pyrenees. *Journal of Petrology*, (2), 117–134. doi:10.1093/petrology/Special_Volume.2.117

Nardini, I., Armienti, P., Rocchi, S., Dallai, L., & Harrison, D. (2009). Sr-Nd-Pb-H-O isotope and geochemical constraints on the genesis of Cenozoic magmas from the West Antarctic Rift. *Journal of Petrology*, *50*(7), 1359–1375. doi:10.1093/petrology/egn082

Natali, C., Beccaluva, L., Bianchini, G., & Siena, F. (2011). Rhyolites associated to Ethiopian CFB: Clues for initial rifting at the Afar plume axis. *Earth and Planetary Science Letters*, *312*(1–2), 59–68. doi:10.1016/j.epsl.2011.09.059

Natali, C., Beccaluva, L., Bianchini, G., Ellam, R. M., Savo, A., Siena, F., & Stuart, F. M. (2016). High-MgO lavas associated to CFB as indicators of plume-related thermochemical effects: The case of ultra-titaniferous picrite-basalt from the Northern Ethiopian-Yemeni Plateau. *Gondwana Research*, *34*, 29–48. doi:10.1016/j.gr.2016.02.009

Navon, O., & Stolper, E. M. (1987). Geochemical Consequences of Melt Percolation: The Upper Mantle as a Chromatographic Column. *The Journal of Geology*, *95*(3), 285–307. doi:10.1086/629131

Nelson, W. R., Furman, T., van Keken, P. E., Shirey, S. B., & Hanan, B. B. (2012). OsHf isotopic insight into mantle plume dynamics beneath the East African Rift System. *Chemical Geology*, *320–321*, 66–79. doi:10.1016/j.chemgeo.2012.05.020

Newsom, H. E., White, W. M., Jochum, K. P., & Hofmann, A. W. (1986). Siderophile and chalcophile element abundances in oceanic basalts, Pb isotope evolution and growth of the Earth's core. *Earth and Planetary Science Letters*, *80*(3–4), 299–313. doi:10.1016/0012-821X(86)90112-3

Niu, Y. L. (1997). Mantle melting and melt extraction processes beneath ocean ridges: Evidence from abyssal peridotites. *Journal of Petrology*, *38*(June), 1047–1074. doi:10.1093/petrology/38.8.1047

Nyblade, A. A., Owens, T. J., Gurrola, H., Ritsema, J., & Langston, C. A. (2000). Seismic evidence for a deep upper mantle thermal anomaly beneath east Africa. *Geology*, *28*(7), 599. doi:10.1130/0091-7613(2000)28<599:SEFADU>2.0.CO;2

Oppenheimer, C., Moretti, R., Kyle, P. R., Eschenbacher, A., Lowenstern, J. B., Hervig, R. L., & Dunbar, N. W. (2011). Mantle to surface degassing of alkalic magmas at Erebus volcano, Antarctica. *Earth and Planetary Science Letters*, *306*(3–4), 261–271. Panter, K. S., Hart, S. R., Kyle, P., Blusztanjn, J., & Wilch, T. (2000). Geochemistry of Late Cenozoic basalts from the Crary Mountains: Characterization of mantle sources in Marie Byrd Land, Antarctica. *Chemical Geology*, *165*, 215–241. doi:10.1016/S0009-2541(99)00171-0

Orlando, A., Abebe, T., Manetti, P., Santo, A. P., & Corti, G. (2006). Petrology of mantle xenoliths from Megado and Dilo, Kenya rift, Southern Ethiopia. *Ofioliti*, *31*(December), 71–87.

Panter, K. S., Blusztajn, J., Hart, S. R., Kyle, P. R., Esser, R., & McIntosh, W. C. (2006). The origin of HIMU in the SW Pacific: Evidence from intraplate volcanism in Southern New Zealand and Subantarctic Islands. *Journal of Petrology*, *47*(9), 1673–1704. doi:10.1093/petrology/egl024

Panter, K. S., Hart, S. R., Kyle, P., Blusztanjn, J., & Wilch, T. (2000). Geochemistry of Late Cenozoic basalts from the Crary Mountains: Characterization of mantle sources in Marie Byrd Land, Antarctica. *Chemical Geology*, *165*, 215–241. doi:10.1016/S0009-2541(99)00171-0

Patchett, P. J. (1983). Hafnium isotope results from mid-ocean ridges and Kerguelen. *Lithos*, *16*(1), 47–51. doi:10.1016/0024-4937(83)90033-6

Patchett, P. J., & Tatsumoto, M. (1980). Hafnium isotope variations in oceanic basalts. *Geophysical Research Letters*, *7*(12), 1077–1080. doi:10.1029/GL007i012p01077

Paton, C., Hellstrom, J., Paul, B., Woodhead, J., & Hergt, J. (2011). Iolite: Freeware for the visualisation and processing of mass spectrometric data. *Journal of Analytical Atomic Spectrometry*, *26*(January), 2508. doi:10.1039/c1ja10172b

Pearce, J. A., & Parkinson, I. J. (1993). Trace element models for mantle melting: application to volcanic arc petrogenesis. *Geological Society, London, Special Publications*, *76*(1), 373–403. doi:10.1144/GSL.SP.1993.076.01.19

Pearson, D., Canil, D., & Shirey, S. (2003). Mantle samples included in volcanic rocks: xenoliths and diamonds. *Treatise on Geochemistry*, *2*, 171–275.

Perinelli, C., Armienti, P., & Dallai, L. (2006). Geochemical and O-isotope constraints on the evolution of lithospheric mantle in the Ross Sea rift area (Antarctica). *Contributions to Mineralogy and Petrology*, *151*(3), 245–266. doi:10.1007/s00410-006-0065-8

Pertermann, M., & Hirschmann, M. (2003). Anhydrous partial melting experiments on MORB-like eclogite: phase relations, phase compositions and mineral–melt partitioning of major elements at 2–3 GPa. *Journal of Petrology*, *44*(12), 2173–2201. doi:10.1093/petrology/egg074

Pik, R., Deniel, C., Coulon, C., Yirgu, G., & Marty, B. (1999). Isotopic and trace element signatures of Ethiopian flood basalts: Evidence for plume-lithosphere interactions. *Geochimica et Cosmochimica Acta*, *63*(15), 2263–2279. doi:10.1016/S0016-7037(99)00141-6

Pik, R., Marty, B., & Hilton, D. R. (2006). How many mantle plumes in Africa? The geochemical point of view. *Chemical Geology*, *226*(3–4), 100–114. doi:10.1016/j.chemgeo.2005.09.016

Pilet, S., Baker, M., & Stolper, E. (2008). Metasomatized lithosphere and the origin of alkaline lavas. *Science*, *320*(5878), 916–919.

Pilet, S., Hernandez, J., Sylvester, P., & Poujol, M. (2005). The metasomatic alternative for ocean island basalt chemical heterogeneity. *Earth and Planetary Science Letters*, *236*(1–2), 148–166. doi:10.1016/j.epsl.2005.05.004

Portnyagin, M., Almeev, R., Matveev, S., & Holtz, F. (2008). Experimental evidence for rapid water exchange between melt inclusions in olivine and host magma. *Earth and Planetary Science Letters*, *272*(3–4), 541–552. doi:10.1016/j.epsl.2008.05.020

Ramirez, C., Nyblade, A., Hansen, S. E., Wiens, D. A., Anandakrishnan, S., Aster, R. C., Huerta, A.D., Shore, P., & Wilson, T. (2016). Crustal and upper-mantle structure beneath ice-covered regions in Antarctica from S -wave receiver functions and implications for heat flow. *Geophysical Journal International*, *204*(3), 1636–1648. https://doi.org/10.1093/gji/ggv542

Reisberg, L., & Zindler, A. (1986). Extreme isotopic variations in the upper mantle: evidence from Ronda. *Earth and Planetary Science Letters*, *81*, 29–45. doi:10.1016/0012-821X(86)90098-1

Reisberg, L., Lorand, J.-P., & Bedini, R. M. (2004). Reliability of Os model ages in pervasively metasomatized continental mantle lithosphere: a case study of Sidamo spinel peridotite xenoliths (East African Rift, Ethiopia). *Chemical Geology*, *208*(1–4), 119–140. doi:10.1016/j.chemgeo.2004.04.008

Riley, T. R., Leat, P. T., Pankhurst, R. J., & Harris, C. (2001). Origins of Large Volume Rhyolitic Volcanism in the Antarctic Peninsula and Patagonia by Crustal Melting. *Journal of Petrology*, *42*(6), 1043–1065. doi:10.1093/petrology/42.6.1043

Rilling, S. (2009). Geochronological and geochemical assessment of Cenozoic volcanism from the Terror Rift region of the West Antarctic Rift System, Ph.D. dissertation, Dep. of Geol. Sci., Univ. of Michigan, Ann Arbor, Michigan, USA.

Rilling, S., Mukasa, S., Wilson, T., Lawver, L., & Hall, C. (2009). New determinations of $^{40}Ar/^{39}Ar$ isotopic ages and flow volumes for Cenozoic volcanism in the Terror Rift, Ross Sea, Antarctica. *Journal of Geophysical Research: Solid Earth*, *114*(B12). doi:10.1029/2009JB006303

Ritsema, J., Nyblade, A. A., Owens, T. J., Langston, C. A., & VanDecar, J. C. (1998). Upper mantle seismic velocity structure beneath Tanzania, east Africa: Implications for the stability of cratonic lithosphere. *Journal of Geophysical Research: Solid Earth*, *103*(B9), 21201–21213. doi:10.1029/98JB01274

Ritzwoller, M. H., Shapiro, N. M., Levshin, A. L., & Leahy, G. M. (2001). Crustal and upper mantle structure beneath Antarctica and surrounding oceans. *Journal Of Geophysical Research-Solid Earth*, *106*(12), 30645–30670. doi:10.1029/2001JB000179

Rocchi, S. (2002). Cenozoic magmatism in the western Ross Embayment: Role of mantle plume versus plate dynamics in the development of the West Antarctic Rift System. *Journal of Geophysical Research*, *107*(B9). doi:10.1029/2001JB000515

Rocchi, S., Tonarini, S., Armienti, P., Innocenti, F., & Manetti, P. (1998). Geochemical and isotopic structure of the early Palaeozoic active margin of Gondwana in northern Victoria Land, Antarctica. *Tectonophysics*, *284*, 261–281. doi:10.1016/S0040-1951(97)00178-9

Rocholl, A., Stein, M., Molzahn, M., Hart, S. R., & Wörner, G. (1995). Geochemical evolution of rift magmas by progressive tapping of a stratified mantle source beneath the Ross Sea Rift, Northern Victoria Land, Antarctica. *Earth and Planetary Science Letters*, *131*, 207–224. doi:10.1016/0012-821X(95)00024-7

Rogers, N., Macdonald, R., & Fitton, J. (2000). Two mantle plumes beneath the East African rift system: Sr, Nd and Pb isotope evidence from Kenya Rift basalts. *Earth and Planetary …*, *176*, 387–400.

Rogers, N. W. (2006). Basaltic magmatism and the geodynamics of the East African Rift System. *Geological Society, London, Special Publications*, *259*(1), 77–93. https://doi.org/10.1144/GSL.SP.2006.259.01.08

Rooney, T. O., Hanan, B. B., Graham, D. W., Furman, T., Blichert-Toft, J., & Schilling, J.-G. (2012a). Upper Mantle Pollution during Afar Plume-Continental Rift Interaction. *Journal of Petrology*, *53*(2), 365–389. doi:10.1093/petrology/egr065

Rooney, T. O., Hart, W. K., Hall, C. M., Ayalew, D., Ghiorso, M. S., Hidalgo, P., & Yirgu, G. (2012b). Peralkaline magma evolution and the tephra record in the Ethiopian Rift. *Contributions to Mineralogy and Petrology*, *164*, 407–426. doi:10.1007/s00410-012-0744-6

Rooney, T. O., Herzberg, C., & Bastow, I. D. (2012c). Elevated mantle temperature beneath East Africa. *Geology*, *40*(1), 27–30. doi:10.1130/G32382.1

Rooney, T. O., Nelson, W. R., Dosso, L., Furman, T., & Hanan, B. (2014). The role of continental lithosphere metasomes in the production of HIMU-like magmatism on the northeast African and Arabian plates. *Geology*, *42*(5), 419–422. doi:10.1130/G35216.1

Rossetti, F., Storti, F., Busetti, M., Lisker, F., Di Vincenzo, G., Laufer, A. L., … Salvini, F. (2006). Eocene initiation of Ross Sea dextral faulting and implications for East Antarctic neotectonics. *Journal of the Geological Society*, *163*(1), 119–126. doi:10.1144/0016-764905-005

Rowe, M. C., & Lassiter, J. C. (2009). Chlorine enrichment in central Rio Grande Rift basaltic melt inclusions: Evidence for subduction modification of the lithospheric mantle. *Geology*, *37*(5), 439–442. doi:10.1130/g25530a.1\r10.1029/ TC003i007p00741

Rudnick, R. L., McDonough, W. F., & Chappell, B. W. (1993). Carbonatite metasomatism in the northern Tanzanian mantle: Petrographic and geochemical characteristics. *Earth and Planetary Science Letters*, *114*(4), 463–475. https://doi.org/10.1016/0012-821X(93)90076-L

Ruppel, C. (1995). Extensional processes in continental lithosphere. *Journal of Geophysical Research*, *100*, 24187. doi:10.1029/95JB02955

Saal, A. E., Hauri, E. H., Langmuir, C. H., & Perfit, M. R. (2002). Vapour undersaturation in primitive mid-ocean-ridge basalt and the volatile content of Earth's upper mantle. *Nature*, *419*(6906), 451–455. doi:10.1038/nature01073

Salters, V. J. M., & Hart, S. R. (1991). The mantle sources of ocean ridges, islands and arcs: the Hf-isotope connection. *Earth and Planetary Science Letters*, *104*(2–4), 364–380. doi:10.1016/0012-821X(91)90216-5

Salters, V. J. M., & White, W. M. (1998). Hf isotope constraints on mantle evolution. *Chemical Geology*, *145*, 447–460. doi:10.1016/S0009-2541(97)00154-X

Salvini, F., Brancolini, G., Busetti, M., Storti, F., Mazzarini, F., & Coren, F. (1997). Cenozoic geodynamics of the Ross Sea region, Antarctica: Crustal extension, intraplate strike-slip faulting, and tectonic inheritance. *Journal of Geophysical Research: Solid Earth*, *102*(B11), 24669–24696. doi:10.1029/97JB01643

Schilling, J., Bergeron, M., & Evans, R. (1980). Halogens in the Mantle Beneath the North Atlantic. *Philosophical Transactions of the Royal Society of London Series A Mathematical and Physical Sciences*, *297*(1431), 147–178. Retrieved from http://rsta.royalsocietypublishing.org/content/297/1431/147.short

Sgualdo, P., Aviado, K., Beccaluva, L., Bianchini, G., Blichert-Toft, J., Bryce, J. G., … Siena, F. (2015). Lithospheric mantle evolution in the Afro-Arabian domain: Insights from Bir Ali mantle xenoliths (Yemen). *Tectonophysics*, *650*, 3–17. doi:10.1016/j.tecto.2014.11.025

Shaw, J. E., Baker, J. a., Kent, a. J. R., Ibrahim, K. M., & Menzies, M. a. (2007). The geochemistry of the Arabian lithospheric mantle - A source for intraplate volcanism? *Journal of Petrology*, *48*(8), 1495–1512. doi:10.1093/petrology/egm027

Siddoway, C. S., Baldwin, S. L., Fitzgerald, P. G., Fanning, C. M., & Luyendyk, B. P. (2004). Ross sea mylonites and the timing of intracontinental extension within the West Antarctic rift system. *Geology*, *32*(1), 57–60. doi:10.1130/G20005.1

Sieminski, A., Debayle, E., & Lévêque, J. J. (2003). Seismic evidence for deep low-velocity anomalies in the transition zone beneath West Antarctica. *Earth and Planetary Science Letters*, *216*, 645–661. doi:10.1016/S0012-821X(03)00518-1

Sims, K. W. W., Maclennan, J., Blichert-Toft, J., Mervine, E. M., Blusztajn, J., & Grönvold, K. (2013). Short length scale mantle heterogeneity beneath Iceland probed by glacial modulation of melting. *Earth and Planetary Science Letters*. doi:10.1016/j.epsl.2013.07.027

Stefano, C. J., Mukasa, S. B., Andronikov, a., & Leeman, W. P. (2010). Water and other volatile systematics of olivine-hosted melt inclusions from the Yellowstone hotspot track. *Contributions to Mineralogy and Petrology*, *161*(4), 615–633. doi:10.1007/s00410-010-0553-8

Stein, M., Navon, O., & Kessel, R. (1997). Chromatographic metasomatism of the Arabian—Nubian lithosphere. *Earth and Planetary Science Letters*, *152*, 75–91. doi:10.1016/S0012-821X(97)00156-8

Stern, R. J., Ali, K. A., Abdelsalam, M. G., Wilde, S. A., & Zhou, Q. (2012). U–Pb zircon geochronology of the eastern part of the Southern Ethiopian Shield. *Precambrian Research*, *206–207*, 159–167. doi:10.1016/j.precamres.2012.02.008

Storey, B. C., Leat, P. T., & Ferris, J. K. (2001). The location of mantle-plume centers during the initial stages of Gondwana breakup. In *Special Paper 352: Mantle plumes: their identification through time* (Vol. 352, pp. 71–80). Geological Society of America. doi:10.1130/0-8137-2352-3.71

Storti, F., Balestrieri, M. L., Balsamo, F., & Rossetti, F. (2008). Structural and thermochronological constraints to the evolution of the West Antarctic Rift System in central Victoria Land. *Tectonics*, *27*(4). doi:10.1029/2006TC002066

Stracke, A., Bizimis, M., & Salters, V. J. M. (2003). Recycling oceanic crust: Quantitative constraints. *Geochemistry, Geophysics, Geosystems*, *4*(3). doi:10.1029/2001GC000223

Stracke, A., Hofmann, A. W., & Hart, S. R. (2005). FOZO, HIMU, and the rest of the mantle zoo. *Geochemistry, Geophysics, Geosystems*, *6*(5), n/a-n/a. doi:10.1029/2004GC000824

Stracke, A., Snow, J. E., Hellebrand, E., von der Handt, A., Bourdon, B., Birbaum, K., & Günther, D. (2011). Abyssal peridotite Hf isotopes identify extreme mantle depletion. *Earth and Planetary Science Letters*, *308*(3–4), 359–368. doi:10.1016/j.epsl.2011.06.012

Sun, S. -s., & McDonough, W. F. (1989). Chemical and isotopic systematics of oceanic basalts: implications for mantle composition and processes. *Geological Society, London, Special Publications*, *42*(1), 313–345. doi:10.1144/GSL.SP.1989.042.01.19

Teklay, M., Scherer, E. E., Mezger, K., & Danyushevsky, L. (2010). Geochemical characteristics and Sr–Nd–Hf isotope compositions of mantle xenoliths and host basalts from Assab,

Eritrea: implications for the composition and thermal structure of the lithosphere beneath the Afar Depression. *Contributions to Mineralogy and Petrology*, *159*(5), 731–751. doi:10.1007/s00410-009-0451-0

Thomas, R. J., Roberts, N. M. W., Jacobs, J., Bushi, A. M., Horstwood, M. S. A., & Mruma, A. (2013). Structural and geochronological constraints on the evolution of the eastern margin of the Tanzania Craton in the Mpwapwa area, central Tanzania. *Precambrian Research*, *224*, 671–689. doi:10.1016/j.precamres.2012.11.010

Thorpe, R. S., & Smith, K. (1974). Distribution of Cenozoic volcanism in Africa. *Earth and Planetary Science Letters*, *22*(1), 91–95. doi:10.1016/0012-821X(74)90068-5

Toramaru, A., & Fujii, N. (1986). Connectivity of melt phase in a partially molten peridotite. *Journal of Geophysical Research*, *91*(B9), 9239. doi:10.1029/JB091iB09p09239

Trail, D., Bruce Watson, E., & Tailby, N. D. (2012). Ce and Eu anomalies in zircon as proxies for the oxidation state of magmas. *Geochimica et Cosmochimica Acta*, *97*, 70–87. doi:10.1016/j.gca.2012.08.032

Trey, H., Cooper, A. K., Pellis, G., della Vedova, B., Cochrane, G., Brancolini, G., & Makris, J. (1999). Transect across the West Antarctic rift system in the Ross Sea, Antarctica. *Tectonophysics*, *301*(1–2), 61–74. doi:10.1016/S0040-1951(98)00155-3

Trua, T., Esperança, S., & Mazzuoli, R. (1998). The evolution of the lithospheric mantle along the N. African Plate: geochemical and isotopic evidence from the tholeiitic and alkaline volcanic rocks of the Hyblean plateau, Italy. *Contributions to Mineralogy and Petrology*, *131*, 307–322. doi:10.1007/s004100050395

van Wijk, J., van Hunen, J., & Goes, S. (2008). Small-scale convection during continental rifting: Evidence from the Rio Grande rift. *Geology*, *36*(7), 575–578. doi:10.1130/G24691A.1

Vervoort, J. (2014). Lu-Hf Dating : The Lu-Hf Isotope System Lu-Hf Dating : The Lu-Hf Isotope System. *Encyclopedia of Scientific Dating Methods*, (January). doi:10.1007/978-94-007-6326-5

Vervoort, J. D., & Blichert-Toft, J. (1999). Evolution of the depleted mantle: Hf isotope evidence from juvenile rocks through time. *Geochimica et Cosmochimica Acta*, *63*(3–4), 533–556. doi:10.1016/S0016-7037(98)00274-9

Vervoort, J., & Patchett, P. (1999). Relationships between Lu–Hf and Sm–Nd isotopic systems in the global sedimentary system. *Earth and Planetary …*, *168*, 79–99. Retrieved from http://www.sciencedirect.com/science/article/pii/S0012821X99000473

Vetel, W., & Le Gall, B. (2006). Dynamics of prolonged continental extension in magmatic rifts: the Turkana Rift case study (North Kenya). *Geological Society, London, Special Publications*, *259*(1), 209–233. doi:10.1144/GSL.SP.2006.259.01.17

Vogel, T. a., Flood, T. P., Patino, L. C., Wilmot, M. S., Maximo, R. P. R., Arpa, C. B., … Stimac, J. a. (2006). Geochemistry of silicic magmas in the Macolod Corridor, SW Luzon, Philippines: Evidence of distinct, mantle-derived, crustal sources for silicic magmas. *Contributions to Mineralogy and Petrology*, *151*, 267–281. doi:10.1007/s00410-005-0050-7

Walter, M. J. (1998). Melting of Garnet Peridotite and the Origin of Komatiite and Depleted Lithosphere. *Journal of Petrology*, *39*(1), 29–60. doi:10.1093/petroj/39.1.29

Watson, T., Nyblade, A., Wiens, D. a., Anandakrishnan, S., Benoit, M., Shore, P. J., … VanDecar, J. (2006). P and S velocity structure of the upper mantle beneath the Transantarctic Mountains, East Antarctic craton, and Ross Sea from travel time tomography. *Geochemistry, Geophysics, Geosystems*, *7*(7), n/a-n/a. doi:10.1029/2005GC001238

Weaver, B. L. (1991). The origin of ocean island basalt end-member compositions: trace element and isotopic constraints. *Earth and Planetary Science Letters*, *104*, 381–397. doi:10.1016/0012-821X(91)90217-6

Weiss, Y., Class, C., Goldstein, S. L., & Hanyu, T. (2016). Key new pieces of the HIMU puzzle from olivines and diamond inclusions. *Nature*, *537*(7622), 666–670. doi:10.1038/nature19113

White, R. S., McKenzie, D., & O'Nions, R. K. (1992). Oceanic crustal thickness from seismic measurements and rare earth element inversions. *Journal of Geophysical Research*, *97*(Table 2), 19683. doi:10.1029/92JB01749

White, W. M., Albarède, F., & Télouk, P. (2000). High-precision analysis of Pb isotope ratios by multi-collector ICP-MS. *Chemical Geology*, *167*(3–4), 257–270. doi:10.1016/S0009-2541(99)00182-5

White, W., & Hofmann, A. (1982). Sr and Nd isotope geochemistry of oceanic basalts and mantle evolution. *Nature*, *296*(29), 821–825. Retrieved from http://www.nature.com/nature/journal/v296/n5860/abs/296821a0.html

Wilch, T. I., & McIntosh, W. C. (2000). Eocene and Oligocene volcanism at Mount Petras, Marie Byrd Land: implications for middle Cenozoic ice sheet reconstructions in West Antarctica. *Antarctic Science*, *12*(4), 477–491. doi:10.1017/S0954102000000560

Willbold, M., & Stracke, A. (2006). Trace element composition of mantle end-members: Implications for recycling of oceanic and upper and lower continental crust. *Geochemistry, Geophysics, Geosystems*, *7*(4), G04004. doi:10.1029/2005GC001005

Willbold, M., & Stracke, A. (2010). Formation of enriched mantle components by recycling of upper and lower continental crust. *Chemical Geology*, *276*(3–4), 188–197. doi:10.1016/j.chemgeo.2010.06.005

Wilson, T. J., Lawver, L. A., Henrys, S. A., Mukasa, S., Horgan, H., Weiderspahn, M., Davis, M., Whittaker, J., Lowe, A., & Watson, M. (2004). Cruise Report NBP0401 19 January to 18 February 2004 - McMurdo Station to McMurdo Station, Ross Sea, Antarctica, *Institute of Geological and Nuclear Sciences Science Report, 2004/03,* 85

Wittig, N., Baker, J. a., & Downes, H. (2007). U–Th–Pb and Lu–Hf isotopic constraints on the evolution of sub-continental lithospheric mantle, French Massif Central. *Geochimica et Cosmochimica Acta*, *71*(5), 1290–1311. doi:10.1016/j.gca.2006.11.025

Wolfenden, E., Ebinger, C., Yirgu, G., Deino, A., & Ayalew, D. (2005). Evolution of the northern Main Ethiopian rift: birth of a triple junction. *Earth and Planetary Science Letters*, *224*(1–2), 213–228. doi:10.1016/j.epsl.2004.04.022

Woodhead, J. D. (1996). Extreme HIMU in an oceanic setting: the geochemistry of Mangaia Island (Polynesia), and temporal evolution of the Cook—Austral hotspot. *Journal of Volcanology and Geothermal Research*, *72*(1–2), 1–19. doi:10.1016/0377-0273(96)00002-9

Wörner, G. (1999). Lithospheric dynamics and mantle sources of alkaline magmatism of the Cenozoic West Antarctic Rift System. *Global and Planetary Change*, *23*, 61–77. doi:10.1016/S0921-8181(99)00051-X

Zack, T., & Brumm, R. (1998). Ilmenite/liquid partition coefficients of 26 trace elements determined through ilmenite/clinopyroxene partitioning in garnet pyroxene. In: 7th International Kimberlite Conference. Gurney, J.J., Gurney, J.L., Pascoe, M.D. and Richardson, S.H. (Editors), Red Roof Design, Cape Town. 986-988.

Zhao, D. (2007). Seismic images under 60 hotspots: Search for mantle plumes. *Gondwana Research*, *12*(4), 335–355. doi:10.1016/j.gr.2007.03.001

Zipfel, J., & Worner, G. (1992). Four- and five-phase peridotites from a continental rift system: evidence for upper mantle uplift and cooling at the Ross Sea margin (Antarctica). *Contrib. Mineral. Petrol., 111,* 24-36. doi:10.1007/BF00296575